Linear, Nonlinear, and Tunable Guided Wave Modes for High-Power (GaAl)As Semiconductor Lasers

Thesis by

David Glenn Mehuys

In Partial Fulfillment of the Requirements
for the Degree of
Doctor of Philosophy

California Institute of Technology
Pasadena, California
1990
(Submitted June 28, 1989)

To

Mom and Dad

Acknowledgements

First, I would like to thank my thesis advisor, Amnon Yariv, for providing a most stimulating and creative environment in which to engage in graduate study. In addition to interactions with him and with the ensemble of talented people that form his research group, I have benefited greatly from the facilities that have evolved under his guidance through several generations of graduate students.

Second, I would like to extend my deepest gratitude to my colleague and office-mate, Michael Mittelstein. His keen physical insight, practical wisdom, and words of encouragement were not only a constant inspiration, but added immensely to my knowledge of quantum electronics and optics. I remember very fondly many sessions at the whiteboard, the testing stage, and with a very non-compliant reactive ion etcher.

Third, I would like to thank several other members of Professor Yariv's group from whose collaboration I greatly benefited. Chris Lindsey and Kaz Mitsunaga taught me much about basic semiconductor laser fabrication and testing. Lars Eng provided, through many iterations of MBE growth, the bulk of the high quality, quantum well material used in my experiments. I am also indebted to Jeff Ungar and Rona Sarfaty of Ortel Corporation for providing MOCVD material. Joseph Salzman, Bill Marshall, and Robert Lang helped to guide my work through countless fruitful hours of discussion.

Fourth, I thank Jana Mercado for her encouragement and advice on non-technical matters, Desmond Armstrong and Ali Ghaffari for expert technical assistance, and Paula Samazan for helping me utilize Caltech's libraries efficently.

In addition, I must thank Aaron Fenster and his group at Toronto General Hospital for showing me how much fun a research environment can be. Also at the University of Toronto, many discussions with Jeff Hall and Sergei Dmitrevsky contributed strongly to my decision to attend graduate school in general, and Caltech in particular.

Finally, I am indebted most of all to my friends and family for their continued support, and for reminding me not to let school "get in the way" of a good education. To Charlotte Newcomb: through our time together over the past 10 months, I have grown intellectually, emotionally, and spiritually. Our friendship has been the most rewarding element of my Caltech experience, and from it I draw the strength to meet new challenges. And to Mom and Dad, Bruce and Glenn, and Grandpa: your unfailing love and encouragement have sustained and uplifted me for almost five years here, and provided me with a refuge when I needed it most. It is with great pleasure that I share this accomplishment with you.

Abstract

High-power, coherent radiation from semiconductor lasers is attractive for such diverse applications as free-space communication, optical data storage, and microsurgery. However, several factors conspire to prevent near-ideal performance from broad area devices and laser arrays. Waveguides wider than a few microns support many lateral modes with poor gain discrimination. Consequently, such modes are easily "mixed" by perturbations in gain and refractive index caused by gain saturation, thermal gradients, and inhomogeneities that are due to imperfect crystal growth. This causes spatially localized modes, multimode operation, and reduced spatial coherence, all of which lead to farfields broader than the "diffraction limit."

In this thesis, we have investigated the influence of gain saturation on the lateral modes of broad area structures and laser arrays. Analytical and numerical techniques have been developed to solve self-consistently for mode shapes and propagation constants as a function of injected current density above threshold. For example, our analysis indicates that the gain-saturated modes of broad area lasers consist of an integer number of phase-locked "filaments." In gain-guided quantum well lasers, these nonlinear modes are observed to oscillate into narrow, single-lobed farfields, which broaden only slightly with increased power output up to the 500 mW level. Conversely, laser arrays have been widely touted as structures that suppress unwanted filamentation in favor of spatial mode control. Indeed, in this work we have demonstrated supermode control at the 100 mW power level by varying the diffraction region length in diffraction-coupled arrays. Both theoretically and experimentally, however, we have found the lateral modes of laser arrays to be unstable with increased current injection. Waveguides that are phase-matched below threshold become detuned under the influence of gain saturation, so that interguide power transfer is reduced. This decreases the injection-locking bandwidth, and ultimately, the spatial coherence. While undesirable for a laser oscillator, this property may be attractive for all-optical switching in nonlinear directional couplers.

Finally, we have considered marrying the high-power, coherent output of broad area lasers and laser arrays with the broadband tunability possible in semiconductor lasers. In particular, the steplike density of states unique to quantum well structures results in gain spectra that are broader and flatter than comparable spectra of double heterostructure lasers. Experimentally, we have tuned uncoated, single quantum well stripe lasers in a grating-coupled external cavity over a range >125 nm centered about 800 nm. Similarly tuned broad area lasers output in excess of 200 mW (pulsed) into a single longitudinal mode over 80 nm, and buried heterostructure lasers were operated continuously over 90 nm. We expect that in the future, such devices could provide a compact, rugged, more efficient alternative to dye lasers.

Table of Contents

Chapter One

Introduction

Chapter Two

Nonlinear Lateral Modes of Broad Area Lasers

Chapter Three

Asymmetric Tailored-Gain Broad Area Lasers

Chapter Four

(GaAl)As Laser Tunable Over 125 nm

Chapter Five

Coupled-Wave Model for Multiple Stripe Semiconductor Lasers

Chapter Six

Supermode Control in Diffraction-Coupled Laser Arrays

Chapter Seven

Nonlinear Lateral Modes of Laser Arrays

CHAPTER

One

Introduction

1.0 Introduction

Semiconductor lasers fabricated from III-V materials such as $Ga_{1-x}Al_xAs$ and $Ga_{1-x}In_xAs_{1-y}P_y$ have the potential to provide inexpensive, compact, and efficient sources of coherent radiation in the infrared (IR) wavelength region 650-1550 *nm*. Near IR wavelengths from 750-880 *nm* are accessed by $Ga_{1-x}Al_xAs$ and find applications in optical data storage, free-space communication, solid-state laser pumps (*e.g.,* Nd:YAG), short-haul fiber optic communications, laser printers, and compact disc players. Also, much of the basic physics has been gleaned from this material system because the maturing growth techniques of molecular beam epitaxy (MBE) and metal organic chemical vapor deposition (MOCVD) allow for the fabrication of near-ideal heterostructures. Longer IR wavelengths between 1000 and 1550 *nm* are accessed by the quaternary system $Ga_{1-x}In_xAs_{1-y}P_y$ and bracket the minimum loss and group velocity dispersion wavelengths of silica optical fibers at 1300 and 1550 *nm*, respectively. This is therefore the material of choice on which to base long-haul fiber optic communication systems. In addition, visible and near-visible wavelengths from 650-750 *nm* are currently a subject of great interest. For example, red lasers based on (GaAl)(InP) are commercially attractive as replacements for HeNe lasers at 633 *nm* in such products as bar-code scanners and laser pointers. More exciting are potential medical applications such as photodynamic therapy

(PDT), whereby photosensitive drugs are activated, *in vivo*, under optical irradiation piped down an endoscope to release a prescribed chemical dose for local tumor treatment. At present, such drugs are photosensitive only at HeNe wavelengths, but effort is under way to develop others that absorb at near IR wavelengths to take advantage of the reduced tissue absorption there and the high power available from (GaAl)As semiconductor lasers.

In this thesis, we have targeted high-power, coherent, broadband tunable devices for applications in space, medicine, spectroscopy or wherever organic dye lasers have been utilized as IR sources. The prospect of supplanting a table-top, optically pumped instrument that is less than 1% energy efficient with a rugged, current-pumped, 50% efficient semiconductor laser smaller than a grain of salt is very attractive. As such, our research has dwelled on characterizing the above-threshold regime of wide-aperture semiconductor lasers and laser arrays, which currently offer output power in the 0.1-1.0 Watt regime. Figure 1.1 gives a sketch of the power and beam performance currently available commercially, in addition to the requirement for space-based communication, for example.

In particular, the influence of gain saturation nonlinearities has been emphasized here in order to clarify the "ideal" performance level to which such devices aspire. Analytical and numerical techniques have been developed to solve self-consistently for electromagnetic modes and their propagation constants as a function of injected current density above threshold. Experimental fabrication and characterization of a number of device geometries in (GaAl)As have been achieved. Quantum well lasers have been used exclusively because of their superior characteristics, especially with regard to overall energy efficiency and broadband tuning capability.

In this chapter, the groundwork will be laid with respect to the interaction of radiation and matter in quantum well heterostructures. Concepts of gain and loss,

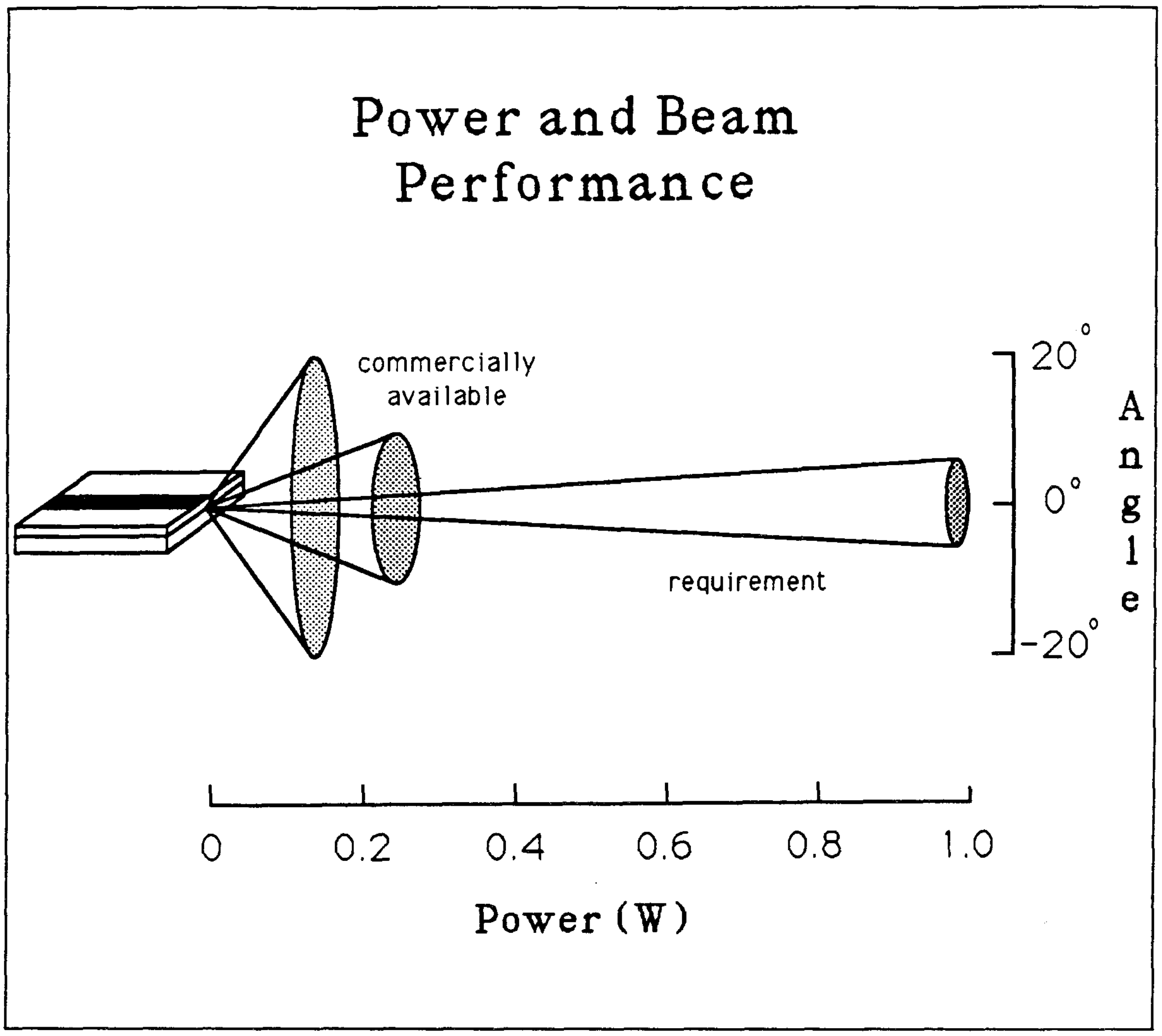

Figure 1.1 Commercially available semiconductor lasers at 850 nm emit approximately 100 mW of power into a beamwidth 4^o by 10^o. The requirement for space-based communication is closer to 1 Watt into a circular spot a few degrees in diameter.

index and gain waveguiding, and gain saturation are reviewed in order to extract the relevant quantities for the design and characterization of high-power semiconductor lasers. In addition, reviewing these basic concepts places all subsequent approximations and assumptions in the foreground.

1.1 Lasing in Semiconductors

The general requirements for laser oscillation are gain and feedback, as shown in Figure 1.2(a). In a semiconductor, the feedback can be conveniently provided by facets cleaved along parallel crystalline planes. The GaAs/air interface has a Fresnel reflectivity of 0.31, so that with moderate internal distributed losses, the photon lifetime inside the cavity is approximately a few round trips, providing sufficient feedback for lasing. Gain is achieved by providing a population inversion within the semiconductor, as is obtained conveniently at the junction of a forward-biased, degenerately doped *pn* junction. Figures 1.2(b) and (c) illustrate these concepts within a homojunction diode laser, as first demonstrated[1-3] in 1962. Such lasers could be fabricated via a simple *p*-diffusion into an *n*-type substrate, and threshold current densities on the order of $J_{th} \simeq 10\ kA/cm^2$ were achieved.

Since this first demonstration of lasing in GaAs, there have been two "quantum leaps" in the technology which have significantly advanced the state-of-the-art. The first, in 1969, was the invention of the double-heterostructure (DH) laser[4,5]. This innovation made possible continuous wave (CW) operation of (GaAl)As diode lasers at room temperature. Figure 1.3 shows the conduction and valence band edges of the diode under full forward bias. By sandwiching a thin layer ($\simeq$ 0.1-0.2 μm) of undoped, low-bandgap, high refractive index GaAs between two cladding layers (one *p*-doped, the other *n*-doped) of higher bandgap, lower refractive index (GaAl)As, a dielectric waveguide is formed which tightly confines the optical mode to the "active" region where the population inversion is established. This strong overlap between optical mode and active region provides efficient use of the injected carriers in supplanting the inherent absorption with gain. DH laser structures in the 1960's and 1970's were grown primarily by liquid phase epitaxy (LPE) and achieved threshold current densities on the order of $J_{th} \simeq 1\ kA/cm^2$.

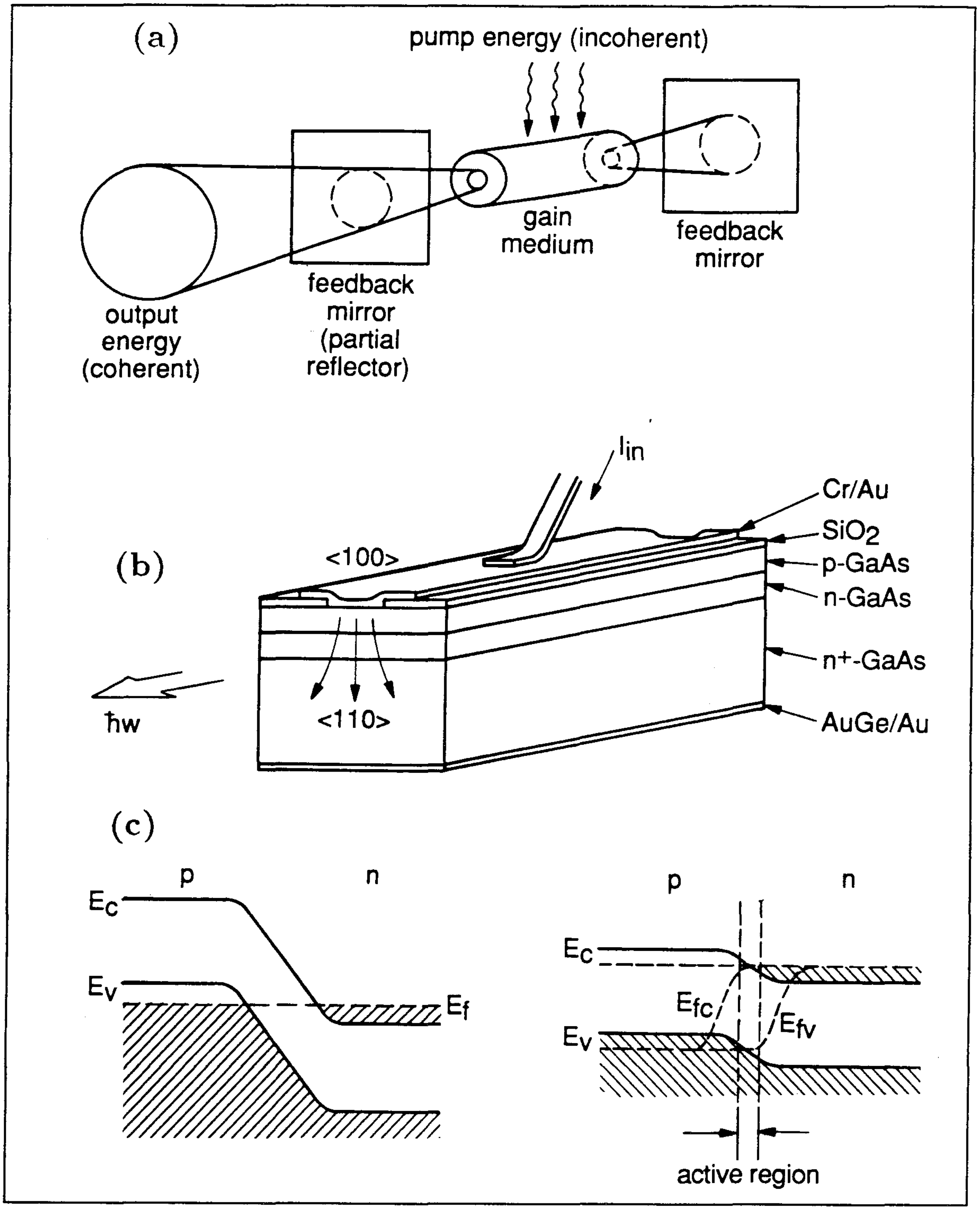

Figure 1.2 (a) The general requirements for laser oscillation are gain and feedback, as shown schematically here. (b) The homojunction GaAs semiconductor laser (*c.*1962) pumped by electrical current satisfies the requirements of (a). (c) Band diagram perpendicular to the junction with no bias (left) and with strong forward bias (right). Population inversion (and hence gain) is created at the junction.

The second quantum leap occurred with the introduction of *separate* confinement heterostructures for the charge carriers and for the transverse optical radiation field. In particular, since 1981, the graded-index, separate-confinement heterostructure single quantum well (GRINSCH-SQW) laser[6] has become an industry standard. Figure 1.3 shows the corresponding band diagram and waveguide profiles for this new laser. The width of the inner heterostructure (*i.e.,* the quantum well) is made comparable to the deBroglie wavelength of electrons ($\simeq 75\ \AA$ at room temperature, for an electron energy of kT). As a result, the properties of the QW-confined charge carriers differ from the DH case to reflect the 2-dimensional nature of the carrier gas. The consequences are important, for example, with respect to tunability and linewidth. Furthermore, the reduction in active volume by about a factor of 10 from the DH case reduces the absorption of the optical mode under zero pumping by a proportional amount. Thus threshold current densities as low as $J_{th} \simeq 0.1$ kA/cm^2 have been achieved[7]. As shown, the outer heterostructure is not abrupt, but is *graded* in order to funnel carriers down smoothly to the quantum well (QW) (through electron-electron and electron-phonon interactions), where they become trapped and recombine. The overall width ($\simeq 0.4\ \mu$m) and refractive index step ($\simeq 0.2$) of the GRIN layers are chosen so that the waveguide so formed supports only the fundamental transverse optical mode, as shown in Figure 1.3. To fabricate such a complex structure with high precision requires very sophisticated epitaxial growth techniques, and the success of the GRINSCH-SQW laser owes much to the maturity of MBE and MOCVD technologies.

1.2 Carrier-Induced Gain and Refractive Index

The interaction between radiation and matter that takes place inside a semiconductor laser is manifest in the complex-valued dielectric constant $\epsilon(\omega)$ – that is, as a property of the medium, which is seen by traveling electromagnetic waves of

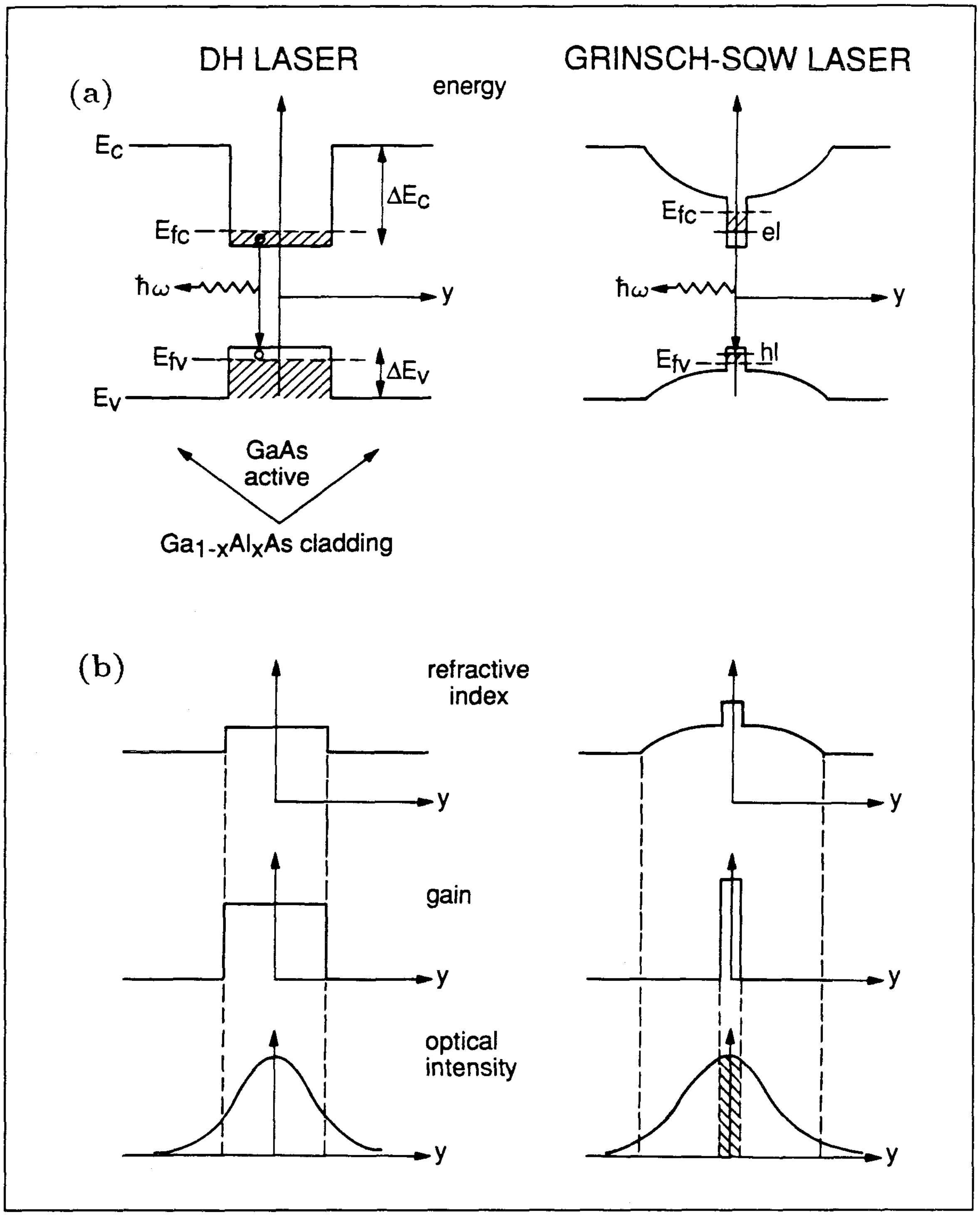

Figure 1.3 The double heterostructure (DH) laser (left) vs. the graded-index, separate-confinement heterostructure, single quantum well (GRINSCH-SQW) laser (right). (a) Band diagrams under full forward bias. (b) Gain and refractive index profiles perpendicular to the junction plus the transverse optical modes which they support.

radian frequency ω. In actual fact, the material response to an electric field is manifest as the polarization, rather than as the electric field, so that the fundamental quantity is not the dielectric constant $\epsilon(\omega)$ but the susceptibility $X(\omega)$, related to ϵ via

$$\epsilon(\omega) = \epsilon_0\big(1 + X(\omega)\big) \tag{1.1}$$

where ϵ_0 is the permittivity of free space. We distinguish between the resonant component $\chi(\omega)$ and the non-resonant component χ_0 of the semiconductor susceptibility: $X(\omega) = \chi_0 + \chi(\omega)$. Hence, $(1 + \chi_0) \equiv n_0^2$, where n_0 is the non-resonant refractive index. The *resonant* component of the susceptibility is complex-valued:

$$\chi(\omega) = \chi_r(\omega) + i\chi_i(\omega) \tag{1.2}$$

to allow for changes in the phase ($\chi_r(\omega) \leftrightarrow$ dispersion) and amplitude ($\chi_i(\omega) \leftrightarrow$ gain) of electromagnetic waves propagating in such a medium (see Equation (1.7)). In gas lasers and solid-state lasers, such as Nd:YAG, the active species are mutually decoupled so that the radiation field can be considered as interacting with a collisionally broadened 2-level system. In this simpler case, the resonant susceptibility $\widehat{\chi}$ can be written[8]

$$\begin{aligned} \widehat{\chi}_r(\omega) &= A\big[f_c(\omega) - f_v(\omega)\big]\frac{\omega_0 - \omega}{(\omega_0 - \omega)^2 + 1/T_2^2} \\ \widehat{\chi}_i(\omega) &= A\big[f_c(\omega) - f_v(\omega)\big]\frac{1/T_2}{(\omega_0 - \omega)^2 + 1/T_2^2} \end{aligned} \tag{1.3}$$

where ω_0 is the frequency of the optical field, $\hbar\omega$ is the energy separation of the states of the 2-level system, T_2 is the mean time between phase-destroying collisions (*i.e.*, phase-damping time), f_c and f_v are the occupation factors of the upper and lower states, and A is a constant proportional to the dipole matrix element.

In a semiconductor, the active states are blurred into *bands* in accordance with the Pauli exclusion principle, the upper transition "level" being the conduction

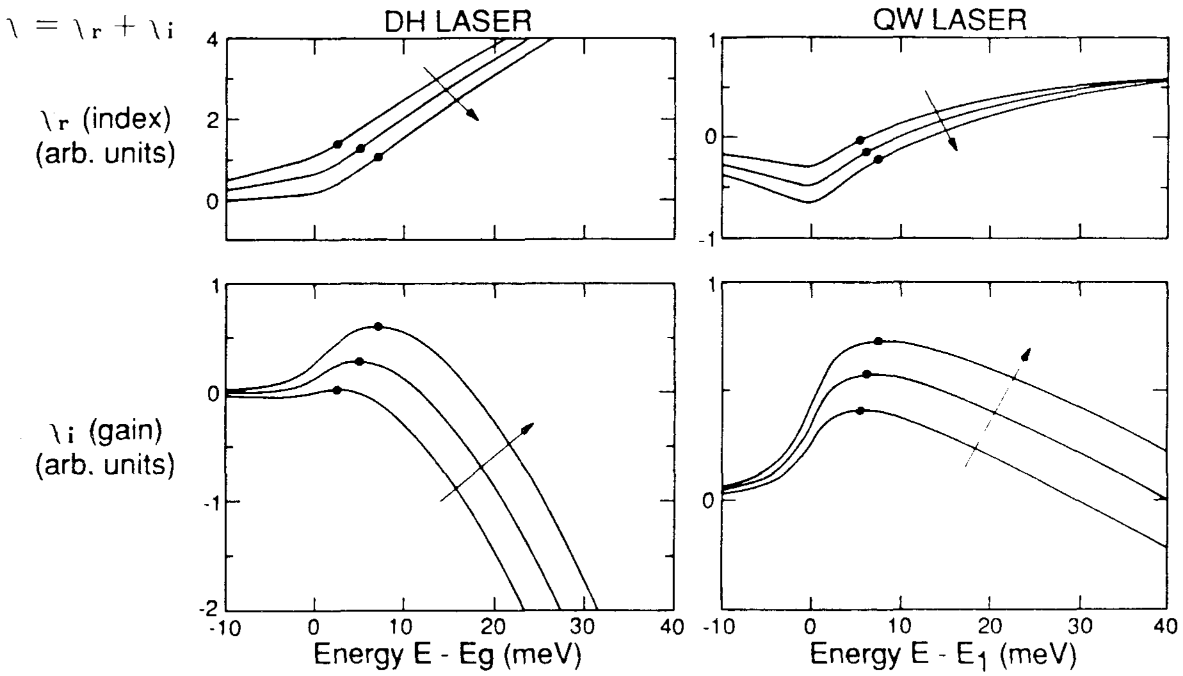

Figure 1.4 (a) Real and (b) imaginary parts of the complex-valued susceptibility function $\chi(\omega)$ for the two cases of double heterostructure and quantum well lasers, as a function of photon energy. The imaginary part is directly proportional to the laser gain, while the real part gives the change in refractive index from its non-resonant value. The different curves correspond to different values of injected carrier density, increasing in the direction of the arrow.

band and the lower being the valence band. Within each band, carrier populations thermalize with a characteristic time T_2 because of electron-electron and electron-phonon interactions. On time scales long compared to T_2, such as is considered here, states within the bands act independently. Thus we consider the conduction band - valence band system to be an ensemble of collisionally broadened 2-level systems with transition energies spanning over the reduced density of states function $\rho(\omega)$. The dielectric susceptibility of the semiconductor is then written as[8]

$$\begin{aligned} \chi_r(\omega_0) &= \int_{-\infty}^{+\infty} \rho(\omega)\, \widehat{\chi}_r(\omega,\omega_0)\, d\omega \ , \\ \chi_i(\omega_0) &= \int_{-\infty}^{+\infty} \rho(\omega)\, \widehat{\chi}_i(\omega,\omega_0)\, d\omega \ . \end{aligned} \tag{1.4}$$

This simple broadening has very important consequences for the gain and refractive index lineshapes as a function of the carrier population inversion. Figure 1.4 illustrates $\chi(\omega)$ for the two cases of the DH and QW laser for comparison. Whereas the gain lineshape $\widehat{\chi}_i(\omega)$ of the 2-level system is a classic Lorentzian, in a semiconductor the gain lineshape is determined primarily by the reduced density of states function $\rho(\omega)$ and the Fermi occupation factor $f_c(\omega) - f_v(\omega)$, since $kT >> 1/T_2$ typically. In contrast to $\widehat{\chi}_i(\omega)$, the gain lineshape $\chi_i(\omega)$ is *asymmetric* with respect to its peak; this causes a detuning of the zero crossing of $\chi_r(\omega)$ away from the peak of $\chi_i(\omega)$. The net result is an index coupling $\Delta\chi_r$, which changes as a function of carrier density. That is, gain fluctuations $\Delta\chi_i$ that are due to fluctuations in carrier density are additionally manifest as fluctuations in the index of refraction of the medium. For the DH and QW lasers, $\chi(\omega)$ is plotted for several quasi-Fermi energies corresponding to realistic carrier densities (few $\times 10^{18}\ cm^{-3}$) in the active region. The photon energies of peak gain are marked as a function of carrier density. Clearly, as the carrier density increases, the peak gain increases ($d\chi_i(\omega)/dN > 0$), while the corresponding index decreases ($d\chi_r(\omega)/dN\chi_r(\omega) < 0$). The consequences of this carrier-dependent gain and refractive index coupling are of considerable importance in modeling the waveguiding properties of semiconductor lasers.

1.3 The Effective Index Method

In order to predict realistically the electromagnetic modes of semiconductor lasers, and the coupling between said modes, an accurate model for the inherent waveguides must be constructed. In Section 1.2 we illustrated how the local susceptibility (and through Equation (1.1), the dielectric constant) is a function of the local carrier population. In order to construct the 2-dimensional complex dielectric constant profile, we relate the susceptibility $\chi(\omega_0)$ to the bulk gain and refractive index seen by a plane electromagnetic wave of frequency ω_0:

$$\vec{\mathcal{E}}(z,t) = \hat{\mathbf{x}}\ E\ e^{i\{k(\omega_0)z-\omega_0 t\}} \tag{1.5}$$

where $k(\omega_0)$ is its propagation constant, and $\hat{\mathbf{x}}$ is a unit vector in the x-direction. Upon substitution of Equation (1.1) for $\epsilon(\omega)$ into $k(\omega_0) = \omega_0\sqrt{\mu_0\epsilon(\omega_0)}$, we obtain

$$k(\omega_0) \cong \frac{n_0\omega_0}{c}\left\{1 + \frac{\chi(\omega_0)}{2n_0^2}\right\} . \tag{1.6}$$

Since $\chi(\omega_0) = \chi_r(\omega_0) + i\chi_i(\omega_0)$, we obtain the following correspondences between the resonant susceptibility $\chi(\omega_0)$ and the gain $g(\omega_0)$ and index of refraction $n(\omega_0)$:

$$\begin{aligned} n(\omega_0) &= n_0\left\{1 + \frac{\chi_r(\omega_0)}{2n_0^2}\right\} \\ g(\omega_0) &= -\frac{k_0\chi_i(\omega_0)}{n_0} \end{aligned} \tag{1.7}$$

where $k_0 = 2\pi/\lambda_0$. Alternatively, gain is often expressed as an imaginary component of the index of refraction, as follows:

$$Im\{n\} = \frac{\chi_i(\omega_0)}{2n_0^2} = -\frac{g(\omega_0)}{2k_0} . \tag{1.8}$$

In a semiconductor laser, the electric field $\vec{\mathcal{E}}(x,y,z,t)$ is a complicated superposition of many lateral (x-dependent), transverse (y-dependent), and longitudinal (z-dependent) modes, all of which oscillate at different frequencies. To simplify analysis, we consider oscillation at the *single* frequency ω_0, thereby selecting a single longitudinal mode, and we assume for the electric field a traveling wave solution along the axial (z) direction of the form^9

$$\vec{\mathcal{E}}(x,y,z,t) = \hat{\mathbf{x}}\ E(x)F(x,y)e^{i(\beta z-\omega_0 t)} \tag{1.9}$$

where $\beta = k_0\eta$ and η is the complex modal propagation constant ("effective mode index"). Transverse electric (TE) polarization is assumed because of its higher Fresnel reflectivity at the facets, which results in a lower threshold modal gain (in this thesis, Fabry-Perot lasers are considered exclusively). In (1.9), $E(x)$ is the lateral mode we wish to determine, and $F(x,y)$ is the transverse mode, which is usually a slowly varying function of the lateral coordinate, x.

The procedure for determining $F(x,y)$, $E(x)$, and η in the case of a stripe geometry laser is indicated graphically in Figure 1.5. Briefly, cross sections of the 2-dimensional complex index profile are constructed in the transverse (y) direction at fixed x, as in Figure 1.5(c). The transverse optical mode $F(x,y)$ and its effective index $n_{eff}(x)$ are the eigensolutions of this waveguide. The lateral mode $E(x)$ and its modal propagation constant β are the eigensolutions of the complex profile subsequently constructed from $n_{eff}(x)$, as shown in Figure 1.5(d). This technique, known as the *effective index approximation*[9], is valid when the lateral refractive index and electric field variations are much slower than the transverse ones.

In practice, the intermediate step of finding the eigensolutions $F(x,y)$ and $n_{eff}(x)$ are often omitted for simplicity. The transverse modal gain is proportional to the imaginary component $n_{eff,i}(x)$, and can be estimated by reducing the peak gain of the active region by the transverse optical confinement factor:

$$n_{eff,i}(x) \simeq g(x) \times \frac{d}{W_{eff}} \equiv \Gamma g(x) \tag{1.10}$$

where $g(x)$ is the peak gain, d is the active region width, and W_{eff} is the effective width of the transverse optical mode. The ratio d/W_{eff} is defined to be the transverse optical confinement factor Γ. Similarly, a value for $n_{eff,r}(x)$ is often assumed. While the absolute value of $n_{eff,r}(x)$ is not critical, the change $\Delta n_{eff,r}(x)$ in $n_{eff}(x)$ that is due to the presence of lateral variations in transverse structure or in injected carrier density determines $E(x)$ and η. In the case of injected carrier

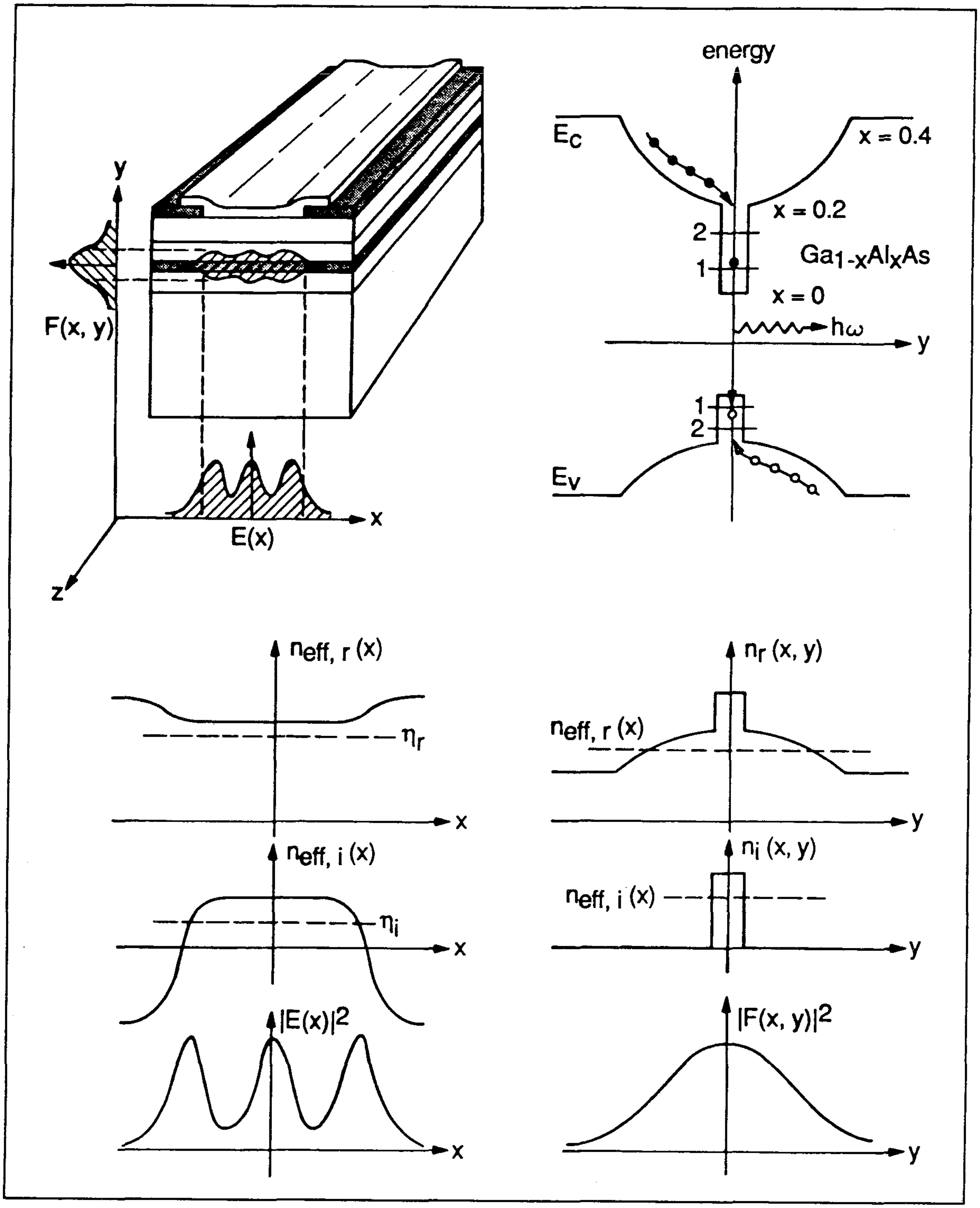

Figure 1.5 The effective index model for a stripe geometry laser. (a) Coordinate definitions showing transverse and lateral optical modes. (b) Band diagram in the transverse dimension. (c) Transverse gain $n_i(x, y)$ and index $n_r(x, y)$ profiles at a particular value of x, with the transverse mode $F(x, y)$. (d) Lateral gain $n_{eff,i}(x)$ and index $n_{eff,r}(x)$ profiles, with the lateral mode $E(x)$.

density, $\Delta n_{eff,r}(x)$ is often assumed to be simply related to the change $\Delta n_{eff,i}(x)$ in the gain that is due to injected carriers[10]:

$$\Delta n_{eff,r}(x) = -b \times \Delta n_{eff,i}(x) \tag{1.11}$$

where $b > 0$ is referred to as the antiguiding parameter. In general, b is a function of frequency ω_0 and carrier density $N(x)$. In the limit of small changes in carrier density, b is simply given by

$$b = -\frac{dn_{eff,r}}{dN} \Big/ \frac{dn_{eff,i}}{dN} = -\frac{d\chi_r}{dN} \Big/ \frac{d\chi_i}{dN} \ . \tag{1.12}$$

Figure 1.6 plots b as a function of photon energy for the cases of DH and QW lasers, corresponding to the gain and index spectra of Figure 1.4. Furthermore, the photon energies of peak gain for each of 3 carrier densities is also indicated. The figure illustrates that b decreases with increasing carrier density for the DH, but increases for the QW laser. This is because the differential gain (proportional to $d\chi_i/dN$) as a function of carrier density exhibits a peak[11]; for the QW laser the operational point lies on the decreasing side of that peak, while for the DH laser the opposite is true.

Using Equations (1.10) and (1.11), the complex refractive index is taken to be

$$n_{eff}(\omega_0) = n_{eff,0}(\omega_0) - (b + i)\frac{\Gamma g(\omega_0)}{2k_0} \tag{1.13}$$

where $n_{eff,0}$ is the complex index of refraction at the carrier density corresponding to optical transparency. Solutions for $E(x)$ and η are then determined by solution of the complex-valued Helmholtz equation (*i.e.,* 1-dimensional, reduced wave equation) at a particular fixed frequency ω_0 corresponding to the frequency of peak gain:

$$\frac{d^2E(x)}{dx^2} + k_0^2\left\{n_{eff}^2(x) - \eta^2\right\}E(x) = 0 \ . \tag{1.14}$$

The solution $E(x)$ is referred to as a "lateral mode". η is its effective modal index; that is, $\beta = k_0\eta$ is its propagation constant.

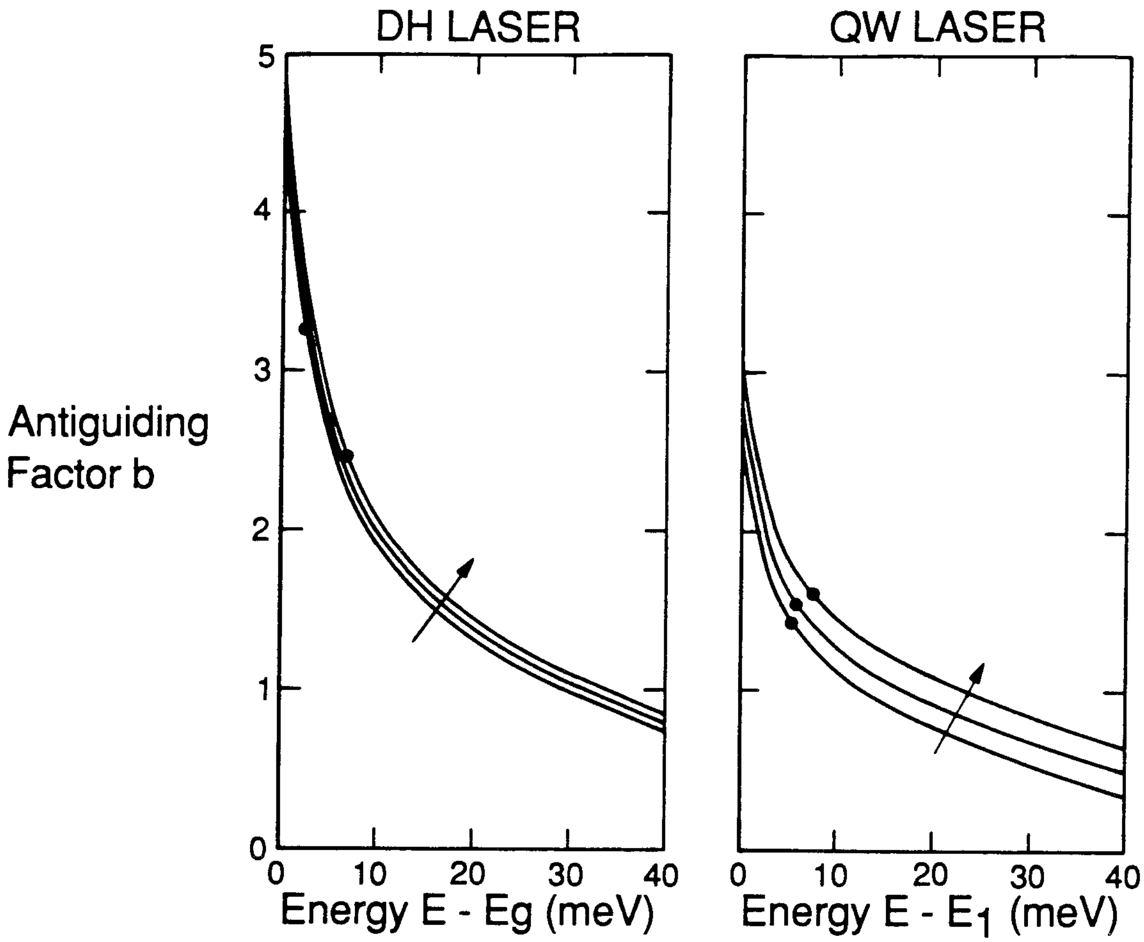

Figure 1.6 Antiguiding parameter b calculated according to Equation (1.12) for the case of DH and QW lasers. The different curves correspond to increasing values of injected carrier densities. Solid circles correspond to the operating points indicated in Figure 1.5.

1.4 The Duality of Gain and Index Waveguiding

In the stripe geometry laser of Figure 1.5, the lateral mode is guided by a profoundly different mechanism from the transverse mode. Light diverging in the transverse direction is channeled by total internal reflection so that, outside the positive index waveguide, the electromagnetic field is evanescent and decays exponentially. Energy is stored in the exponential tails but there is no Poynting power flow there. The electromagnetic wavefront is flat, indicating power flow only in the axial direction. Light which is guided chiefly by total internal reflection will be termed *index-guided.* The lateral waveguide, however, exhibits a *negative* index step that is due to the carrier-induced refractive index coupling of the gain. Thus, for angled incidence, light is refracted out of the waveguide. The Helmholtz equation, (1.14), yields a solution $E(x)\cos(kx)$ which, like the index-guided case, consists of two plane waves propagating at equal but opposite angles to the longitudinal axis. However, the constituent plane waves experience gain in traversing the waveguide and hence do not have equal amplitudes everywhere across the width (exactly analogous to the longitudinal direction). Since the core region experiences higher gain than does the cladding, the modal wavefront is advanced there. This directs Poynting power into the cladding (an additional loss) in order to equalize the energy derived from stimulated emission everywhere in the mode. Such a field propagates self-consistently along the longitudinal axis and thereby satisfies the definition of a lateral mode. We will call such modes *gain-guided.* Rather than rely on total internal reflection at the core-cladding interfaces to guide the light, gain-guided modes rely on a continuous generation of photons within the guide itself to compensate for those lost at those interfaces.

The difference in transverse and lateral guiding mechanisms leads to astigmatism in the laser output. Upon divergence at the cleaved facet, the wavefront is *curved* in the lateral plane as if it would emanate from a smaller aperture a few microns deep into the semiconductor. More importantly, the difference in power flow in the cladding regions of index-guided and gain-guided waveguides leads to qualitative differences in the way such modes *couple* to one another when placed in close proximity. This coupling is important for designing and characterizing phased array lasers for high-power applications, and also for integrated optic or photonic switching devices.

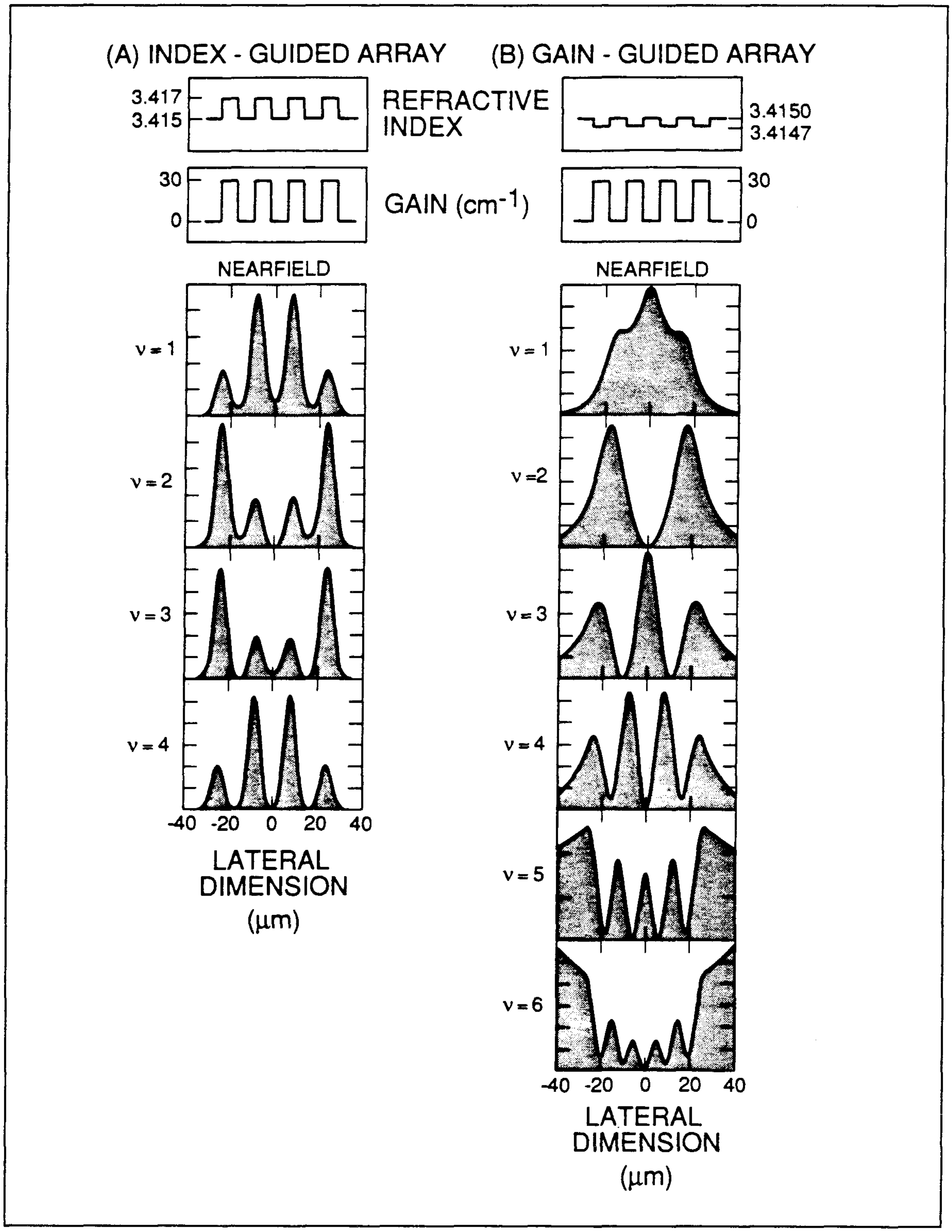

Figure 1.7 Lateral guided wave modes for 4-element, index-guided (a) and gain-guided (b) laser arrays.

Figure 1.7 shows the lateral guided wave modes calculated numerically[12] for 4-element, index-guided and gain-guided waveguide arrays, respectively. Each guide alone supports *only the fundamental mode.* In the index-guided structure, power is exchanged between guides via a slow leakage through the evanescent fields (analogous to electron tunneling between adjacent quantum wells). Coupled-mode theory provides an excellent description of the behavior of such weakly coupled devices[13] whether operated as laser oscillators, integrated optic switches, or directional couplers. The gain-guided structure, on the other hand, supports *more* modes than would be expected from a coupled-mode analysis. This is because coupling between gain-guided modes is *inherently strong* because of their similarity to radiation modes. Poynting power is actively exchanged via radiation through the lossy regions in arrays of such waveguides. The spatially periodic carrier injection due to the electrodes writes a complex-valued dielectric grating into the medium, that serves to couple the plane waves in each waveguide via distributed reflections. Thus, index-guided and gain-guided structures are in this sense *duals* of one another, and we will find it fruitful to emphasize this difference.

1.5 Gain Saturation Nonlinearity

The complex refractive index is additionally dependent on the electromagnetic field intensity through the modulation of the carrier population that accompanies stimulated emission. As laser threshold is surpassed, the electromagnetic modal gain becomes clamped at the level of the resonator losses, as is required for steady-state operation. Charge carriers introduced into the active region by additional pumping are depleted by stimulated emission in proportion to the increasing intensity of the optical field. However, the optical field is not of spatially uniform intensity, and the steady-state carrier population reflects it. The result is a spatially varying complex susceptibility (*i.e.*, gain and refractive index). In particular, where the then into the Helmholtz equation, (1.14), yields the complex-valued, non-analytic, eigenvalue equation that determines the nonlinear lateral laser modes.

Figure 1.9 depicts the effect of gain saturation for the case of fundamental mode oscillation in a stripe geometry laser. The lateral gain and refractive index profiles, plus the self-consistent mode intensity and wavefront, are shown below threshold (dashed lines) and above threshold (solid lines). Since the refractive index above threshold is increased where the optical intensity is highest, the waveguide is effectively narrowed, tending to further increase the peak intensity. The accompanying local decrease in gain is termed *spatial hole-buring.* This positive feedback will be shown to self-stabilize as the spatial hole burned in the gain profile approaches transparency. However, this "self-focusing" mechanism has the following deleterious effects:

(i) the output power is a sublinear function of the pump current since the carriers become utilized less efficiently as the overlap of the optical field and the current injection decreases with increasing current injection,

(ii) the gain near the stripe edges increases until at some point the second-order lateral mode has enough modal gain to overcome its losses. The resultant multilateral mode operation is manifest as kinks in the light-current curve,

(iii) in order to propagate self-consistently, the wavefront of the self-focused mode is retarded near the intensity peaks to reflect the locally low gain there, which is a source of wavefront aberrations,

(iv) coupled waveguides that are phase-matched at low optical intensities become detuned if the intensity varies from channel to channel. The resultant decreased interguide power transfer leads to a degradation in the mutual coherence of the composite structure.

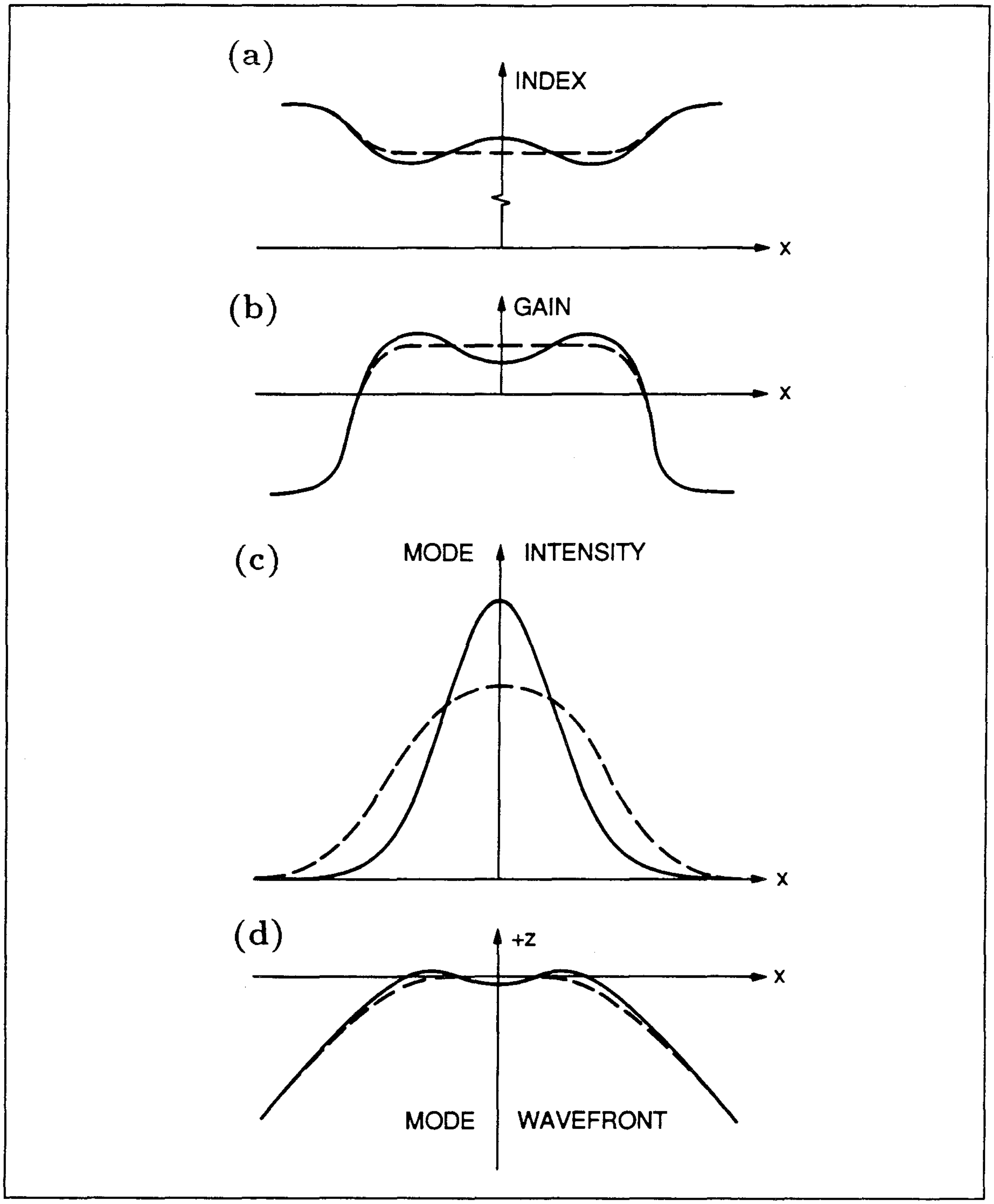

Figure 1.8 Self-focusing that is due to gain saturation in a stripe geometry laser. Dashed lines show the fundamental lateral mode below threshold: (a) refractive index, (b) gain, (c) mode intensity, and (d) mode wavefront. Above threshold (solid lines), feedback from the mode intensity into the gain and refractive index profiles causes self-focusing, reducing the lateral width of lasing and causing wavefront aberrations.

1.6 Synopsis

To reiterate: in this thesis, we probe issues fundamental to the achievement of high-power, coherent, frequency-tunable emission from (GaAl)As semiconductor lasers. These issues, such as lateral mode discrimination and gain saturation, have been addressed in two ways: (i) the distribution of high output power over mutually coupled diodes (laser arrays), and (ii) the optimization of individual laser diode Fabry-Perot resonators (including external cavity lasers). This section provides a synopsis of the thesis; the work herein is based largely upon the publications listed as References 16-24.

Chapter One has laid the groundwork and the assumptions for several of the concepts utilized in the following six chapters. In particular, the concepts of gain-coupled refractive index, duality of gain and index waveguiding, and the intensity-dependent index of refraction have been introduced and/or reviewed where applicable.

Chapters Two to Four discuss primarily high-power and single frequency operation from broad area quantum well lasers. Chapter Two details the implications of the gain saturation nonlinearity for the lateral modes of broad area lasers. The theory developed raises fundamental questions about mode selection in the above-threshold regime. Chapter Three discusses a means of improving the poor mode discrimination inherent in the devices of Chapter Two. This method, "gain tailoring," selects single plane-wave states as the laser eigenmodes, resulting in single-lobed farfields for all of the higher order modes. Finally, Chapter Four demonstrates that high power operation from gain-guided lasers can be achieved at a single frequency via operation in a dispersive external cavity. Furthermore, single quantum well lasers are demonstrated to be wavelength-tunable over a record range of 125 nm.

Chapters Five to Seven illustrate the duality of gain-guided and index-guided coupled semiconductor lasers. Chapter Five presents a novel theory of gain-guided laser arrays, based on laterally coupled plane waves. The theory is applied in the design of a high-power array/broad area hybrid laser. Chapter Six presents theory and experiments of laser arrays with diffractive coupling. By optimizing the device geometry, supermode selection is achieved with high mode discrimination. Finally, in Chapter Seven, we extend the nonlinear analysis of Chapter Two to index-guided laser arrays. While deleterious for laser oscillation, the gain saturation nonlinearity may in future be exploited to fabricate photonic switching devices such as nonlinear directional couplers.

Whereas index-guided laser arrays have, in the past, been successfully modeled by coupled-mode theory[13], this thesis extends the present understanding of high-power devices to both gain-guided laser arrays and broad area lasers.

References

[1] R.N. Hall, G.E. Fenner, J.D. Kingsley, T.J. Soltys, and R.O. Carlson, "Coherent light emission from GaAs junctions," *Phys. Rev. Lett.* **9**, 366-368 (1962).

[2] M.I. Nathan, W.P. Dumke, G. Burns, F.H. Dills, and G. Lasher, "Stimulated emission of radiation from GaAs pn junctions," *Appl. Phys. Lett.* **1**, 62-64 (1962).

[3] T.M. Quist, R.J. Keyes, W.F. Krag, B. Lax, A.L. McWhorter, R.H. Rediker, and H.J. Zeiger, "Semiconductor maser of GaAs," *Appl. Phys. Lett.* **1**, 91-92 (1962).

[4] J. Hayashi, M.B. Panish, and P.W. Foy, "A low-threshold room-temperature injection laser," *IEEE J. Quant. Electr.*, **QE-5** 211-212 (1969).

[5] H. Kressel and H. Nelson, "Close confinement GaAs pn-junction laser with reduced optical loss at room temperature," *RCA Rev.* **30**, 106-113 (1969).

[6] W.T. Tsang, "A graded index waveguide separate confinement laser with very low threshold and a narrow Gaussian beam," *Appl. Phys. Lett.* **39**, 134-136 (1981).

[7] H.Z. Chen, A. Ghaffari, H. Morkoc, and A. Yariv, "Very low threshold current densities (under 100 A/cm^2) in (AlGa)As GRINSCH-SQW lasers grown by MBE," *Electron. Lett.* **23**, 1334-1335 (1987).

[8] K. Vahala, L.C. Chiu, S. Margalit, and A. Yariv, "On the linewidth enhancement factor α in semiconductor injection lasers," *Appl. Phys. Lett.* **42**, 631-633 (1983).

[9] W. Streifer and E. Kapon, "Application of the equivalent index method to DH diode lasers," *Appl. Opt.* **18**, 3724-3725 (1979).

[10] For example: G.H.B. Thompson, *Physics of Semiconductor Lasers* (Wiley, New York, 1981).

[11] Y. Arakawa, K. Vahala, and A. Yariv, "Dynamic and spectral properties of semiconductor lasers with quantum well and quantum wire effects," *Surface Science* **174**, 155-162 (1986).

[12] C. Lindsey, "High Power Phased Array and Tailored Gain Semiconductor Lasers," Ph.D. Thesis, California Institute of Technology (1986).

[13] A. Yariv, "Coupled-mode theory for guided wave optics," *IEEE J. Quant. Electr.* **QE-9**, 919-933 (1973).

[14] G.H.B. Thompson, "A theory for filamentation in semiconductor lasers, including the dependence of the dielectric constant on injected current density," *Optoelectronics* **4**, 257-310 (1972).

[15] For example: K. Lau and A. Yariv, "High frequency current modulation of semiconductor injection lasers," in *Semiconductors and Semimetals, vol. 22*, 69-152 (Academic Press, Orlando, 1985).

[16] C.P. Lindsey, D. Mehuys, and A. Yariv, "Linear tailored gain broad area semiconductor lasers," *IEEE J. Quantum Electron.* **QE-23**, 775-787 (1987).

[17] D. Mehuys, M. Mittelstein, J. Salzman, and A. Yariv, "Saturable nonlinear dielectric waveguide with applications to broad area lasers," *Opt. Lett.* **12**, 953-955 (1987).

[18] D. Mehuys, R.J. Lang, M. Mittelstein, J. Salzman and A. Yariv, "Self-stabilized nonlinear lateral modes of broad area lasers," *IEEE J. Quantum Electron.* **QE-23**, 1909-1920 (1987).

[19] D. Mehuys and A. Yariv, "Coupled-wave theory of multiple-stripe semiconductor injection lasers," *Opt. Lett.* **13**, 571-573 (1988).

[20] D. Mehuys, K. Mitsunaga, L. Eng, W.K. Marshall, and A. Yariv, "Supermode control in diffraction-coupled semiconductor laser arrays," *Appl. Phys. Lett.* **53**, 1165-1167 (1988).

[21] T.R. Chen, D. Mehuys, Y.H. Zhuang, M. Mittelstein, P.L. Derry, and A. Yariv, "Broad area tandem semiconductor laser," *Appl. Phys. Lett.* **53**, 1468-1470 (1988).

[22] M. Mittelstein, D. Mehuys, A. Yariv, J.E. Ungar, and R. Sarfaty, "Broadband tunability of gain-flattened quantum well semiconductor lasers with an external grating," *Appl. Phys. Lett.* **54**, 1092-1094 (1989).

[23] D. Mehuys, M. Mittelstein, A. Yariv, R. Sarfaty, and J.E. Ungar, "Optimized Fabry-Perot (GaAl)As quantum well lasers tunable over 105 nm," *Electron. Lett.* **25**, 143-145 (1989).

[24] D. Mehuys and A. Yariv, "Nonlinear supermodes of index-guided semiconductor laser arrays," unpublished.

CHAPTER

Two

Nonlinear Lateral Modes of Broad Area Lasers

2.0 Introduction

In principle, the most direct way to increase the optical power available from a semiconductor laser is to increase the volume of the lasing mode. It is not sufficient merely to increase the pump level because the resonator facets are susceptible to catastrophic optical damage at high power densities. The simplest practical recourse is to increase the lateral dimension. In the past, stripe geometry lasers wider than about 10 μm exhibited filamentary nearfields that were not stable with respect to increased current injection and gave rise to equally unstable farfield patterns. Thus stripe geometry lasers were fabricated to support only a single *filament*,[1] and the high-power effort shifted toward building phased arrays of such lasers. It was difficult, however, to fabricate arrays in which adjacent elements were coupled in-phase. In fact, twin-lobed farfield patterns were the rule rather than the exception, because the preferred lasing mode in uniform arrays is not the fundamental supermode[2] of the array. Subsequently, many schemes have been proposed to favor the fundamental supermode, and several groups have reported laser arrays oscillating into a single-lobed farfield[3-13]. However, all of the above require an additional degree of complexity in array design and fabrication, and true single lateral mode operation remains difficult to achieve over a large range of injected current density. More elaborate schemes such as unstable resonator geometries[14] show promise but are still technologically immature.

Recently, wide ($\geq$ 100 μm) uniform gain, broad area, quantum well lasers have been demonstrated[15] to oscillate coherently into a nearly diffraction-limited single-lobed farfield pattern. The emission was stable over a large range of injected current, and a gradual broadening of the farfield with increasing power level was the only apparent degradation. The nearfield was characterized by a relatively flat amplitude with a small ($\simeq$ 10%) superimposed ripple; the ripple period was close to 10 μm. Figure 2.1 illustrates the experimentally measured nearfield of a 100 μm wide, broad area laser at several different current levels, up to 6 I_{th}, and the farfield at 1.2 I_{th}. The stability of the nearfield and the narrowness of the farfield cannot be explained by the simple linear theory of gain-guided structures. This led to renewed interest in the basic properties and expected performance of such devices. In this chapter, we investigate the theoretical behavior of these broad area lasers.

In particular, we intend to characterize the optical modes consistent with a heavily saturated gain profile. Our devices were driven up to 60 times threshold[16], so we are most interested in characterizing the high-power regime. In this regime, the intensity dependence of the carrier density and the resulting changes in the refractive index *must* be included in the analysis. Thompson, in 1972, analyzed optical nonlinearities that are due to carrier depletion and found them to introduce a third-order nonlinearity in the field equation[17]. His solutions in unbounded media were either solitary filaments, or periodic solutions consisting of adjacent filaments coupled either in phase or in antiphase. A serious limitation of his approach was the restriction to real refractive index variations only. As he pointed out, this restriction made it impossible to match his multifilament solutions to lossy boundaries, and thus excluded the eigenfunctions of gain-guided lasers (which we introduce).

Since then, much of the work in the literature has focused on analysing the stability of solitary filaments[18–21] and providing design guidelines[22] for narrow stripe-geometry lasers. In this work, we focus on the multifilament solutions that

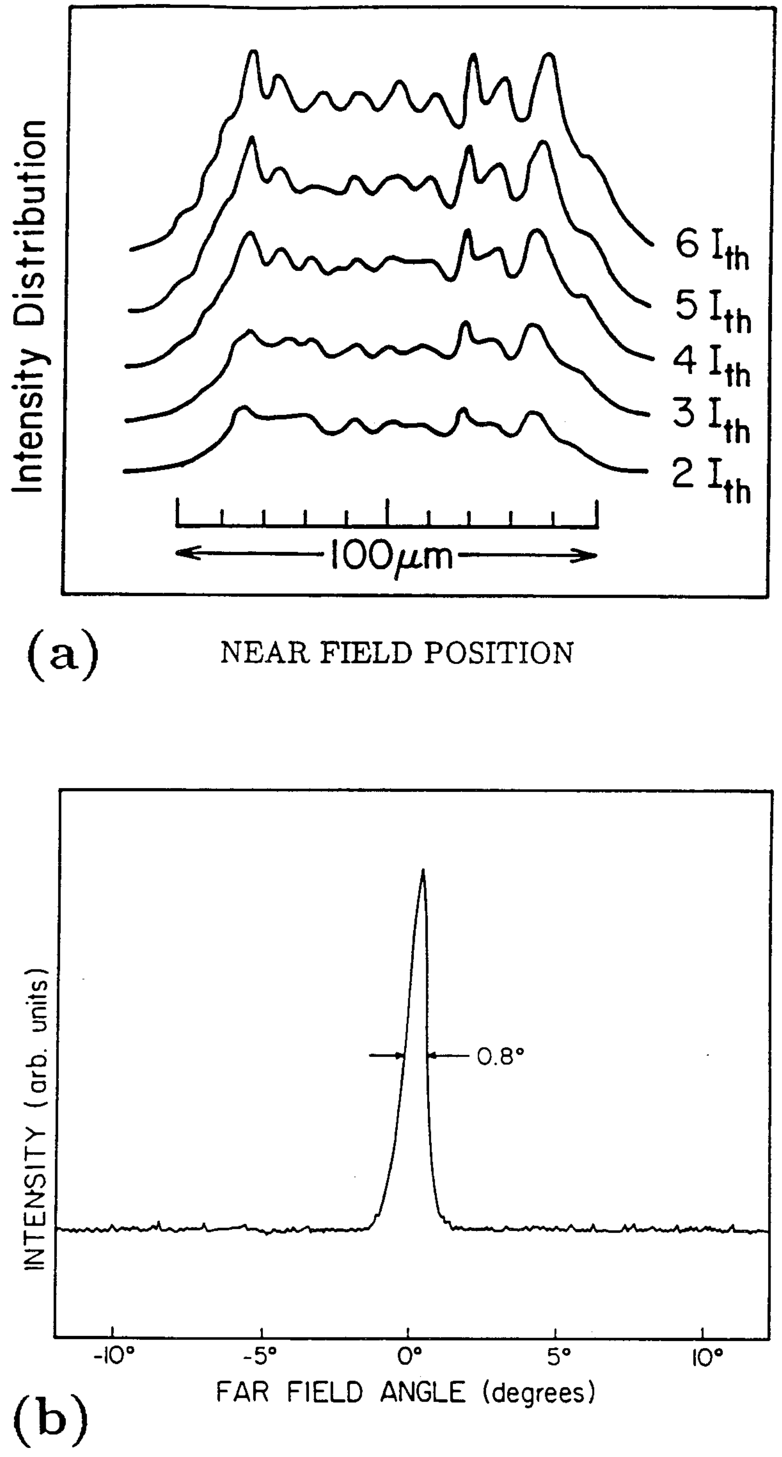

Figure 2.1 *(a) Nearfield intensity of a 100 μm wide broad area laser at several currents up to 6 I_{th}. (b) The farfield close to threshold, at 0.8° in width, is less than twice the diffraction limit.*

are important in broad area lasers. However, since the modulation depth of these solutions is relatively small, it is somewhat misleading to characterize these solutions as *coupled filaments*. Rather, the intensity modulation of the electric field introduces a spatial perturbation into the gain and refractive index profiles of the broad area waveguide. The below-threshold, gain-guided modes are thereby *coupled* to one another, so that each alone is *not* a self-consistent eigensolution. Rather, the self-consistent eigensolution can be regarded as a complex *superposition* of the below-threshold modes. Thus the multifilament solutions, which we introduce here, are analogous to the *supermodes* of multielement laser arrays. An important distinction to make is that the exact superposition is a function of pump current, reflecting the nonlinear nature of the problem. Moreover, the nonlinearity is saturable , and we show that gain saturation is responsible for the *stabilization* of filament size. Lateral carrier diffusion does not play a significant role in this stabilization.

2.1 Carrier-Dependent Refractive Index

In this section the complex refractive index is written to include the carrier dependence. As the physical origin of the self-focusing mechanism lies in the local depression of the gain profile by stimulated emission (spatial hole-burning), this is what we shall quantify first. It will then be incorporated into the effective refractive index. Figure 2.2(a) shows a broad area device of the type we shall consider. The laser shown is a single quantum well, separate-confinement heterostructure, and is known to give very low threshold densities[24]. Parts (b) and (c) show representative optical modes of the transverse and lateral waveguides, respectively. The transverse mode is index-guided, and for the single quantum well of thickness L_y, it is characterized by a small optical confinement factor Γ.

The lateral waveguide is formed by the perturbation in the gain and index profiles introduced by the steady-state carrier distribution under the current stripe,

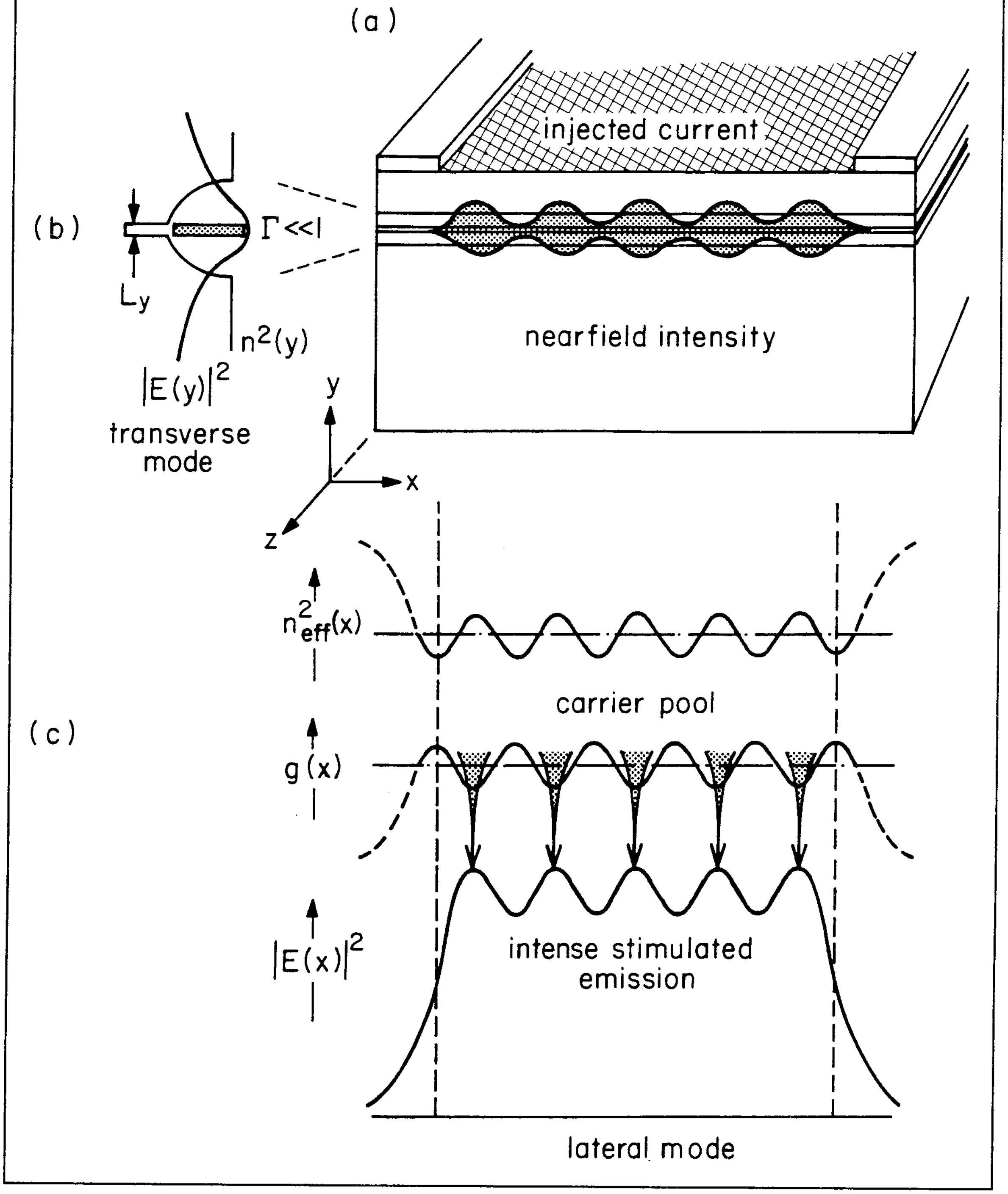

Figure 2.2 *(a) Stripe-geometry broad area laser with coordinate system used in this analysis. (b) Fundamental transverse mode of graded-index, single quantum well structure, showing very small optical confinement factor. (c) Nonlinear lateral mode as observed from our best devices. The gain is locally depleted by stimulated emission in the high-intensity regions, leading to an increase in the local refractive index and the phenomenon of self-focusing.*

as indicated in Figures 1.5 and 2.1. In the carrier rate equation, we shall consider one-dimensional variables, having separated out the longitudinal dependence and integrated out the transverse dependence. When the lateral mode "sees" an effective index n_{eff}, the steady-state rate equation becomes[19,20]

$$\frac{J(x)}{e} = \left(\frac{c}{n_{eff}}\right) \Gamma\, g(N(x))\, P(x) + \frac{N(x)}{\tau_{sp}} - D\, \frac{d^2N(x)}{dx^2}, \tag{2.1}$$

where

$J(x) =$ injected current density $[\mathrm{cm}^{-2}s^{-1}]$

$N(x) =$ carrier density $[\mathrm{cm}^{-2}]$

$P(x) =$ photon density in lateral mode $E(x)$ $[\mathrm{cm}^{-2}]$

$g(x) =$ spatial gain profile in the quantum well $[\mathrm{cm}^{-1}]$

$\tau_{sp} =$ spontaneous lifetime $[s]$

$D =$ lateral diffusion coefficient $[\mathrm{cm}^2V^{-1}s^{-1}]$.

Equation (2.1) states that at a given position x, the carriers gained by injected current are balanced in steady state by losses that are due to stimulated and spontaneous emission and by lateral diffusion. Note that in contrast to Equation (1.15), Equation (2.1) includes lateral carrier diffusion. In this section, we will quantify its contribution. Non-radiative recombination processes can be lumped into the spontaneous emission lifetime τ_{sp}. We define a normalized saturated gain profile $\gamma(x)$, as:

$$\gamma(x) \equiv \frac{g(x) - g_{th}}{g_{th}} = \frac{g'_{th}}{g_{th}}(N(x) - N_{th}) \ , \tag{2.2}$$

where, as is customary[17], we have linearized about the threshold gain $g_{th} \equiv g(N_{th})$. The corresponding linearization with respect to current density is shown in Figure 2.3. g'_{th} is the differential gain (with respect to carrier density) at threshold. The dimensionless quantity $\gamma(x)$ quantifies the spatial hole-burning, giving the deviation from threshold gain in units of the threshold gain. Equation (2.1) can now be

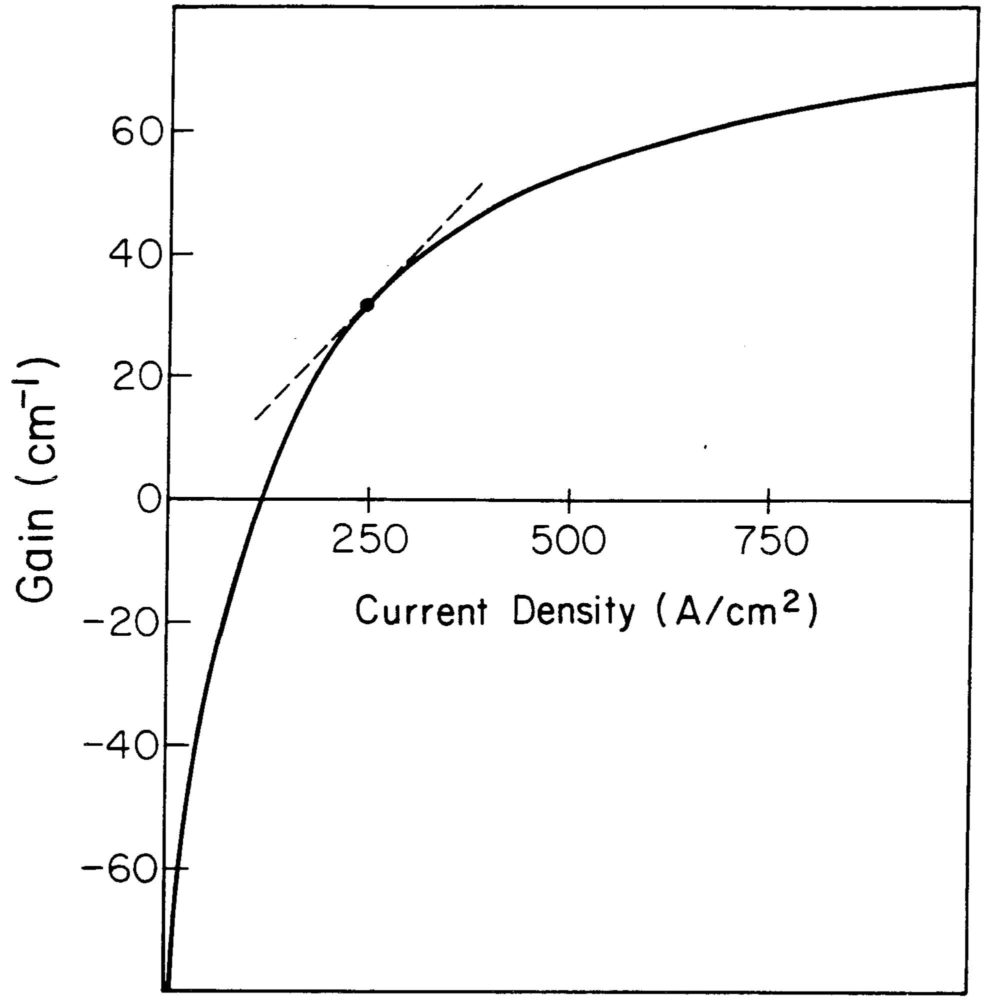

Figure 2.3 *Linearization of the gain-current density relation about the threshold gain,* g_{th}. *In this analysis, threshold current is proportional to threshold carrier density, and thus the slope of the dashed line is proportional to the differential gain,* g'_{th}. *The curve shown is based on experimental data for GRINSCH-SQW lasers*[15].

expressed as a second-order, linear, ordinary differential equation in the normalized saturated gain profile:

$$L_{sp}^2 \frac{d^2\gamma(x)}{dx^2} - \left[1 + \frac{P(x)}{P_{sat}}\right]\gamma(x) = \frac{P(x)}{P_{sat}} - \frac{J(x) - J_{th}}{J_{sat}}, \tag{2.3}$$

where the following definitions have been made:

$$L_{sp}^2 \equiv D\tau_{sp} \ , \tag{2.4a}$$

$$P_{sat} \equiv \frac{n_{eff}/c}{\Gamma g'_{th}\tau_{sp}} \ , \tag{2.4b}$$

$$J_{th} \equiv \frac{eN_{th}}{\tau_{sp}} \ , \tag{2.4c}$$

$$J_{sat} \equiv \frac{eg_{th}}{\tau_{sp}g'_{th}} \ . \tag{2.4d}$$

L_{sp} is the diffusion length when the carrier lifetime is determined solely by spontaneous emission, and J_{th} is the threshold current density. Equation (2.3) has no simple solution, as the diffusion operator, $\mathbf{L}$, is x−dependent:

$$\mathbf{L}(x) \equiv L_{sp}^2 \frac{d^2}{dx^2} - \left[1 + \frac{P(x)}{P_{sat}}\right], \tag{2.5}$$

and $P(x)$ is still unknown. We can, however, find an approximate solution in terms of $P(x)$. Since $P(x) \geq 0$ for all x, it is appropriate to find a WKB approximation for the Green's function of $\mathbf{L}(x)$ [25]:

$$G_{WKB}(x,x') = \frac{1}{2L_{sp}} \frac{\exp\left\{-\frac{1}{L_{sp}}\left|\int_{x'}^{x}\sqrt{1+\frac{P(t)}{P_{sat}}}dt\right|\right\}}{\left[\left(1+\frac{P(x)}{P_{sat}}\right)\left(1+\frac{P(x')}{P_{sat}}\right)\right]^{1/4}}. \tag{2.6}$$

The Green's function is integrated against the right-hand side of (2.3) and the integral is expanded asymptotically in powers of the diffusion length. The result for the saturated gain profile is as follows:

$$\gamma(x) \sim \gamma_0(x) + \frac{L_{sp}^2}{1+\frac{P(x)}{P_{sat}}}\frac{d^2\gamma_0(x)}{dx^2} + O\left\{\frac{L_{sp}^4}{\left(1+\frac{P(x)}{P_{sat}}\right)^2}\right\}, \tag{2.7}$$

where

$$\gamma_0(x) = \frac{\frac{J(x)-J_{th}}{J_{sat}} - \frac{P(x)}{P_{sat}}}{1+\frac{P(x)}{P_{sat}}} \tag{2.8}$$

is the solution *when diffusion is neglected* (*viz.,* Equation (1.16)). To interpret (2.7) in our context, consider a saturated gain profile that reflects a self-modulated nearfield. While the level of the losses determines the average gain level, regions of relatively high (low) optical intensity cause regions of local depression (elevation) in the gain. This effect, which is due to stimulated emission, is dominant and is represented by the first term in Equation (2.7). In addition, diffusion will cause some of the carriers to shift from regions of high gain to regions of low gain—filling in the gaps—and this effect is represented by the second term in (2.7); it is a correction to the first term.

Now, suppose that $\gamma(x)$ oscillates about zero with a periodicity defined by transverse wavevector k_t. Compared to the first term in (2.7), the diffusion term is of order $k_t^2 L_{sp}^2/(1+\frac{P(x)}{P_{sat}})$. If $k_t L_{sp}$ is small compared to one, then certainly $k_t^2 L_{sp}^2 \ll 1$, and the diffusion correction is small; as the power increases over P_{sat}, it becomes smaller yet. That is, the diffusion length, being proportional to the square root of the carrier lifetime, is reduced in the presence of stimulated emission. Note that P_{sat} can be interpreted as the photon density at which the stimulated emission rate equals the spontaneous emission rate, since at this intensity the carrier lifetime is reduced by a factor of two. This is in accordance with other common definitions of the saturation intensity [17,26].

Since modulation in $P(x)$ occurs only on spatial scales longer than L_{sp}, and the effects of diffusion become vanishingly small at high power, we neglect them. As a result, we take (2.8) as the saturated gain profile. It remains to incorporate this expression into the complex refractive index, n_{eff}. Observing the traveling wave convention (1.9) leads to the relationship

$$n_{eff}^2(x) = n_0^2 - \frac{n_0}{k_0}\Gamma g_{th}(b+i)\gamma(x), \tag{2.9}$$

where n_0 is the effective index of refraction corresponding to the threshold gain level, and b is the antiguiding factor (positive, with convention (1.9)). Note that in our model, b is identical to the linewidth enhancement factor, α, at threshold carrier density. Finally, we establish the dependence of n_{eff}^2 on field $E(x)$, rather than on photon density $P(x)$, by making use of the following relation:

$$|E(x)|^2 = \frac{2\hbar\omega}{n_0^2}\frac{\Gamma P(x)}{L_y}, \tag{2.10}$$

where $\hbar\omega$ is the lasing transition energy and L_y is the previously mentioned active layer thickness. The field strength at saturation is then (from (2.4b) and (2.10))

$$E_{sat}^2 = \frac{2\hbar\omega}{n_0^2}\frac{n_{eff}}{c}\frac{1}{g'_{th}L_y\tau_{sp}}. \tag{2.11}$$

We further define

$$\epsilon_{sat} \equiv \frac{n_0}{k_0} b\,\Gamma g_{th}, \tag{2.12}$$

and note for future reference that ϵ_{sat} is proportional to the product of the antiguiding factor b and the modal threshold gain Γg_{th}. Equation (2.9) for the carrier-dependent dielectric constant becomes, finally,

$$n_{eff}^2(x) = n_0^2 + \epsilon_{sat}(1 + \frac{i}{b})\frac{|E(x)|^2 - E_{sat}^2\frac{J(x)-J_{th}}{J_{sat}}}{|E(x)|^2 + E_{sat}^2}. \tag{2.13}$$

Equation (2.13) predicts, as expected, an increase in both the real and imaginary parts of n_{eff}^2 in regions where $|E(x)|^2$ is large. That is, the gain is decreased, while the refractive index is increased. Furthermore, at threshold, $J = J_{th}$ and $P = 0$, which gives $n_{eff}^2 = n_0^2$ as desired. At low field intensity, $|E(x)|^2 \ll E_{sat}^2$, this expression is of the form common to the nonlinear optics literature[27]: $n^2(x) = n_0^2 + n_2 \cdot I(x)$, where $I \propto |E|^2$ is the optical intensity. However, in our case, the nonlinearity in the effective index is ***saturable***. As seen from (2.13), the maximum local increase in dielectric constant occurs in the saturated limit $|E(x)|^2 \gg E_{sat}^2$, and is given by ϵ_{sat}. It can be appreciated from (2.12) that the parameter ϵ_{sat} represents the depression in dielectric constant incurred via pumping from transparency to threshold current density. To minimize self-focusing, it should be as small as possible. Equation (2.12) indicates that to accomplish this, small values for the antiguiding factor, optical confinement factor, and threshold gain are desired. All of these quantities are smaller in quantum well (QW) lasers than in regular double heterostructure (DH) lasers, and thus we conclude that the nonlinear action is *weaker* in QW lasers. ϵ_{sat} has been measured in both QW and DH lasers and is known to be smaller by a factor of 2 in the case of the QW lasers[28]. In very low threshold QW lasers, this improvement may be doubled again.

2.2 Solution of Nonlinear Complex-valued Field Equation

Incorporating the complex effective refractive index (2.13) into the Helmholtz equation, (1.14), gives the following second order, nonlinear, nonanalytic, complex eigenvalue problem to be solved for the modes of the broad area laser:

$$\frac{1}{k_0^2}\frac{d^2E(x)}{dx^2} + \left\{ n_0^2 - \eta^2 + (1+\frac{i}{b})\epsilon_{sat}\frac{|E(x)|^2 - E_{sat}^2\frac{J(x)-J_{th}}{J_{sat}}}{|E(x)|^2 + E_{sat}^2} \right\} E(x) = 0 \; . \qquad (2.14)$$

As can be deduced from phase-plane arguments, Equation (2.14) supports periodic solutions of the form $E(x) = E_0(1 + me(x))$, where E_0 represents the average field amplitude and $e(x)$ is a periodic function that contains the filamentary self-modulation. Here m is a modulation depth small compared to unity, so the composite solution has no nulls. Thompson identified such multifilament solutions in his treatise, and it is evident that corresponding solutions exist in the complex case for a laser of infinite width. For our laser of *finite width*, we take a solution of the form

$$E \equiv E_0 e^{a+i\phi} \qquad (2.15)$$

so that amplitude variations appear in a and phase variations in ϕ. As such, small modulation solutions are characterized by small a, in which case appropriate linearizations can be easily made. Let ξ be a dimensionless position coordinate: $x \equiv \xi d$, where d is the half-width of the laser. Since $E(0) \neq 0$, we consider only even solutions for $E(\xi)$, and thus our task is to solve the problem on the interval $0 < \xi < 1$. In the normalized coordinates, Equation (2.15) becomes

$$a'' + i\theta' + a'^2 + i2a'\theta - \theta^2 + L(a) = 0, \tag{2.16}$$

where $\theta(\xi) \equiv \phi'(\xi)$ (note that the equation depends only on the phase gradient θ, not on the absolute phase ϕ). The intensity-dependent refractive index term is included in the last term of (2.16):

$$L(a) \equiv k_0^2 d^2 \Big\{ n_0^2 - \eta^2 + (1 + \frac{i}{b}) \epsilon_{sat} \frac{E_0^2 e^{2a} - E_{sat}^2 \frac{J - J_{th}}{J_{sat}}}{E_0^2 e^{2a} + E_{sat}^2} \Big\}. \tag{2.17}$$

The term $L(a)$ can be linearized for the case of $|a| \ll 1$ (small modulation depth):

$$L(a) = L_0 + L_1 \cdot a + O(a^2), \tag{2.18}$$

with

$$L_0 = k_0^2 d^2 (n_0^2 - \eta^2) + \frac{1}{2}(1 + \frac{i}{b}) k_0^2 d^2 \epsilon_{sat} (1 - \sigma) \ , \tag{2.19a}$$

$$L_1 = (1 + \frac{i}{b}) q_0^2 \ , \tag{2.19b}$$

and where the following definitions have been made:

$$\sigma \equiv \frac{\frac{J - J_{th}}{J_{sat}} + 1}{\frac{E_0^2}{E_{sat}^2} + 1} \ , \tag{2.20a}$$

$$\mu \equiv \frac{E_0^2}{E_0^2 + E_{sat}^2} \ , \tag{2.20b}$$

$$q_0^2 \equiv 2 k_0^2 d^2 \sigma \mu \epsilon_{sat} \ . \tag{2.20c}$$

Here σ is a dimensionless quantity related to the ratio between pump and field intensities, and in our model, is constrained by energy conservation to be an $O(1)$ term. On the other hand, μ gives the approximate ratio of stimulated to stimulated + spontaneous emission, and saturates smoothly towards unity in the high-power limit. q_0^2 is proportional to the $\sigma\mu$ product, and (as we shall see) corresponds to the squared filament wavevector.

We have solved Equation (2.16) (subject to the linearization (2.18)) *analytically*. The bulk of the derivation appears as Appendix 2A. At this point, we merely summarize the result.

In addition to the filamentary self-modulation, which we expect to vary on a short length scale of $O(10\mu\text{m})$, we allow for a global phase curvature and a *slowly varying* amplitude variation, over the broad width of the laser, to satisfy the loss requirement of the amplified, gain-guided mode. We separate the two as

$$a = a_f + a_s \; , \tag{2.21a}$$

$$\theta = \theta_f + \theta_s \; , \tag{2.21b}$$

where f denotes "fast" (or "filament") and s denotes "slow."

The fast and slow variables are decoupled by an appropriate averaging procedure. The fast, or self-modulation terms, are

$$a_f = m(\xi) \cos \int q_r \, d\xi \; , \tag{2.22a}$$

$$\theta_f = m(\xi) \Big[-\frac{q_0^2}{b q_r} \sin \int q_r \, d\xi - 2\theta_s \cos \int q_r \, d\xi \Big] \; , \tag{2.22b}$$

$$\phi_f(\xi) \simeq m(\xi) \Big[\frac{q_0^2}{b q_r^2} \cos \int q_r \, d\xi - 2\frac{\theta_s}{q_r} \sin \int q_r \, d\xi \Big] \; , \tag{2.22c}$$

where m and q_r are the slowly varying modulation depth and filament wavenumber, given by

$$m(\xi) = m_0 \Big(1 + \rho \sinh^2(\chi_0 \xi) \Big)^{1/2\rho} , \qquad \rho \equiv 1 + \frac{4b^2\chi_0^2}{q_0^2} \tag{2.23a}$$

$$\int q_r \, d\xi = q_0 \xi + \frac{2b^2\chi_0}{q_0} \left(\chi_0 \xi - \tanh(\chi_0 \xi) \right) \; , \tag{2.23b}$$

and m_0 is the modulation depth at the center of the device.

The slow amplitude and phase variations are

$$a_s = \frac{b^2\chi_0^2}{q_0^2}\tanh^2(\chi_0\xi) - \frac{1}{2}(m^2(\xi) - m_0^2) \ , \tag{2.24a}$$

$$\theta_s = b\chi_0 \tanh(\chi_0\xi) \ , \tag{2.24b}$$

$$\phi_s = b\ln\cosh(\chi_0\xi). \tag{2.24c}$$

These solutions are parameterized by m_0 and χ_0. Later it will be shown how these quantities are related to the real and imaginary parts of the eigenvalue, η.

The parameter χ_0 appears throughout, and we pause to discuss its significance. Locally, the *angle*, Θ, between the optical axis and the direction of phase and energy propagation is, for small angles (in radians),

$$\Theta(\xi) = \frac{1}{\Re e(\beta)}\frac{d\phi}{dx} = \frac{\lambda_0}{2n\pi d}\theta(\xi), \tag{2.25}$$

where n is the real refractive index and $\theta = \theta_s + \theta_f$, as before. Thus, from (2.24b), $\lambda_0 b\chi_0/2n\pi d$ is the maximum slowly varying angle of off-axis propagation, while d/χ_0 is the lateral position of the "knee" of the hyperbolic tangent. The value of χ_0 is set by matching to the fields outside the gain stripe. As a rule, the larger the change in n_{eff} is at the boundary, the larger χ_0 must be to accommodate it. Note that solutions in media of infinite extent are obtained by putting $\chi_0 = 0$, while m_0 is unspecified.

Thus, depending on the magnitude of χ_0 compared to unity, the phase front can be approximately parabolic over the width of the device ($\chi_0 < 1$), or else quickly approach a linear asymptote on either side ($\chi_0 \gg 1$). The important consequence of this fact is that in the former case, the farfield will be essentially single-lobed, while in the latter case a sharply defined, double-lobed far field will result. Consequently, it is desirable to minimize the change in n_{eff} at the edge of the gain stripe to reduce χ_0 and get a narrow farfield.

The primary structure in the nearfield pattern is the self-modulation. Its wavenumber in the center of the laser is q_0, defined by (2.20c) as

$$q_0^2 = 2\sigma k_0^2 d^2 \epsilon_{sat} \frac{E_0^2}{E_0^2 + E_{sat}^2}. \tag{2.26}$$

This is an *intensity-dependent* quantity, small at low intensity, but quickly increasing to a limiting value. Hence, the filament spacing stabilizes as saturation intensity is surpassed.

Since the filament width saturates, the number of filaments must also stabilize. From Equation (2.22a) we infer the number of lobes in the nearfield to be

$$N = \lceil 1 + \int_0^1 \frac{q_r}{\pi} d\xi \rceil \geq \lceil 1 + \frac{q_0}{\pi} \rceil \ , \tag{2.27}$$

where $\lceil ... \rceil$ denotes the greatest integer less than or equal to the argument. The variable q_r is always greater than or equal to q_0 (Equation (2.23b)), which establishes a lower bound for N. The squared wavenumber q_0^2 saturates to $2\sigma k_0^2 d^2 \epsilon_{sat}$. Recall that σ is an $O(1)$ quantity and can be taken as unity for purposes of discussion. As we mentioned earlier, ϵ_{sat} is the difference in real dielectric constant between transparency and threshold. This difference comes from unsaturable losses (chiefly mirror losses). For a laser of width W, we have

$$N \geq \lceil 1 + W/W_f \rceil, \tag{2.28}$$

where W_f is a saturated filament spacing given by

$$W_f \equiv \sqrt{\frac{\pi \lambda_0 / n_0}{b[\alpha + (1/L)\ln(1/R)]}} \ , \tag{2.29}$$

where L is the laser length, R is the facet reflectivity and α is the distributed loss constant. Thus, unsaturable losses in addition to the mirror losses decrease the saturated filament spacing and increase the number of filaments. These losses give rise to the differing number of filaments observed in DH and QW lasers.

In order to quantify this analysis, we choose ϵ_{sat} to characterize the wafers grown in our laboratory by Molecular Beam Epitaxy. For a single quantum well device of length $L = 500$ μm, the relevant values are $\Gamma g_{th} = 30$ cm^{-1} and $b = 2$ [29]. The value of b has been estimated experimentally for (GaAl)As lasers to lie in the range 2 to 6 [30], with the lower values more appropriate for quantum well lasers (in agreement with Figure 1.6). At $\lambda = 0.845$ μm, this gives $\epsilon_{sat} = 2.7 \times 10^{-3}$, and a saturated filament spacing of ~ 12 μm. This value justifies our decision to neglect diffusion effects in formulating (2.14). For a device 100 μm wide, the estimated lower bound on filament number is $N = 9$. This estimate agrees well with the experimental nearfield trace of Figure 2.1.

At this point, the solutions are parameterized by the modulation depth m_0, phase gradient χ_0, and the field amplitude E_0. It remains to relate m_0 and χ_0 to the eigenvalue, η. We make implicit definitions of $\Delta_{r,i}$ in terms of η as follows:

$$k_0^2 d^2 (n_0^2 - \eta^2) \simeq 2 n_0 k_0^2 d^2 (n_0 - \eta) \equiv \frac{1}{2}\left(\Delta_r + i\frac{\Delta_i}{b}\right). \tag{2.30}$$

Thus, $\Delta_{r,i}$ gives *the deviation of the eigenvalue from the effective index at threshold.* From Equation (2.19a) we have

$$L_0 \equiv L_0^r + i L_0^i \ , \tag{2.31a}$$

$$\text{where} \quad L_0^r = \frac{1}{2}\left(\Delta_r + k_0^2 d^2 \epsilon_{sat}(1-\sigma)\right) \ , \tag{2.31b}$$

$$\text{and} \quad L_0^i = \frac{1}{2b}\left(\Delta_i + k_0^2 d^2 \epsilon_{sat}(1-\sigma)\right) \ . \tag{2.31c}$$

Using Equations (2.A7), (2.A24)-(2.A25) (from Appendix 2A) leads to

$$\Delta_r = k_0^2 d^2 \epsilon_{sat}(\sigma - 1) - m_0^2 q_0^2 \ , \tag{2.32a}$$

$$\Delta_i = k_0^2 d^2 \epsilon_{sat}(\sigma - 1) - 2 m_0^2 q_0^2 - 2 b^2 \chi_0^2 \ . \tag{2.32b}$$

Thus, solving for the physically meaningful quantities of modulation depth m_0 and the slow phase gradient χ_0 by boundary matching is equivalent to determining the normalized eigenvalues Δ_r and Δ_i.

A physically important parameter is the modal gain, G_m, defined to be the rate at which the traveling-wave solution grows. For purposes of discussion, we allow the modal gain to be different from the threshold gain, Γg_{th}, and thus we examine all traveling-wave solutions. Since $G_m - \Gamma g_{th} = -2k_0 \Im m(\eta - n_0)$, we have

$$G_m = \Gamma g_{th} + \frac{\Delta_i}{2b\Re e(n_0)k_0 d^2} \, . \tag{2.33}$$

Ultimately, energy conservation requires $\Delta_i = 0$ for a lasing mode, and this determines the unknown field amplitude E_0 in terms of m_0 and χ_0 via Equation (2.32*b*). The three terms in Δ_i correspond to three physical mechanisms that affect the gain. The first is proportional to $\sigma - 1$. Recall that σ is related to the ratio of pump intensity to field intensity. An increase in σ indicates an increase in the pump level (or decrease in the optical power), which reduces the amount of gain saturation. The second term, proportional to m_0^2, reflects the inefficiency introduced by modulation in the nearfield pattern. In comparison of a field with a modulated nearfield to one without, where both experience the same *modal* gain, the *average* gain level consistent with the modulated field is increased by an amount proportional to the square of the modulation depth; that amount appears here. The third term, proportional to χ_0^2, reflects the losses that are due to phase curvature, or off-axis propagation. Energy propagating at an angle to the optical axis is absorbed by the lossy boundaries; this effect also reduces the gain.

2.3 The Outer Solution and Boundary Matching

Beyond the gain stripe ($\xi \geq 1$), the pump current is zero. However, several processes conspire to prevent the gain from immediately taking on its unpumped value. Current spreading will cause the current injected into the active region to taper off at the edge of the gain stripe. Optical pumping also occurs, which partially bleaches the unpumped material. Our model of n_{eff} is based on a linearization of the gain about the threshold gain, and extension of this model into the unpumped region would be clearly inaccurate. In addition, the roll-off rate of n_{eff} would be of the same order of magnitude as q_0. Consequently, the separation of scales we used in the previous section of this chapter would be inappropriate.

However, the exact shape of the gain distribution outside the gain stripe affects only slightly the rate at which the field grows or decays at the edge of the gain stripe, which in turn determines the values that the inner solution must take on there. For our model, we will assume that the effective index of refraction outside the stripe has a functional form that satisfies the following criteria:

(i) $n_{eff} = n_0$ at the edge of the gain stripe.

(ii) n_{eff} rolls off smoothly to its full absorption value, defined to be n_1.

In addition, we would like the specific functional form to allow for a closed-form, analytic solution. These criteria are satisfied if we take

$$n_{eff}^2 \equiv n_0^2 + B \tanh \kappa(\xi - 1) + C \tanh^2 \kappa(\xi - 1), \tag{2.34}$$

where

$$B + C = n_1^2 - n_0^2, \tag{2.35}$$

and κ characterizes the roll-off rate.

Our approximate solution beyond the gain stripe is, therefore, the solution of the Helmholtz equation, (1.14), with this effective index; that is,

$$E(\xi) = E_1 e^{-D(\xi-1)} \operatorname{sech}^{F/\kappa} \kappa(\xi - 1), \tag{2.36}$$

where the complex constants D and F satisfy

$$F^2 + \kappa F + 2DF = -(n_1^2 - n_0^2) \ , \tag{2.37a}$$

$$D^2 - \kappa F = -\frac{1}{2}(\Delta_r + i\frac{\Delta_i}{b}) \ . \tag{2.37b}$$

The appropriate branches to select are $\Re e(D) \geq 0$ and $\Re e(F) \geq 0$. The eigenvalues are determined by the requirement that the field E and its first derivative E' be continuous at the edge of the gain stripe ($\xi = 1$). Both conditions can be met by the requirement

$$\left.\frac{E'}{E}\right|_{\xi=1^-} = \left.\frac{E'}{E}\right|_{\xi=1^+} \ . \tag{2.38}$$

Consequently, the transcendental equation that determines the eigenvalues and modal gain is:

$$a'(1) + i\theta(1) = -D. \tag{2.39}$$

2.4 Discussion of the Multifilament Solutions

We can now solve the eigenvalue equation for m_0 and χ_0 and substitute the results into our expressions for the lateral mode. In Figure 2.4(a) and (b) we have plotted the lateral power distribution and local phase angle, respectively, for a 10–filament mode of a 100 μm wide device, for current pumping $J = 6J_{th}$, $J_{th}/J_{sat} = 3$, $b = 2$, and $\epsilon_{sat} = 2.7 \times 10^{-3}$. The unsaturated (amplitude) loss outside the gain stripe is taken to be 90 cm^{-1}, and κ corresponds to a 10% – 90% roll-off distance of 20 μm in n_{eff}. The number of lobes in the nearfield pattern, 10, is higher than our estimate, reflecting the additional contributions to q_r that come from χ_0. As we said, χ_0 is set by boundary effects; consequently, lossier boundaries on the gain stripe will increase the number of lobes in the nearfield. This pattern is very similar to the experimental trace reported in Reference 15 (reproduced in Figure 2.4(c)) in the size and spacing of the lobes and the increase in modulation

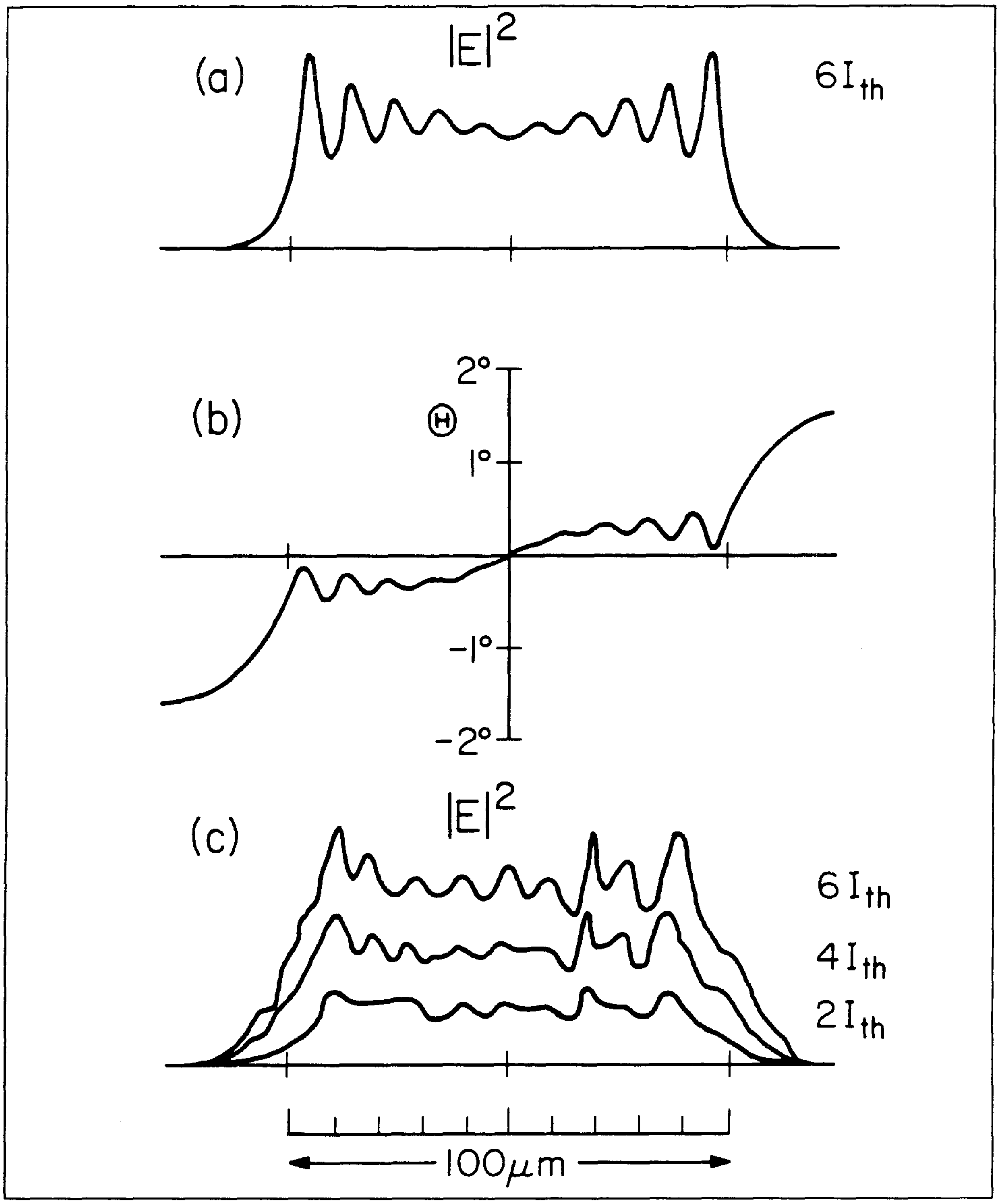

Figure 2.4 *Our analytical solution for the lowest-σ 10-filament mode of a device with half-width $d = 50$ μm, $\epsilon_{sat} = 2.7 \times 10^{-3}$ and $\Gamma g_{th} = 30$ cm^{-1}. The spreading parameter at the edges is $\kappa^{-1} = 20$ μm. (a) Nearfield intensity. (b) Local phase-front angle. The slow component of the phase-front angle reaches 0.32^{o} at the lossy boundary, corresponding to emission off-axis of about 1.1^{o} outside the facet. (c) Experimental trace of nearfield intensity of 100 μm wide device at several points above threshold*[15].

depth towards the edge of the stripe. In addition, we can estimate the width of the far field from the largest local, average phase angle under the gain stripe. In Figure 2.4(a), the average phase angle (inside the facet) is approximately, from Equation (2.25), 0.32^o, which yields a farfield width of 2.1^o outside the laser; that, too, is in agreement with Reference 15.

Next, let us consider the lateral mode spectrum. In the linear case, this spectrum is characterized by a finite set of modes, each with a *distinct modal gain.* The mode with the highest modal gain is deemed to be the lasing mode at threshold. However, the situation is more complex in the associated nonlinear problem. In addition to modal gain, G_m, each mode must also be characterized by a *field amplitude*, E_0, at a given injected current density. This added degree of freedom allows a finite set of lateral modes to have *the same modal gain* by allowing the individual amplitudes to vary.

This multiplicity is illustrated in Figure 2.5. Here we plot the modal gain as a function of σ for modes containing 8–13 filaments. If the resonator losses are 30 cm^{-1}, then all solutions with matching modal gain are candidates for lasing modes. For comparison, the gain of a uniform plane wave of the same E_0 is also plotted. None of the lateral modes is as efficient as a plane wave in extracting gain. That is to be expected because the lateral modes have the absorbing boundaries to contend with. The boundaries introduce losses in two ways. First, they induce a spatial modulation, which lowers the extraction efficiency by an amount proportional to m_0^2. Secondly, as we have said, they impart an overall phase curvature to the field, which directs energy off the axis of propagation and into the absorbing walls. The relative contributions of these two mechanisms are plotted in Figure 2.6 for the lowest-σ mode (*i.e.*, the 10-filament mode). Their explicit contribution to the modal gain can be seen in Equations (2.32–33). The two contributions combine to give each mode an upper cutoff in σ. As σ increases (and thus power decreases), the modal gain for

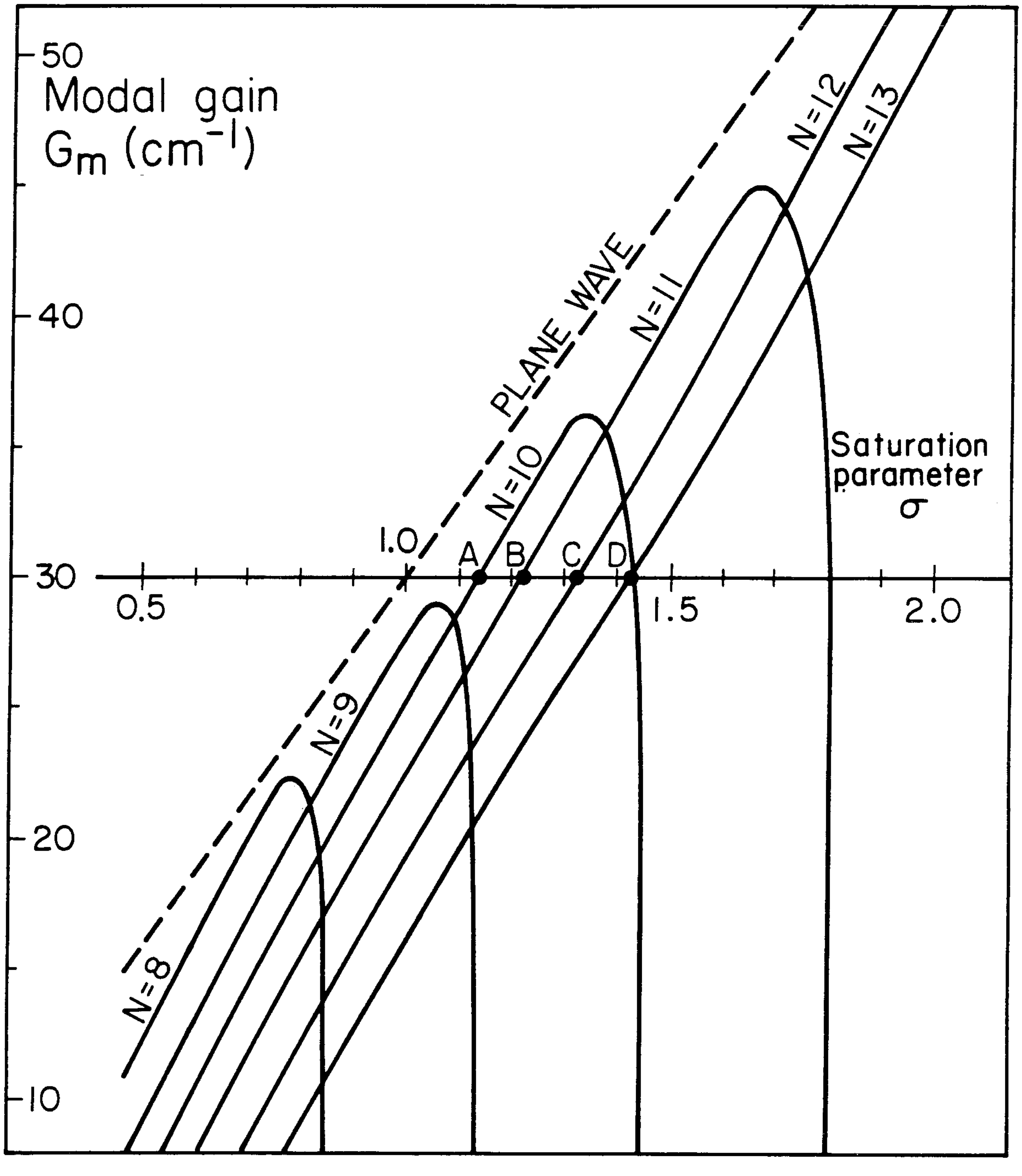

Figure 2.5 *Traces of the $N = 8$ through 13 filament solutions in the modal gain vs. σ plane, with conditions as in Figure 2.4. All modes have lower modal gain than the plane wave, as a result of the modulation depth and phase curvature induced by the boundaries. For a resonator with threshold gain of 30 cm^{-1}, allowable modes must satisfy the steady-state condition $G_m = \Gamma g_{th}$ ($\Delta_i = 0$).*

any given lateral mode will tend to increase as well, because the gain is becoming less and less saturated. However, the saturated filament spacing is becoming ever smaller, and the penalty that the mode pays is an increased modulation depth. Eventually, the modulation penalty overwhelms the benefits of gain saturation; the modal gain falls off again, and the cutoff appears. Fortunately, higher-order modes (meaning more filaments) have successively higher cutoff-σ's, so higher modal gains are always possible with higher-order modes.

We have made the assumption that for a given Γg_{th}, the field pattern with the greatest power (lowest σ) is the actual lasing mode. However, at a given threshold gain, solutions exist for all the lateral modes that are above cutoff. In Figure 2.7 we plot the lateral power distribution for the 4 lowest-order modes with modal gains of 30 cm^{-1}. Successively higher-order modes have more lobes, smaller modulation depth, and more phase curvature (as can be inferred from the correction to the filament wavenumber given in Equation (2.23*b*)).

Finally, we comment briefly on the issue of modal selection. In linear theory, the rule is: The mode with the most gain wins. In a nonlinear system, the lasing mode is determined not by modal gain, but by a *stability analysis.* It is possible (but not likely) that the mode with the smallest σ is unstable, while a mode with a higher σ is stable. Alternatively, for certain operating points there may be multiple stable points (as is the case in coupled-cavity lasers[31]). The plausibility of this latter scenario may become more apparent by considering longitudinal variations within the laser. In a Fabry-Perot laser, the average optical intensity is not a constant, but is minimized somewhere between the two facets. Likewise, the material gain is maximized in the central region. According to our analysis, different modes may be favored in different regions of the resonator. The round-trip σ of a lateral/longitudinal mode combination would thus be a weighted average of the local σ, and this average would be the arbiter of which mode lases.

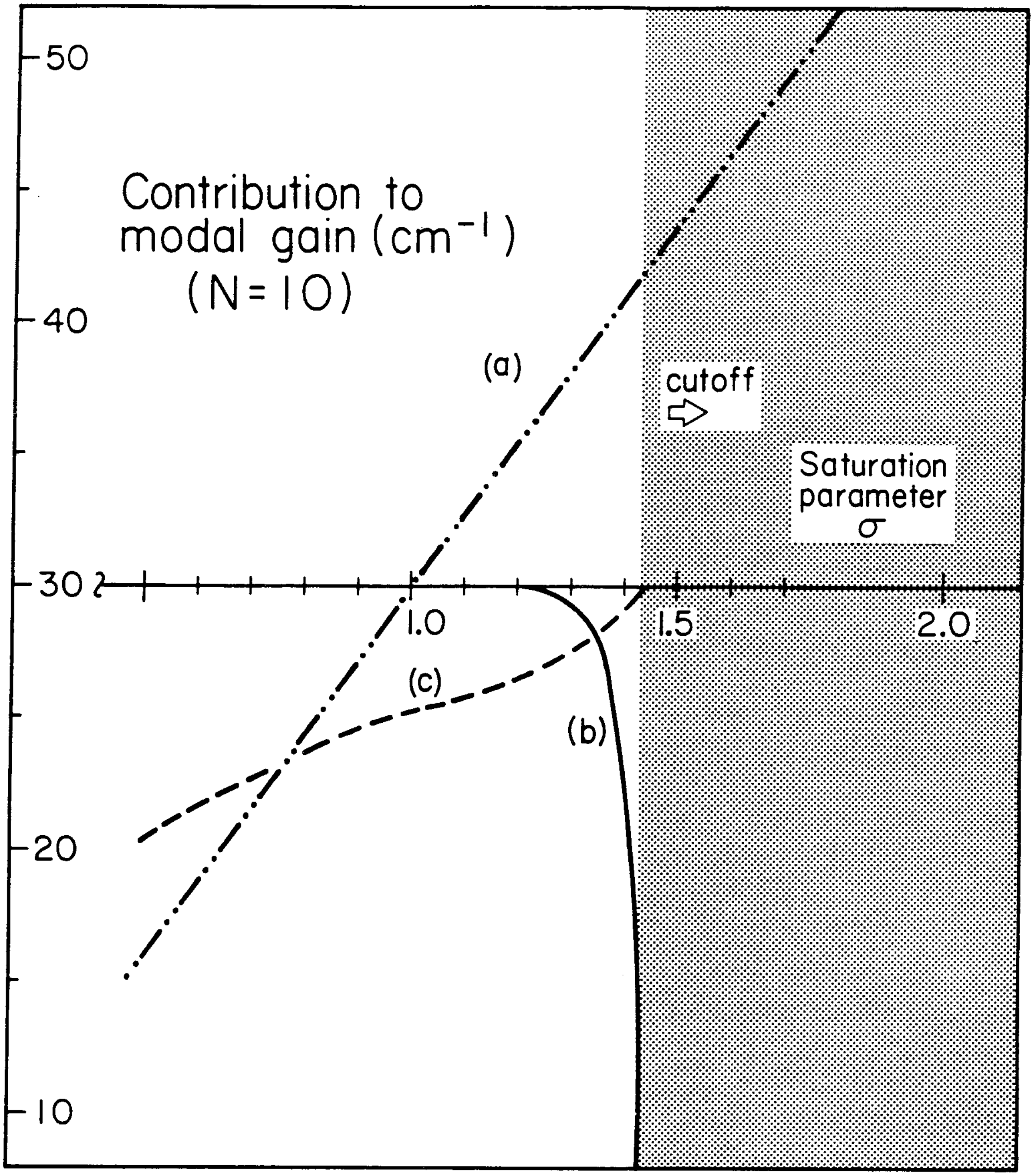

Figure 2.6 *Relative contribution to modal gain from (a) pumping* ($\sigma - 1$), *(b) modulation depth* (m), *and (c) phase curvature* (χ) *for the* $N = 10$ *filament solution in Figure 3. Huge losses incurred by increasing modulation lead to an upper "cutoff" in* σ. *The* $N = 10$ *solution does not exist beyond cutoff.*

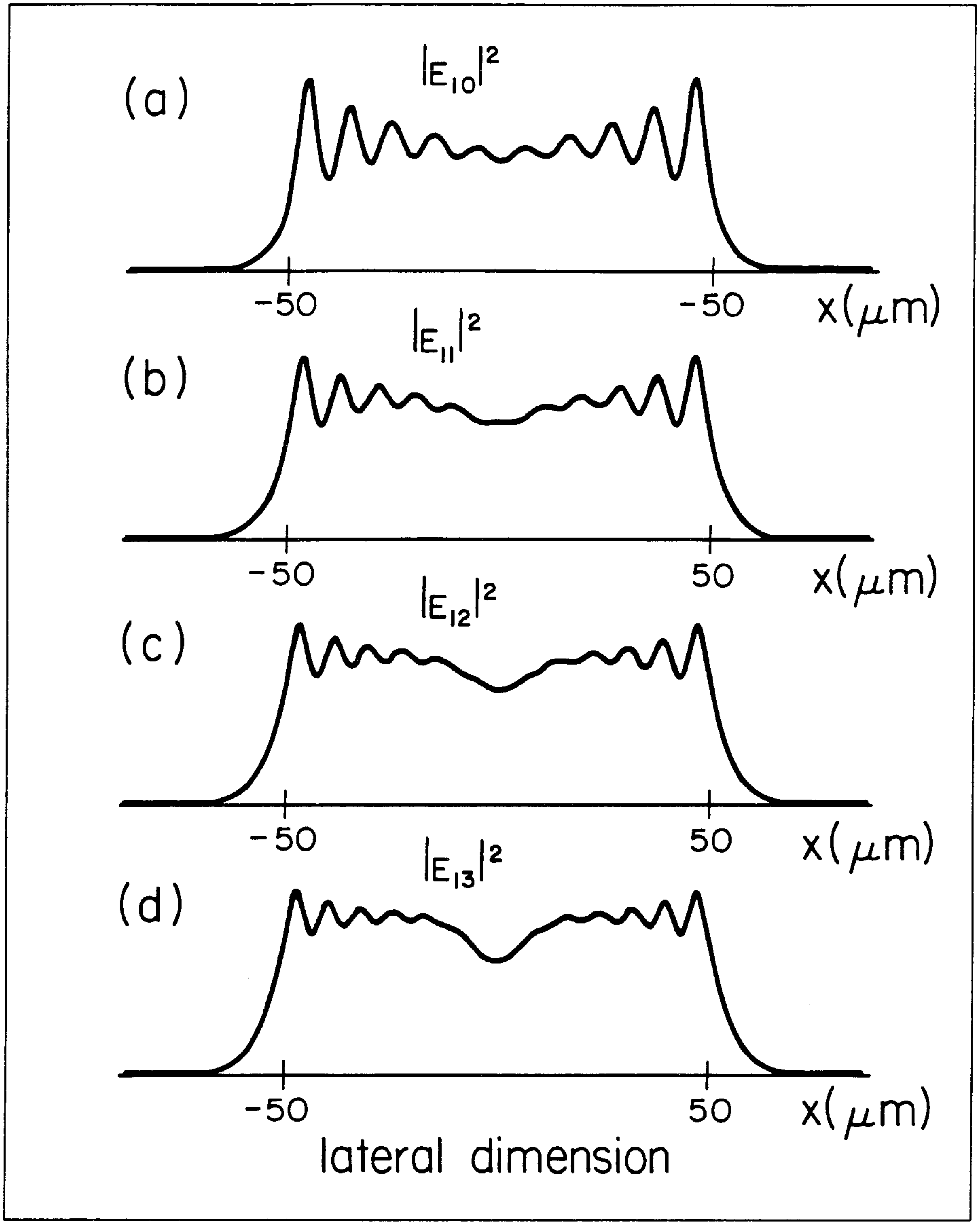

Figure 2.7 *Nearfield intensities for the $N = 10$, 11, 12 and 13 filament solutions for the 30 cm^{-1} loss resonator. Parts (a) – (d) correspond to modes A – D in Figure 2.5.*

Concerning stability, for the unsaturated case where $|E(x)|^2 \ll E_{sat}^2$, the Helmholtz equation can be expressed in the form of the nonlinear Schrödinger equation. This equation is one of a class that admits soliton-like solutions, which are known to be unstable against many types of perturbation[32]. Thus, in the low-power regime, the laser may exhibit instability. Above saturation intensity, however, the nonlinearity is much weaker and the self-guiding mechanism is stabilized.

2.5 Light-Current Curves

In our analysis, we have exploited the perturbation technique of multiscaling to decouple the slowly varying, gain-guiding mechanism from the quickly varying, self-focusing mechanism. This technique breaks down when the intensity-dependent filament size is of the same order as the laser stripe width. This can happen at low powers (near threshold) where the nonlinearity is weak, or for stripe widths narrow enough to be comparable with the saturated filament spacing. In this work, we concern ourselves only with *broad* area lasers, of widths typically 50-100 μm. In order to explore the low-power regime near threshold, a numerical solution of the nonlinear wave equation, (2.14), is required.

Moreover, the numerical solution represents an independent confirmation of our analytical work. Figure 2.8 illustrates the result of a self-consistent numerical integration of Equation (2.14) for a uniform gain broad area laser of width 100 μm. The nearfield intensity and phase angle are shown in (a) and (b) at a pump level of 6 I_{th}, and can be compared with the analytical result shown in Figure 2.4. Apart from a slightly larger filament size, the numerical result compares very favorably with the analytical one. The farfield corresponding to the nearfield of Figure 2.8(a) and (b) is shown in Figure 2.8(c). In agreement with the experimental result, it is narrow and single-lobed.

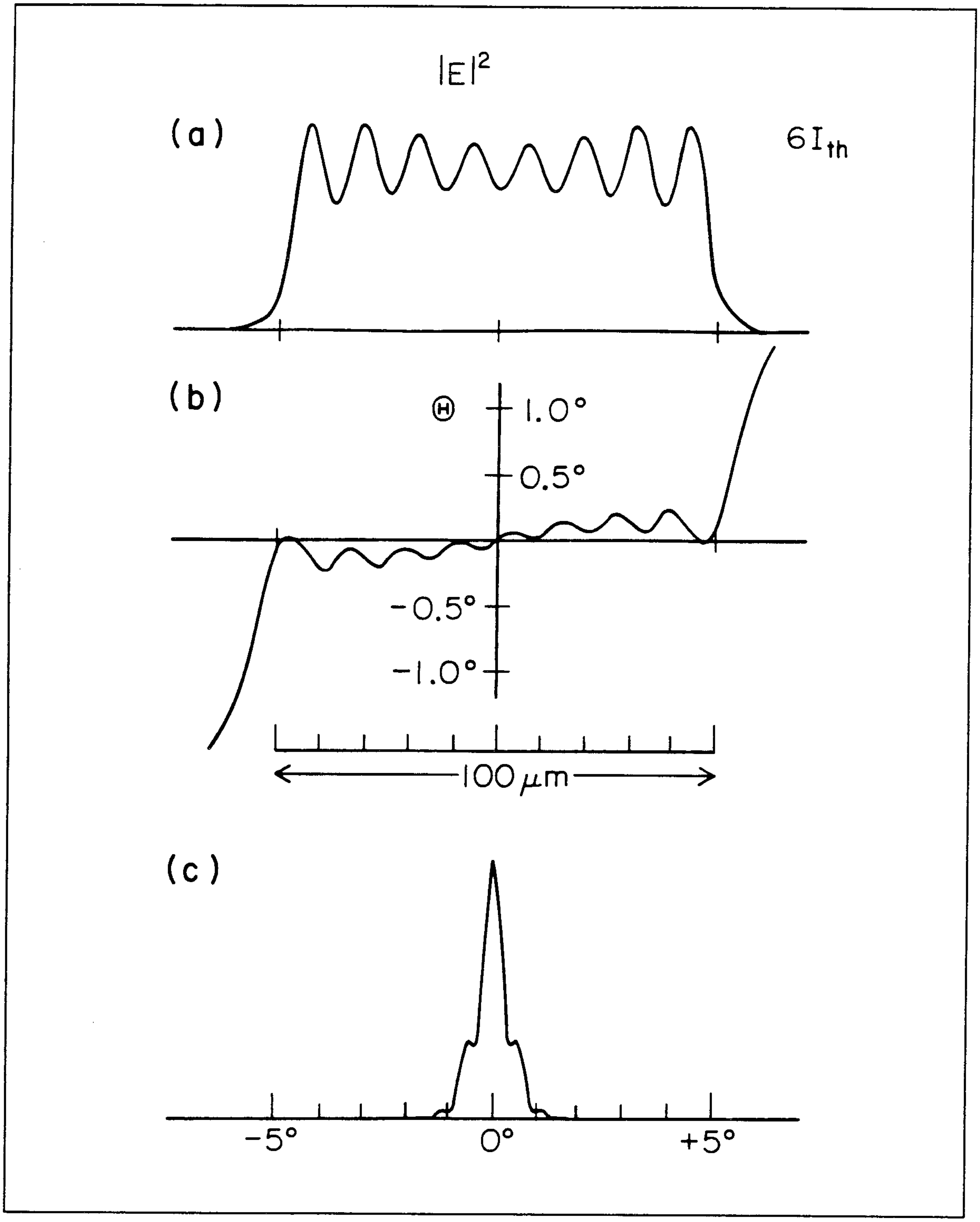

Figure 2.8 *Numerical solution of the N=8 filament mode for a 100 μm wide broad area laser, at a pump level* $I = 6I_{th}$*: (a) nearfield intensity, (b) nearfield phase angle, and (c) farfield intensity.*

As the pump level is reduced to near threshold, the filament size broadens so that the *optimum* number of filaments within the multifilament solution is reduced. This is illustrated in Figure 2.9, which shows the optical power output via each N-filament mode as a function of electrical pump power fed to the 60 μm wide laser. In accordance with the discussion of Section 1.4, self-focusing causes the filaments to narrow as the pump current is increased. As a result, a mode with N filaments utilizes the available gain *less efficiently* than one with N+1 filaments beyond some optimum pump current, causing a rollover in the optical power output. This is evident for the modes shown in Figure 2.9. The mode competition for available gain results in kinks in the light-current curve. Because of the self-stabilizing mechanism, the *range* of drive currents where a given mode is preferred increases substantially at higher output powers.

Numerical solutions also afford the flexibility of altering the boundary conditions at the edges of the current stripe. In particular, it was predicted theoretically[33] that gain guides strongly discriminate against multifilament modes composed of adjacent filaments coupled π radians out of phase. It was determined numerically that these additional modes do exist, but have threshold currents 10-20% higher than the in-phase modes shown in Figure 2.9. In index-guided broad area lasers, this discrimination is reversed, again in accordance with the theoretical prediction.

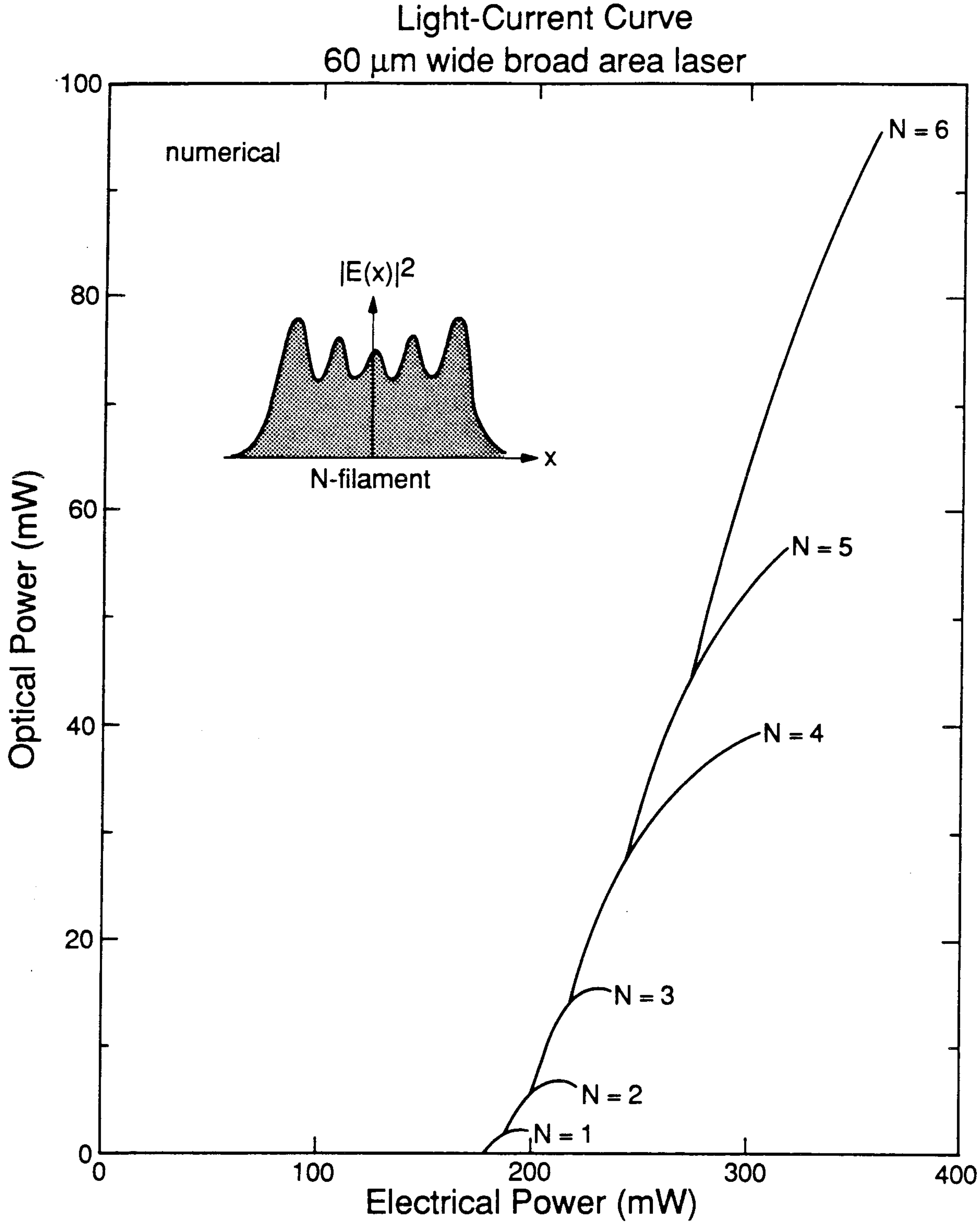

Figure 2.9 *Light output power (mW) vs. electrical input power (mW) for a 60 µm-wide, broad area laser. Curves are shown, for individual N-filament nonlinear modes, to roll over because of self-focusing. Competition from higher-order modes gives rise to kinks in the overall light-current curve.*

2.6 Conclusions

To summarize, in this chapter we have determined, both analytically and numerically, the lateral modes of broad area lasers that are self-consistent with a saturated gain and refractive index profile. We have indicated two different ways in which to regard these modes: the first is that of coupled filaments, and the second is of broad area supermodes. In either case, we conclude that since the self-focusing nonlinearity is saturable, the self-consistent eigensolutions stabilize at high output powers. The strength of the nonlinearity, as governed by the parameter ϵ_{sat}, is proportional to the product of the antiguiding factor b and the modal threshold gain Γg_{th}. As both parameters are smaller in quantum well than in double heterostructure lasers, we found improved broad area performance in quantum well lasers. Indeed, further improvement over quantum well lasers may be realized by *quantum wire* broad area lasers.

Until recently, stable, uniform nearfield patterns have not been commonly observed, as an excellent crystal growth over the entire laser is required to realize spatially uniform gain and index profiles. We have seen from Figure 2.5 that the different longitudinal modes differ in modal gain by only a few cm^{-1}. Furthermore, in numerical calculations we have found that variations in local gain of a fraction of a cm^{-1} will disrupt the smooth lateral structure. To some degree, the effects of longitudinal propagation can smooth out the effects of inhomogeneities. Nevertheless, the broad area laser remains extremely sensitive to such effects. Possibly, the destabilizing effect of material defects can be overcome by structures such as the recently demonstrated "controlled filament" laser[34]. In this structure, the effective mirror reflectivity is modulated in the lateral dimension in order to induce filaments at prescribed positions. The present analysis indicates that this structure can be optimized if the reflectivity modulation is chosen with the same periodicity as the saturated filament spacing of the parent broad area laser.

2.7 Appendix 2A

This appendix details the solution of Equation (2.16). After dividing into real and imaginary parts, this equation becomes

$$a_f'' + a_s'' + (a_f' + a_s')^2 - (\theta_f + \theta_s)^2 + L_0^r + L_1^r(a_f + a_s) = 0 \qquad (2.A1a)$$

$$\theta_f' + \theta_s' + 2(a_f' + a_s')(\theta_f + \theta_s) + L_0^i + L_1^i(a_f + a_s) = 0 \qquad (2.A1b)$$

where, for example, L_0^r denotes the real part of L_0. The fast variables a_f, θ_f, are those that vary on a spatial scale of $O(2\pi/q_0)$; the slow variables a_s, θ_s vary on a spatial scale of $O(1)$. To exploit the existence of two distinct length scales, we spatially average Equations (2.A1) over a distance long compared to $2\pi/q_0$, but short compared to 1, leaving

$$a_s'' + a_s'^2 - \theta_s^2 + L_0^r + L_1^r a_s + \langle a_f'^2 - \theta_f^2 \rangle = 0 \ , \qquad (2.A2a)$$

$$\theta_s' + 2a_s'\theta_s + L_0^i + L_1^i a_s + 2\langle a_f'\theta_f \rangle = 0 \ . \qquad (2.A2b)$$

$\langle ... \rangle$ denotes spatial averaging over the fast scale; Equations (2.A2a–b) vary on the slow scale. They determine the slowly varying quantities a_s and θ_s.

Keeping highest-order terms (dropping $a_s'^2$,a_s'') leads to the following two coupled equations for the slowly varying amplitude and phase gradient:

$$-\theta_s^2 + L_0^r + L_1^r a_s + \langle a_f'^2 - \theta_f^2 \rangle = 0 \ , \qquad (2.A3a)$$

$$\theta_s' + 2a_s'\theta_s + L_0^i + L_1^i a_s + 2\langle a_f'\theta_f \rangle = 0 \ . \qquad (2.A3b)$$

Noting from Equation (2.19b) that $L_1^r = bL_1^i$, we can eliminate a_s easily from these equations, leaving the following equation in θ_s:

$$b\theta_s' + \theta_s(\theta_s + 2ba_s') = b^2\chi^2(\xi), \qquad (2.A4a)$$

where

$$b^2\chi^2(\xi) \equiv L_0^r - bL_0^i + \langle a_f'^2 - \theta_f^2 \rangle - 2b\langle a_f'\theta_f \rangle. \qquad (2.A4b)$$

Neglecting $2ba_s'$ with respect to θ_s, $(2.A4a)$ becomes

$$b\theta_s' = b^2\chi^2(\xi) - \theta_s^2. \tag{2.A5}$$

We choose initial conditions $a_s(0) = 0$, $a_s'(0) = 0$, $\theta_s(0) = 0$, which together with $(2.A3a)$ imply

$$L_0^r + \langle {a_f'}^2 - \theta_f^2 \rangle\big|_0 = 0. \tag{2.A6}$$

Then

$$b\chi^2(0) = -L_0^i - 2\langle a_f'\theta_f \rangle\big|_0. \tag{2.A7}$$

By approximating $\chi \simeq \chi(0) \equiv \chi_0$ (to be checked in Appendix 2B), we can integrate $(2.A5)$ for the slowly varying phase gradient, and then determine the slowly varying amplitude from Equation $(2.A3a)$:

$$\theta_s = b\chi_0 \tanh(\chi_0\xi) \tag{2.A8a}$$

$$a_s = \frac{1}{L_1^r}\left(\tanh^2(\chi_0\xi) - L_0^r - \langle {a_f'}^2 - \theta_f^2 \rangle\right) \tag{2.A8b}$$

We spatially averaged Equations $(2.A1)$ to obtain the slow equations, $(2.A2)$. Upon subtracting Equation $(2.A2)$ from $(2.A1)$, we are left with the fast equations:

$$a_f'' + ({a_f'}^2 - \langle {a_f'}^2 \rangle) + 2a_f'a_s' - (\theta_f^2 - \langle \theta_f^2 \rangle) - 2\theta_f\theta_s + L_1^r a_f = 0 \tag{2.A9a}$$

$$\theta_f' + 2(a_f'\theta_f - \langle a_f'\theta_f \rangle) + 2a_f'\theta_s + 2a_s'\theta_f + L_1^i a_f = 0. \tag{2.A9b}$$

Equations (2.A9a–b) describe a harmonic oscillator system with a slowly varying resonance frequency. The terms in parentheses act as driving terms at double the resonant frequency; their corresponding response will be smaller than the fundamental, and we neglect them in favor of the fundamental response. Of the remaining terms, we keep only those of $O(q_0^2)$ and neglect the $O(q_0)$ and $O(1)$ terms. Equations $(2.A9)$ then simplify to

$$a_f'' - 2\theta_s\theta_f + L_1^r a_f = 0 \tag{2.A10a}$$

$$\theta_f' + 2\theta_s a_f' + L_1^i a_f = 0. \tag{2.A10b}$$

In view of the slowly varying coefficients, we form a WKB-type solution

$$a_f \sim c_1 \, e^{i\int q \, d\xi} \tag{2.A11a}$$

$$\theta_f \sim c_2 \, e^{i\int q \, d\xi} \tag{2.A11b}$$

with slowly varying $q(\xi)$. Together, Equations (2.A10) become the following eigenvalue system

$$\begin{pmatrix} -q^2 + q_0^2 & -2\theta \\ \frac{q_0^2}{b} + iq2\theta_s & iq \end{pmatrix} \begin{pmatrix} c_1 \\ c_2 \end{pmatrix} = \begin{pmatrix} 0 \\ 0 \end{pmatrix} . \tag{2.A12}$$

The characteristic equation is

$$q^2 = q_0^2 + 4\theta_s^2 - i\frac{q_0^2 2\theta_s}{bq}. \tag{2.A13}$$

Taking q to be of the form $q_r - iq_i$, then $q^2 = q_r^2 - q_i^2 - i2q_rq_i$. Assuming that $q_r^2 \gg q_i^2$, we take

$$q^2 = q_r^2 - i2q_rq_i. \tag{2.A14}$$

Comparing Equations (2.A13) and (2.A14) gives

$$q_r^2 = q_0^2 + 4\theta_s^2 \tag{2.A15a}$$

$$q_i = \frac{\theta_s}{b} \frac{q_0^2}{q_0^2 + 4\theta_s^2}. \tag{2.A15b}$$

There are two solutions for q_r (equal magnitude, opposite sign), and one for q_i. Thus, the two solutions of (2.A13) for the propagation constant are

$$q_\pm = \pm q_r - iq_i \ , \tag{2.A16}$$

where henceforth q_r is understood to be the positive root of (2.A15a). Note that $q_i \ll q_r$, as assumed. Now, a_f and θ_f are real quantities. Symmetry dictates the choice of a_f as

$$a_f = \frac{m_0}{2}\left(e^{i\int q_+ d\xi} + e^{i\int q_- d\xi}\right) = m_0 e^{\int q_i d\xi} \cos \int q_r d\xi. \tag{2.A17}$$

The quantity $m(\xi) \equiv m_0 \exp \int q_i d\xi$ is the slowly varying modulation depth. The phase θ_f is then determined by the eigenvector of Equation (2.A12). We have

$$\left.\frac{c_2}{c_1}\right|_{\pm} = i\frac{q_0^2}{bq_\pm} - 2\theta_s \simeq \pm i\frac{q_0^2}{bq_r} - 2\theta_s. \tag{2.A18}$$

Then

$$\begin{aligned}\theta_f &= \frac{m_0}{2}\left[\left.\frac{c_2}{c_1}\right|_{+} e^{i\int q_+ d\xi} + \left.\frac{c_2}{c_1}\right|_{-} e^{i\int q_- d\xi}\right] \\ &= m(\xi)\left(-\frac{q_0^2}{bq_r}\sin\int q_r d\xi - 2\theta_s \cos\int q_r d\xi\right).\end{aligned} \tag{2.A19}$$

Finally, let's estimate how the modulation depth and filament wavenumber vary across the half-width of the device. From (2.A15b) and (2.A8a) we have

$$\int q_i d\xi = \frac{q_0^2}{b}\int \frac{\theta_s}{q_0^2 + 4\theta_s^2} d\xi = \frac{1}{2\rho}\ln(1 + \rho \sinh^2(\chi_0 \xi)), \tag{2.A20a}$$

where

$$\rho \equiv 1 + \frac{4b^2\chi_0^2}{q_0^2}. \tag{2.A20b}$$

Hence the modulation depth is

$$m(\xi) = m_0 e^{\int q_i d\xi} = m_0\Big(1 + \rho \sinh^2(\chi_0\xi)\Big)^{1/2\rho}. \tag{2.A21}$$

Thus, the modulation depth is at a minimum, m_0, at the center of the device, and increases monotonically towards the boundary. For the filament wavevector, we will find that $2\theta_s \leq q_0$, so $q_r = \sqrt{q_0^2 + 4\theta_s^2} \approx q_0 + 2\theta_s^2/q_0$. Then

$$\int q_r d\xi = q_0\xi + \frac{2b^2\chi_0}{q_0}(\chi_0\xi - \tanh(\chi_0\xi)). \tag{2.A22}$$

At the middle of the device, the wavevector is simply q_0, and it, too, increases monotonically towards the boundary.

Finally, recalling the slow equations, (2.$A3$), we can now evaluate the averaged quantities that depend on the fast solutions a_f and θ_f:

$$\langle\theta_f^2\rangle = \frac{m^2}{2}\left(\frac{q_0^2}{b^2}\frac{q_0^2}{q_0^2+4\theta_s^2}+4\theta_s^2\right) \qquad (2.A23a)$$

$$\langle {a_f'}^2\rangle = \frac{m^2}{2}\left(\frac{\theta_s^2}{b^2}\left(\frac{q_0^2}{q_0^2+4\theta_s^2}\right)^2+q_0^2+4\theta_s^2\right) \qquad (2.A23b)$$

$$\langle a_f'\theta_f\rangle = \frac{m^2}{2}\left(\frac{q_0^2}{b}-\frac{2\theta_s^2}{b}\frac{q_0^2}{q_0^2+4\theta_s^2}\right). \qquad (2.A23c)$$

This enables explicit evaluation of the slowly varying amplitude; together (2.$A23$) and (2.$A8b$) give

$$a_s = \frac{1}{q_0^2}\left[b^2\chi_0^2\tanh^2\chi_0\xi - L_0^r - \frac{m^2}{2}q_0^2\right], \qquad (2.A24)$$

where terms of relative order $1/b^2$ have been neglected. This equation can be simplified further. By imposing the condition $a_s(0)=0$, we infer from (2.$A24$) that $L_0^r = -\frac{1}{2}m_0^2q_0^2$. Equation (2.$A24$) becomes

$$a_s = \frac{b^2\chi_0^2}{q_0^2}\tanh^2\chi_0\xi - \frac{1}{2}\left(m^2(\xi)-m_0^2\right). \qquad (2.A25)$$

The last calculation we need is the quantity χ. From Equation (2.$A4b$) we have

$$b^2\chi^2 = L_0^r - bL_0^i + \frac{m^2}{2}\frac{q_0^2}{q_0^2+4\theta_s^2}\left[\frac{\theta_s^2q_0^2}{b^2(q_0^2+4\theta_s^2)} - q_0^2\left(1+\frac{1}{b^2}\right)\right]. \qquad (2.A26)$$

To a good approximation (lowest order in $1/b^2$),

$$b^2\chi^2 \simeq L_0^r - bL_0^i - \frac{m^2}{2}\frac{q_0^4}{q_0^2+4\theta_s^2}. \qquad (2.A27)$$

2.8 Appendix 2B

In the solution of Equation (2.A5),

$$b{\theta_s}' = b^2\chi^2(\xi) - \theta_s^2, \qquad (2.B1)$$

we made the approximation that $\chi(\xi)$ was a constant, χ_0. The actual expression for $\chi(\xi)$ is

$$\chi^2(\xi) - \chi_0^2 = \frac{1}{2b^2}\left[(m_0^2 - m^2(\xi))q_0^2 + m^2(\xi)q_0^2\left(\frac{4\theta_s^2}{q_r^2}\right)\right]. \qquad (2.B2)$$

While $\chi(\xi) = \chi_0$ at $\xi = 0$, the difference could conceivably become significant when $m(\xi) \gg m_0$. We can make an estimate of the error by taking

$$\theta_s = \theta_{s0} + \theta_{s1}, \quad \theta_{s1} \ll \theta_{s0}, \qquad (2.B3)$$

where θ_{s0} satisfies (2.A8). Substituting (2.B3) into (2.B2) gives

$$b\theta_{s1}' + 2\theta_{s0}\theta_{s1} + \theta_{s1}^2 = b^2(\chi^2(\xi) - \chi_0^2). \qquad (2.B4)$$

We neglect θ_{s1}^2 (we are assuming that the error is small) and substitute (2.B1) for $\chi^2(\xi) - \chi_0^2$, to get

$$\theta_{s1}' + \frac{2}{b}\theta_{s0}\theta_{s1} = \frac{q_0^2}{2b^2}\left(m_0^2 - m^2(\xi)\frac{q_0^2}{q_r^2}\right). \qquad (2.B5)$$

(2.B5) has the solution

$$\theta_{s1} = \frac{m_0^2 q_0^2}{2b}\operatorname{sech}^2\chi_0\xi \int_0^\xi d\zeta \cosh^2\chi_0\zeta \left[1 - \frac{q_0^2(1+\rho\,\sinh^2\chi_0\zeta)^{1/\rho}}{q_0^2 + 4b^2\chi_0^2\tanh^2\chi_0\zeta}\right]. \qquad (2.B6)$$

The integral in (2.B6) does not have a simple closed-form expression, but we are interested only in determining the approximate size of θ_{s1} relative to θ_{s0}. We asymptotically expand (2.B6) for large and small χ_0, yielding

$$\frac{\theta_{s1}}{\max(\theta_{s0})} = \frac{\theta_{s1}}{b\chi_0} \sim \begin{cases} \frac{m_0^2 q_0^2}{4b^2\chi_0^2} & \text{as } \chi_0 \to \infty\ , \\ -\frac{m_0^2 q_0^2}{6b}\chi_0\xi^3 & \text{as } \chi_0 \to 0\ . \end{cases} \qquad (2.B7)$$

While θ_{s1} undergoes a sign change at some intermediate value of χ_0, neither expression becomes $O(1)$ for reasonable values of m_0, q_0, and χ_0. Therefore, the original approximation is valid.

References

[1] J.C. Dyment, "Hermite-Gaussian mode patterns in GaAs junction lasers," *Appl. Phys. Lett.* **10**, 84-86 (1967).

[2] E. Kapon, J. Katz and A. Yariv, "Supermode analysis of phase-locked arrays of semiconductor lasers," *Opt. Lett.* **10**, no. 4, 125-127 (1984).

[3] J. Katz, E. Kapon, C. Lindsey, J.S. Smith, S. Margalit, U. Shreter and A. Yariv, "Phase-locked semiconductor laser array with separate contacts," *Appl. Phys. Lett.* **43**, 1257-1260 (1984).

[4] E. Kapon, C. Lindsey, J. Katz, S. Margalit and A. Yariv, "Chirped arrays of diode lasers for supermode control," *Appl. Phys. Lett.* **45**, 200-202 (1984).

[5] D. Ackley, "Phase-locked injection laser arrays with non-uniform stripe spacing," *Electron. Lett.* **20**, 695-697 (1984).

[6] L. Figueroa, C. Morrison, H.D. Law and F. Goodwin, "Twin-channel laser with high cw power and low beam divergence," *J. Appl. Phys.* **56**, 3357-3359 (1984).

[7] Y. Twu, A. Dienes, S. Wang and J.R. Whinnery, "High power coupled-ridge waveguide semiconductor laser arrays," *Appl. Phys. Lett.* **45**, 709-711 (1984).

[8] S. Mukai, C. Lindsey, J. Katz, E. Kapon, Z. Rav-noy, S. Margalit and A. Yariv, "Fundamental mode oscillation of a buried ridge waveguide laser array," *Appl. Phys. Lett.* **45**, 834-835 (1984).

[9] C. Lindsey, E. Kapon, J. Katz, S. Margalit and A. Yariv, "Single-contact tailored gain phased array of semiconductor lasers," *Appl. Phys. Lett.* **45**, 722-24 (1984).

[10] C. Lindsey, P. Derry and A. Yariv, "Tailored gain broad area semiconductor laser with single-lobed diffraction-limited farfield pattern," *Electron. Lett.* **21**, no. 16, 671-673 (1985).

[11] D. Welch, D. Scifres, P. Cross, H. King, W. Streifer, R.D. Burnham, J. Yaeli and T. Paoli, "High power cw operation of phased array diode lasers with diffraction-limited output beam," *Appl. Phys. Lett.* **47**, 1134-1136 (1985).

[12] L. Goldberg, H.F. Taylor, J.F. Welles and D. Scifres, "Injection locking of coupled-stripe diode laser arrays," *Appl. Phys. Lett.* **46**, 236-238 (1985).

[13] J.P. Hohimer, A. Owyoung and G.R. Hadley, "Single-channel injection locking of a diode laser array with a cw dye laser," *Appl. Phys. Lett.* **47**, 1244-1246 (1985).

[14] J. Salzman, T. Venkatesan, R. Lang, M. Mittelstein and A. Yariv, "Unstable resonator cavity semiconductor lasers," *Appl. Phys. Lett.* **46**, 218-220 (1985).

[15] A. Larsson, M. Mittelstein, Y. Arakawa and A. Yariv, "High efficiency broad area single quantum well lasers with narrow single-lobed farfield pattern prepared by MBE," *Electron. Lett.* **22**, no. 2, 79-81 (1986).

[16] M. Mittelstein, J. Salzman, A. Larsson and A. Yariv, unpublished.

[17] G.H.B. Thompson, "A theory for filamentation in semiconductor lasers," *Optoelectronics* **4**, 257-310 (1972).

[18] F.R. Nash, "Mode guidance parallel to the junction plane of double heterostructure GaAs lasers," *J. Appl. Phys.* **44**, 4696-4707 (1973).

[19] P.A. Kirkby, A.R. Goodwin, G.H.B. Thompson and P.R. Selway, "Observations of self-focusing in stripe geometry semiconductor lasers and the development of a comprehensive model of their operation," *IEEE Journal of Quantum Electronics* **QE-13**, 705-719 (1977).

[20] R. Lang, "Lateral transverse mode instability and its stabilization in stripe-geometry injection lasers," *IEEE Journal of Quantum Electronics* **QE-15**, 718-726 (1979).

[21] S. Wang, C.Y. Chen, A. Liao and L. Figueroa, "Control of mode behavior in semiconductor lasers," *IEEE Journal of Quantum Electronics* **QE-17**, 453-468 (1981).

[22] L. Figueroa, T. Holcomb, K. Burghard, D. Bullock, C. Morrison, L. Zinkiewicz and G.A. Evans, "Modeling of the optical characteristics for twin-channel laser structures," *IEEE Journal of Quantum Electronics* **QE-22**, 2141-2149 (1986).

[23] W. Streifer and E. Kapon, "Application of the equivalent index method to DH diode lasers," *Appl. Opt.* **18**, no. 22, 3724-3725 (1979).

[24] W. Tsang, "Extremely low threshold AlGaAs graded-index waveguide separate confinement heterostructure lasers grown by molecular beam epitaxy," *Appl. Phys. Lett.* **40**, 217-219 (1982).

[25] C. Bender and S. Orszag, *Advanced Mathematical Methods for Scientists and Engineers*, p.499 (McGraw-Hill, New York, 1978).

[26] A. Yariv, *Optical Electronics*, p.142 (3^{rd} ed.) (Holt, Rinehart and Winston, New York, 1985).

[27] G. Stegeman and C. Seaton, "Nonlinear integrated optics," *J. Appl. Phys.* **58**, R57-R78 (1985).

[28] N. Dutta, N. Olsson and W. Tsang, "Carrier-induced refractive index change in AlGaAs quantum well lasers," *Appl. Phys. Lett.* **45**, 836-837 (1984).

[29] Y. Arakawa and A. Yariv, "Theory of gain, modulation response and spectral linewidth in AlGaAs quantum well lasers," *IEEE Journal of Quantum Electronics* **QE-21**, no. 10, 1666-1674 (1985).

[30] J. Buus, "Principles of semiconductor laser modelling," *IEE Proc.* **132-J**, no. 1, 42-51 (1985).

[31] R. J. Lang and A. Yariv, "Intermodal stability of a coupled-cavity laser," *IEEE J. Quantum Electron.* **QE-22**, pp. 631-636 (1986).

[32] M. Ablowitz and A. Segur, *Solitons and the Inverse Scattering Transform*, pp.271-273 (Studies in Applied Mathematics, Princeton, 1981).

[33] D. Mehuys, M. Mittelstein, J. Salzman and A. Yariv, "Saturable nonlinear dielectric waveguide with applications to broad area semiconductor lasers," *Opt. Lett.* **12**, 953-955 (1987).

[34] J. Salzman, A. Larsson and A. Yariv, "Phase locked controlled filament laser," *Appl. Phys. Lett.* **49**, 611-613 (1986).

CHAPTER

Three

Asymmetric Tailored-Gain Broad Area Lasers

3.0 Introduction

In the previous chapter, we briefly detailed experimental emission characteristics of broad area lasers that appeared anomalous in light of the established linear theories of gain-guided structures. As a result, we proposed and demonstrated theoretically that the nonlinearity introduced by gain saturation could be responsible for narrow, single-lobed farfield emission that persists into the high-power regime.

However, the fraction of broad area lasers exhibiting this anomalous behavior is quite small. Others exhibit classic filamentary behavior by which multiple filaments form but are not phase-locked. On the other hand, there are some devices that exhibit considerable coherence over, say, 50 μm wide apertures, and whose behavior *can* be adequately explained by linear theories. Two examples follow.

Figure 3.1 shows the nearfield intensity, spectrally-resolved nearfield intensity, and the farfield intensity of a 60 μm-wide broad area laser at three different current levels above threshold. We observe that the nearfield is characterized by a large dc term with a small ripple, as in the nonlinear modes, and that the number of ripples increases from 3 to 5 to 7 as the current is increased. The farfield, however, is *broad* (full width half max $\simeq 5^o$ at threshold) *in contrast* to that of the nonlinear modes, and broadens further with increased current pumping. The origin of these features is revealed in the spectrally resolved nearfield. At each pumping level, we observe a multiplet of spatial modes, each with a different lateral intensity profile, repeated

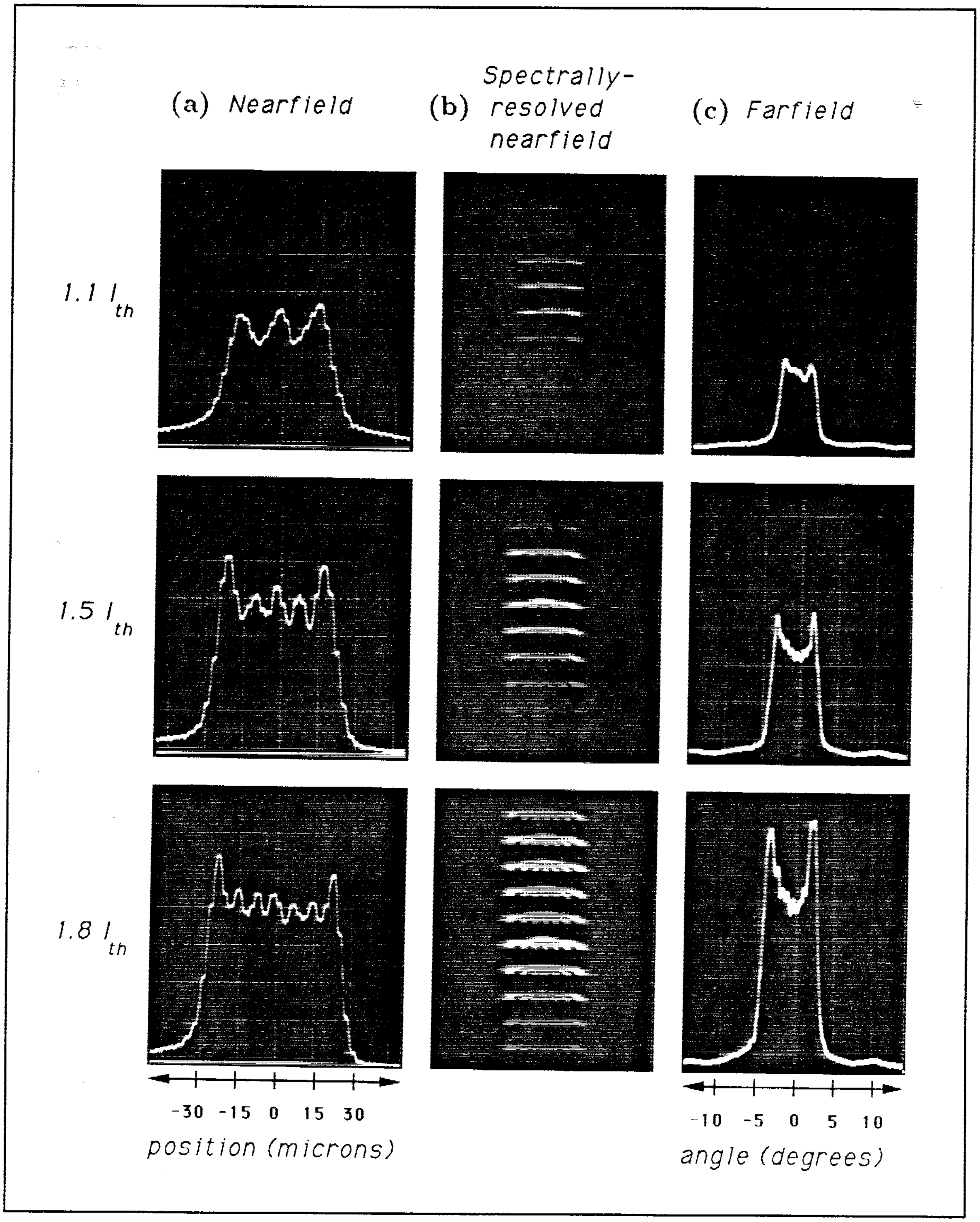

Figure 3.1 *Free-running characteristics of a 60 μm-wide, broad area laser at the three current levels* $1.1I_{th}$, $1.5I_{th}$ *and* $1.8I_{th}$: *(a) nearfield intensity, (b) spectrally-resolved nearfield intensity, and (c) farfield intensity. For the spectrally-resolved nearfield, wavelength increases towards the top of the photo.*

at the longitudinal mode spacing of 3.5 Å. Both the number of longitudinal modes and the number of spatial modes within each multiplet increase with the pump level. This is the result of, respectively, spectral and spatial gain saturation. This saturation is depicted schematically in Figure 3.2.

Figure 3.2(a) shows the gain as solid lines for 3 different current levels, $I_3 > I_2 > I_1$. Shown as discrete points are the loss and oscillation frequency of the different spatial (lateral) modes, as calculated from a linear analysis. At $I = I_1$, only the $\nu = 1$ modes participate in the lasing. However, Figure 3.2(b) shows that the $\nu = 1$ mode saturates the gain incompletely because it has less than unit overlap with the injected current density. At some elevated current level, $I = I_2$, therefore, the $\nu = 2$ mode reaches threshold and also participates in the lasing, as shown in Figure 3.2(a). By extension, the $\nu = 3$ mode reaches threshold at $I = I_3$. Thus, higher order spatial modes participate in lasing at higher injected current densities. Since each spatial mode oscillates at a *different* frequency, they are mutually incoherent. The incoherent sum of their nearfield and farfield intensities can be seen from Figure 3.2(b) to give rise to the measured patterns shown in Figure 3.1. Note especially that just the $\nu = 1$ mode has a single-lobed farfield. All others are twin-lobed, with lobe separations that increase slightly with mode index. The spectrally integrated farfield is therefore box-like, and broadens *in proportion to the number of lateral modes* that participate in the lasing. This behavior has been observed with high uniformity GRINSCH-SQW broad area lasers grown by MOCVD.

We turn now to a second example of controlled behavior from high-uniformity broad area lasers. Figure 3.3 shows the nearfield intensity, spectrally-resolved nearfield, and farfield intensity from this second class of devices, at an elevated current level $I = 1.75 I_{th}$. In contrast to the first class, the spectrally-resolved

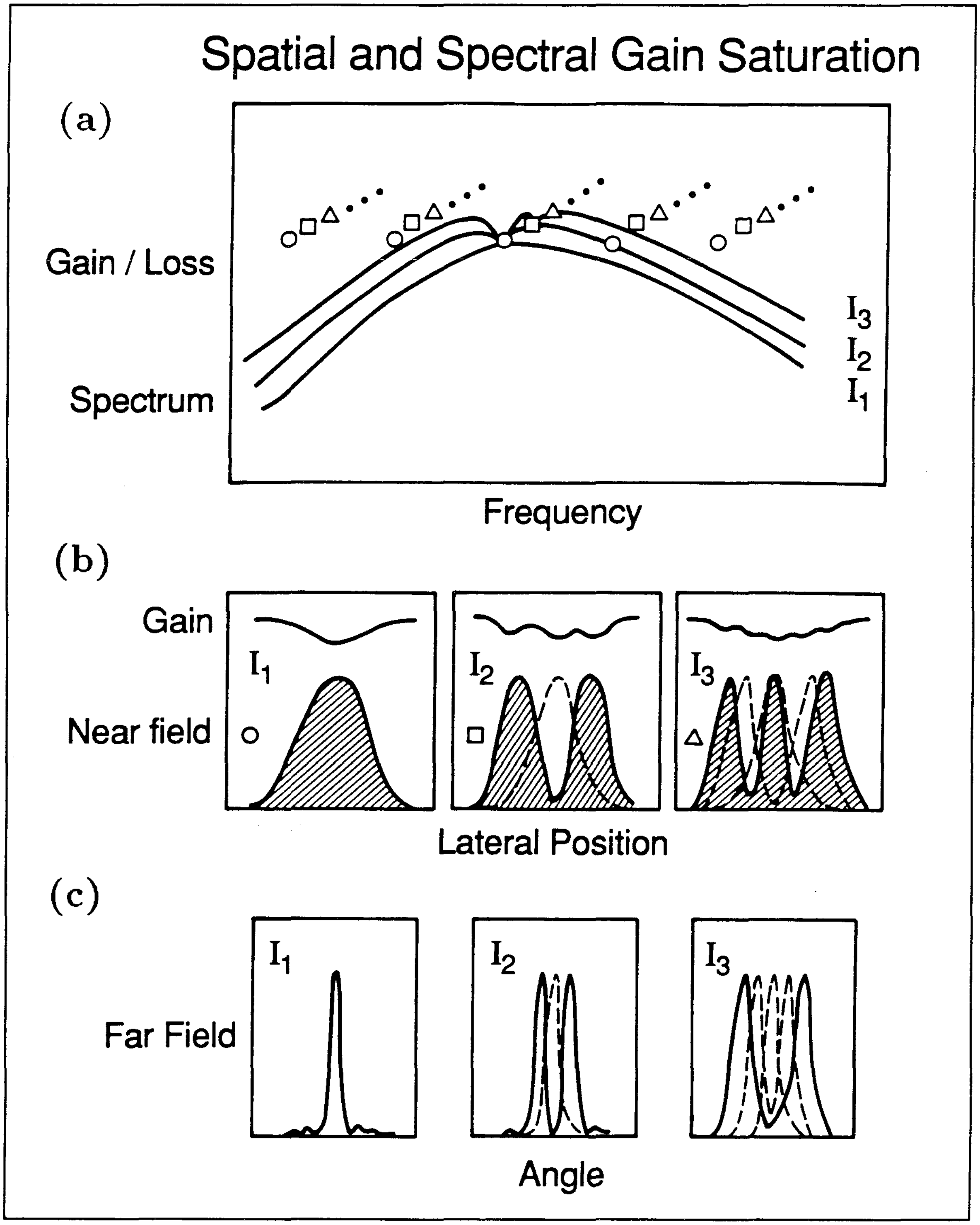

Figure 3.2 *Spatial and spectral gain saturation in broad area lasers: (a) gain spectra at three current levels matching losses of the lowest-order waveguide modes, (b) spatial hole burning gives rise to multilateral mode oscillation, and (c) broad farfields.*

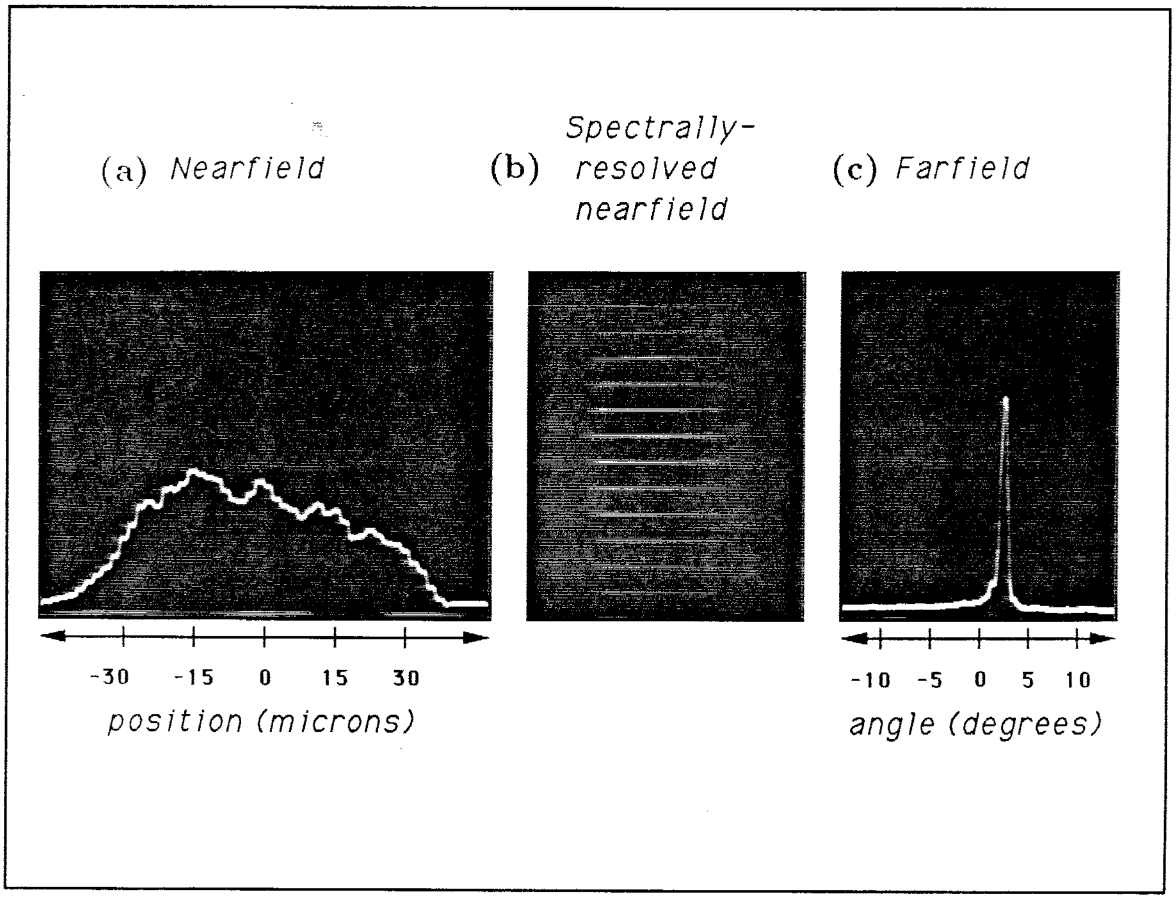

Figure 3.3 *Free-running emission characteristics of a 60 μm-wide, broad area laser, purportedly with a slight asymmetric gain gradient: (a) nearfield intensity, (b) spectrally-resolved nearfield intensity, and (c) farfield intensity, all at the current level* $I = 1.75 I_{th}$.

nearfield shows a *single* spatial mode repeated at several longitudinal mode frequencies, and the farfield is narrow and single-lobed. However, that single lobe is *not normal* to the facet, and *shifts* by about one beamwidth as I is increased from I_{th} to 1.75 I_{th}. Asymmetry is also observed in the nearfield intensity. As we will show, this asymmetry can result from the introduction of an asymmetric gain gradient across the width of symmetric devices such as those discussed in the previous example. In the process, the gain discrimination between competing lateral modes

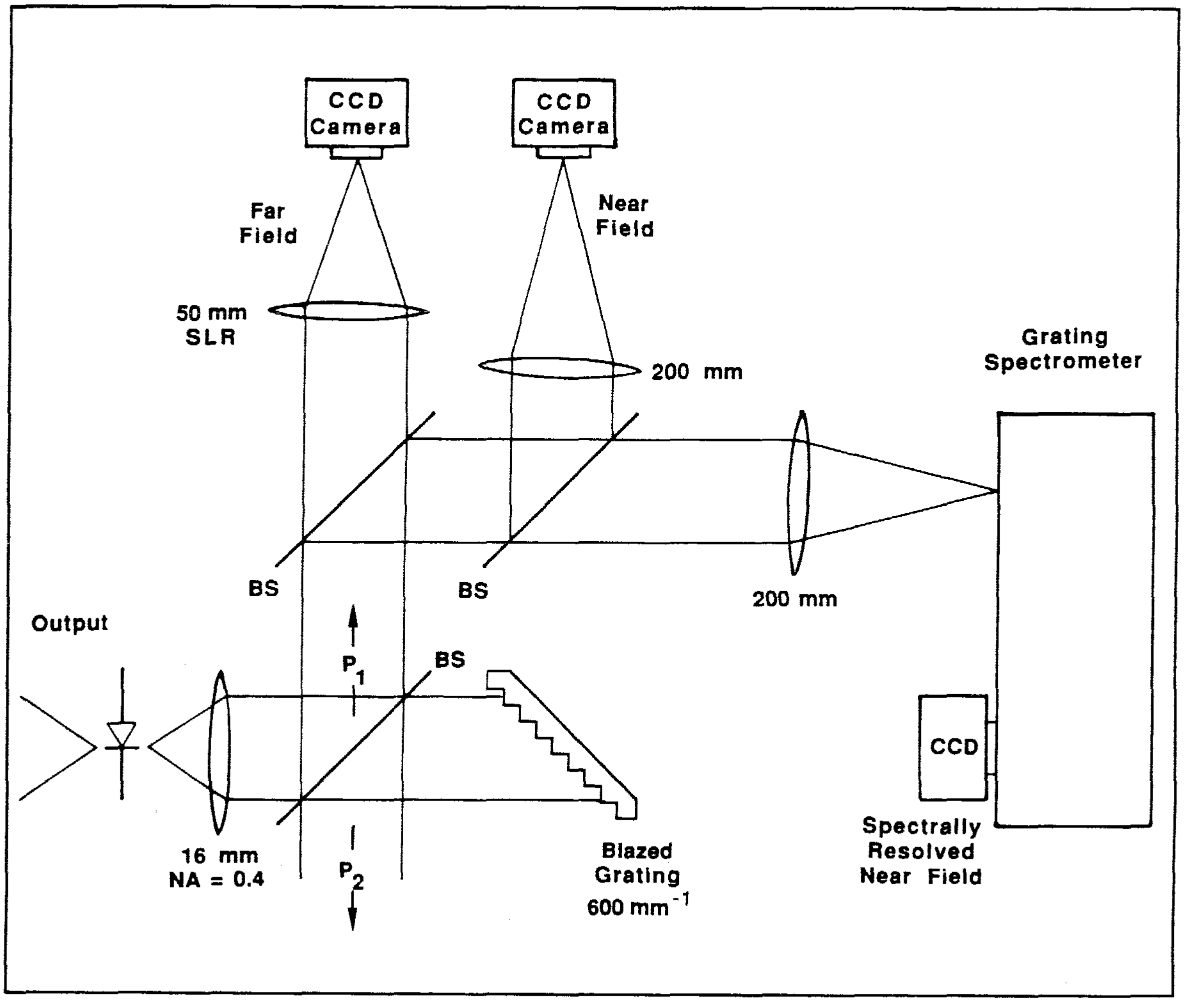

Figure 3.4 *Experimental apparatus: light from the rear laser facet is collimated, dispersed by the grating and refocussed onto the laser. The collimated beam is intercepted by an* $R = 8\%$ *beamsplitter in order to image the nearfield, spectrally-resolved nearfield, and the farfield.*

is *increased.* Thus, the onset of multilateral mode operation, as illustrated in Figure 3.2, is *delayed* until higher injection currents, to obvious advantage.

In order to examine this device more closely, a small amount of optical feedback was added by coupling the laser to an external cavity comprised of a collimating lens and a diffraction grating, as shown in Figure 3.4. When the grating is tuned to reflect in first order, this external cavity images a spectrally-resolved, spatially inverted nearfield back onto the rear facet of the semiconductor laser. It thus has the dual purpose of *symmetrizing* the lateral dimension (via the inversion) and enforcing *single longitudinal mode* operation (via dispersal of the spectrum perpendicular to the epitaxial layers). The resulting integrated and spectrally-resolved nearfields are shown in Figure 3.5 along with the farfield intensity, shown *superimposed on that with the grating blocked* (*i.e.,* Figure 3.3(c)). As is evident, the laser operates in a single longitudinal mode. Most likely, because of the box-like farfield observed, several lateral modes are also lasing but remain unresolved by the grating monochromator. The resolution of the lens-grating pair is about 2.2 Å, and that of the monochromator about one-tenth of that. We note immediately that the grating-decoupled farfield is offset from 0^o by more than one beamwidth. This result is consistent with the predictions of the forthcoming analysis.

That the asymmetry is consistent with a gain profile that is *graded* across the device width can be seen as follows: the more common double-lobed farfields observed for symmetric devices are indicative of the two "plane-wave" components, propagating with equal but opposite lateral k-vectors, which comprise each lateral mode (see Section 5.0). An asymmetric gain gradient *suppresses* one of these components so that, in the farfield, a single lobe is radiated that is *offset* from the normal. The mechanism is as follows: in order for the lateral mode to propagate self-consistently, it must grow uniformly upon propagation along the laser axis. To accomplish this in the presence of a lateral gain gradient requires the modal wavefront to be *skewed*, thereby directing to the low-gain side photons generated on the high-gain side. This wavefront tilt compensates for the spatial imbalance in the photon generation rate. In addition, as will be shown, the gain gradient spatially *segregates* the lateral modes. Thus, the mode that is localized more in the high-gain region has the highest modal gain, and the gain discrimination between this mode and all others is *increased* over the uniform gain case. As such, we expect

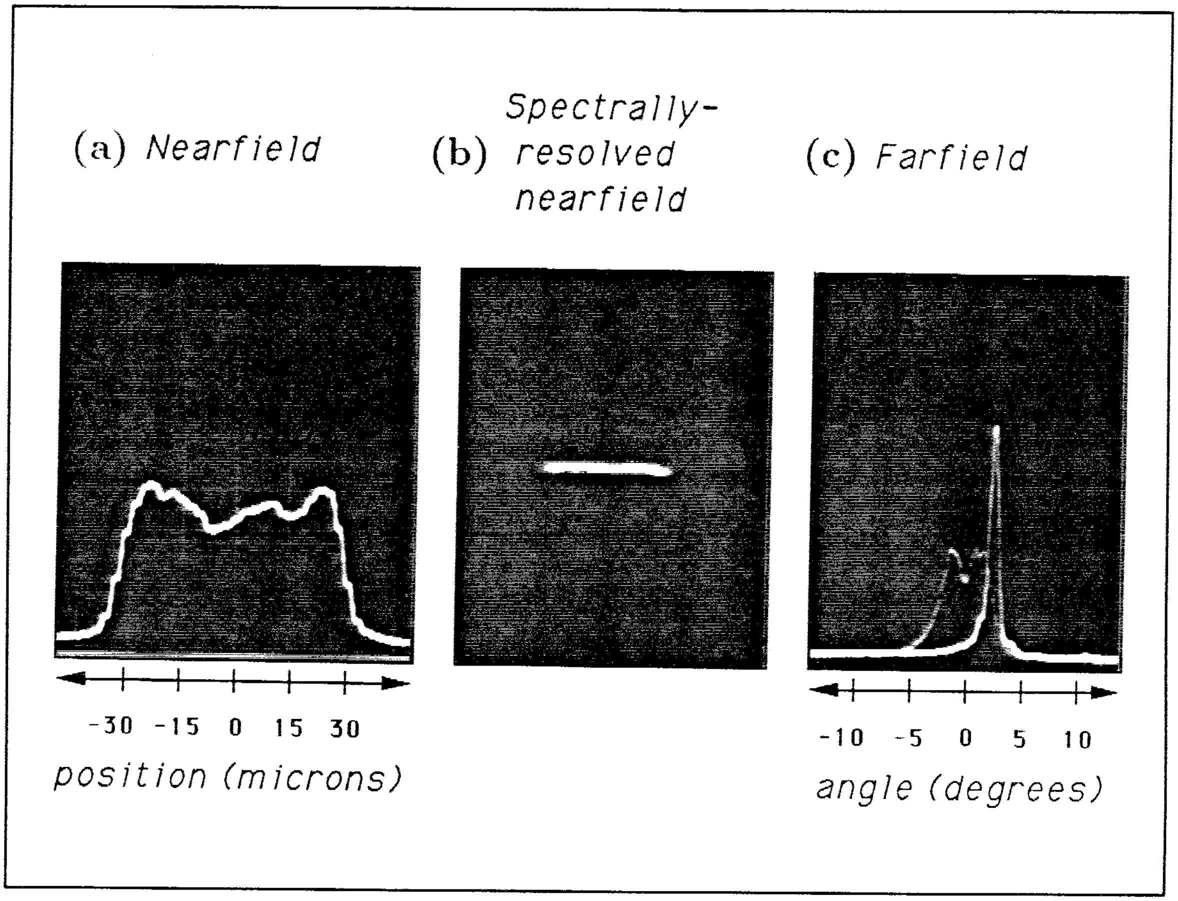

Figure 3.5 *Emission characteristics of the laser of Figure 3.3 under grating-coupled operation at* $I = 1.5I_{th}$*: (a) nearfield intensity, (b) spectrally-resolved nearfield intensity, and (c) farfield intensity at the current level* $I = 1.1I_{th}$ *under grating-coupled (dashed) and uncoupled (solid) operation.*

single-lateral mode oscillation to persist to higher currents than the uniform gain case. This expectation is borne out by the experimental results.

In application of this principle, Lindsey et al. have demonstrated[1,2] intentionally gain-tailored broad area lasers, by varying the fractional coverage of injecting metal-to-p^+ GaAs contact relative to Schottky-blocking metal-to-p GaAlAs contact over the surface of a broad area laser via halftone photolithography. The enhanced current spreading provided by a thick upper cladding layer smears out the effects of the discrete dots and gives rise to a smooth, nonuniform spatial gain distribution within the active region. In this manner, an approximately linear, asymmetric gain profile was created via incorporation of the gain dependence on injected carrier density. This scheme is illustrated in Figure 3.6. The gain-tailoring principle has also been applied to laser arrays in order to induce fundamental supermode operation[3-5].

In the following analysis, we determine the unsaturated optical eigenmodes of a linear, asymmetric, tailored-gain waveguide. We will show that the highly nonuniform gain profile in halftone, tailored-gain broad area lasers plays an important role in the suppression of the lateral mode control problem observed in uniform gain devices. For example, we show that the higher order lateral modes of these lasers have farfield patterns that are *all single-lobed* and only slightly displaced from the fundamental. Thus even under multi-lateral mode oscillation, the farfield pattern remains single-lobed, albeit with a slightly larger beamwidth. In addition, the beam emission angle at threshold is sensitive to the exact value of the antiguiding factor, b; consequently use is made of asymmetric tailored-gain broad area lasers with varying spatial gain gradients to make a *measurement* of b for the case of a multiple quantum well active region.

3.1 Path Analysis of the Linear Tailored-Gain Waveguide

In a linear asymmetric waveguide, we model the complex effective index of refraction, $n(x)$, by

$$n_{eff}(x) = \begin{cases} n_e & -\infty < x \leq 0^- \\ n_0 - \sigma k_0 x & 0^+ \leq x \leq \ell^- \\ n_e & \ell^+ < x < \infty \end{cases} \tag{3.1}$$

where n_e is the (constant) complex index of refraction external to the guide, n_0 and σ are also complex constants, and ℓ is the width of the guide. Throughout this chapter, we will denote the real and imaginary parts of the complex index of

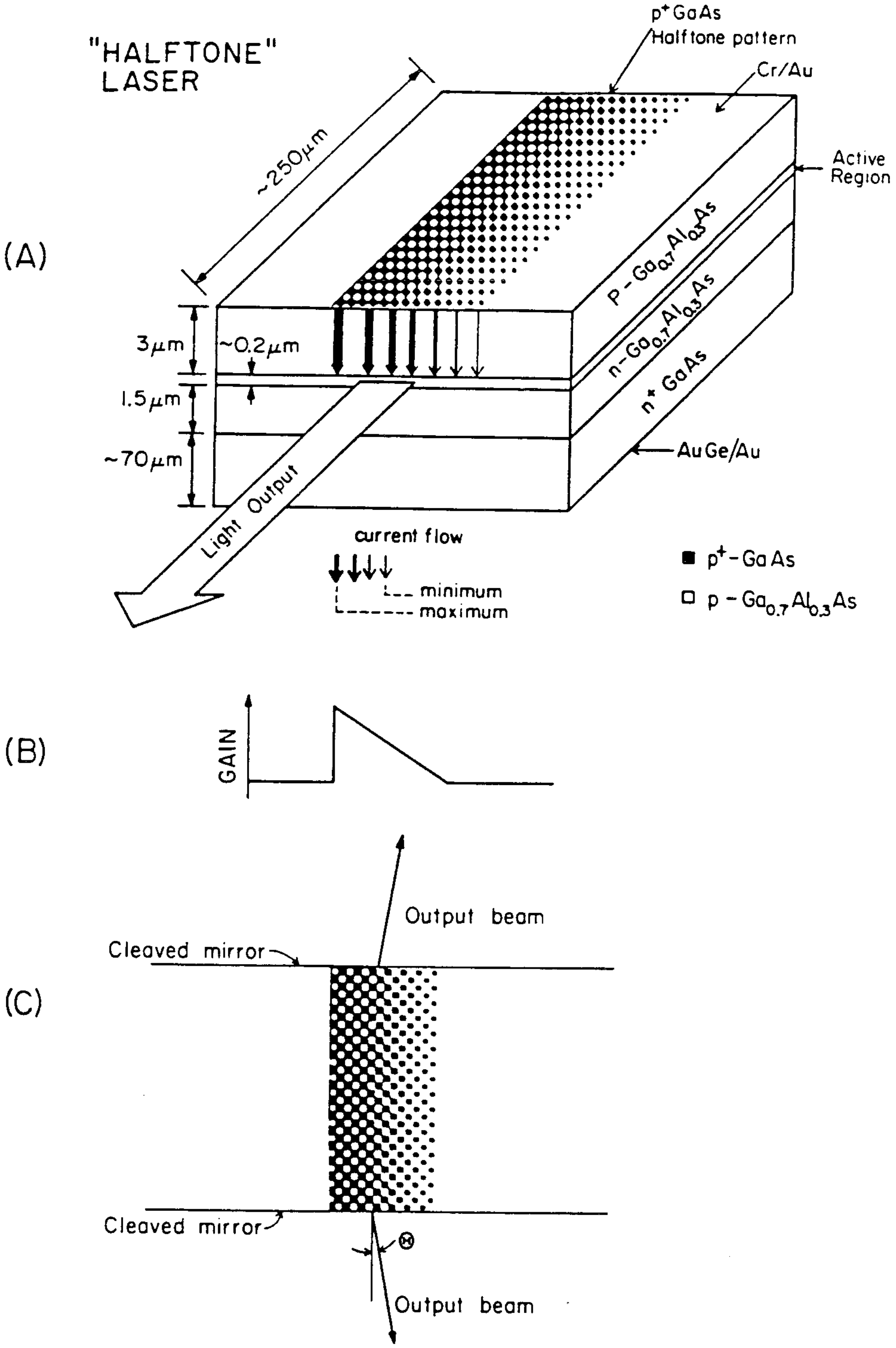

Figure 3.6 *Halftone tailored-gain semiconductor laser: (a) perspective view showing varying fraction of injecting (black) to noninjecting (white) p-contact, (b) idealized gain profile across the laser width, and (c) top view showing the output beam offset from the normal direction.*

refraction by $n_{eff}(x) = \bar{n}_{eff}(x) + i\bar{\bar{n}}_{eff}(x) = \bar{n}_{eff}(x) - i\gamma(x)/2k_0$. Hence, $\bar{n}_{eff}(x)$ denotes the ordinary (real) index of refraction, and $\gamma(x) = -2k_0\bar{\bar{n}}_{eff}(x)$ is the spatially dependent modal gain. Thus, n_e and n_0 are written as:

$$\begin{aligned} n_e &= \bar{n}_e - i\gamma_e/2k_0 \ , \\ n_0 &= \bar{n}_0 - i\gamma_0/2k_0 \ . \end{aligned} \tag{3.2}$$

The inset of Figure 3.7(a) shows the waveguide which we will use for illustrative purposes throughout this chapter. It is 120 μm wide with a gain gradient of 1 $\text{cm}^{-1}/\mu\text{m}$.

The gradient of the complex index of refraction within the guide ($0 \leq x \leq \ell$) is given by σk_0. σ is a dimensionless quantity that plays a key role in determining the properties of the waveguide, and is defined by

$$\sigma = -s(b+i) \qquad (s, b > 0) \ . \tag{3.3}$$

Here b is the antiguiding factor, and the real constant s is related to the guide parameters by

$$s = \frac{\gamma_0 - \gamma_\ell}{2k_0^2\ell} \ . \tag{3.4}$$

It should be noted that in this model, there will always be a step discontinuity in the index of refraction $n_{eff}(x)$ at the left edge of the guide ($x = 0$), while there will be a corresponding step discontinuity at the right edge of the guide ($x = \ell$) only if $\gamma_\ell \neq \gamma_e$ (*i. e.*, $n_e \neq n_\ell = n_0 - \sigma k_0 \ell$). After substituting (3.1) into (1.14), and dropping the term second order in x, the Helmholtz equation inside the guide becomes

$$\frac{d^2E}{dx^2} + k_0^2(n_0^2 - \eta^2 - 2n_0k_0\sigma x)E = 0 \ . \tag{3.5}$$

This equation has the general solution

$$E(x) = a\,\text{Ai}(z) + b\,\text{Bi}(z), \qquad z = \rho + \omega x \ , \tag{3.6}$$

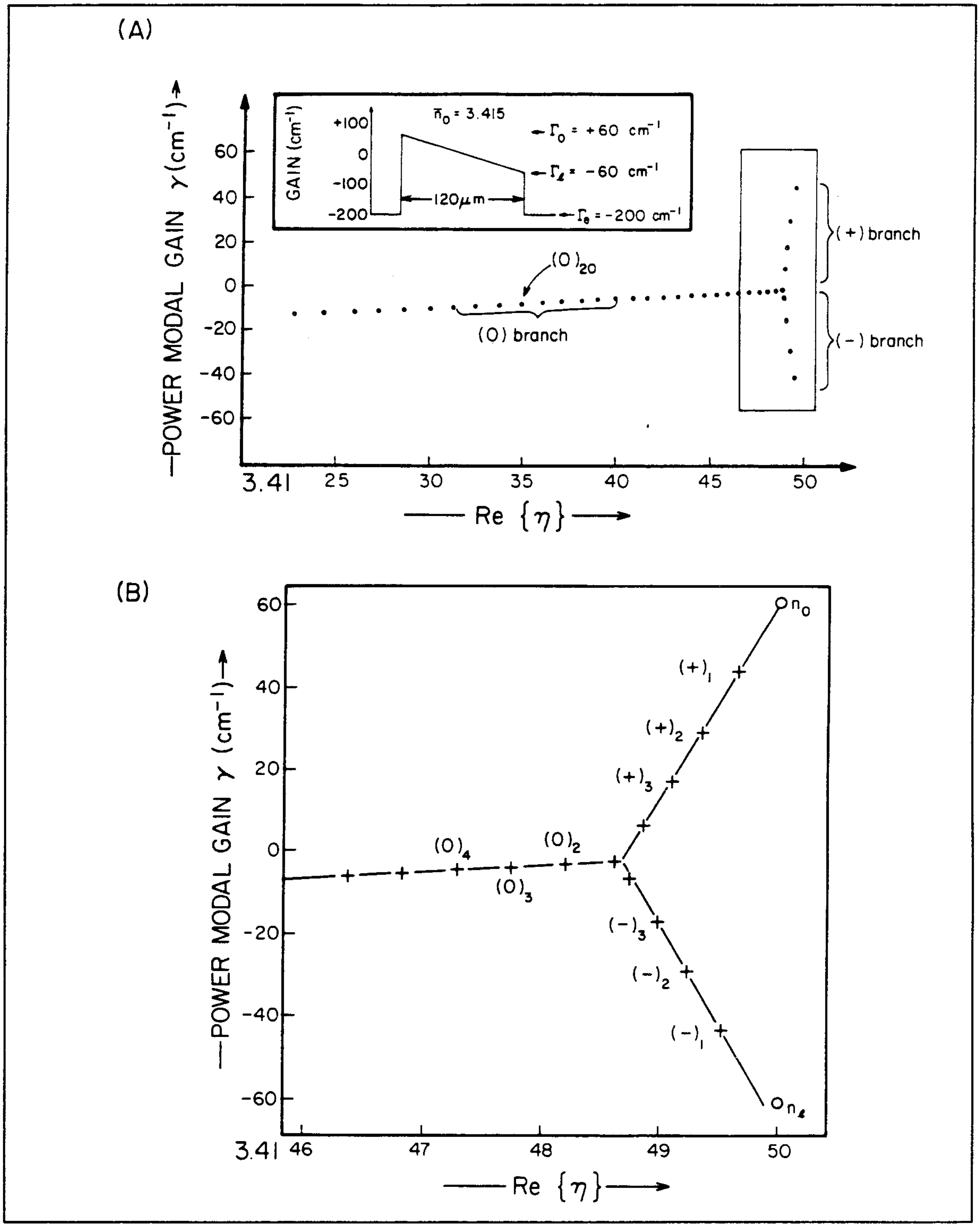

Figure 3.7 *(a) Mode diagram for an asymmetric linear, tailored-gain waveguide showing location of eigenmodes in the complex η plane. (b) Enlargement of boxed region in part (a) showing modes on the (+) , (0) , and (–) branches.*

where a and b are complex constants, $\mathrm{Ai}(z)$ and $\mathrm{Bi}(z)$ are Airy functions, and ρ and ω are defined by

$$\begin{aligned} \rho &\equiv \frac{k_0^2}{\omega^2}(\eta^2 - n_0^2) \ , \\ \omega &\equiv k_0(2n_0\sigma)^{\frac{1}{3}} \ . \end{aligned} \tag{3.7}$$

The *argument* to the Airy functions, $z = \rho + \omega x$, describes a straight line $\mathcal{L}$ in the complex z−plane with one endpoint at $z = \rho$ and the other at $z = \rho + \omega\ell$. The length of $\mathcal{L}$ is $|\omega\ell|$, while the angle ψ it makes with the real axis is given by $\psi = \angle\omega = \tan^{-1}\frac{\Im\mathrm{m}\{\omega\}}{\Re\mathrm{e}\{\omega\}}$. For the case of pure index guiding, ψ is zero, and $\mathcal{L}$ lies on the real axis. In the case of pure gain-guiding ($b = 0$), as considered in Figure 3.7, σ is a pure, imaginary number:

$$\sigma = -i\,s \qquad \text{(pure gain-guiding, } s \text{ real)} \tag{3.8}$$

where s is related to the guide parameters by Equation (3.4). Then we can write ω as

$$\omega = k_0(2n_0 s)^{\frac{1}{3}}(-i)^{\frac{1}{3}} \ . \tag{3.9}$$

There are three distinct families of modes, which will be referred to as the (+) , (0) , and (−) branches, corresponding to the three branches of the cube root. Since $\bar{\bar{n}}_0 \ll \bar{n}_0$, the angle ψ is determined almost entirely by the cube root of $(-i)$, which has the values $e^{-i\pi/6}$, $e^{-i5\pi/6}$, and $e^{+i\pi/2}$. The angle ψ then takes on the values ∓30°, and +90°. The inclusion of index antiguiding ($b \neq 0$) effects a *rotation* of $\mathcal{L}$ in the complex plane; this will be discussed in Section 3.4.

The quantity ωl determines the length and orientation of the line $\mathcal{L}$ in the complex plane. To determine its endpoint at $z = \rho$, the eigenvalue η is required. The normalized eigenmodes will be completely specified when the ratio of the coefficients a/b in Equation (3.6) is known. This ratio is determined by requiring E and dE/dx to be continuous at the edges of the guide and bounded at infinity. Requiring the field to decay exponentially as $x \to -\infty$, and matching the boundary conditions at the left edge of the guide, we derive the following expression for the ratio a/b inside the guide:

$$\left.\frac{a}{b}\right|_{x=0} = -\frac{\sqrt{\rho_e}\mathrm{Bi}(\rho) - \mathrm{Bi}'(\rho)}{\sqrt{\rho_e}\mathrm{Ai}(\rho) - \mathrm{Ai}'(\rho)} , \tag{3.10}$$

where the prime ($'$) denotes a derivative with respect to the argument, and

$$\rho_e = \frac{k_0^2}{\omega^2}(\eta^2 - n_e^2) \, . \tag{3.11}$$

Similar consideration at the right side of the guide leads to

$$\left.\frac{a}{b}\right|_{x=\ell} = -\frac{\sqrt{\rho_e}\mathrm{Bi}(\rho+\omega\ell) + \mathrm{Bi}'(\rho+\omega\ell)}{\sqrt{\rho_e}\mathrm{Ai}(\rho+\omega\ell) + \mathrm{Ai}'(\rho+\omega\ell)} . \tag{3.12}$$

Inside the guide, the ratios $(a/b)|_{x=0}$ and $(a/b)|_{x=\ell}$ both describe the same linear combination of $\mathrm{Ai}(z)$ and $\mathrm{Bi}(z)$. Setting them equal yields the following eigenvalue equation for η:

$$\frac{\sqrt{\rho_e}\mathrm{Bi}(\rho) - \mathrm{Bi}'(\rho)}{\sqrt{\rho_e}\mathrm{Ai}(\rho) - \mathrm{Ai}'(\rho)} - \frac{\sqrt{\rho_e}\mathrm{Bi}(\rho+\omega\ell) + \mathrm{Bi}'(\rho+\omega\ell)}{\sqrt{\rho_e}\mathrm{Ai}(\rho+\omega\ell) + \mathrm{Ai}'(\rho+\omega\ell)} = 0. \tag{3.13}$$

This equation may also be obtained by the more common method of solving a 4×4 determinant; the present method has the advantage that it explicitly yields the ratio a/b.

Equation (3.13) was solved numerically for the eigenvalues η_ν, where ν is the mode index. The mode structure in the complex effective index plane for our model waveguide is illustrated in Figure 3.7(a). An enlargement of the boxed region is shown in Figure 3.7(b). Three distinct families of modes exist in a pattern resembling a sideways "Y": the high modal gain (+) and the low modal gain (−) branches boast a large gain discrimination between modes, while the middle (0) branch, being the remnant of the uniform gain ($s = 0$) structure, includes modes having nearly the same modal gain. Unlike the case of a wide, uniform gain guide, the mode discrimination between the fundamental and higher-order modes in an asymmetric tailored-gain waveguide can be large, typically 10 cm^{-1}.

Since the lateral modes on the (+) branch will be the first to lase, these are then the most important ones to characterize. To accomplish this, we examine the Airy functions of complex argument. For convenience, the magnitude and phase of both Airy functions are illustrated over the complex plane in Figure 3.8. The arrows indicate directions of *increasing* magnitude and phase.

In order to proceed with the theoretical analysis, it is necessary to determine which one of the terms $a\,\mathrm{Ai}(z)$ or $b\,\mathrm{Bi}(z)$ provides the dominant contribution to E in Equation (3.6). Numerical solution of (3.13) shows that on the (+) and (−) branches, $a/b \gg 1$ and thus $\mathrm{Ai}(z)$ comprises the dominant part of the solution. This is easily understood after referring to Figure 3.9(a), which shows the paths $\mathcal{L}(+)$ and $\mathcal{L}(-)$ superimposed on $|\mathrm{Ai}(z)|$. Along these paths, the profile of $|\mathrm{Ai}(z)|$ is consistent with a well-confined mode, while that of $|\mathrm{Bi}(z)|$ is not (see Figure 3.8(b)). Only when the endpoint $z = \rho + \omega\ell$ lies near the Stokes line at $\angle z = \frac{\pi}{3}$ does $\mathrm{Bi}(z)$ make a significant contribution to the (+) and (−) eigenmodes. Thus, the solutions $E_{\nu}^{(\pm)}(x)$ of the Helmholtz equation, (1.14), can be expressed in terms of $\mathrm{Ai}(z)$ alone in guides for which $|\omega|\,\ell$ is suitably large.

The nearfield profiles along lines $\mathcal{L}(+)$ ($\psi = -30°$) are shown in Figure 3.10(a). These profiles are virtually identical to those obtained by numerical solution of the problem[6]. Note that these modes are concentrated near the high-gain end of the waveguide ($x = 0$). The $\nu = 1$ mode has the largest spatial overlap with the lateral gain profile and thus has the highest modal gain at threshold. As is evident from Figure 3.7(b), it also has the highest effective index of any mode on the (+) branch, and will henceforth be referred to as the "fundamental" mode of the waveguide.

The paths $\mathcal{L}(-)$ ($\psi = +30°$) are also illustrated in Figure 3.9(a) Since here the zero of the Airy function occurs at $z = \rho + \omega\ell$, the nearfields are concentrated in the lossy regions of the waveguide, as illustrated in Figure 3.10(a).

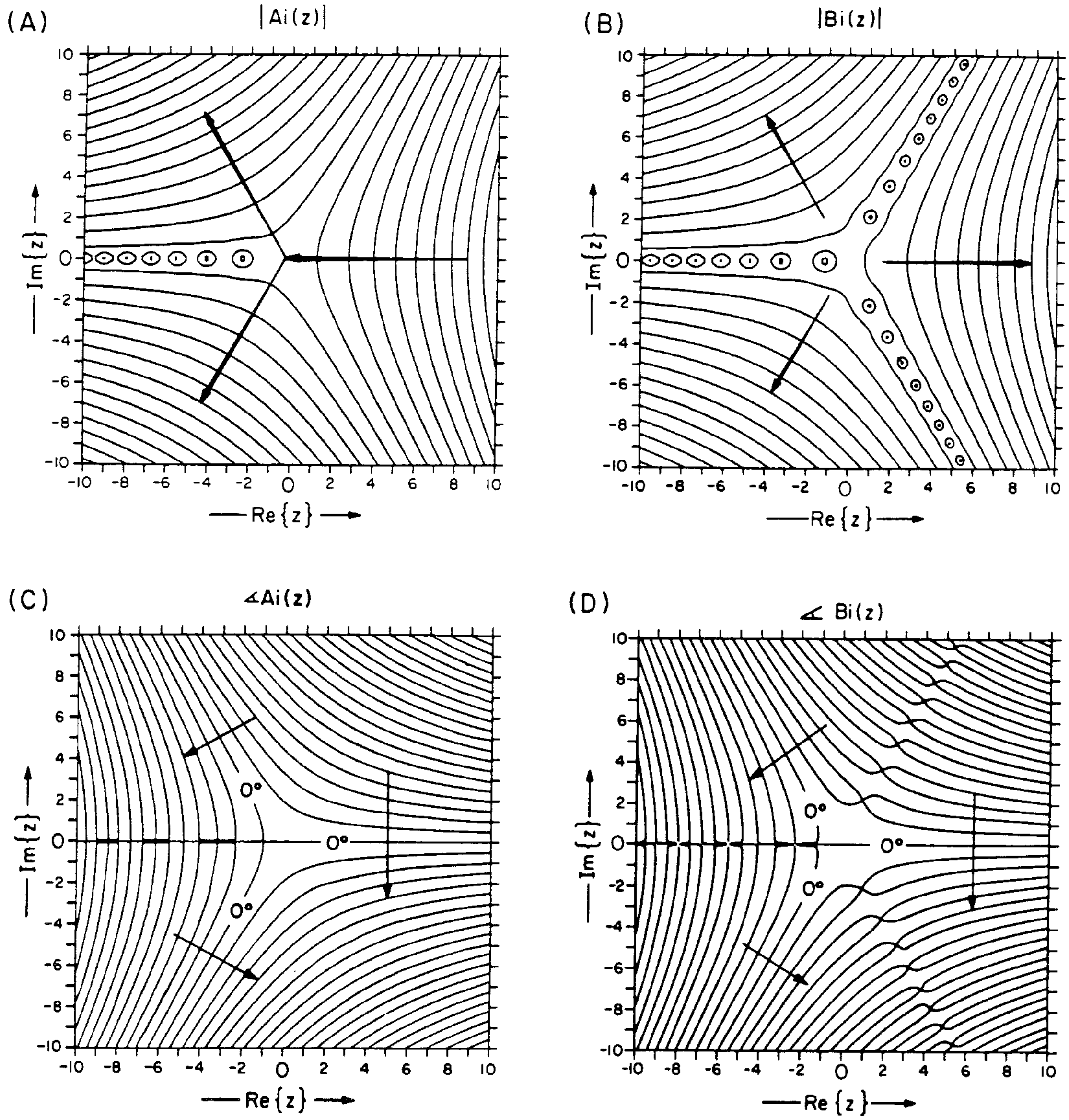

Figure 3.8 *Level lines for the magnitude of (a)* Ai(z), *and (b)* Bi(z); *the arrows show the direction of increasing magnitude. Lines of constant phase for (c)* Ai(z) *and (d)* Bi(z); *the arrows show the direction of increasing phase. The contours in (a) and (b) differ by a factor of ten and by* $\pi/4$ *in (c) and (d).*

Similarly, on the (0) branch, $a/b \ll 1$, as Bi(z) provides a better match to the boundary conditions at the edges of the waveguide. The paths $\mathcal{L}(0)$ ($\psi = +90°$), shown in Figure 3.9(b), imply that Bi(z) provides the best description of a confined mode. Because of the symmetry of Bi(z) about the positive real axis, the nearfield

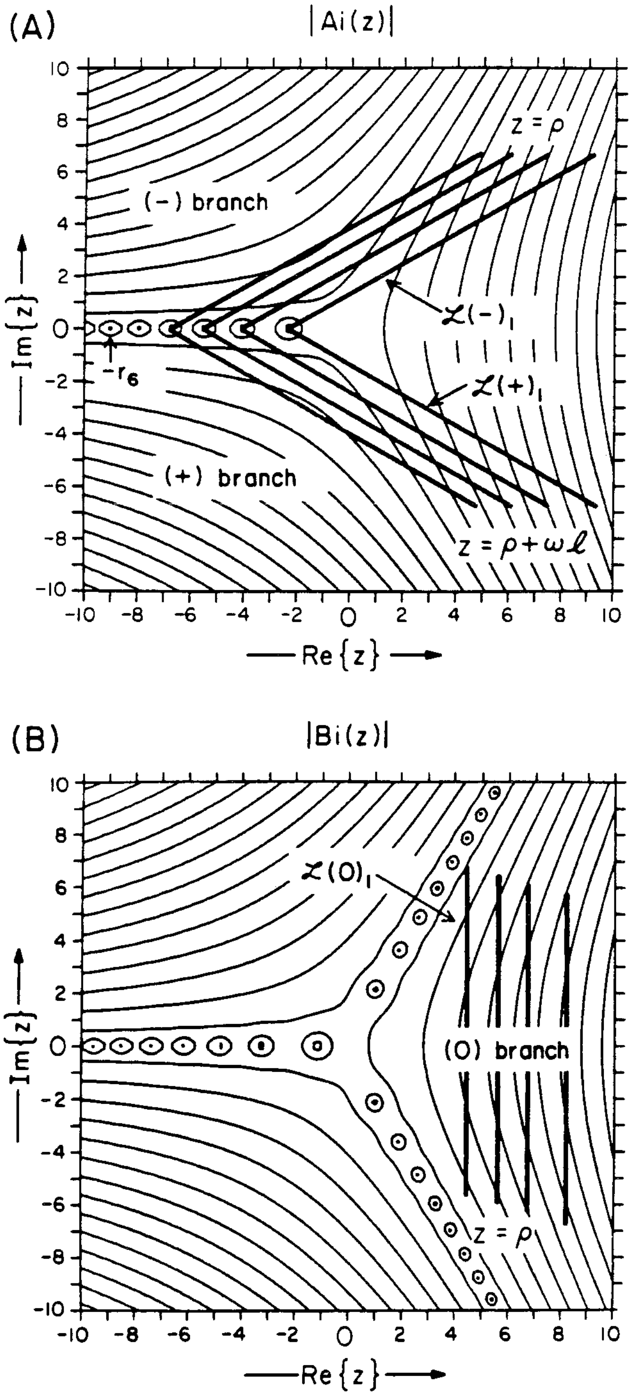

Figure 3.9 *Path of the argument to the Airy function for the waveguide of Figure 3.7. (a) (+) and (−) branches, and (b) (0) branch.*

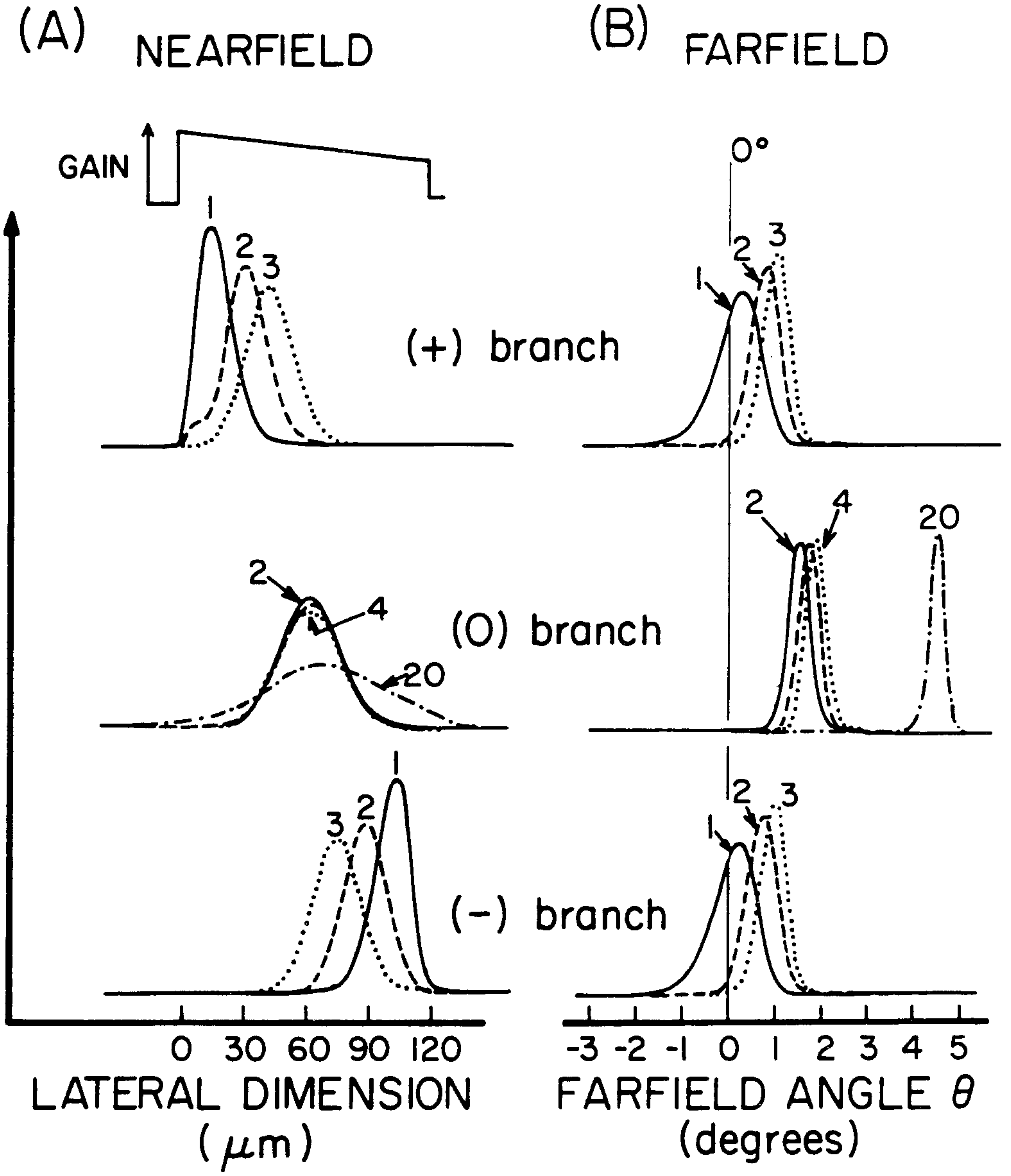

Figure 3.10 *(a) Intensity nearfield patterns, and (b) farfield patterns for the modes of Figure 3.7.*

patterns of these modes are approximately centered within the waveguide. These modes therefore have a modal gain intermediate to modes on the (+) branch and modes on the (−) branch. They correspond to the (0) branch of Figure 3.7(a), and are also plotted in Figure 3.10.

3.2 Eigenvalues of the Linear Tailored-Gain Waveguide

Once it has been determined that the contribution of $\mathrm{Ai}(z)$ dominates that due to $\mathrm{Bi}(z)$ on the principal (+) branch, it becomes possible to derive very simple analytical expressions for the mode effective indices and modal gains: Figure 3.9(a) shows $\mathcal{L}(+)$ starting near a zero of $\mathrm{Ai}(x)$ and ending in the sector of exponential decay $|\angle| z < \pi/3$. At the left edge of the guide, $E(0) = a\,\mathrm{Ai}(\rho)$, where ρ is given by Equation (3.7). Setting ρ equal to one of the (real) zeros $-r_\nu$ of the Airy function gives

$$-r_\nu \simeq \rho_\nu = \frac{k_0^2}{\omega^2}(\eta_\nu^2 - n_0^2) \ . \tag{3.14}$$

Approximating $(\eta_\nu^2 - n_0^2)$ by $2n_0(\eta_\nu - n_0)$ then yields an expression for the ν^{th} eigenvalue η_ν:

$$\eta_\nu \simeq n_0 - \frac{1}{2n_0}\frac{\omega^2}{k_0^2} r_\nu \ . \tag{3.15}$$

We note in passing that the ν^{th} zero of $\mathrm{Ai}(z)$ is approximately[7]

$$-r_\nu \simeq \left[\frac{3}{2}\left(\nu - \frac{1}{4}\right)\pi\right]^{2/3} . \tag{3.16}$$

After using the definition of ω in Equation (3.7) for the case of pure gain-guiding ($\sigma = -is$), taking the principal branch of ω, and equating the real and imaginary parts, we obtain an expression for $\eta = \bar{\eta} + i\bar{\bar{\eta}}$ on the (+) branch:

$$\begin{aligned} \bar{\eta}_\nu^{(+)} &\simeq \bar{n}_0 - \frac{1}{2}\epsilon_\nu \ , \\ \bar{\bar{\eta}}_\nu^{(+)} &\simeq \bar{\bar{n}}_0 + \frac{\sqrt{3}}{2}\epsilon_\nu \ , \end{aligned} \tag{3.17}$$

where

$$\epsilon_\nu \equiv \left|\frac{s^2}{2n_0}\right|^{1/3} r_\nu . \tag{3.18}$$

In the complex η plane, therefore, the mode structure is particularly simple: All the modes of the principal branch lie on a straight line emanating from the point $(\bar{n}_0\,,\,\bar{\bar{n}}_0)$, and making an angle $\tan^{-1}(-\sqrt{3}) = -60°$ with the real axis. The modes are spaced along this line according to the zeros of the Airy function, with the higher-order modes being more closely spaced together.

Since the modal gain $\gamma_\nu^{(+)}$ is related to $\bar{\bar{\eta}}_\nu$ through (3.2), we can write

$$\begin{aligned}\gamma_\nu^{(+)} &\simeq \gamma_0 - k_0\sqrt{3}\epsilon_\nu \\ &\simeq \gamma_0 - \sqrt{3}k_0\left|\frac{s^2}{2n_0}\right|^{1/3} r_\nu \;.\end{aligned} \tag{3.19}$$

Since $0 < r_1 < r_2 \ldots$, the fundamental mode has the highest modal gain and hence will be the lasing mode at threshold. At threshold, the modal gain $\gamma_1^{(+)}$ of the fundamental mode must equal the mirror losses γ_m (scattering losses are probably insignificant in such a wide gain-guided laser). Equation (3.19) may be inverted to give the required peak gain γ_0 at threshold in terms of Γ_m and the gain gradient s.

The mode discrimination $\Delta\gamma_\nu^{(+)}$ between any two modes is given by

$$\begin{aligned}\Delta\gamma_\nu^{(+)} &\equiv \gamma_\nu^{(+)} - \gamma_{\nu+1}^{(+)} \\ &\simeq \sqrt{3}k_0\left|\frac{s^2}{2n_0}\right|^{1/3} \delta_\nu \qquad \delta_\nu \equiv |r_\nu - r_{\nu+1}|\;,\end{aligned} \tag{3.20}$$

where, as indicated, δ_ν is the spacing between the zeros of $\mathrm{Ai}(x)$. The mode discrimination scales *sublinearly* with the gain gradient, and is greatest between the fundamental $\nu = 1$ and the next higher order $\nu = 2$ mode. Our numerical analysis[6] indicates that Equation (3.20) is accurate to within a few percent for the waveguide of Figure 3.7(a).

In an entirely analogous manner, formulae for the propagation constants of modes on the $(-)$ branch may be determined by setting $\rho + \omega\ell$ equal to a zero of the Airy function. The effect of the additional term $\omega\ell$ leads to slightly different expressions for the eigenvalues $\eta_\nu^{(-)}$ and modal gain $\gamma_\nu^{(-)}$:

$$\begin{aligned} \bar{\eta}_\nu^{(-)} &\simeq \bar{n}_\ell - \frac{1}{2}\epsilon_\nu \ , \\ \bar{\bar{\eta}}_\nu^{(-)} &\simeq \bar{\bar{n}}_\ell - \frac{\sqrt{3}}{2}\epsilon_\nu \ , \\ \gamma_\nu^{(-)} &\simeq \gamma_\ell + \sqrt{3}k_0 \left| \frac{s^2}{2n_0} \right|^{1/3} r_\nu \ . \end{aligned} \tag{3.21}$$

The approximations for the eigenvalues on the $(-)$ branch lie on a straight line emanating from the point $(\bar{n}_\ell, \bar{\bar{n}}_\ell)$. The angle that this line makes with the real axis is +60°, so that it makes an angle of 120° with the corresponding $(+)$ line. In this case the $\nu = 1$ mode on the $(-)$ branch has the *lowest* modal gain of all the modes. We remark that Equation (3.21) is not as accurate as (3.19) for truncated waveguides, in which $n_\ell \neq n_0 - \sigma k_0 \ell$, because of the perturbation introduced by the discontinuous truncated region at the lossy edge of the guide. As a result of their low modal gains, however, modes on the $(-)$ branch are unlikely to lase, and so the error is unimportant from a practical point of view.

Finally, modes on the (0) branch have nearly constant modal gains, and are composed almost entirely of $\mathrm{Bi}(z)$. It is not possible to obtain simple, closed-form analytic expressions for the eigenvalues for these modes. Once again, however, since they have low modal gains compared to those on the $(+)$ branch, the formulae are not required.

3.3 Nearfield and Farfield Patterns

The nearfield patterns of the lowest-order eigenmodes of our model waveguide were illustrated in Figure 3.10. As can be inferred from the paths $\mathcal{L}(+)$, shown in Figure 3.9(a), all of the low-order modes have single-lobed nearfield patterns. Prior to deriving analytic approximations for the nearfields, we determine the position within the guide, χ_ν, of peak intensity of the ν^{th} mode. Referring to Figure 3.11,

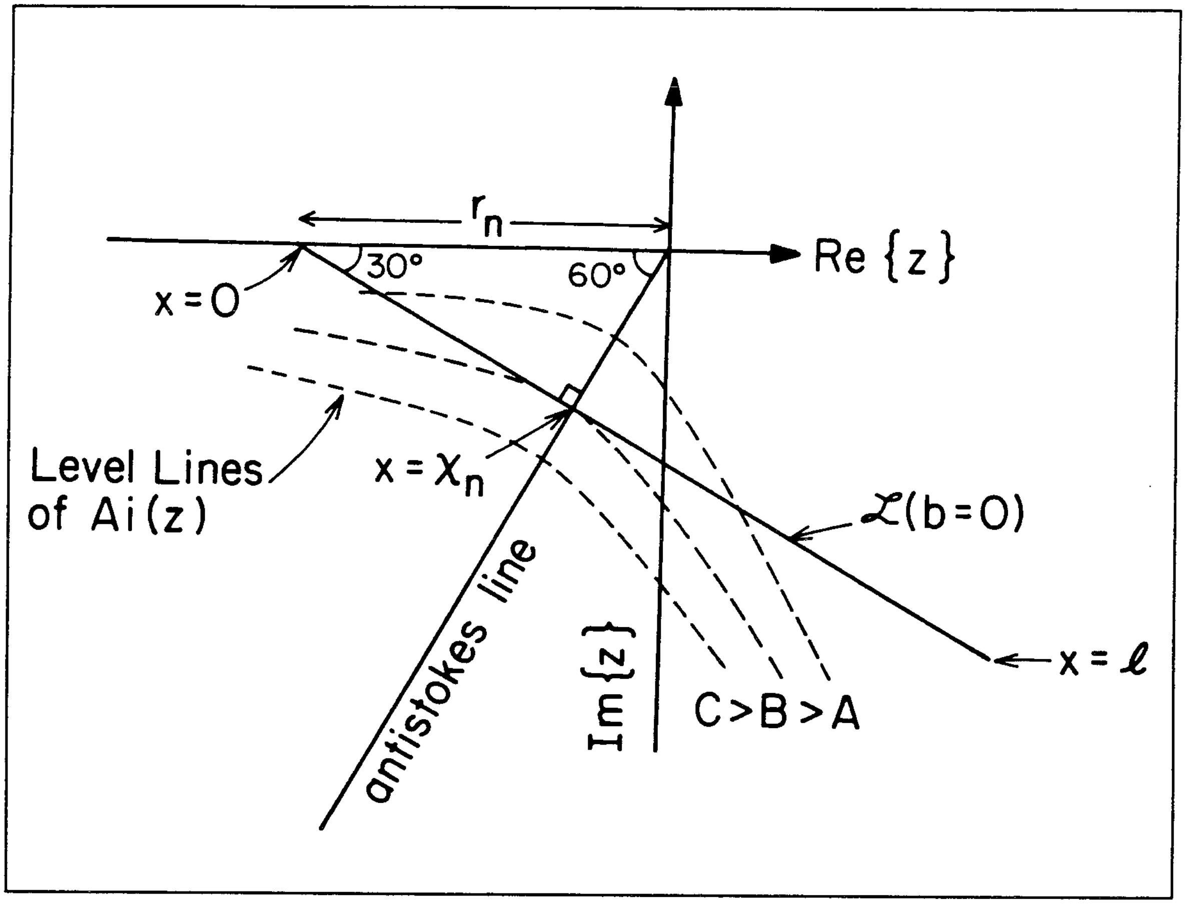

Figure 3.11 *Calculation of the nearfield pattern showing geometric construction for determining* χ_ν.

we see that along the path $\mathcal{L}$, $|\mathrm{Ai}(z)|$ reaches its maximum when $\mathcal{L}$ is tangent to the level lines of $\mathrm{Ai}(z)$. These level lines are perpendicular to the lines of constant phase of $\mathrm{Ai}(z)$. The anti-Stokes line associated with the principal branch is asymptotic to (see Figure 3.8(c)) the line of constant phase that makes an angle of −60° with the negative real axis. The corresponding tangent line is therefore at an angle of −30°, which is precisely the angle ψ that $\mathcal{L}$ makes with the negative real axis for the case of no index antiguiding. Setting $\rho_\nu \simeq -r_\nu$, a simple geometric construction yields the following expression for χ_ν:

$$\chi_\nu = \frac{\sqrt{3}}{2}\frac{r_\nu}{|\omega|}. \tag{3.22}$$

It should be noted that for a wide guide, the position of the mode within the guide χ_ν depends only on the gain gradient, and is independent of both the peak gain γ_0 and the width ℓ of the guide. The mode maxima are separated within the guide by (using (3.7))

$$\Delta\chi_\nu = \frac{\sqrt{3}}{2k_0}\left|2n_0 s\right|^{-1/3}\delta_\nu \ , \tag{3.23}$$

where s is given by (3.4) and δ_ν by (3.20).

Equation (3.23) leads to a particularly simple expression for the modal gains on the principal branch; taking $g = (\gamma_0 - \gamma_\ell)/\ell$ as the spatial gain gradient, the expressions for the modal gain and mode discrimination become

$$\begin{aligned} \gamma_\nu^{(+)} &= \gamma(\chi_\nu) \ , \\ \Delta\gamma_\nu^{(+)} &= g\Delta\chi_\nu \ . \end{aligned} \tag{3.24}$$

That is, the modal gain is given simply by the *value of the spatial gain at the point where the electric field has its peak value.* This suggests that to first order, the mode intensity profile is symmetric about its peak position, and that its width is much less than the width of the waveguide.

To find an expression for the nearfield pattern, we approximate the Airy function Ai(z) along the lines $\mathcal{L}(+)$. To wit, the leading asymptotic behavior of Ai(z) as $|z| \to \infty$ is[7]

$$\mathrm{Ai}(z) \sim \begin{cases} \frac{1}{2}\pi^{-1/2}(-z)^{-1/4}\left(e^{+i\left(\frac{2}{3}(-z)^{3/2}-\frac{\pi}{4}\right)} + e^{-i\left(\frac{2}{3}(-z)^{3/2}-\frac{\pi}{4}\right)}\right), & \frac{\pi}{3} < |\angle z| < \frac{5\pi}{3} \ , \\ \frac{1}{2}\pi^{-1/2}z^{-1/4}e^{-\frac{2}{3}z^{3/2}}, & |\angle z| < \pi \ . \end{cases} \tag{3.25}$$

The first expression includes the zeros on the negative real axis, and is the one we use. In constructing Figure 3.8, we have found this result to be accurate to within 10% to 15% even for $|z|$ as small as 2 or 3. Its simple analytical form further motivates its exploitation here.

We write z in terms of the rectangular coordinates $z = u' + iv'$ and rotate the coordinate system to new variables u and v so that u lies along the anti-Stokes line

$\angle z = e^{-i2\pi/3}$ and v lies perpendicular to it (*i. e.*, along $\mathcal{L}$). Along the line $\mathcal{L}$, u is constant and v is linearly related to the lateral position x within the guide:

$$\begin{aligned} u &= \frac{r_\nu}{2} \, , \\ v &= |\omega| \, (x - \chi_\nu) \, . \end{aligned} \tag{3.26}$$

Below the negative real axis, the + exponential provides the dominant contribution to $\mathrm{Ai}(z)$. The radicals may be simplified by making a binomial expansion about $v = 0$ with $v \ll u$:

$$\begin{aligned} (u+iv)^{3/2} &\approx u^{3/2} \left[1 + i\frac{3}{2}\frac{v}{u} - \frac{3}{8}\left(\frac{v}{u}\right)^2 \right] \, , \\ (u+iv)^{-1/4} &\approx u^{-1/4} \left[1 + \left(\frac{v}{4u}\right)^2 \right]^{1/2} e^{-i\frac{v}{4u}} \, . \end{aligned} \tag{3.27}$$

After substituting (3.27) and (3.26) into (3.25) and dropping an unimportant constant, the expression for the electric field reduces to

$$E(x) \simeq e^{-(x-\chi_\nu)^2/2w_\nu^2} \, e^{+i\phi_\nu (x-\chi_\nu)} \, . \tag{3.28}$$

That is, the nearfield pattern is approximately Gaussian with half-width w_ν, centered at χ_ν and multiplied by a linear phase variation ϕ_ν, where χ_ν is given by (3.22), and w_ν and ϕ_ν are given by

$$\begin{aligned} w_\nu &= \frac{(2r_\nu)^{1/4}}{|\omega|} \, , \\ \phi_\nu &= |\omega| \left[\left(\frac{r_\nu}{2}\right)^{1/2} - \frac{1}{2r_\nu} \right] . \end{aligned} \tag{3.29}$$

The normalized nearfield intensity $I_\nu(x)$ is therefore

$$I_\nu(x) \simeq \frac{1}{\sqrt{\pi w_\nu^2}} e^{-(x-\chi_\nu)^2/w_\nu^2} \, . \tag{3.30}$$

The intensity nearfield patterns may be found for the $(-)$ branch in a similar manner. The exact (numerical) nearfield intensities and phases[6] for representative modes on each of the three branches is plotted in Figure 3.12(a). All of the modes are very nearly Gaussian in profile with linear phase variations over the region of appreciable intensity. Higher order terms in the expansion of Equation (3.27) lead to slightly asymmetric nearfield patterns with some curvature in the phase fronts, in closer agreement with the numerical result.

Once $E_\nu(x)$ has been found to have such a simple form, it is trivial to calculate its farfield pattern. In the Fraunhofer approximation, the farfield pattern $F_\nu(\theta)$ is given by the square of the Fourier transform of $E_\nu(x)$ times an obliquity factor. The wide, asymmetric, tailored-gain broad area lasers of interest here have very narrow farfield patterns near the axis, and thus the obliquity factor may be ignored. Making use of the shift and convolution Fourier Transform theorems, the intensity farfield pattern may be written as

$$\begin{aligned} F_\nu(\theta) &= \left| \mathcal{F} e^{-(x-\chi_\nu)^2/2w_\nu^2} \star \mathcal{F} e^{i\phi_\nu(x-\chi_\nu} \right|^2 \\ &= \left| e^{-\theta^2/4\Sigma_\nu^2} \star \delta(\theta - \Theta_\nu) \right|^2 \\ &= e^{-(\theta-\Theta_\nu)^2/2\Sigma_\nu^2} \ , \end{aligned} \tag{3.31}$$

where $\mathcal{F}$ denotes a $(-i)$ Fourier Transform, and $\star$ denotes the convolution operation. The emission angle Θ_ν, and beamwidth Σ_ν, *after refraction at the resonator facet*, are given by

$$\begin{aligned} \Theta_\nu(^\circ) &= \left(\frac{180}{\pi}\right) \frac{\phi_\nu}{k_0} = \left(\frac{180}{\pi}\right) |\omega| \left[\left(\frac{r_\nu}{2}\right)^{1/2} - \frac{1}{2r_\nu} \right] \ , \\ \Sigma_\nu(^\circ) &= \left(\frac{180}{\pi}\right) \frac{1}{k_0} \frac{1}{w_\nu} = \left(\frac{180}{\pi}\right) \frac{|\omega|}{k_0 (2r_\nu)^{1/4}} \ . \end{aligned} \tag{3.32}$$

Farfield patterns for the $(-)$ branch may be calculated similarly, and are, in fact, identical (except for an unimportant global phase factor) to those on the $(+)$ branch.

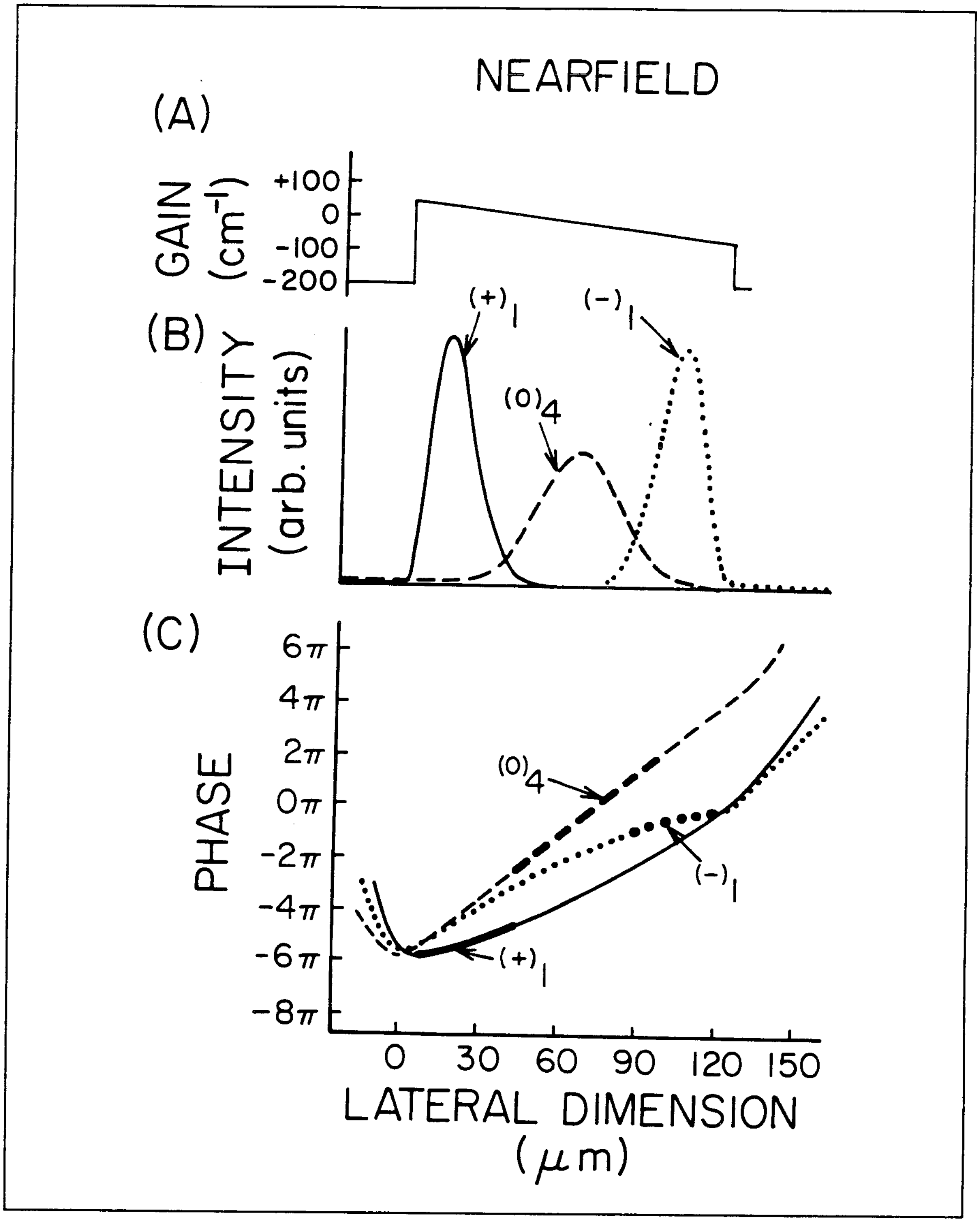

Figure 3.12 *(a) The waveguide of Figure 3.7, (b) the nearfield patterns of selected modes on each of the three branches, and (c) the corresponding phases. Note that all the nearfield patterns are approximately Gaussian in shape, and that the phase fronts are nearly linear.*

The farfield patterns corresponding to all nearfield modes of Figure 3.10(a) are plotted in Figure 3.10(b). We see that the farfield patterns for all modes are emitted slightly off-axis, are single-lobed and approximately Gaussian in shape, in agreement with Equation (3.31). This stands in marked contrast to the farfield patterns of all real index-guided and symmetric gain guided lasers, for which only the fundamental mode has a single-lobed farfield pattern. Physically, we understand this as follows: All of the low-order eigenmodes are well confined within the guide. Hence, each experiences a nearly linear gain gradient across its width. The self-consistent solution inside the laser resonator thus requires a net power flow from the side of high gain to the side of low gain. As a consequence, the phase front of the guided wave is tilted with respect to the optical axis, and power is emitted in the farfield at an angle Θ_ν off-axis, towards the low-gain side of the laser.

In real index-guided and symmetric gain-guided lasers, power flow directed off-axis at an angle Θ_ν must be balanced by an equal component at $-\Theta_\nu$. The asymmetric tailored-gain waveguide disrupts this symmetry by reinforcing one component at the expense of the other. This may be seen analytically by examining Equation (3.25). The $+$ and $-$ exponentials describe power propagation at opposite angles to the optical axis. Choosing the gain slope $s > 0$ forces the lines $\mathcal{L}(+)$ below the negative real axis, and the $+$ exponential is dominant (power flow reinforced at Θ_ν). On the other hand, choosing $s < 0$ would cause the $-$ exponential to dominate. On the negative real axis (Stokes line), *neither* term is dominant. This switching of dominance is exactly the Stokes phenomenon. Thus, the small amount of power that travels in the opposite lateral direction is described by the subdominant term of (3.25), which we neglected, and contributes to farfield emission at an angle $-\Theta_\nu$.

We stress that our analysis is predicated on achieving distinct $(+)$ and $(-)$ branches in the mode structure. A suitable degree of asymmetry is required to accomplish this. Since the nearfield patterns of the low order eigenmodes on the

(+) ((−)) branch are strongly localized in the high gain (low gain) half of the guide, a number ν modes appear on each if the guide width (ℓ) and gain gradient (through ω) satisfy

$$\frac{|\omega|\,\ell}{2} \geq \chi_\nu + 2\frac{w_\nu}{|\omega|} \simeq \frac{\sqrt{3}}{2} r_\nu + 2(2r_\nu)^{1/4} \ . \tag{3.33}$$

Of some practical importance is the fact that the farfield patterns of the higher order modes on the (+) branch are only slightly displaced from the fundamental. From (3.16) and (3.32), we see that the angles of emission of higher-order modes scale approximately as $\nu^{\frac{1}{3}}$. Thus, under high-power operation, when multilateral mode operation is a certainty, the beamwidth will degrade gradually, becoming slightly broader and shifting very slightly in angle. This analytical result is borne out by experimental data[1,2].

3.4 Measurement of the Antiguiding Parameter

In the interest of simplicity, the preceding analysis considered only the case of a pure gain waveguide with no index variation. The effect of the antiguiding parameter b on the eigenmodes may be determined by recalling the definition of σ in (3.3), *viz.* $\sigma = -s(b+i)$. Rewriting σ as

$$\sigma(b) = \sigma(0)\,(1 - ib) \ , \tag{3.34}$$

then

$$\begin{aligned} \omega(b) &= \omega(0)\,(1 - ib)^{1/3} \ , \\ |\omega(b)| &= |\omega(0)|\ (1 + b^2)^{1/6} \ , \\ \angle\omega(b) &= \angle\omega(0) - \frac{1}{3}\tan^{-1} b \ . \end{aligned} \tag{3.35}$$

Aside from a slight increase in its length, the principal effect on $\mathcal{L}$ is a clockwise rotation about $-r_\nu$ of $\frac{1}{3}\tan^{-1} b$ radians (see Figure 3.13(a)). The expression for the eigenvalues on the (±) branch becomes slightly more complicated:

$$\eta_\nu^{(\pm)} \simeq n_{\binom{0}{\ell}} \mp \left|\frac{\sigma^2}{2n_0}\right|^{1/3} e^{-i\Phi^{(\pm)}} r_\nu \tag{3.36}$$

where $\Phi^{(\pm)} = \frac{2}{3}\tan^{-1} b \pm \frac{\pi}{3}$. The mode discrimination for the $(\pm)$ branch becomes

$$\Delta\gamma_\nu^{(\pm)}(b) = (1+b^2)^{1/3}\left[\cos 2\varphi \pm \frac{1}{\sqrt{3}}\sin 2\varphi\right]\Delta\gamma_\nu^{(\pm)}(0)\ , \tag{3.37}$$

where $\varphi = \frac{1}{3}\tan^{-1} b$. When compared with the case of no index antiguiding, for $b = 3$, the mode discriminations on the $(+)$ branch are increased by about a factor of two. The cluster of modes centered about the middle of the guide (*i. e.*, the (0) branch) is relatively insensitive to the effect of the antiguiding parameter. As a result the number of modes on the $(+)$ branch actually decreases with increasing b, consistent with the notion that index antiguiding should shift the high-gain modes towards the lower-gain regions of the waveguide.

Qualitatively, the effect of antiguiding on the nearfield patterns may be determined with the aid of Figure 3.13(a) and a simple geometrical argument. As b increases from 0, the angle ψ that $\mathcal{L}$ makes with the real axis increases. As a result, $\mathcal{L}$ becomes tangent to the level lines of $\mathrm{Ai}(z)$ at a point farther removed from $x = 0$, implying that the position χ_ν of the maximum intensity of E has shifted towards the low gain side of the waveguide. Furthermore, as these latter level lines are less strongly curved than those near the origin, the width of the mode increases as well. Nearfield profiles along the two lines of $\mathcal{L}(b = 0)$ and $\mathcal{L}(b = 3)$ in Figure 3.13(a) are compared in Figure 3.13(b).

A quantitative generalization of the technique used earlier to determine the nearfield and farfield patterns is included as Appendix 3A. At this point we simply quote the relations for position of the nearfield peak $\chi_\nu(b)$,

$$\chi_\nu(b) = \frac{2}{\sqrt{3}}\,\frac{1}{(1+b^2)^{1/6}}\,\frac{\sin(\theta + \pi/3)}{\cos(\theta + \varphi)}\,\chi_\nu(0)\ , \tag{3.38}$$

half-width of the nearfield distribution $w_\nu(b)$,

$$w_\nu^2(b) = \frac{\sqrt{2\sin(\pi/6 + \varphi)/\cos(\theta + \varphi)}}{(1+b^2)^{1/3}\cos(2\varphi + \theta/2)}\,w_\nu^2(0)\ , \tag{3.39}$$

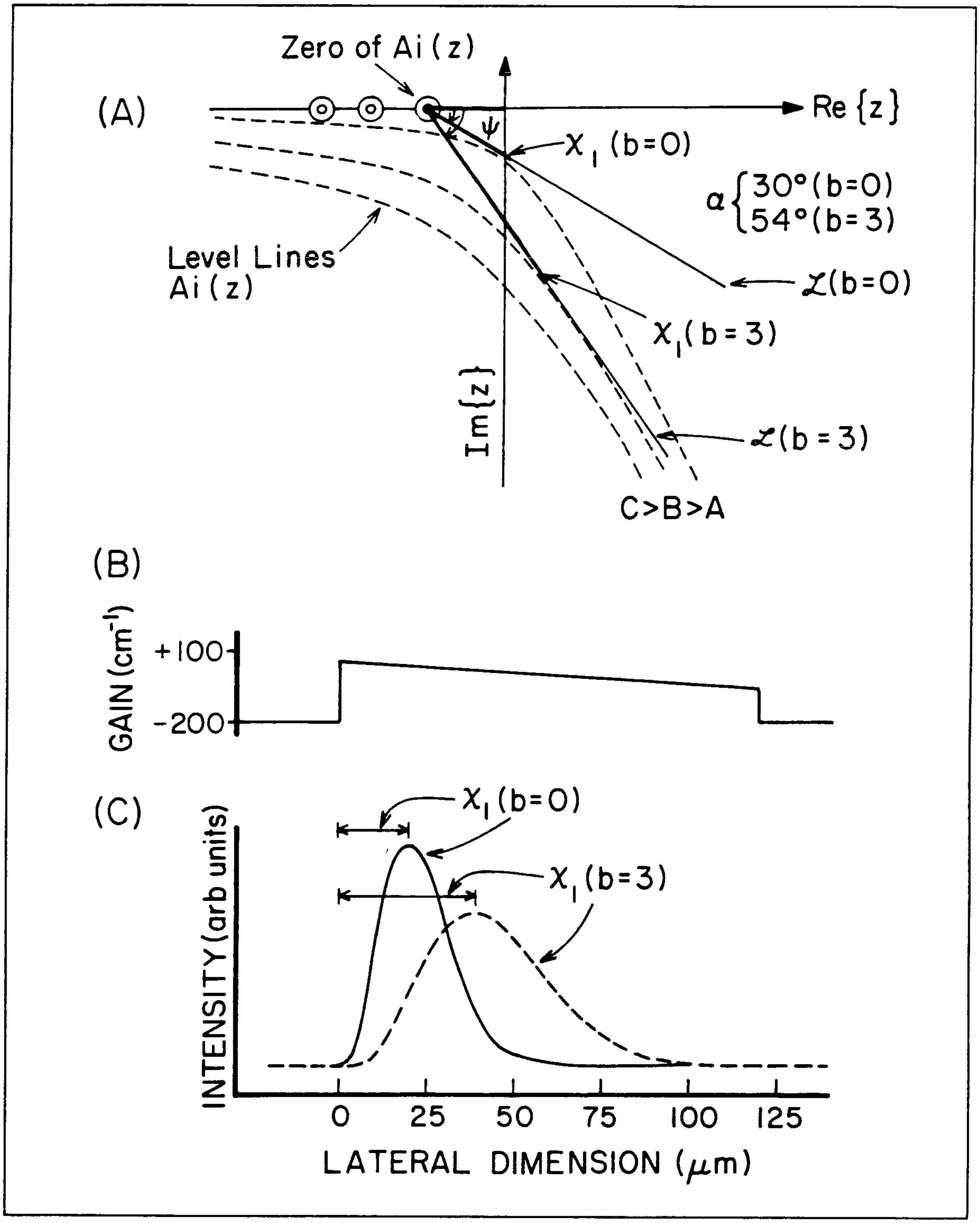

Figure 3.13 *(a) Effect of the antiguiding parameter b on the path of the argument to the Airy function throughout the complex plane. (b) Spatial gain profile. (c) Effect of the antiguiding factor on the nearfield patterns.*

and farfield emission angle $\Theta_\nu(b)$

$$\Theta_\nu(b) \simeq (1+b^2)^{1/2}\sqrt{\frac{2\sin(\pi/6+\varphi)}{\cos(\theta+\varphi)}}\;\Theta_\nu(0) \;, \tag{3.40}$$

all expressed in terms of their values in the no antiguiding case. The angles φ and θ are functions of b defined as follows:

$$\begin{aligned} \varphi &= \frac{1}{3}\tan^{-1} b \;, \\ \tan\theta &= 3\tan\varphi \;. \end{aligned} \tag{3.41}$$

For example, when $b = 3$, w_ν increase by a factor of 2, χ_ν by a factor of 3, and Θ_ν by a factor of 4.

When the antiguiding factor is included, the farfield *beamwidth* remains approximately constant because the increase in the width of the nearfield is offset by an increase in the phase curvature. The major effect of antiguiding on the farfield patterns is to shift Θ_ν to larger angles. Θ_ν is a sensitive function of b, and therefore knowledge of the guide parameters (made possible via the halftone process described earlier) allows estimation of the antiguiding factor.

Figure 3.14 shows the pulsed, low duty cycle nearfield and farfield patterns for a linear tailored-gain broad area laser 60 μm wide fabricated via halftone photolithography[6]. The farfield pattern is narrow and single-lobed up to greater than $3I_{th}$, emitting up to 200 mW into 2.3°. The large gain discriminations predicted by our model imply that near threshold, these devices operate in the fundamental lateral mode. The peak of the farfield should, therefore, be shifted off-axis by the angle $\Theta_1^{(+)}$ as given by Equation (3.40). To estimate b, we shall measure $\Theta_1^{(+)}$ for devices fabricated with several different gain gradients, s.

For a successful experiment, it is necessary to estimate the gain gradient, s, defined in Equation (3.4). The constant γ_0 is fixed by the requirement that, at threshold, the modal gain of the lasing mode $\gamma_1^{(+)}$ must precisely equal the sum of

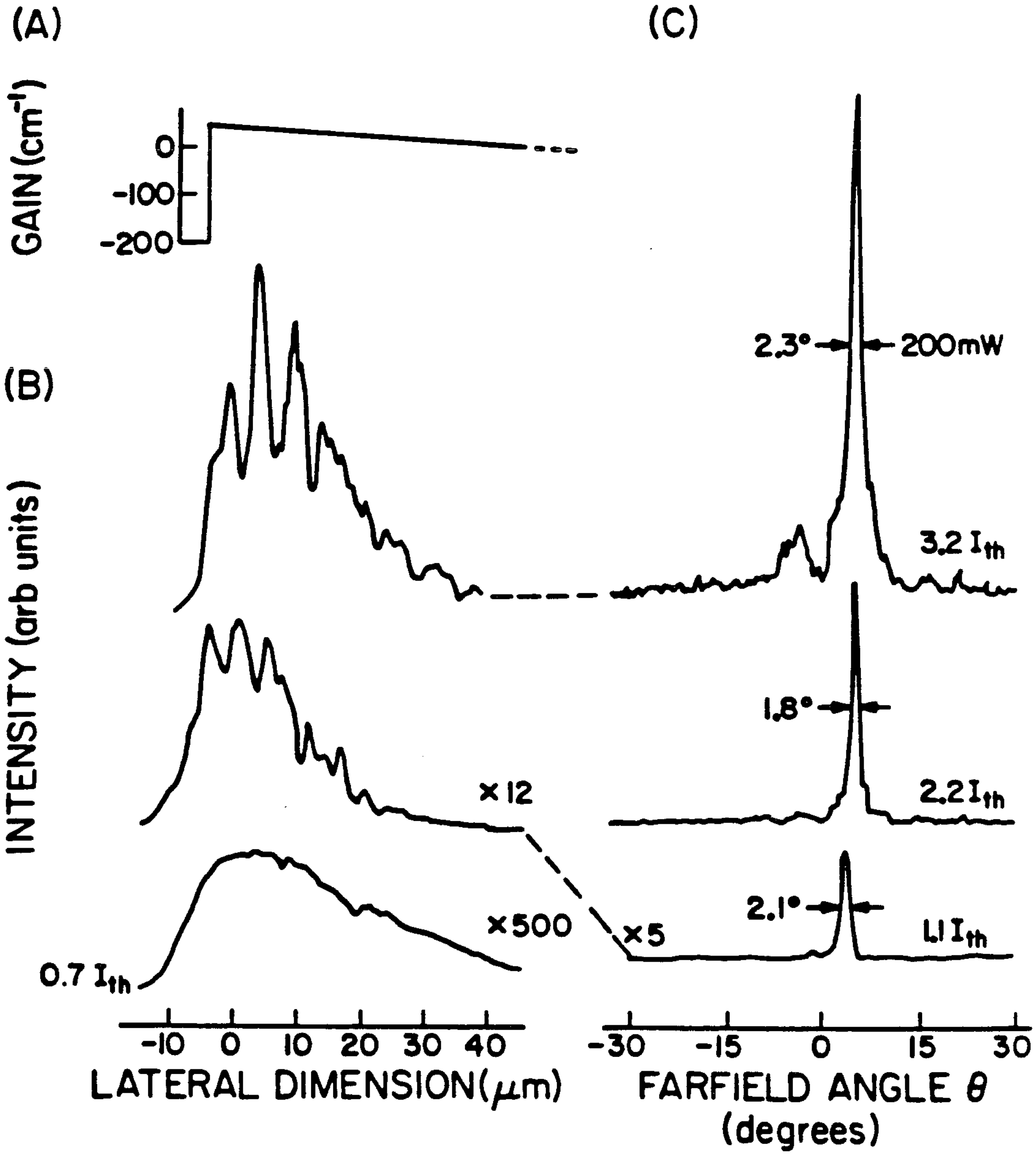

Figure 3.14 *Experimental (a) nearfield and (b) farfield patterns for a halftone laser* 60 μm *wide. Note the nearly linear spatial gain profile as evidenced by the spontaneous emission pattern at* $0.7 I_{th}$.

losses, typically about 40 cm^{-1} for a device 250 μm long. In an asymmetric tailored-gain halftone laser in which the fraction of injecting contact varies between 100% at the left edge of the laser and 0% at the right edge, light will be emitted only where the gain is greater than zero. We can estimate the position of transparency by examining the amplified spontaneous emission profile just below threshold. Together with γ_0, this determines the gain gradient.

Equation (3.40) may then be used to calculate the position of the off-axis farfield beam position $\Theta_1^{(+)}$ as a function of the antiguiding factor b. Figure 3.15 plots the theoretically expected emission angles for several values of the antiguiding factor along with experimental data from halftone, asymmetric,tailored-gain lasers with differing gain gradients. We find a value $b = 2.5 \pm 0.5$, which is in agreement with earlier published results[8].

The threshold currents I_{th} and external differential quantum efficiencies η_{ext} of tailored-gain lasers depend upon the extent to which the waveguide is truncated at the low gain region, because light is emitted only over those portions of the laser that are pumped to transparency (≥ 0 cm^{-1}). Thus, carriers injected into the net lossy regions of the laser (indicated by the shaded regions of Figure 3.16(a)) will increase I_{th} and decrease η_{ext} but will not increase the optical output. Figure 3.16(b) plots the excess current above threshold, $I - I_{th}$, vs. the optical power emitted per facet for pulsed, low duty cycle operation of lasers with uncoated mirrors and for various device widths ℓ. The total (two-mirror) differential quantum efficiency η_{ext} is also indicated. As expected, η_{ext} rises as the width of the laser decreases. However, decreasing the width of the laser makes it more susceptible to the adverse effects of gain saturation, leading to some power's being radiated into a small sidelobe at $-\Theta$.

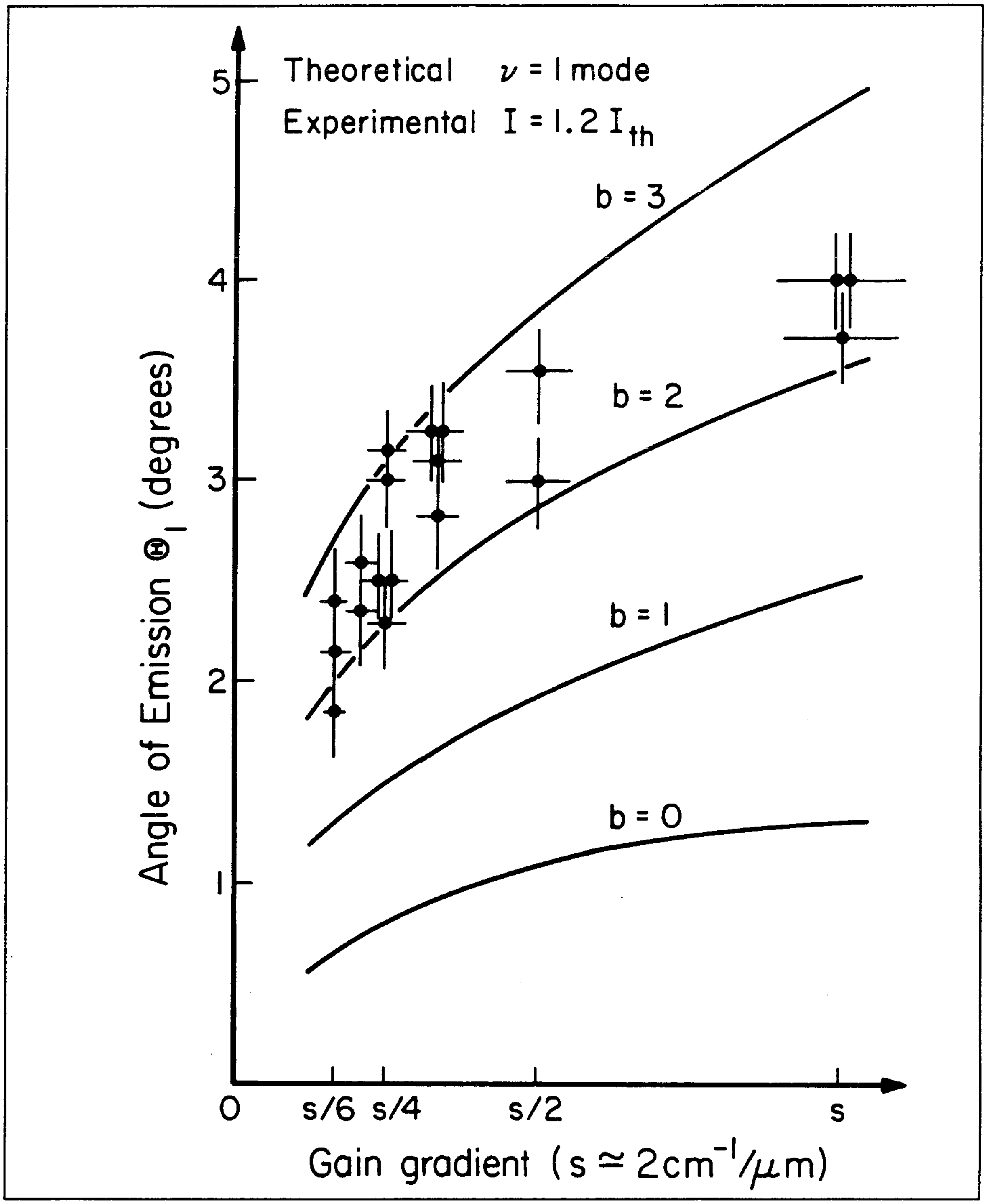

Figure 3.15 *Plot of the beam emission angle θ as a function of the antiguiding parameter b and spatial gain gradient. The experimental data points fit $b = 2.5$, in agreement with previously published results.*

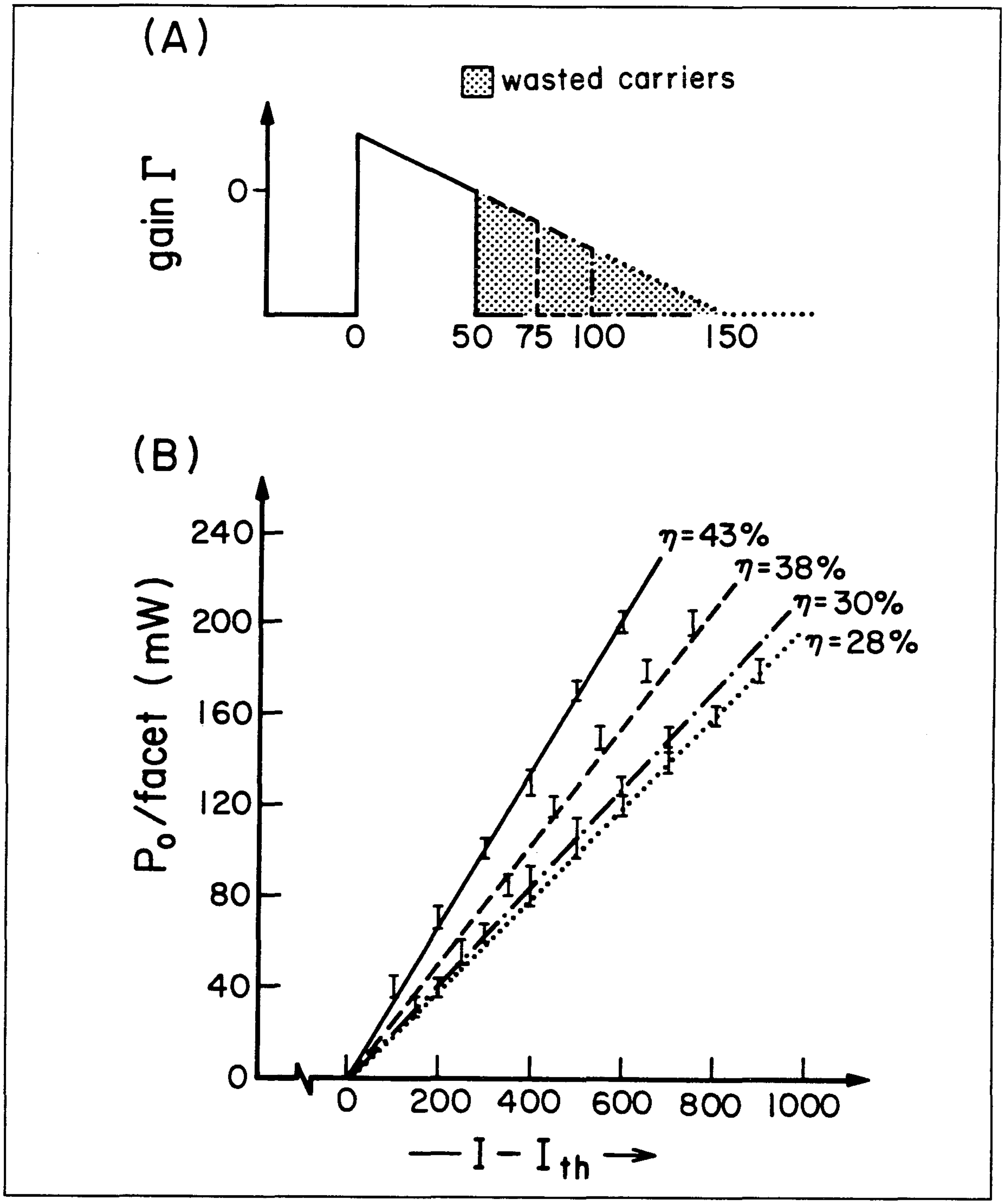

Figure 3.16 *Light-current curves for tailored-gain, broad area lasers. (a) Waveguide model for various truncated waveguides. The shaded areas represent regions of the waveguide, which are pumped below transparency, and therefore waste carriers. (b) Experimental light-current curves showing variation of two-mirror differential quantum efficiency η as a function of device width.*

3.5 Conclusions

In conclusion, we analyzed the lateral optical eigenmodes of such lasers in terms of the Airy function of complex argument. Unlike uniform phased arrays of semiconductor lasers, the fundamental mode in a tailored-gain laser is the lasing mode at threshold, thus making possible the narrow, single-lobed farfield patterns. The mode discrimination between the fundamental and higher-order modes may be controlled by variation of the spatial gain gradient, and varies sublinearly with it. We also showed that unlike all real index-guided lasers or symmetric gain-guided lasers, the higher-order modes of asymmetric tailored-gain lasers do not have nulls in their nearfield patterns, and that the corresponding farfield patterns are all asymmetric, single-lobed, and only slightly displaced from the fundamental. This theory therefore provides a satisfactory explanation for the experimental results presented in Section 3.0. Finally, we made use of halftone asymmetric tailored-gain lasers to estimate the antiguiding factor.

3.6 Appendix 3A

To calculate the nearfield and farfield patterns when real index antiguiding is included, we once again first calculate χ_ν, the position of the peak electric field intensity within the guide. We determine the point at which $\mathcal{L}$ becomes tangent to the level lines of $\mathrm{Ai}(z)$, and rotate the coordinate system so that a Taylor expansion may be used to evaluate the field distribution. When antiguiding is present ($b \neq 0$), χ_ν no longer lies on the anti-Stokes line. The exact evaluation of the level lines of $\mathrm{Ai}(z)$ yield complicated expressions, so we approximate them in the rotated $u - v$ coordinate system by a family of hyperbolas:

$$u^2 - \frac{v^2}{3} = c^2 , \qquad (3A.1)$$

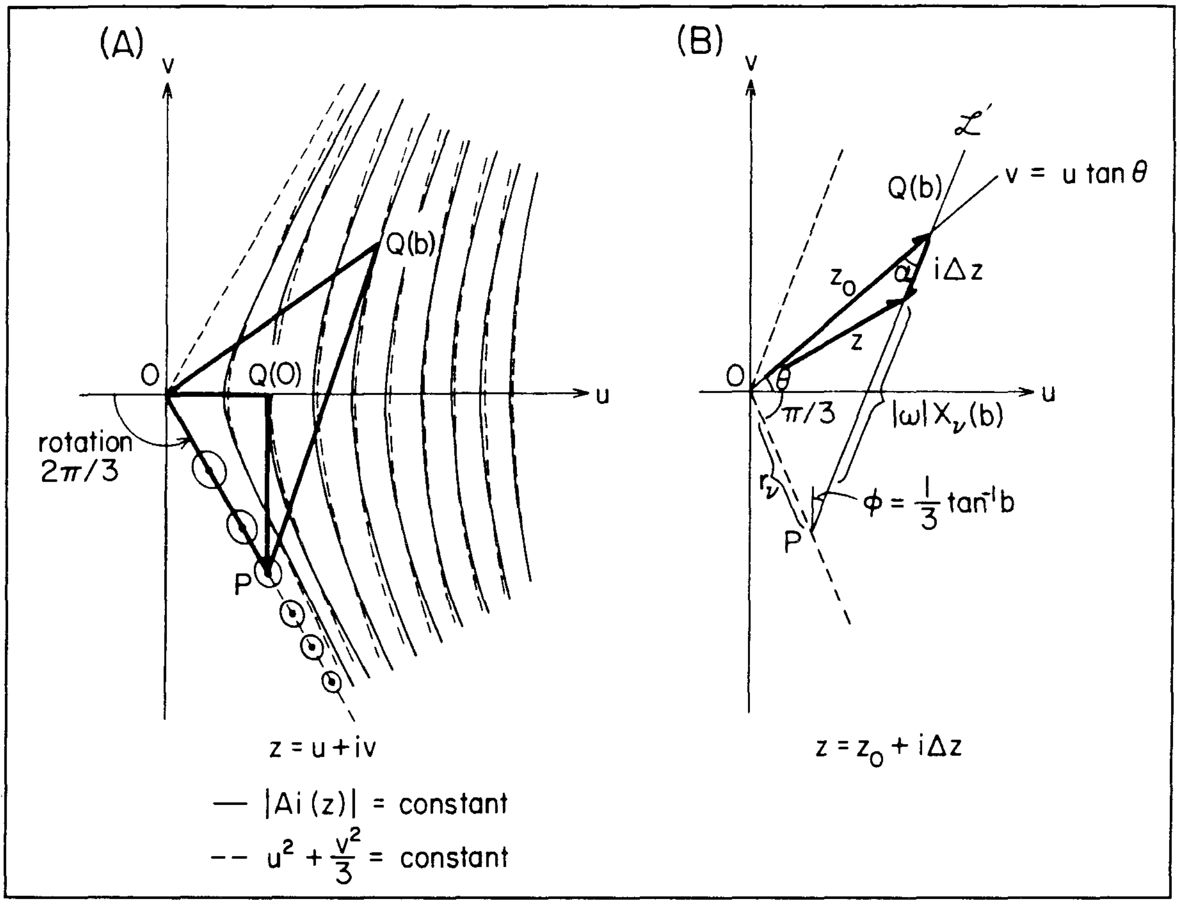

Figure 3.17 *(a) Hyperbolic approximation to level lines of* Ai(z) *in the rotated coordinate system. (b) Geometric construction for approximation to nearfield patterns.*

where c^2 is a positive real constant. This family is centered at the origin, and is asymptotic to $(u/v) = \pm\sqrt{3}$. Figure 3.17(a) plots the level lines of Ai(z) (solid curves) superimposed upon this family of hyperbolas (dashed curve), which shows that although the approximation is a good one, it may be slightly improved by a small empirical adjustment to the factor 3 in (3A.1).

Along with this family of hyperbolae, Figure 3.17(a) plots $\mathcal{L}'$, the path of the argument of the Airy function in the rotated coordinate system. Figure 3.17(b) shows the geometrical relationships among the various quantities more clearly. The equations for the lines $\mathcal{L}'_\nu$ are

$$u = u_\nu + m\,v \ , \tag{3A.2}$$

where u_ν is a constant depending on the mode index ν through the root $-r_\nu$ of the Airy function. The slope of this line m is given by

$$m = \tan\varphi = \tan\left(\frac{1}{3}\tan^{-1}b\right) . \tag{3A.3}$$

This line $\mathcal{L}'_\nu$ is tangent to a level line of the rotated $\mathrm{Ai}(z)$ when the two slopes in the (u, v) plane are equal. From (3A.1), we have

$$\frac{du}{dv} = \frac{1}{3}\frac{v}{u}. \tag{3A.4}$$

Setting this equal to m in (3A.3), we obtain an equation for the locus of points at which the lines $\mathcal{L}'_\nu$ are tangent to the level lines of the rotated $\mathrm{Ai}(z)$:

$$v = -3\tan\left(\frac{1}{3}\tan^{-1}b\right)\,u. \tag{3A.5}$$

Note that angle θ in the figure is given by $\theta = \tan^{-1}\left[3\tan\left(\frac{1}{3}\tan^{-1}b\right)\right]$, and that when $b = 0$, $\theta = 0$. In other words, $\mathcal{L}'_\nu(b = 0)$ corresponds to the positive real axis (rotated anti-Stokes line) as expected. Furthermore, as $b \to \infty$, $\theta \to \pi/3$ and $\mathcal{L}'_\nu$ becomes asymptotic to the rotated Stokes line of $\mathrm{Ai}(z)$. For a typical value of $b = 2.5$, $\theta = 51.5°$.

Once the tangency point has been located, the geometrical construction shown in Figure 3.17(b) may be used to determine χ_ν. $|\omega|\,\chi_\nu(b)$ is determined by the Sine Law:

$$\frac{r_\nu}{\sin\alpha} = \frac{|\omega|\,\chi_\nu(b)}{\sin(\frac{\pi}{3}+\theta)}. \tag{3A.6}$$

The two angles $\pi/3 + \theta$ and $\alpha = \pi/2 - (\theta + \varphi)$ are known, and so is the side of length r_ν, so that

$$\chi_\nu(b) = \frac{\sin(\theta + \pi/3)}{\cos(\theta + \varphi)}\frac{r_\nu}{|\omega|}. \tag{3A.7}$$

Note that when $b = 0$ we have $\theta = \varphi = 0$ and $|\omega|\,\chi_\nu(0) = (\sqrt{3}/2)r_\nu$ as in (3.22). Using this latter equation, we can therefore rewrite

$$\chi_\nu(b) = \frac{2}{\sqrt{3}}\,\frac{1}{(1+b^2)^{1/6}}\,\frac{\sin(\theta+\pi/3)}{\cos(\theta+\varphi)}\,\chi_\nu(0). \tag{3A.8}$$

With $b = 3$, χ_ν increases by a factor of three.

We next determine the nearfield pattern $E_\nu(x)$ by an expansion about the field maximum χ_ν. We recall that that the path $\mathcal{L}'_\nu$ is defined by $z = \rho + \omega x$ with $0 \le x \le \ell$ in the unrotated coordinate system. In the coordinate system that has been rotated by $\pi/3$, this becomes

$$z = r_\nu e^{-i\pi/3} + i\,e^{-i\varphi}\,|\omega|\,x. \tag{3A.9}$$

By adding and subtracting the term $i\,e^{-i\varphi}\,|\omega|\,\chi_\nu$, we rewrite (3A.9) as

$$z = \left[r_\nu e^{-i\pi/3} + i\,e^{-i\varphi}\,|\omega|\,\chi_\nu\right] + i\,e^{-i\varphi}\,|\omega|\,(x-\chi_\nu)\ , \tag{3A.10}$$

which is of the form

$$z = z_0 + i\,\Delta z\ , \tag{3A.11}$$

where

$$\begin{aligned} z_0 &= r_\nu\,\frac{\sin(\varphi+\pi/6)}{\cos(\theta+\varphi)}e^{i\theta} \\ \Delta z &= e^{-i\varphi}\,|\omega|\,(x-\chi_\nu). \end{aligned} \tag{3A.12\&13}$$

Observe that for $b = 0$ we have $z = u + iv$ as in (3.26).

The electric field is given near the anti-Stokes line of $\mathrm{Ai}(z)$ by Equation (3.26) with $u + iv$ replaced by $z_0 + i\Delta z$. Making the appropriate substitutions and simplifications, it becomes

$$E_\nu(z) = \frac{1}{2}\,e^{-i\pi/6}\,e^{-\frac{1}{3}z_0^{3/2}}\,\mathrm{Bi}(z_0)\,\exp\left[-\frac{(\Delta z - 2iz_0)^2}{4z_0^{1/2}}\right]\ . \tag{3A.14}$$

Since z_0 is independent of x, all the lateral field behavior is contained in the last factor of (3A.13). For the case $b = 0$, both z_0 and Δz are real, leading to a Gaussian field distribution with a linear phase variation as given by (3.28). In the general case, z_0 and Δz are complex, leading to a cross coupling between the magnitude and phase terms. However, we may still obtain meaningful insight into the antiguiding case by examining the "magnitude" and "phase" terms individually.

The phase term corresponding to $\phi_\nu(x-\chi_\nu)$ of Equation (3.29) is, from (3A.13),

$$z_0^{1/2}\Delta z = |\omega| \sqrt{\frac{\sin(\pi/6+\varphi)}{\cos(\theta+\varphi)}}\, r_\nu e^{-i(\varphi-\theta/2)}(x-\chi_\nu). \tag{3A.15}$$

Equation (3A.14) is essentially real because the angle $(\varphi-\theta/2)$ is zero for $b=0$ and ∞, rising to only about 5° in between. When $b=0$, (3A.14) reduces to

$$z_0^{1/2}\Delta z = |\omega| \left[\frac{r_\nu}{2}^{1/2}(x-\chi_\nu)\right]. \tag{3A.16}$$

It can be shown that the correction term $(-1/2r_\nu)$ of Equation (3.29) for the case $b=0$ has an associated obliquity factor $\cos(\theta+\varphi)$, which is very small in the range $b=2$ to 3, and is therefore neglected. We can therefore express the phase gradient $\phi_\nu(b)$ in terms of $\phi_\nu(0)$ approximately as

$$\phi_\nu(b) \simeq (1+b^2)^{1/2} \sqrt{\frac{2\sin(\pi/6+\varphi)}{\cos(\theta+\varphi)}}\, \phi_\nu(0). \tag{3A.17}$$

From Equation (3.32), we see that the beam angle increases by about the same amount. For example, taking $b=3$, the ratio $\Theta_\nu(b)/\Theta_\nu(0)$ is 4.

The magnitude term corresponding to $(x-\chi_\nu)^2/2w_\nu^2$ of (3.28) is

$$\frac{\Delta z^2}{4z_0^{1/2}} = \frac{(x-\chi_\nu)^2}{\frac{4}{|\omega|^2}\sqrt{\sin(\pi/6+\varphi)/\cos(\theta+\varphi)r_\nu}}\, e^{-i(2\varphi+\theta/2)}. \tag{3A.18}$$

Of course, it is the real part of (3A.17) that determines the width of the nearfield distribution in the general case $b \neq 0$. The obliquity factor in this case is quite severe since $2\varphi+\theta/2$ approaches $\pi/2$ quite rapidly as $b \to \infty$, thereby implying significant broadening of the nearfield pattern. We then write the halfwidth of the nearfield pattern $w_\nu(b)$ as

$$w_\nu^2(b) = \frac{\sqrt{2\sin(\pi/6+\varphi)/\cos(\theta+\varphi)}}{(1+b^2)^{1/3}\cos(2\varphi+\theta/2)} w_\nu^2(0). \tag{3A.19}$$

For example, when $b = 3$ the nearfield pattern broadens by about a factor of two.

Finally, we note that since (3A.17) has a significant imaginary part, there will be an additional quadratic correction to the linear phase term of (3A.15). However, from (3A.13) we observe that this correction is of order $\Delta z/4z_0$. Thus, it is not expected to contribute much to the absolute angle of beam emission in the farfield, but it will tend to counteract the effect of narrowing the beamwidth because of the increased nearfield width.

References

[1] C. Lindsey, P. Derry, and A. Yariv, "Fundamental lateral mode oscillation via gain tailoring in a broad area semiconductor laser," *Appl. Phys. Lett.* **47**, 560-562 (1985).

[2] C. Lindsey, P. Derry, and A. Yariv, "Tailored gain broad area lasers with single lobed farfield patterns," *Electr. Lett.* **21**, 671-673 (1985).

[3] C. P. Lindsey, E. Kapon, J. Katz, S. Margalit, and A. Yariv, "Single contact tailored gain phased array of semiconductor lasers," *Appl. Phys. Lett.* **45**, 722-724 (1984).

[4] D. F. Welch, D. R. Scifres, P. Cross, W. Streifer, R. D. Burnham, and J. Yaeli, "High power (575mW) single-lobed emission from a phased array laser," *Electr. Lett.* **21**, 603-604 (1985).

[5] D. F. Welch, D. Scifres, P. Cross, H. Kung, W. Streifer, R. D. Burnham, J. Yaeli, and T. L. Paoli, "High power CW operation of a phased array diode laser with diffraction limited output beam," *Appl. Phys. Lett.* **47**, 1134-1136 (1985).

[6] C. Lindsey, Ph.D. Thesis, California Institute of Technology, (University Microfilms Int., Ann Arbor, MI) (1986).

[7] C.M. Bender and S.A. Orszag, *Advanced Mathematical Methods for Scientists and Engineers*, pp. 569-570, McGraw-Hill, New York, (1978).

[8] J. Buus, "Principles of semiconductor laser modelling," *IEE Proc.* **132J**, 42-51 (1985).

CHAPTER

Four

(GaAl)As Laser Tunable Over 125 nm

4.0 Introduction

Semiconductor lasers can provide broadband tunable, single-frequency, narrow linewidth sources of radiation when coupled to an external cavity that contains a frequency-selective tuning element. Tuning of antireflection coated lasers coupled to a diffraction grating has been demonstrated over bandwidths of 50-60 *nm* at 0.8 μm[1,2] and 135 *nm* at 1.5 μm[3], with the latter measuring linewidths less than 10 *kHz*. Similarly, 1.3 μm lasers coupled to single-mode fiber, evanescent grating reflective filters were tuned over 66 *nm* with linewidths less than 50 *kHz*[4]. Recently, quantum well (QW) semiconductor lasers were shown theoretically and experimentally to possess very wide, flat, gain spectra near the onset of second quantized state (n=2) lasing[5,6]. Operating a Fabry-Perot laser at this *gain-flattened* condition is the basis of our tuning experiment.

Figure 4.1 illustrates gain spectra, as calculated according to Equations (1.7) and (1.4), for the DH (left) and GRINSCH-SQW (right) structures defined in the insets. The solid curves represent gain, in *inverse cm*, as a function of photon energy above the GaAs band gap. The dashed lines represent the *maximum* gain (upper, corresponding to infinite pumping) and *maximum* loss (lower, corresponding to zero pumping) seen by the transverse optical mode in both structures. For simplicity, the dashed lines were calculated without Lorentzian broadening (*i.e.,* in (1.4), $\widehat{\chi}_i \rightarrow \delta(\omega - \omega_0)$). Therefore, the gain is directly proportional to the reduced

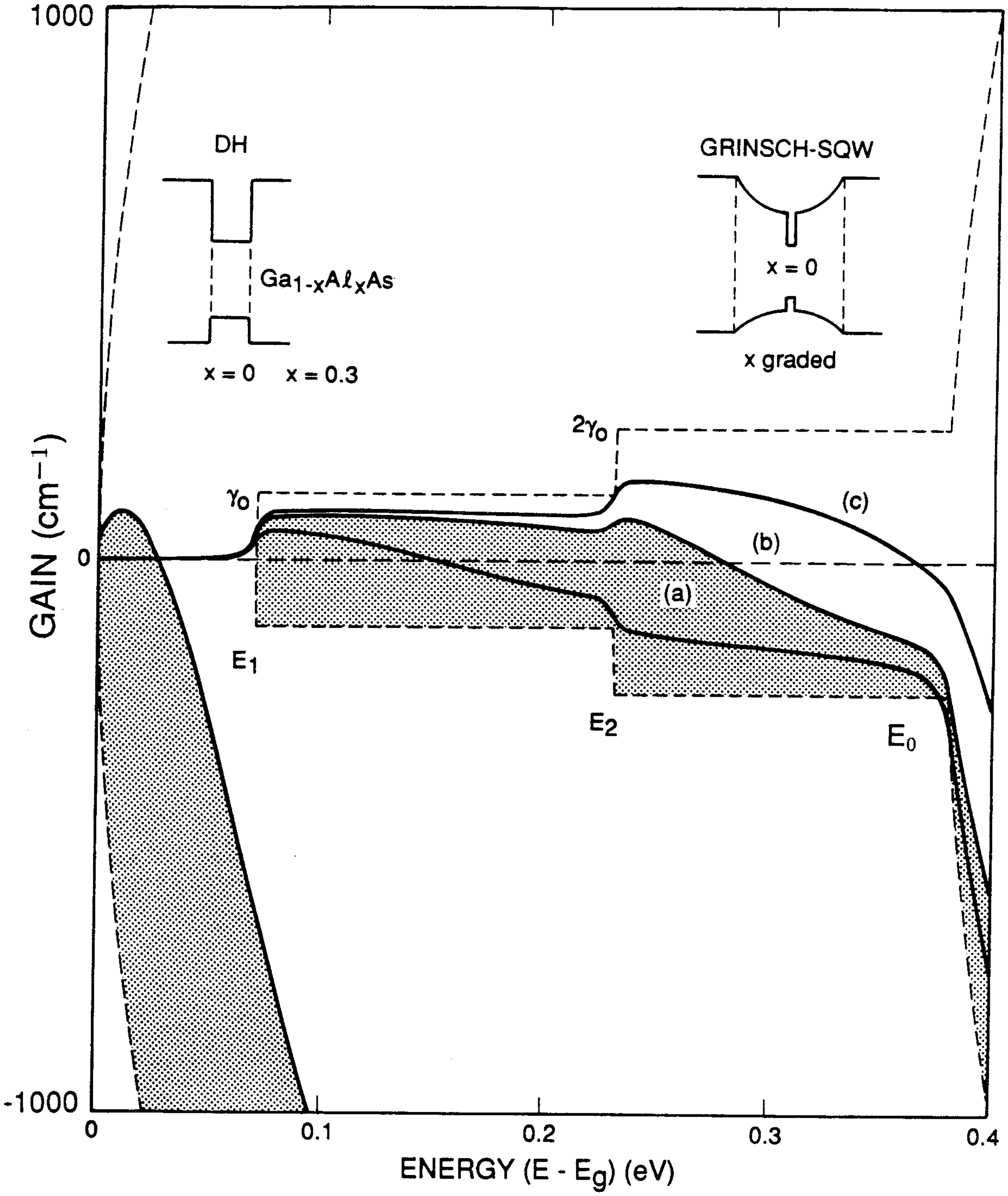

Figure 4.1 *Gain spectra (solid lines) and density of states (dashed lines) for DH laser (left) and QW laser (right) as a function of photon energy above the GaAs band gap. Curves (a), (b), and (c) for the QW laser correspond to quasi-Fermi energies of 75, 270, and 360 meV, respectively. The DH laser gain curve has quasi-Fermi energy 35 meV, corresponding to an injected carrier density equivalent to curve (b) for the QW laser. Thus, at this carrier density, the QW spectrum is* > 5 *times broader than the DH spectrum.*

density of states, $\rho(E)$ (in (1.7), gain $g(\omega_0) = -(k_0/n_0)\rho(\omega_0)$). In the QW, $\rho(E)$ has the familiar staircase shape offset from the GaAs energy gap by the energies E_1 and E_2 of the n=1 and n=2 quantized lasing transitions, respectively. In the GRIN region, however, $\rho(E)$ resembles the $\sqrt{E}$ dependence of bulk semiconductor, as is appropriate for a DH laser. In either laser, the gain available from any spectral region is proportional to the spatial overlap of the guided optical mode with the active region. In comparing QW and DH lasers, the GaAs active layer in the QW laser is typically an order of magnitude smaller. The resulting disparity in transverse mode - active region overlap is manifest in proportionately disparate transverse optical confinement factors, Γ, (defined in (1.10)). That $\Gamma_{QW} \simeq 0.1 \times \Gamma_{DH}$ results in some of the most important advantages of QW lasers, such as ultralow threshold QW lasers[7], and broadband tunable QW lasers, which we introduce here.

As indicated by the shaded area between the DH gain spectrum (solid, left) and its unpumped absorption (dashed, lower left) in Figure 4.1, most of the injected carriers in DH lasers are utilized *not in providing gain*, but in overcoming the inherent absorption. This is in marked constrast to the QW laser. Because of the disparity in Γ, the maximum gain available from a QW laser is reduced by an *order of magnitude* from that of the DH laser. However, by the same token, the unpumped absorption of a QW laser is *also* an order of magnitude less than for DH lasers. Consequently, proportionately fewer carriers are wasted in overcoming absorption in the QW laser, but are used to provide gain. This disparity is manifest in two ways: (i) to achieve the same modal gain, an order of magnitude *less* injected current density is required of QW than of DH lasers, or (ii) for the same injected current density, QW lasers have a greater than fivefold increase in gain bandwidth. The latter property is exploited in this work.

Because of the steplike nature of its density of states, the gain available from a QW laser at any one energy in the spectral range $E_1 < E < E_2$ is limited to a value we define as γ_0. That is, higher gain cannot be obtained there by higher pumping. However, since the density of states doubles above the $n = 2$ transition in the QW, additional gain can be obtained in the spectral region $E_2 < E < E_0$ through *bandfilling*, via additional injected current density. Curves (a), (b), and (c) of Figure 4.1 indicate the SQW gain spectrum for 3 increasing values of injected current density (quasi-Fermi level). At low current density (curve (a)), the QW spectrum is bell-shaped, similar to DH lasers. At higher injected current densities (curves (b) and (c)), a second maximum at $E > E_2$ arises because of the steplike onset of the n=2 subband. As curve (b) indicates, the pumping strength can be adjusted so that the two maxima arising from the n=1 and n=2 subbands are of equal height. Since gain spectrum (b) is very flat, it is referred to as the *gain-flattened* condition. Comparing curve (b) to the gain spectrum of the DH laser, which was calculated for *the same current density* (*i.e.,* the same area between the gain and absorption curves), we find the breadth of the SQW structure to be increased by a factor of > 5 over the DH laser. Note that while both QW and DH spectra broaden with increased current pumping, the QW spectrum is flattest at the gain-flattened condition.

Figure 4.2 illustrates the amplified spontaneous emission as a function of wavelength measured from an SQW buried heterostructure laser. The device was antireflection coated so as to prevent lasing. Spectra are shown as a function of injected current from 0 mA to 40 mA, which corresponds to several kA/cm^2 of injected current density. At low currents, the emission spectra are bell-shaped, with a single peak whose position shifts to shorter wavelengths as the pump level is increased. This peak is due to $n = 1$ quantized state transitions. At 20-25 mA, however, a second peak at substantially shorter wavelength emerges. This peak, from $n = 2$ quantized state transitions, overtakes the $n = 1$ peak at a current level of 35 mA.

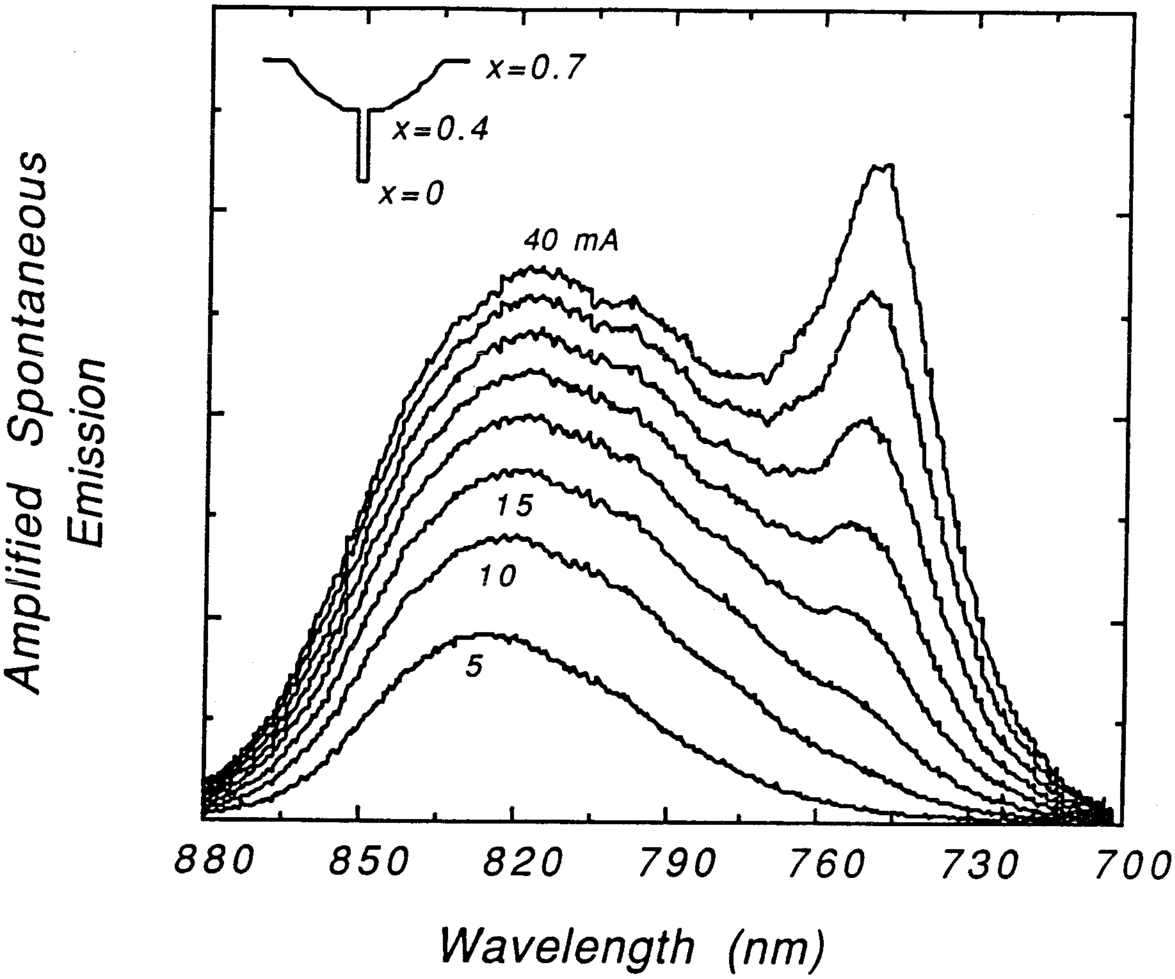

Figure 4.2 *Amplified spontaneous emission spectra of an SQW buried heterostructure laser, as a function of injected current. One facet was antireflection coated to suppress lasing. The appearance of two peaks in the spectrum, of nearly equal height at 35 mA, is strong evidence for the existence of the gain-flattened condition.*

The broad, flat, amplified spontaneous emission spectrum at this current corresponds to pumping at the gain-flattened condition. In this chapter, we optimize the laser resonator losses so as to induce the gain-flattened spectrum, and we demonstrate grating-tuning over a range of 125 nm in 0.8 μm (GaAl)As *uncoated* single QW lasers.

4.1 Grating-coupled Tuning of Single Quantum Well Lasers

The apparatus used for the tuning experiments is illustrated schematically in Figure 4.3. The external cavity consists of a collimating lens and a diffraction grating that together image a spectrally-resolved, spatially inverted nearfield back onto the rear facet of the semiconductor laser. The grating is oriented to reflect in first order; as a result, the spectrum is dispersed perpendicular to the plane of the epitaxial layers. Only the wavelength of a single longitudinal mode of the crystal cavity, at $\lambda = \lambda_0$, is refocussed onto the transverse waveguide, as shown in Figure 4.3. This wavelength-selective feedback provides additional gain for the mode at $\lambda = \lambda_0$, which is manifest as a lower threshold current for lasing at λ_0 than for all other wavelengths. Henceforth, λ_0 will be referred to as the *tuned wavelength.* The resolution of the lens-grating pair, at 2.2 Å, is enough to enforce single-longitudinal mode operation of Fabry-Perot resonators cleaved shorter than approximately 400 μm. Finally, the resultant spectra in the near and far fields were monitored by intercepting the collimated beam with an $R = 8\%$ beamsplitter, while the power output was measured at the front facet of the laser.

In order to achieve optimum tuning, the uncoupled resonator is designed to have a loss *slightly exceeding* the peak gain at the onset of second quantized state lasing. At the pump level required to overcome this loss, the gain spectrum is very flat (*viz,* curve (b) of Figure 4.1), and only a modest amount of external feedback is required for grating-tuning from below the n=1 to above the n=2 transition in the QW. The *resonator requirement* for broadband tuning can then be expressed by equating the maximum modal gain, γ_0, available from first quantized state transitions[7] to the modal losses, $\mathcal{L}$, as follows:

$$\mathcal{L} = \alpha + \frac{1}{2L} \ln \frac{1}{R_1 R_2} \simeq \frac{2\pi \mu^2 m_r}{\lambda_0 \epsilon_0 n_0 \hbar^2 W_{mode}} = \gamma_0 \ , \tag{4.1}$$

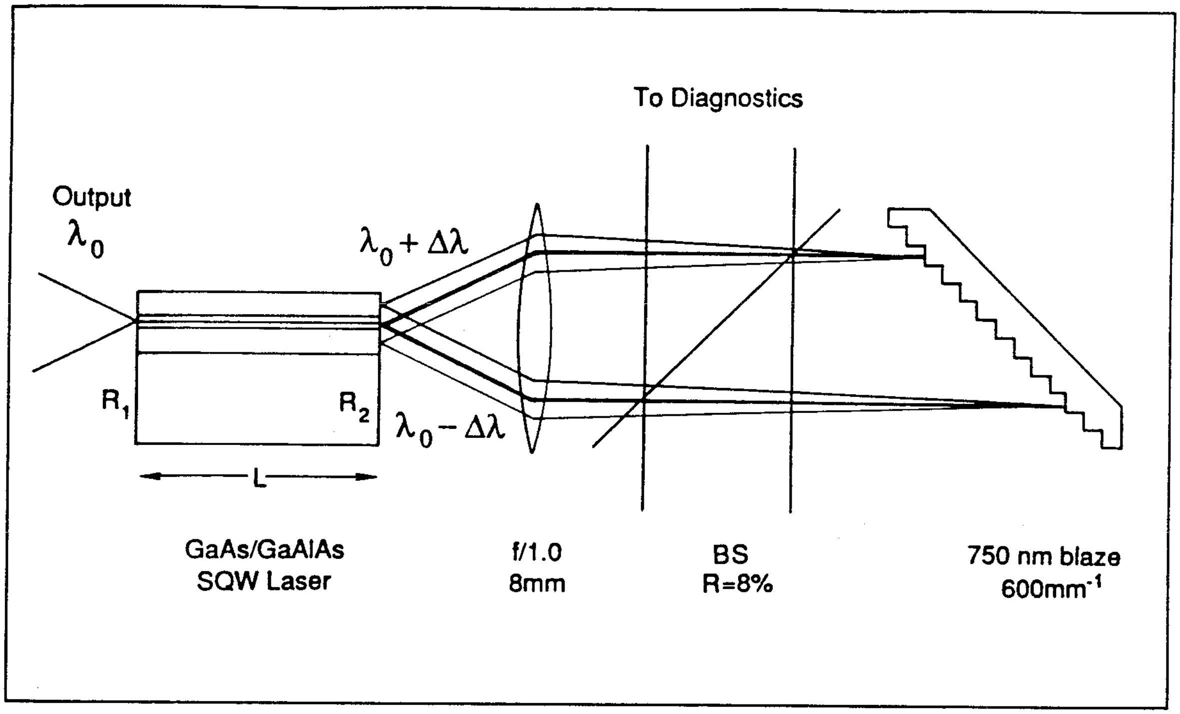

Figure 4.3 *Schematic diagram of the grating-coupled external cavity configuration. Light emitted from the rear facet of the laser is dispersed by the grating so that a spectrum is imaged back onto the facet, providing feedback at the tuned wavelength.*

where α is the distributed guided mode loss, L is the length of the Fabry-Perot resonator, and $R_{1,2}$ are the front and rear facet reflectivities, respectively. Both $\mathcal{L}$ and γ_0 are parameters that can be incorporated into the laser design. Firstly, γ_0 is determined primarily by the design of the GRINSCH-SQW transverse laser structure through W_{mode}, the effective width of the transverse optical mode. In Equation (4.1), μ^2 and m_r are the matrix element and reduced effective mass of the n=1 electron-heavy hole transition, respectively, ϵ_0 is the permittivity of free space, and n_0 is the nonresonant refractive index. In actual fact, the gain at the onset of second quantized state lasing, γ_0', is reduced from γ_0 by finite population inversion (see Figure 4.1), but is increased by contributions from the electron-light hole (n=1) transition. Thus, γ_0 is a reasonable approximation for γ_0'. Typically, $\gamma_0 \simeq$ 60-125 cm^{-1}; for our wafer, we estimate $W_{mode} \simeq 3500$ Å, and as a result $\gamma_0 \simeq 80$ cm^{-1}. Secondly, the resonator loss $\mathcal{L}$ can be varied by changing the cavity length, or the mirror reflectivities, or by incorporating an aperture within the cavity. In this work, lasers were simply cleaved short enough to achieve the elevated loss level $\mathcal{L} = \gamma_0$.

Figure 4.4 shows the result of a detailed numerical calculation of the gain of a GRINSCH-SQW laser near the gain-flattened condition. In addition, the loss of the semiconductor crystal cavity coupled to the lens-grating configuration and tuned to the wavelength $\lambda = \lambda_0$ is superimposed. With the grating blocked, the loss curve intersects the gain curve (b) at a wavelength $\lambda = \lambda_1$. This wavelength ($\lambda_1 = 785$ nm) and the high current density ($J_1 = 1350$ A/cm^2) required to achieve it is consistent with lasing from the $n = 2$ transition. With the grating *coupled* to the crystal resonator, the loss level is reduced at the tuned wavelength ($\lambda_0 = 842$ nm, the wavelength retroreflected by the grating) because of *constructive interference* of the reflection from the external cavity with the regular rear-facet reflection. As such, the loss curve intersects a different gain spectrum, curve (c), consistent with a *reduced* current density $J_0 (= 850 A/cm^2) < J_1$. Thus, J_0 is the threshold current for grating-coupled lasing at wavelength λ_0. In general, $J_0 = J_0(\lambda)$. The dependence of threshold current on the tuned wavelength has been estimated theoretically in the manner just described, and is illustrated in the lower half of Figure 4.4 over the broad tuning range.

For the tuning experiments, lasers were coupled to the external cavity *without antireflection coating* of the cleaved facets. The loss near the tuned wavelength is reduced by the selective feedback to a level an estimated 15 cm^{-1} below that of all other wavelengths (see Figure 4.4). This loss reduction could be increased by anti-reflection coating of the rear laser facet, but the flatness of the gain spectrum makes it unnecessary. Hence, no antireflection coating was applied. The grating was tuned to successive longitudinal modes of the Fabry-Perot laser, and the threshold

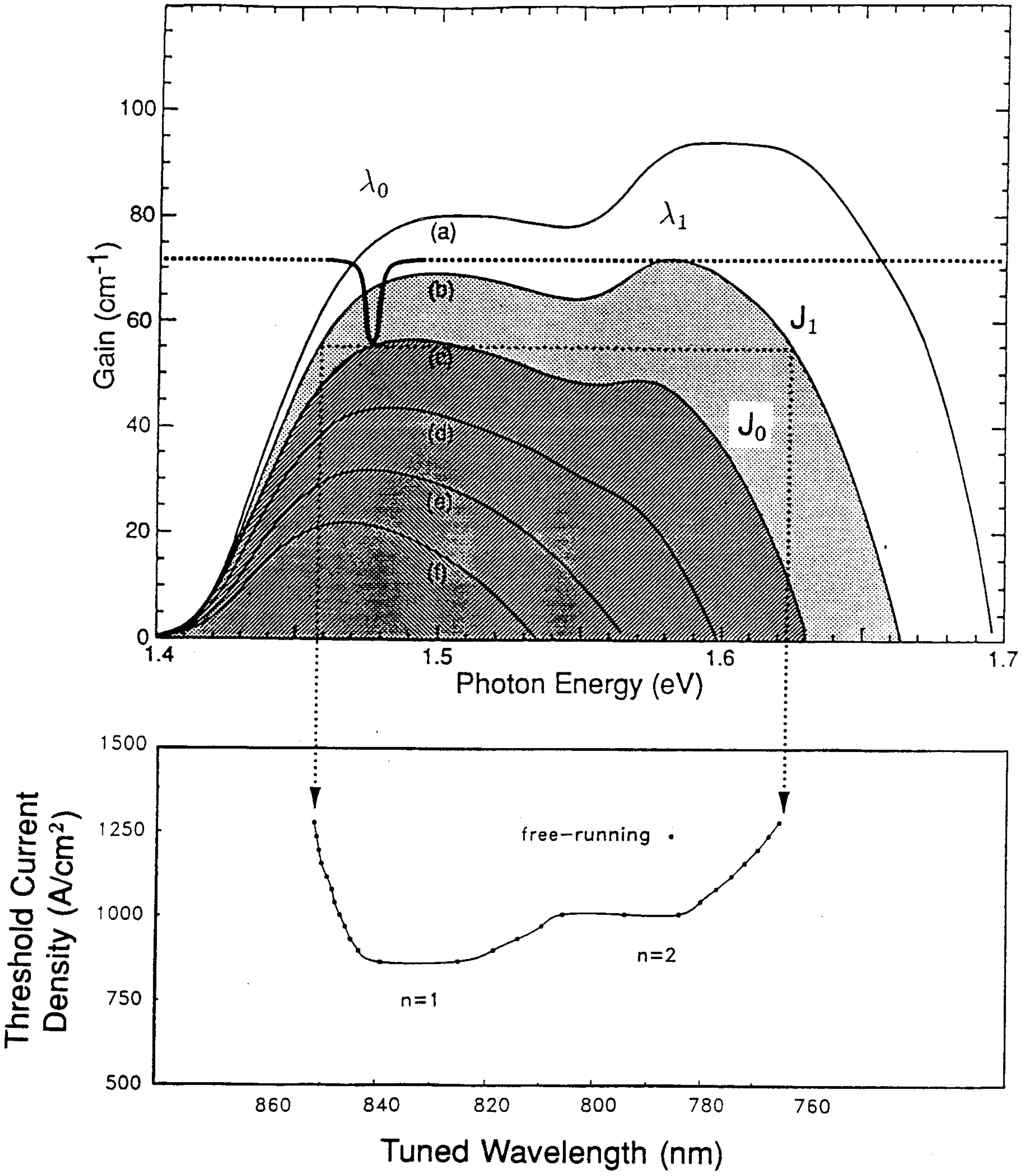

Figure 4.4 *Detailed calculation*^{6} *(upper) of the laser gain and resonator loss as a function of photon energy encompassing the first and second quantized states. The pump current densities for the various spectra are: (a) 1830, (b) 1350, (c) 950, (d) 630, (e) 405, and (f) 255* A/cm^2. *Theoretical prediction (lower) for threshold current density vs. tuned wavelength.*

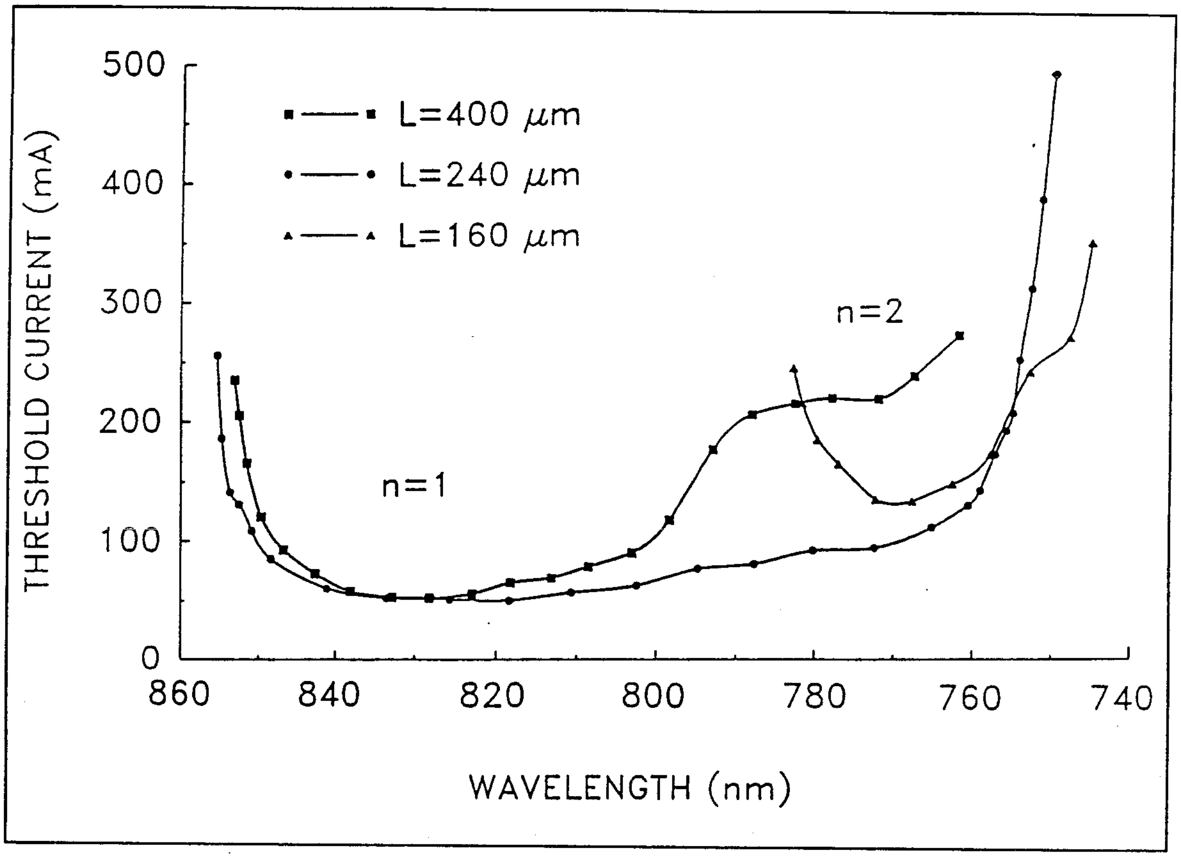

Figure 4.5 *Threshold current measured as a function of grating-tuned wavelength for 10 μm stripe contact lasers cleaved to 3 different lengths. Free-running threshold currents are 90, 130, and 140 mA for devices of length 400, 240, and 160 μm, respectively. The intermediate length of $L = 240$ μm is optimized for broadband tuning from below the first (n=1) to above the second (n=2) quantized states of the single quantum well active region.*

current measured as a function of wavelength for operation under low duty-cycle, pulsed (200 ns, 1 kHz) conditions. In addition, the maximum power output into each tuned longitudinal mode was monitored with an Si photodetector placed near the front laser facet.

In order to determine the effect of the uncoupled resonator loss on the tuning characteristics, lasers of various lengths up to 400 μm were tested. For this experiment, oxide-isolated 10 μm stripe contact lasers were fabricated from a GRINSCH-SQW wafer grown by MOCVD. The QW width was estimated from photoluminescence data to be approximately 75 Å in width. Figure 4.5 illustrates tuning data measured for lasers cleaved to 3 different lengths: L = 400 μm, 240 μm, and 160 μm. For devices of intermediate length, stepwise tuning was achieved at over 300 contiguous longitudinal modes of the Fabry-Perot laser, spanning the wavelength range 750 nm to 855 nm. This 105 nm span represents a tuning range of 13.1% about the center wavelength of 800 nm. The threshold current in free-running operation (i.e., with the grating blocked) for 10 μm-wide lasers was 130 mA, and corresponded to emission at 770 nm. This short wavelength and high current density ($\simeq 2.5$ kA/cm^2) is consistent with lasing from the second quantized state of the quantum well. The threshold in grating-tuned operation was thus reduced below the free-running threshold over 90 nm of the 105 nm tuning range (the minimum threshold current of 50 mA corresponds to a threshold current density of $\simeq 1$ kA/cm^2, in reasonable agreement with the theoretical prediction of Figure 4.4). Within this 90 nm span, lasing was observed in a single longitudinal mode at power levels up to 75 mW for the 10 μm wide devices. As Figure 4.4 indicates, however, devices cleaved significantly longer or shorter than 240 μm did not exhibit such broad, effective tuning characteristics. The reason for designing the resonator loss, $\mathcal{L}$, to be slightly above γ_0' (rather than slightly below) is evident from comparison of the tuning data for the two cases of 240 μm and 400 μm. Only for the 240 μm length was single-longitudinal-mode lasing achieved over most (90 of 105 nm) of the broad tuning range with *a minimum variation in threshold current.*

4.2 Variation in Tuning Range with Quantum Well Width

The tuning range in SQW lasers optimized to operate at the gain-flattened condition scales as the *separation* between the $n = 1$ and $n = 2$ transitions in the QW. Figure 4.6 shows the wavelengths of the electron-heavy hole transitions (solid lines) and the electron-light hole transitions (dashed lines) in GaAs QW's of varying

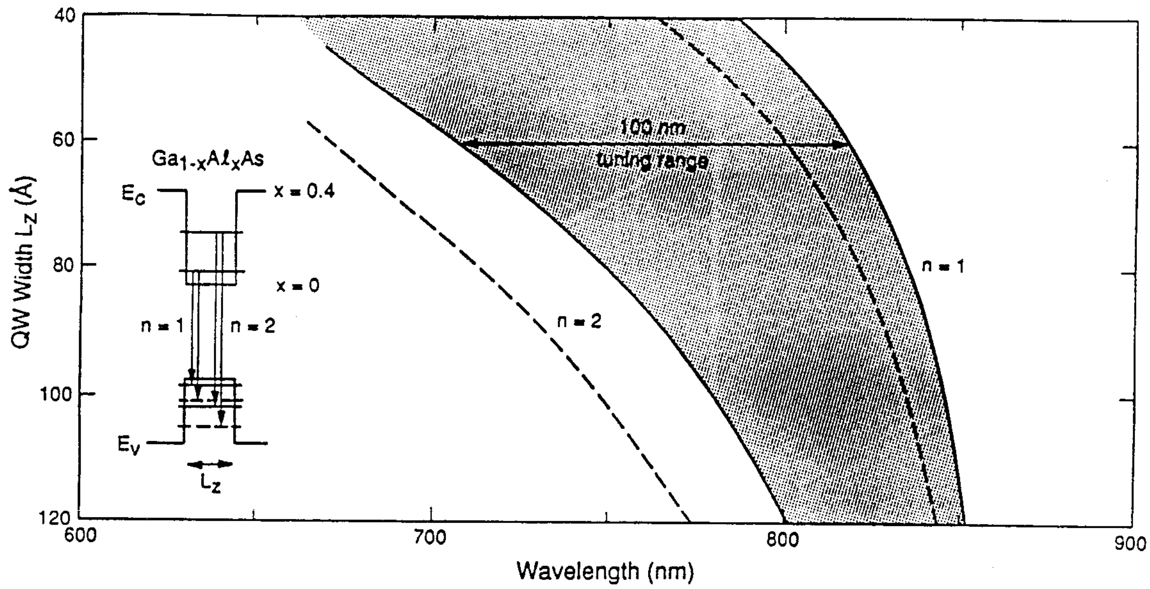

Figure 4.6 *Transition wavelength of the electron-heavy hole (solid) and electron-light hole (dashed) for the $n = 1$ and $n = 2$ states, as a function of GaAs QW width.*

width embedded in $Ga_{0.6}Al_{0.4}As$ confining layers. A good indication of the tuning range is the separation between the $n = 1$ and $n = 2$ electron-heavy hole transition, shown shaded in Figure 4.6. Note that the tuning range increases with decreasing QW width until the n=2 electron level pops out of the QW at $L_z \simeq 45$ Å. This calculation indicates that *decreasing* the QW width from 120 Å to 70 Å *increases* the effective tuning range by a factor of 2. However, this increase in tuning range is achieved only at the expense of an accompanying increase in threshold current density.

To quantify this discussion, we can estimate the current density J_{th} at the onset of second quantized-state lasing as follows:

$$J_{th} = \frac{e\, N_{2-d}^{g-f}}{\tau_{sp}} , \qquad (4.2)$$

where N_{2-d}^{g-f} is the two-dimensional carrier density at the gain-flattened condition. N_{2-d}^{g-f} is estimated, to first order, by totalling up all of the spectral states in the first step of the QW density of states:

$$N_{2-d}^{g-f} \simeq 2\int_{E_1}^{E_2} \rho_{2-d}(E)\, dE = \frac{2m_r}{\pi\hbar^2}(E_2 - E_1)\ . \tag{4.3}$$

The factor of two accounts for bringing the material from full absorption to full gain (see Figure 4.1). Thus, the gain-flattened threshold current density is

$$J_{th} \simeq \frac{2m_r e}{\pi\hbar^2\tau_{sp}}(E_2 - E_1)\ . \tag{4.4}$$

That is, to first order, the threshold current density scales *in proportion* to the separation $E_2 - E_1$ between the onset energy of the first and second quantized state subbands, and thereby in proportion to the tuning range. As inferred from Figure 4.1, this method clearly underestimates the injected carrier density required for second quantized-state lasing at finite temperatures. However, it does predict that, although the tuning range can be extended by narrowing the QW, the cost is an increased current density paid to achieve the gain-flattened condition. Note further that increasing the number of QW's while maintaining the same QW width does not increase the tuning range. In fact, the gain at which lasing switches from the first to the second quantized state doubles, implying that twice the current density is required to achieve the gain-flattened condition.

Tuning characteristics were measured for devices fabricated from wafers with differing QW widths. Broad area lasers were used for these experiments, and were fabricated from GRINSCH-SQW wafers grown by MBE. Figure 4.7 shows the measured threshold current density and output power as a function of wavelength for 60 μm-wide lasers fabricated from QW's of thickness 115 Å and 85 Å. As can be seen, the tuning range, output power level, and threshold current density are all increased for devices with the narrower quantum wells.

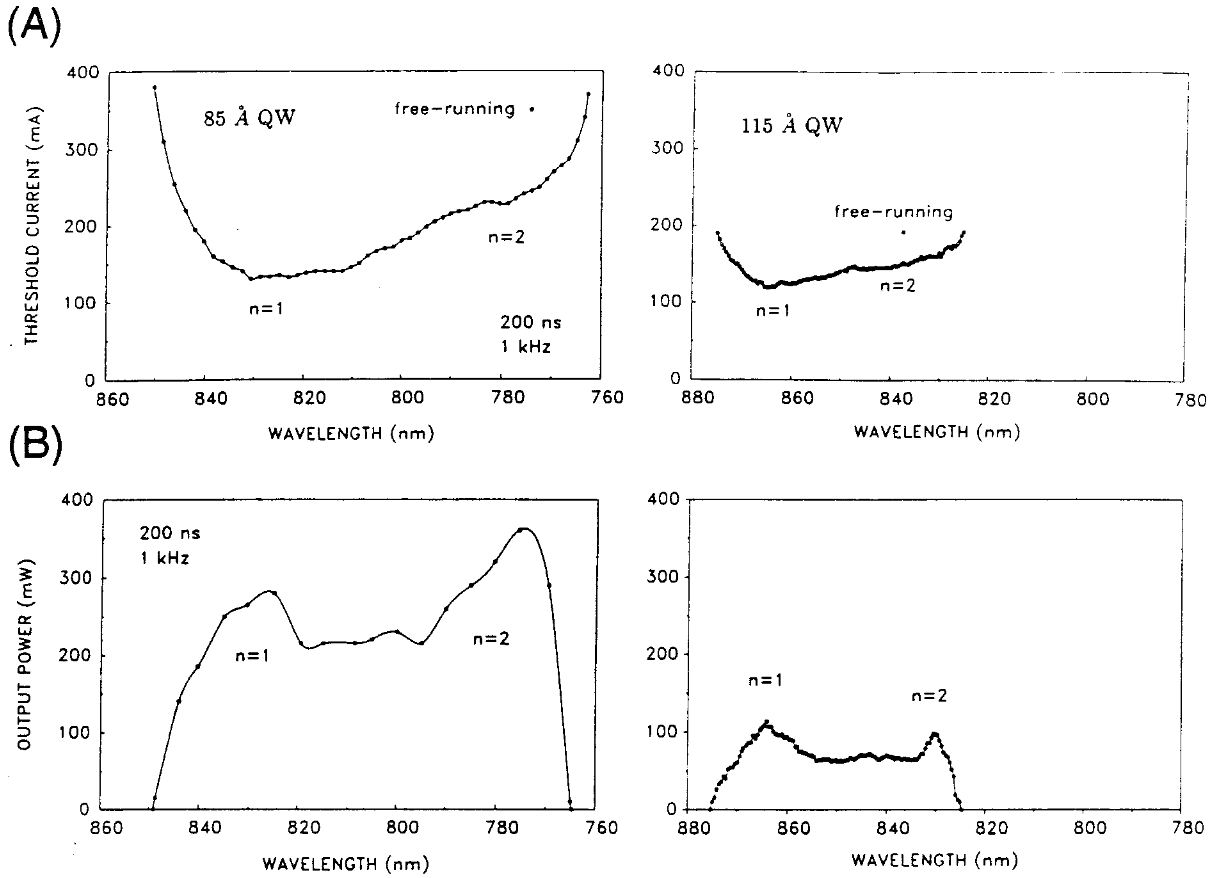

Figure 4.7 *Threshold current density (a) and single-longitudinal mode output power (b) vs. tuned wavelength for 60 μm-wide broad area lasers fabricated from single quantum well material with* $L_z = 85$ *Å (left) and* $L_z = 115$ *Å (right).*

The greatest tuning range to date was achieved with 10 μm-wide oxide-isolated stripe lasers fabricated from a specially designed MBE wafer. The QW was grown narrow, $L_z \simeq 60$ Å, to widely separate the $n = 1$ and $n = 2$ transitions in energy. In order to sufficiently confine the $n = 2$ electron state, it was necessary to increase the Al content at the edge of the QW to $x = 0.4$. The GRIN region was graded parabolically up to $x = 0.7$ at the edge of the cladding. With this structure, a pulsed tuning range of 125 *nm* was achieved, as illustrated in Figure 4.8. This

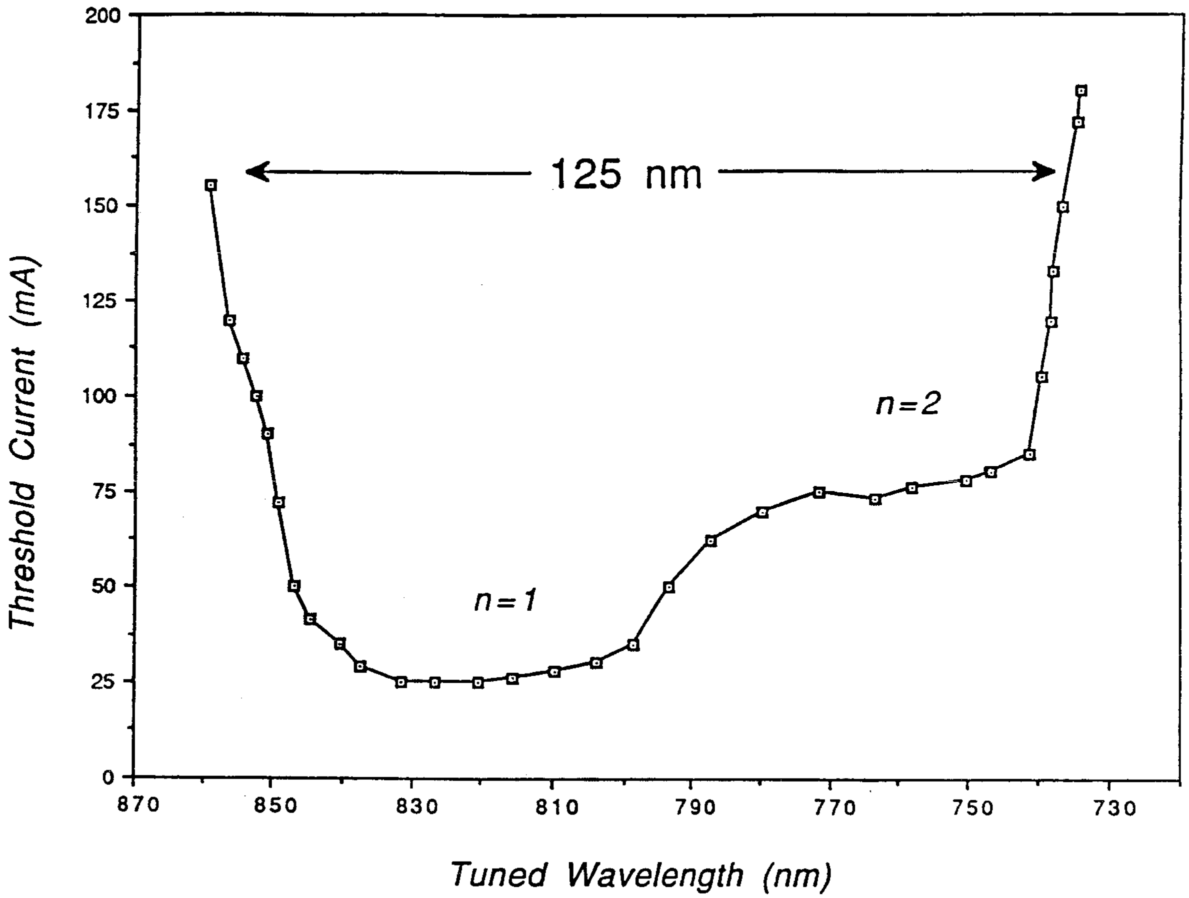

Figure 4.8 *Tuning characteristic of a 120 μm long, uncoated (GaAl)As laser optimized for broadband tuning. The 125 nm tuning span represents a 15.7% tuning range, the largest yet published for a semiconductor laser.*

tuning range, 15.7% about the center wavelength of 800 nm, is by far the largest published to date for any semiconductor laser.

Finally, it is of great practical importance to demonstrate that the broad tuning ranges obtainable from single quantum well lasers are achieved at current densities low enough to allow CW operation. CW experiments were performed on SQW lasers of buried heterostructure geometry. The wafer had a QW width of $L_z \simeq 80$ Å and was grown by MBE. A 1 μm wide mesa was etched and the appropriate regrowth was

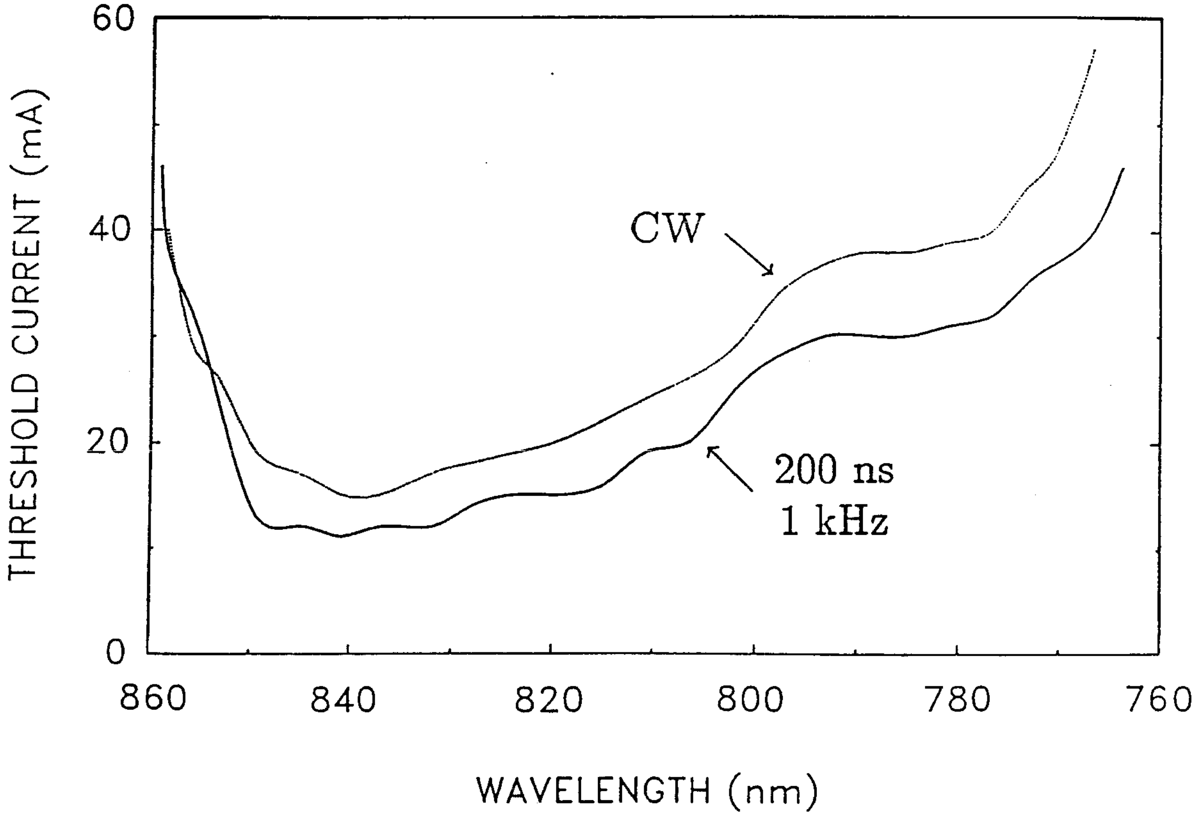

Figure 4.9 *Tuning characteristic of an antireflection coated, buried heterostructure laser operated with pulsed current (solid line), and with direct current (dashed line). The CW characteristic nearly duplicates the pulsed characteristic.*

made by LPE. The device was cleaved to 250 μm length and soldered p-side up onto a copper mount. The front facet was antireflection coated to about 5% reflectivity, low enough to force lasing free-running in the second quantized state. Figure 4.9 shows that 95% of the 95 nm tuning range achieved under pulsed operation is duplicated under CW operation. Furthermore, high-resolution spectroscopy of the laser output performed with a scanning Fabry-Perot interferometer indicated that the CW linewidth is less than 7.5 MHz, the resolution limit of the instrument.

4.3 Coupled-Cavity Model

Previously, we have indicated our theoretical expectations for the threshold current density as a function of grating-tuned wavelength. The curve so constructed (Figure 4.4) compared favorably with the experimental results. The current density required for lasing was determined simply by demanding that the gain provided by current pumping equalled the reduced loss of the composite cavity at the tuned wavelength. Although the gain so provided is a *continuous* function of frequency, the loss of a cavity of fixed optical path length is not expressed by a curve, but rather by a sequence of discrete points. This is because, in addition to overcoming resonator losses, the electromagnetic field must reproduce its *phase* upon completion of one round trip in the composite cavity. In addition to reducing the losses at the tuned wavelength, external feedback alters the longitudinal mode structure of the laser. In this section, we make a more detailed examination of the gain and phase requirements for oscillation in a dispersive cavity.

Figure 4.10 illustrates schematically the mode structure of the grating-coupled dispersive cavity. The composite cavity loss curve away from the tuned wavelength is, in general, composed of multiplets of spatial modes separated by the longitudinal mode frequency spacing, $c/2nL$, of the semiconductor cavity. The corresponding wavelength spacing is typically ~ 4 Å. Each spatial mode has its own modal loss and frequency of oscillation, as shown in Figure 4.10. In the viscinity of the grating-tuned wavelength λ_0, however, the picture is more complicated. Coherent additions of the reflections from the laser facet and the external cavity combine to modulate the effective reflectivity of the external cavity with a period of oscillation aproximately equal to the longitudinal mode frequency spacing, $c/2L_{ex}$, of the external cavity. Since $L_{ex} >> L$, this frequency spacing is a small fraction of the crystal cavity spacing. For example, this spacing is typically 1 GHz (equivalent to 0.02 Å) for a 15 cm-long cavity.

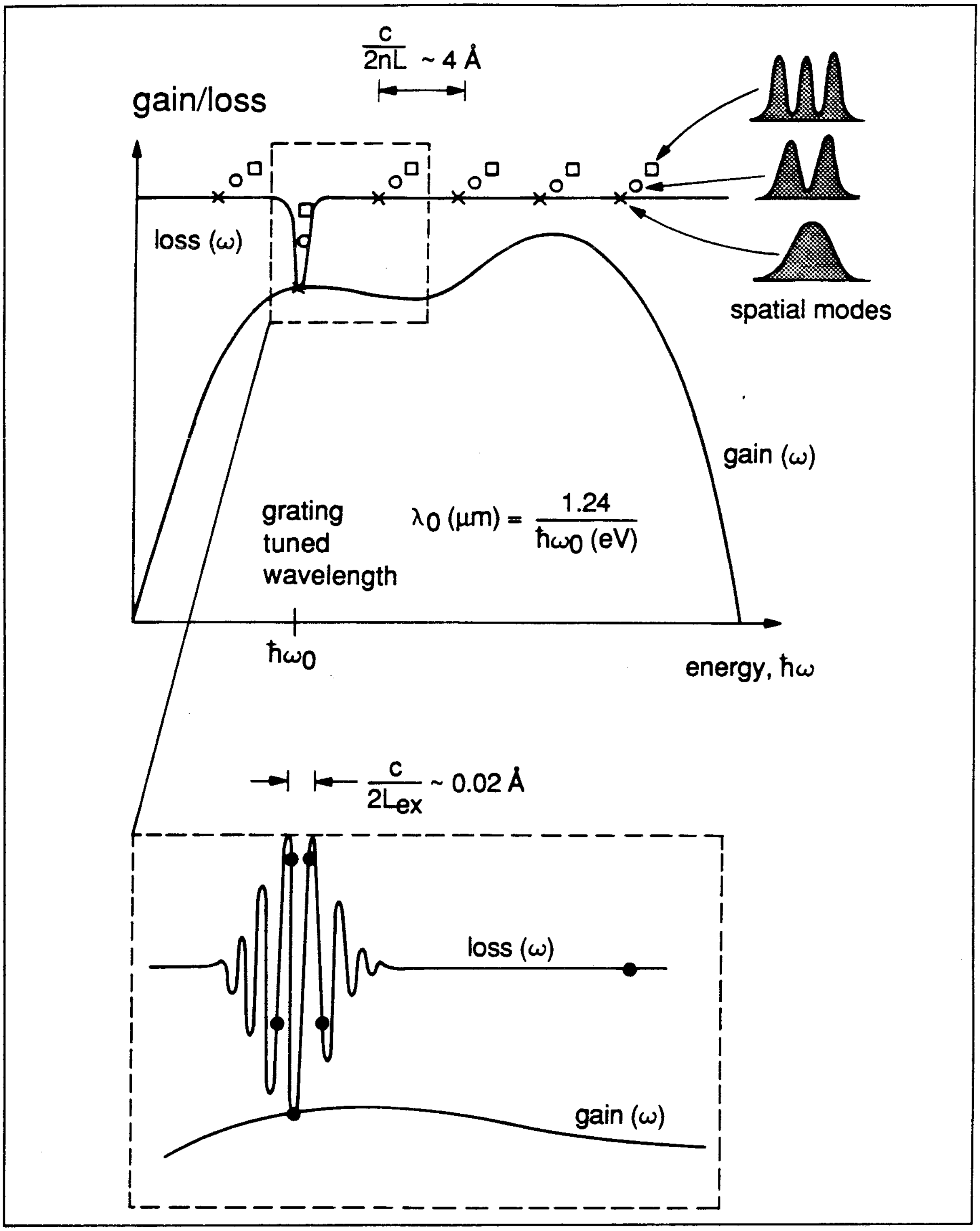

Figure 4.10 *Schematic diagram of the frequency-dependent laser gain (solid curve) and resonator loss (discrete points) near the gain-flattened condition. Near the grating-tuned wavelength, coherent reflections from the external cavity modulate the rear-facet reflectivity with a period corresponding to the length* L_{ex} *of the external cavity.*

A question that should be addressed *a priori* is whether or not it is appropriate to assume coherent reflections from such a long external cavity. If we assume a linewidth $\Delta f = 10$ MHz (typical for a single-mode semiconductor laser), then the coherence time τ_c can be estimated via the uncertainty principle $2\pi\Delta f \cdot \tau_c \sim 1$. The corresponding coherence length $L_c = c\tau_c$ is $\sim 5\ m$. With external feedback, the coherence is improved over that of the crystal cavity alone. This improvement is due to the larger number of photons in the *composite-cavity* lasing mode, which damps the phase sensitivity to spontaneous emissions. Thus, it is valid to consider coherent reflections through many round trips in our short external cavity.

Figure 4.11 shows the coupled-cavity configuration with which we propose to model our grating-coupled external cavity. Let E_1^+ and E_1^- be the right-going and left-going amplitudes of the lasing mode just inside the right crystal facet, and E_2^+ and E_2^- their counterparts in the external cavity, as shown. The following relations can be written by inspection:

$$E_2^+ = \sqrt{1-r^2}\, E_1^+ - rE_2^- \tag{4.5a}$$

$$E_2^- = te^{i\theta}\, E_2^+ \tag{4.5b}$$

$$E_1^- = rE_1^+ + \sqrt{1-r^2}E_2^- \tag{4.5c}$$

$$E_1^+ = r_0 e^{(\gamma-\alpha)L+i\varphi}\, E_1^- \ , \tag{4.5d}$$

where r_0 and r are the modal reflectivities of the left and right crystal facets, $t(\omega)$ is the amplitude transmission through the external cavity, $\theta = 2\omega L_{ex}/c$ is the phase shift upon traversing the external cavity, γ and α are the distributed gain and loss of the laser, and $\varphi = 2n\omega L/c$ is the phase shift upon traversing the semiconductor cavity. The external cavity can be modeled as a frequency-dependent *effective*

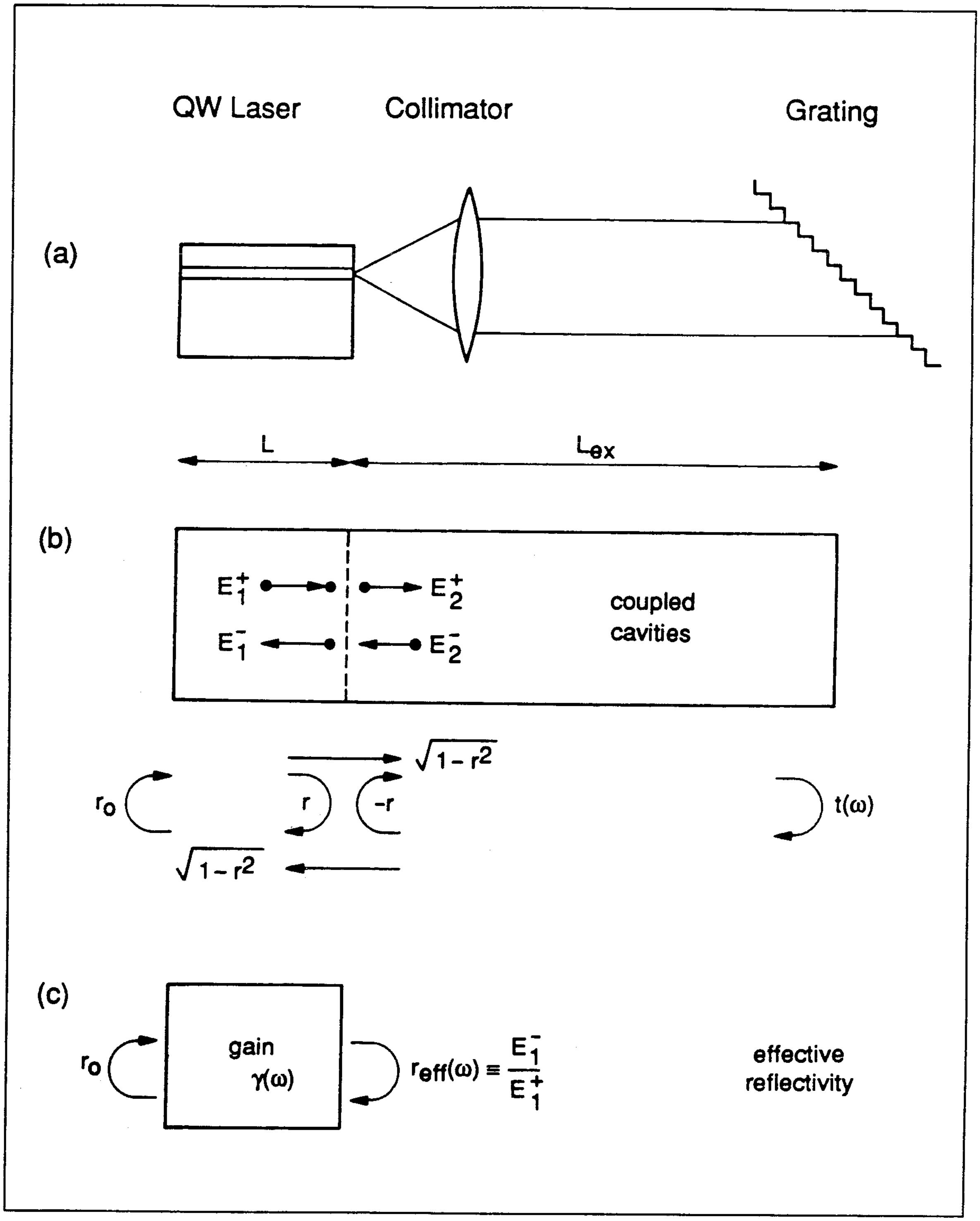

Figure 4.11 *Coupled-cavity model for the grating-coupled external cavity: (a) geometry, (b) definition of right-going and left-going waves within each cavity, and (c) effective reflectivity of the rear facet.*

reflectivity, $r_{eff}(\omega)$, as shown in Figure 4.10(d). By eliminating E_2^+ and E_2^- from Equations (4.5a-c), we obtain for r_{eff}:

$$r_{eff}(\omega) \equiv \frac{E_1^-}{E_1^+} = r + \frac{(1-r^2)te^{i\theta}}{1+rte^{i\theta}} = \frac{r+te^{i\theta}}{1+rte^{i\theta}} \ . \tag{4.6}$$

Together with Equation (4.5d), r_{eff} defines the following round-trip condition:

$$r_0 r_{eff}(\omega)e^{(\gamma-\alpha)L+i\varphi} = e^{i2\pi\cdot m} \ , \quad m \text{ an integer} \ , \tag{4.7}$$

where m is the longitudinal mode index. Solution of Equation (4.7) yields the oscillation frequency ω and the modal gain $\gamma(\omega)$ of the unknown composite-cavity modes:

$$2\pi\cdot m = \angle r_{eff}(\omega) + \varphi(\omega) \ , \tag{4.8a}$$

$$\gamma(\omega) = \alpha + \frac{1}{L}\ln\frac{1}{|r_0 r_{eff}(\omega)|} \ . \tag{4.8b}$$

Equation (4.8a) does not depend on the modal gain γ, and thus may be solved for the allowable oscillation frequencies ω_m. The result is then inserted into (4.8b) to extract the corresponding modal gain $\gamma_m \equiv \gamma(\omega_m)$. For the simplest case of *no* external feedback, $t(\omega) = 0$ and $r_{eff} = r$. Equations (4.8) then give:

$$\begin{aligned} \omega_m &= m\cdot\frac{c}{2nL} \ , \\ \gamma_m &= \alpha + \frac{1}{L}\ln\frac{1}{r_0 r} \ . \end{aligned} \tag{4.9}$$

That is, (ω_m, γ_m) are the usual longitudinal modes of the crystal cavity.

In the non-trivial case $t \neq 0$, we infer from Equation (4.6) that $t = r$ defines a critical condition in the external resonator, since when $\theta(\omega) = \pi$, $r_{eff}(\omega) = 0$. That is, when $r = t$, it is possible to tune the external cavity so that the reflection that is due to the grating-coupled external cavity *exactly cancels* that due to the facet reflection. To see the significance of this possibility, consider detuning ω away from a crystal resonance ω_m (defined by Equation (4.9)). In order to satisfy the phase

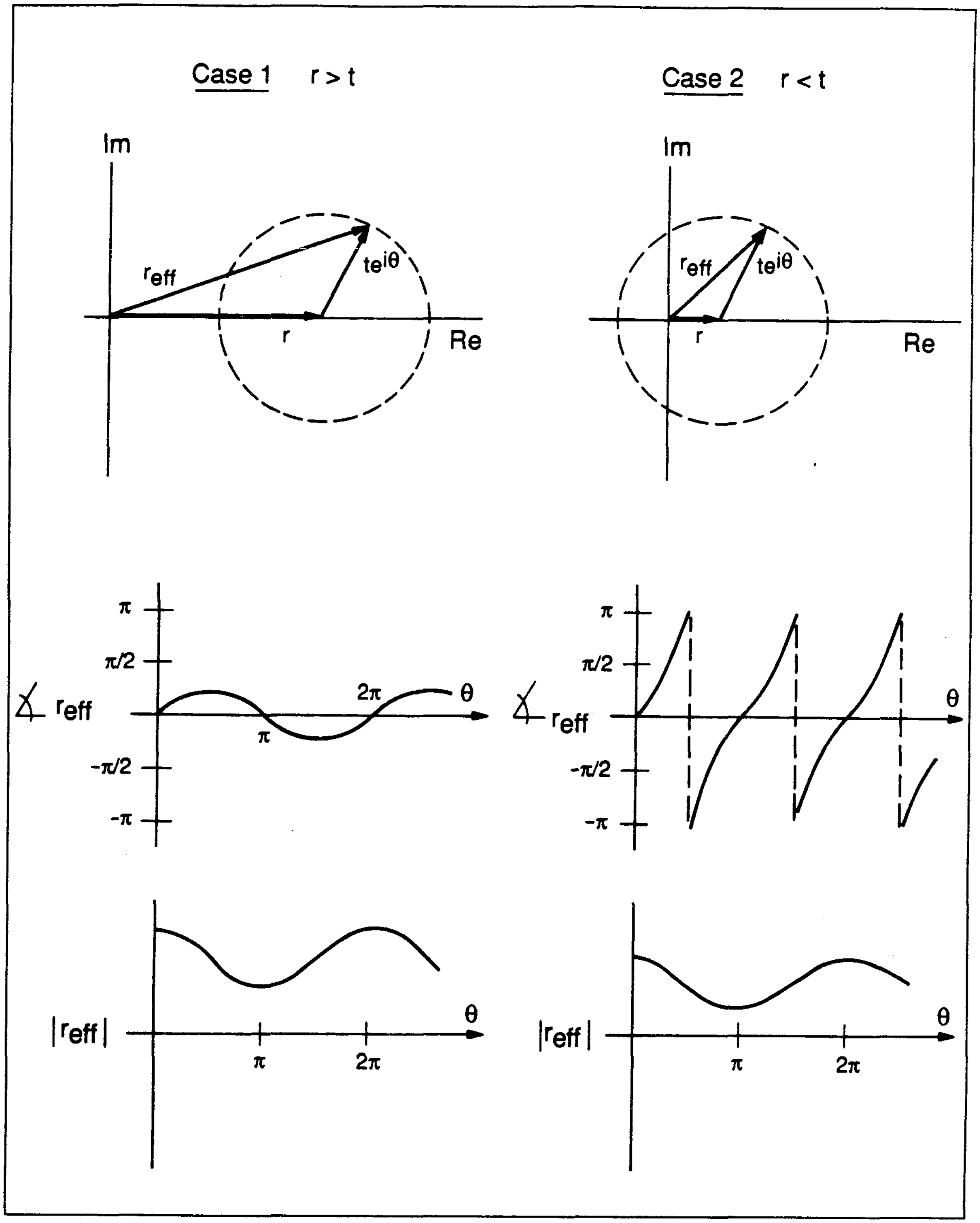

Figure 4.12 *Phasor diagram of* $r_{eff}(\omega)$ *for the two cases of* $r > t$ *(left) and* $r < t$ *(right). The locus of* r_{eff} *corresponding to a* 2π *change of phase* θ *in the external cavity is shown as a dashed line. Below are plotted* $\angle r_{eff}$ *and* $|r_{eff}|$ *as a function of* θ*.*

condition, Equation (4.8a), any detuning in $\varphi(\omega)$ must be *compensated* by an equal but opposite contribution from $r_{eff}(\omega)$ to maintain the same mode index m. As we will show, in the case $r > t$ (weak feedback), only small detunings ($< \pi/2$) from the crystal resonance are allowed. Efforts to tune between contiguous longitudinal modes are greeted with discontinuous jumps, or "mode hops." On the other hand, for $r < t$ (strong feedback), all possible detunings can be compensated in principle. Figure 4.12 plots the locus of $r_{eff}(\omega)$ in the complex plane as the phase of the external cavity is changed (for example, by tuning the frequency), for the two cases $r > t$ and $r < t$. In our experiments, $|rt| << 1$, so we have made the approximation $r_{eff}(\omega) \simeq r + te^{i\theta}$. The resulting phase and amplitude of $r_{eff}(\omega)$ are also plotted as a function of $\theta(\omega)$ for both cases. It is evident that for the case of $r > t$, the phase excursions are *limited* to less than $\pm\pi/2$. For $r < t$, however, the phase excursions of $\angle r_{eff}$ are not limited by $\pm\pi/2$ but rather they *continuously* follow the phase variable $\theta(\omega)$ (although not linearly). Hence, $r < t$ defines a necessary (though not sufficient) condition for the strength of external feedback required to achieve *continuous* tuning between crystal cavity resonances.

Equations (4.8) have been solved under various feedback conditions for tuning within between two longitudinal modes of the crystal cavity. The solution is, in general, a *cluster* of modes, within which modes are roughly spaced by the round-trip frequency through the external cavity, $c/2L_{ex}$. Figure 4.13 shows the gain and frequency of the mode within this cluster *having the minimum threshold gain*, as a function of the tuned frequency. For the case of weak feedback, the cluster is centered near the *crystal* resonance rather than the tuned frequency. As a result, the lasing frequency is not a continuous function of the tuned frequency; it hops from one crystal resonance to the next. The shaded areas represent the gain discrimination between the tuned modes and those without external feedback. In the case of weak feedback, this discrimination is marginal. Thus, the tuned modes are expected to

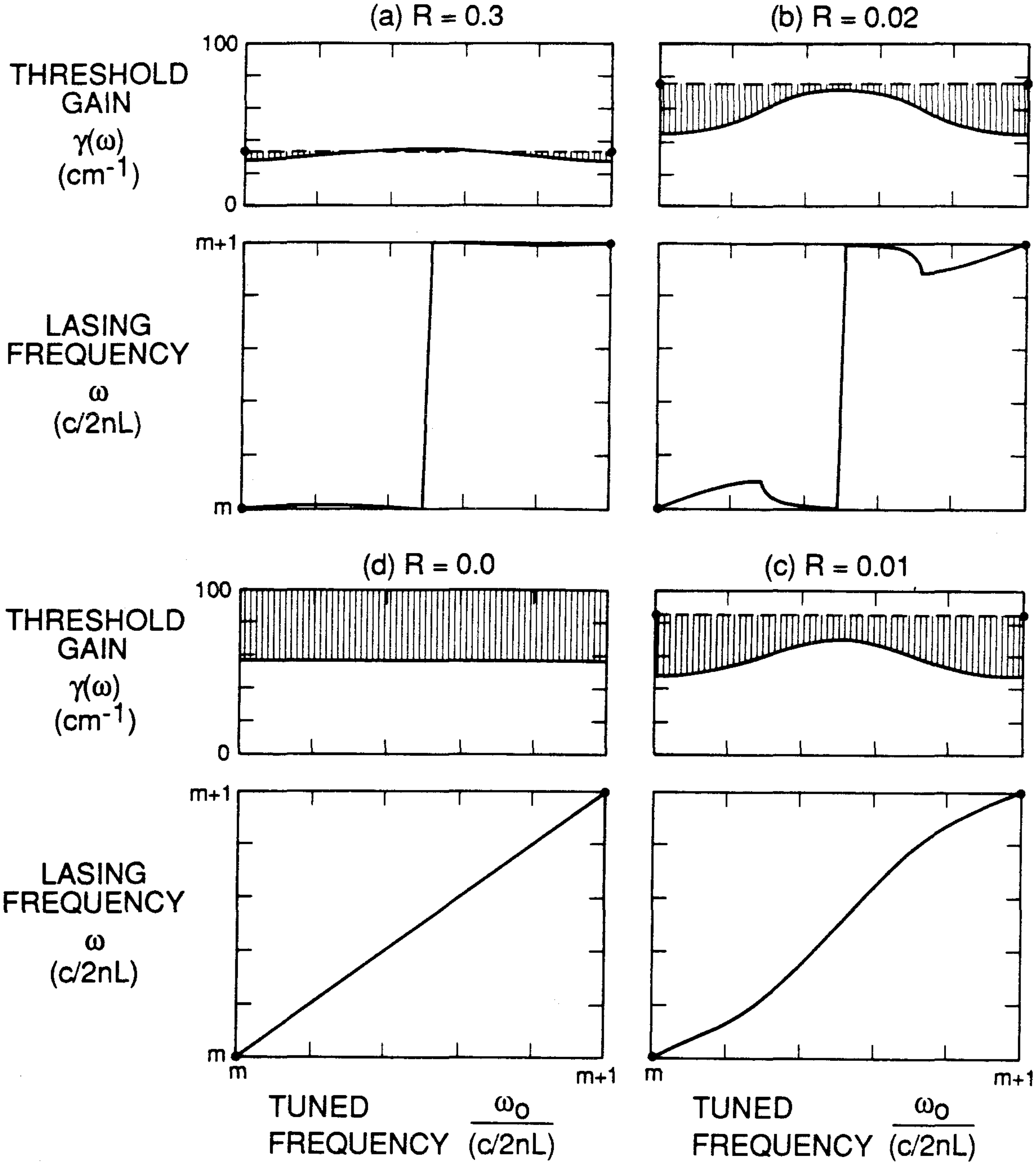

Figure 4.13 *Lasing frequency $\omega/(c/2nL)$ and threshold gain $\gamma(\omega)$ of the composite cavity mode with the minimum threshold gain, shown as a function of the tuned frequency $\omega_0/(c/2nL)$. For weak feedback, (a) and (b), the tuning is discontinuous. For strong feedback, (c) and (d), however, continuous tuning is achieved.*

be very sensitive to fluctuations in geometry, temperature, or current. Figures 4.13 (c) and (d) illustrate the complementary case of strong feedback. In this case, the composite mode of minimum threshold gain is pulled away substantially from the crystal resonance towards the tuned wavelength. The overall tuning characteristics show that, as a result, the lasing frequency follows the tuned frequency continuously between crystal cavity resonances, although not linearly.

It should be noted that in Figure 4.13(c), for example, the lasing frequency hops beween modes of the *composite cavity* as the tuned frequency is varied over a single crystal cavity mode spacing. Since $L_{ex} \gg L$, the steps in the curves are too shallow to be resolved in the figure. True continuous tunability requires an additional degree of freedom with which to vary the optical path length over one mode spacing of the composite cavity. This can be achieved in practice, for example, by insertion of a phase-control electrode in series with the current-pumping electrode of the semiconductor laser. By tuning of the current injected into the phase-control contact, the effective refractive index of the composite cavity can be changed.

4.4 Conclusions

In conclusion, we have demonstrated stepwise tuning of Fabry-Perot single QW semiconductor lasers over ranges approaching those of dye lasers. Tuning in an external grating-tuned cavity over 125 nm under pulsed conditions has been achieved with stripe contact, single QW lasers grown by MBE. The uncoupled resonator loss has been optimized to access a flattened gain spectrum, and a corresponding requirement, Equation (4.1), for broadband tunability was given. Experiments with buried heterostructure lasers indicate that CW tuning ranges in excess of 10% can be achieved at room temperature. With improved contact quality, the CW tuning range is expected to fully duplicate the 15% pulsed characteristic.

In addition, we have proposed a coupled cavity model that identifies $r < t$ as a necessary condition for the strength of external feedback required to achieve *continuous* tunability. This analysis predicts that the composite cavity mode of *minimum threshold gain* can be tuned continuously between crystal cavity resonances. Recently, Petermann has indicated that a stability analysis of the composite-cavity modes predicts that the mode that lases is *not*, in fact, the mode of minimum threshold gain, but that of *minimum linewidth*[9]. This result has yet to be confirmed experimentally.

Finally, it should be noted that none of the results presented in this chapter is exclusive to the (GaAl)As material system, but depend only on the unique properties of quantum wells. It thus appears perfectly feasible that commercial QW semiconductor lasers based on GaInP, GaAlAs, and GaInAsP will provide compact, continuously tunable, solid-state sources of radiation in the wavelength region 650-1500 nm. At moderate output power, and reduced linewidths, these devices could replace dye lasers in many applications.

References

[1] J.E. Epler, N. Holonyak, Jr., R.D. Burnham, C. Lindstrom, W. Streifer, and T.L. Paoli, "Broadband tuning ($\Delta E \simeq 100\ meV$) of $Al_xGa_{1-x}As$ quantum well heterostructure lasers with an external grating," *Appl. Phys. Lett.* **43**, 740-742 (1983).

[2] J.E. Epler, G.S. Jackson, N. Holonyak, Jr., R.L. Thornton, R.D. Burnham, and T.L. Paoli, "Broadband operation of coupled-stripe multiple quantum well AlGaAs laser diodes," *Appl. Phys. Lett.* **47**, 779-780 (1985).

[3] R. Wyatt, K.H. Cameron, and M.R. Matthews, "Tunable narrow line external cavity lasers for coherent optical systems," *Brit. Telecom. Tech. J.* **3**, 5-12 (1985).

[4] W.V. Sorin and S.A. Newton, "Single-frequency output from a broadband-tunable external fiber-cavity laser," *Optics Lett.* **13**, 731-733 (1988).

[5] M. Mittelstein, Y. Arakawa, A. Larsson, and A. Yariv, "Second quantized state lasing of a current pumped single quantum well laser," *Appl. Phys. Lett.* **49**, 1689-1691 (1986).

[6] M. Mittelstein, D. Mehuys, A. Yariv, R. Sarfaty, and J.E. Ungar, "Broadband tunability of gain-flattened quantum well semiconductor lasers with an external grating," paper PD6, *Optcon'88*: OSA Annual Meeting Oct. 31 - Nov. 4, 1988, Santa Clara CA.

[7] P.L. Derry, A. Yariv, K.Y. Lau, N. Bar-Chaim, K. Lee, and J. Rosenberg, "Ultralow threshold GRINSCH-SQW buried heterostructure (GaAl)As lasers with high reflectivity coatings," *Appl. Phys. Lett.* **50**, 1773-1775 (1987).

[8] A. Yariv, *Quantum Electronics*, 3rd ed. (Wiley, New York 1988).

[9] K. Petermann, "External reflection effects in semiconductor diode lasers," paper WG3, *CLEO'89*: Conference on Lasers and Electro-Optics, Apr. 24-28, 1989, Baltimore MD.

CHAPTER

Five

Coupled-Wave Model for Multiple Stripe Semiconductor Lasers

5.0 Introduction

By design, semiconductor laser arrays consist of a number of single-mode waveguides placed in close proximity, so that distributed coupling occurs via modal overlap. The lateral modes of the array are ideally described by superposition of the modes of the uncoupled waveguides, or "supermodes"[1,2]. Indeed, arrays formed from index-guided elements are accurately modeled using supermode (*i.e.,* coupled-mode) theory. However, arrays formed from gain-guided elements, such as oxide-isolated or proton-bombarded stripes, are not. Since the interelement coupling is inherently stronger than for the index-guided case[3,4], the modes of individual gain-guided waveguides do not constitute a good basis from which to construct the lateral modes of the multiple stripe composite waveguide. Numerical modeling predicts mode numbers greater than the number of array elements[5,6], as was shown in Figure 1.7. Furthermore, with the advent of injection-seeding techniques[5] and external grating-tuned cavities[7], the existence of these higher-order modes has been verified experimentally.

Multiple stripe semiconductor lasers are fabricated by placing together a number of parallel electrodes, side by side in the lateral direction. Because of the resulting spatially periodic current injection, the steady-state carrier population within the active region is modulated in the x-direction. Ultimately, the gain and refractive index are also so-modulated according to the results of Section 1.2. In this chapter, we describe an analytical model of multiple-stripe lasers based on laterally counter-propagating plane waves, which are *coupled* by the periodic gain and refractive index variation across the device width. The coupling is similar to that within distributed feedback lasers[8], except that here the feedback takes place in the *lateral* direction, rather than along the laser axis. In addition to describing the low-order modes ($\nu \leq N$), our model correctly predicts the existence of lateral modes of higher order ($\nu > N$) than the number of injection electrodes, N. Furthermore, the higher-order modes predicted for multiple stripe lasers agree well with those found experimentally by injection seeding[5].

Equation (1.9) gave the general form of a traveling-wave solution $\vec{\mathcal{E}}(x,y,z,t)$ within a semiconductor laser resonator. For a symmetric, single-element waveguide, whether index-guided or gain-guided, the lateral mode $E(x)$ assumes the functional form $\cos kx$ (if even in x) or $\sin kx$ (if odd in x). Thus, the traveling-wave solution (1.9) can be written

$$\vec{\mathcal{E}}(x,z,t) = \hat{x}\big(a_0 e^{ikx} + b_0 e^{-ikx}\big) e^{i(\beta z - \omega_0 t)} \ , \tag{5.1}$$

where, for simplicity, the transverse (y-dependent) part of the mode has been omitted. Note that $b_0 = a_0$ for even modes, and $b_0 = -a_0$ for odd modes. Equation (5.1) is, in fact, a plane-wave decomposition $\sum_{-\infty}^{\infty} a_n \exp i(\vec{k}_n \cdot \vec{r} - \omega_0 t)$ of the TE traveling-wave mode. As shown in Figure 5.1, the traveling wave (5.1) is composed of two plane waves, with k-vectors $\pm k_r \hat{x} + \beta_r \hat{z}$, denoted by $\vec{k}_\pm$. Here k_r is the real part of k, and β_r is the real part of β. These two waves propagate at equal but opposite angles $\pm \tan^{-1}(k_r/\beta_r)$ to the z-axis. Incorporating $\vec{k}_\pm$, Equation (5.1) can also be written as

$$\vec{\mathcal{E}}(x,z,t) = \hat{x}\big(a_0 e^{k_i x + \gamma z} \cdot e^{i(\vec{k}_+ \cdot \vec{r} - \omega_0 t)} + b_0 e^{-ik_i x + \gamma z} \cdot e^{i(\vec{k}_- \cdot \vec{r} - \omega_0 t)}\big) \ , \tag{5.2}$$

where $-k_i$ is the imaginary part of k, and $-\gamma$ is the imaginary part of β.

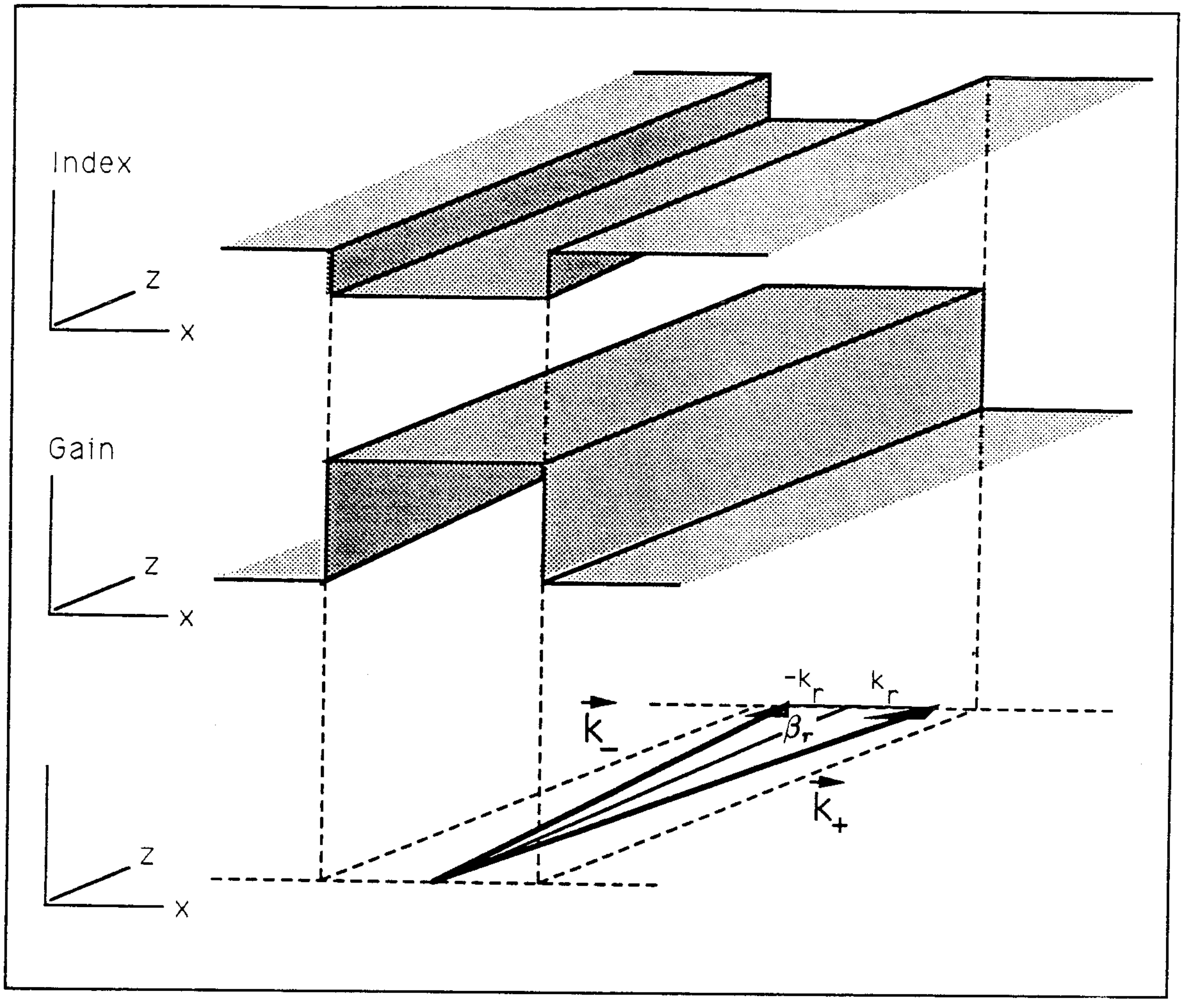

Figure 5.1 *The two constituent plane waves, with wavevectors* $\vec{k}_\pm$, *of the lateral modes of single element symmetric waveguides.*

In a medium with distributed gain or loss, k_i and γ are non-zero. It is common to further factor out the vector, longitudinal, and temporal dependences of (5.2), so as to focus on the x-dependent part, $E(x)$. $E(x)$ satisfies the Helmholtz equation, (1.14); solutions of that eigenvalue equation give rise to the lateral modes $E^\nu(x)$. In that case, $E^\nu(x)$ for our simple waveguide is composed of two *laterally counter-propagating* plane waves:

$$E^\nu(x) = a_0 e^{k_i^\nu x} \cdot e^{ik_r^\nu x} + b_0 e^{-k_i^\nu x} \cdot e^{-ik_r^\nu x} \; . \tag{5.3}$$

Figure 5.2 illustrates the nearfield intensity $|E^{\nu}(x)|^2$, the nearfield phase $\angle E^{\nu}(x)$, and the corresponding plane-wave *amplitudes* $a_0 e^{k_i^{\nu} x}$ and $b_0 e^{-k_i^{\nu} x}$ for the unsaturated $\nu = 10$ lateral modes of 90 μm wide gain and index guides. Observe that for the index guide, $k_i = 0$; consequently the plane-wave amplitudes are constant. However, for the gain guide, $k_i \neq 0$, which gives rise to a slowly varying amplitude variation in the nearfield, and a softening of the phase front, when compared to the index-guided solution. In this chapter, we show that the periodic gain and index modulation induced by the multiple injection stripes *couples* the two plane waves, and modifies their slowly varying amplitudes.

The waveguide prototype for this work is shown in the inset of Figure 5.3: It is a 10-stripe laser with 4.5 μm wide stripes situated on 9 μm centers. As discussed above, the gain and refractive index profiles are modulated in the lateral direction to reflect the spatially periodic current injection. An antiguiding factor of $b = 1.5$ is assumed, along with a loss of 85 cm^{-1} at the sides of the composite waveguide; we estimate these values to be appropriate for low threshold, single quantum well wafers grown by MBE. The interchannel gain of 0 cm^{-1} is intended to model devices with shallow (if any) proton implantation — this model can be inferred from spontaneous emission profiles[7] or from diffraction effects in diode array, traveling-wave amplifiers[9].

Figure 5.3 plots the eigenvalues (mode index and modal gain) for the first 14 modes of this waveguide, as obtained by direct numerical integration of the wave equation. While the $\nu = 10$ mode has the highest modal gain, the next highest modal gains belong to the $\nu = 11$ and 12 modes. This shows the inadequacy of coupled-mode theory when applied to gain-guided devices, since modes with $\nu > 10$ are not predicted by that model.

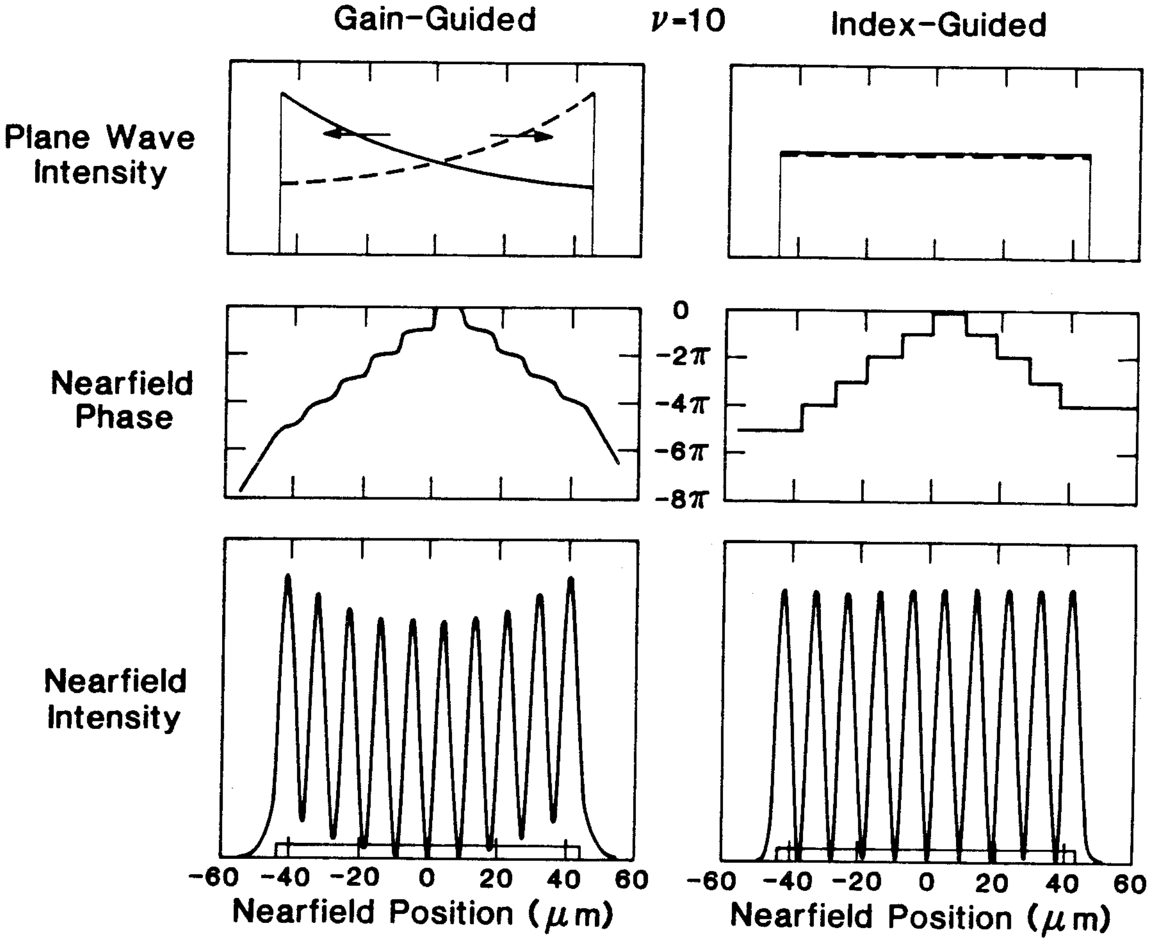

Figure 5.2 *Nearfield intensity, nearfield phase, and composite plane wave amplitudes for the* $\nu = 10$ *lateral modes of 90 μm-wide gain (left) and index (right) guides.*

5.1 Coupled-Wave Theory

To model the multiple-stripe laser, we take an *effective* index distribution

$$n_{eff}^2(x) = \begin{cases} n_0^2 + 2n_1^2 \cos(2\pi \cdot 2x/\Lambda), & |x| < x_0 \\ \overline{n}_0^2, & |x| \geq x_0 \end{cases} \tag{5.4}$$

so that $\Lambda/2$ is the period of the perturbation (*i.e.*, the center-to-center spacing of the electrodes), $2n_1^2$ is its amplitude, and $\overline{n}_0$ is the index of refraction outside

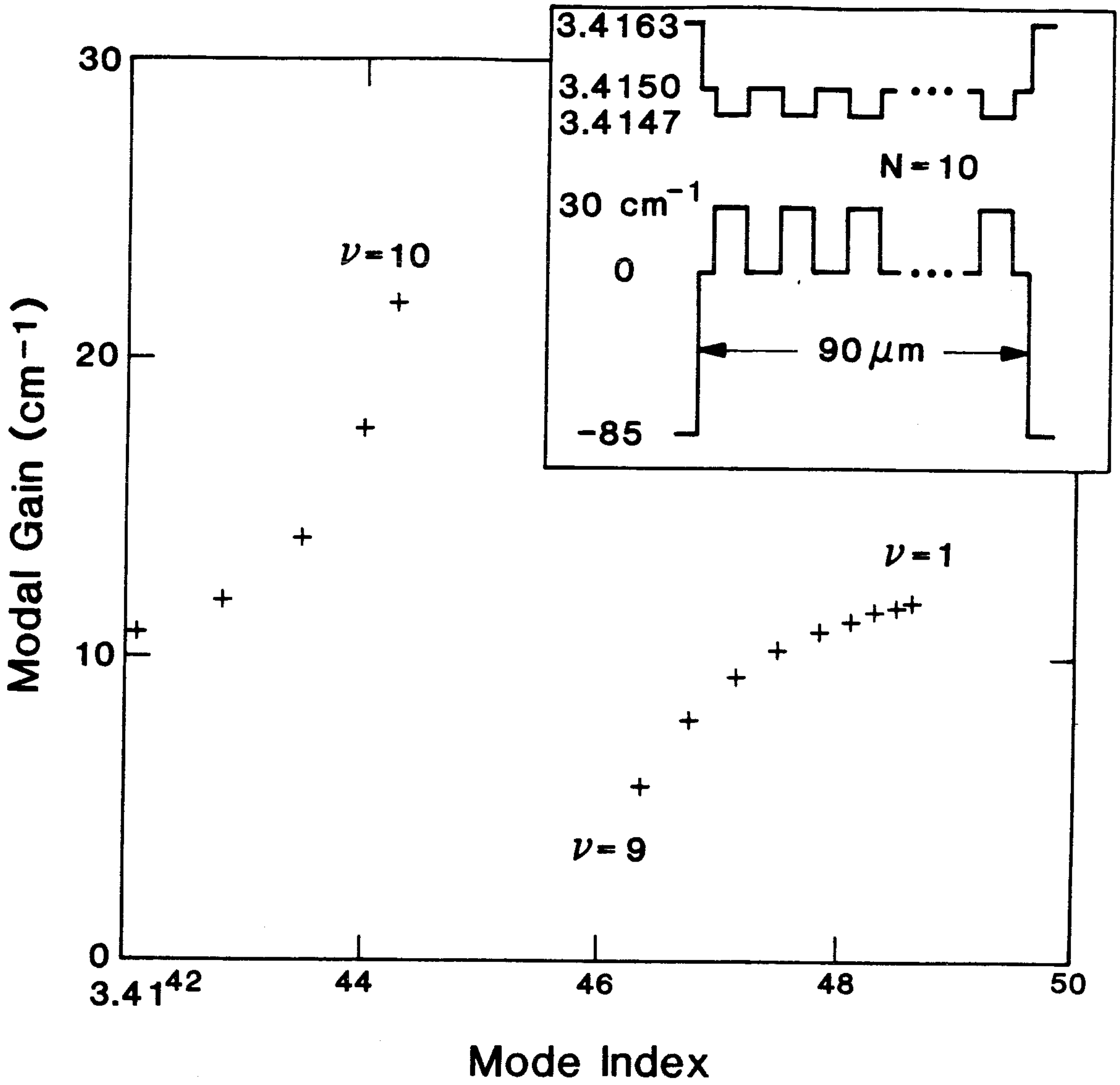

Figure 5.3 *Plot of the lowest 14 eigenvalues (mode index and modal gain) found by numerical integration for the waveguide shown in the inset.*

the laser. With these assumptions, the Helmholtz equation, (1.14), for the lateral modes can be rendered dimensionless and written as

$$\frac{d^2E}{dX^2} + [\Delta + \kappa(e^{i2X} + e^{-i2X})]E = 0, \tag{5.5}$$

where $X = 2\pi x/\Lambda$ is the normalized lateral dimension. As is customary, we have assumed traveling waves of the form $E(x)\exp(ik_0\eta z)$, where $k_0 = 2\pi/\lambda_0$ is the free-space propagation constant, and $k_0\eta$ is the (unknown) propagation constant of the lateral mode $E(x)$. Respectively, Δ and κ are the normalized eigenvalue detuning and effective index perturbation:

$$\Delta = \frac{\Lambda^2}{\lambda_0^2}(n_0^2 - \eta^2) \quad , \quad \kappa = \frac{\Lambda^2}{\lambda_0^2} n_1^2 \ . \tag{5.6}$$

In analogy to the distributed feedback laser, we expect the plane wave coupling to be *distributed* along the laser width, and become manifest as X-dependent coefficients in the plane-wave expansion. We thus take $E(X)$ as the following sum of two laterally counter-propagating waves:

$$E(X) = a(X)\, e^{iX} + b(X)\, e^{-iX}. \tag{5.7}$$

When a and b are constant, the wavevector of E satisfies the Bragg condition; since this does not correspond to wave propagation, we must allow $a(X)$ and $b(X)$ to be slowly varying in X, and thereby incorporate the necessary wavevector detuning from π/Λ. When $\kappa = 0$, a and b are simple exponentials (*viz:* $a_0 e^{ik_i x}, b_0 e^{-ik_i x}$ in (5.3)) and reflect the constant gain under the stripe. When $\kappa \neq 0$, the spatially modulated carrier distribution acts as a *grating* to couple the counter-running waves, and a and b are X-dependent. Substituting (5.7) into (5.5), making the usual slowly varying (adiabatic) approximation (neglecting a'', b''), keeping only the synchronous terms, and setting the slowly varying coefficients of e^{iX} and e^{-iX} equal to zero[8] give the following coupled-mode equations in a and b:

$$\begin{aligned} 2ia' &= (1-\Delta)a - \kappa b \ , \\ -2ib' &= -\kappa a + (1-\Delta)b \ . \end{aligned} \tag{5.8}$$

All of $a(X)$, $b(X)$, and Δ are unknown in Equation (5.8). This is a standard eigenvalue problem, whose general solution is

$$\begin{aligned} a(X) &= A_+ e^{i\Gamma X} + A_- e^{-i\Gamma X} \ , \\ b(X) &= B_+ e^{i\Gamma X} + B_- e^{-i\Gamma X} \ , \end{aligned} \tag{5.9}$$

where $A_\pm$ and $B_\pm$ are complex constants and $\Gamma = \Gamma(\Delta)$ is a normalized wavevector, given by:

$$\Gamma(\Delta) = \frac{1}{2}\sqrt{(1-\Delta)^2 - \kappa^2}. \tag{5.10}$$

From (5.7), we infer that Γ gives the wavevector detuning from the Bragg wavevector. Strict observation of the slowly varying approximation requires $|\Gamma| \ll 1$ in the solution; however, we shall see that reasonable results are obtained even as $|\Gamma| \to 1$. Finally, substituting (5.9) into (5.7) gives the general expression for the lateral mode as

$$E(X) = \left[r_+ e^{i(1+\Gamma)X} + e^{-i(1-\Gamma)X}\right] + r_- \frac{B_-}{B_+}\left[e^{i(1-\Gamma)X} + r_+ e^{-i(1+\Gamma)X}\right], \tag{5.11}$$

where $r_\pm$ are the eigenvectors of the system (5.8):

$$r_\pm \equiv \frac{A_\pm}{B_\pm} = \frac{\kappa}{(1-\Delta) \pm 2\Gamma(\Delta)}. \tag{5.12}$$

At this point there are two unknown, complex constants, B_-/B_+ and the normalized modal propagation constant Δ (or equivalently, the wavevector $\Gamma(\Delta)$). Matching our solution (5.8) for $E(X)$ inside the laser to exponentially decaying solutions of the form $E_1 \ \exp\{-i\sqrt{\Delta - \Delta_0} \ |X\text{-}X_0|\}$ outside, where the index is assumed constant, gives the following two boundary conditions:

$$\left.\frac{E'}{E}\right|_{X=\pm X_0} = \pm i\sqrt{\Delta - \Delta_0} \ , \tag{5.13}$$

where Δ_0 is the complex constant defined by

$$\Delta_0 \equiv \frac{\Lambda^2}{\lambda_0^2}(n_0^2 - \bar{n}_0^2). \tag{5.14}$$

Equation (5.13) represents two equations for the two unknowns B_-/B_+ and $\Gamma(\Delta)$. Symmetry requires $E(-X) = \pm E(X)$, and thus from (5.11), we obtain $B_-/B_+ = \pm r_+$, corresponding to even and odd modes, respectively. Since, from (5.12), $r_+ r_- = 1$, (5.11) reduces to

$$\begin{aligned} E_{even}(X) &= \cos(1-\Gamma)X + r_+ \cos(1+\Gamma)X \ , \\ E_{odd}(X) &= \sin(1-\Gamma)X - r_+ \sin(1+\Gamma)X \ . \end{aligned} \tag{5.15}$$

As $\kappa \to 0$, $r_+ \to 0$ and we recover the modes of the box waveguide. Thus, the second term embodies the distributed feedback, and $\Gamma(\Delta)$ gives the modal detuning from the Bragg wavevector.

To illustrate the result of the coupled-wave approach, we compare the modes (5.15) to those obtained by direct numerical integration of the wave equation. The appropriate parameters to model the device of Figure 5.3 are $\kappa = 0.3 + i\ 0.2$ and $\Delta_0 = -4.0 - i\ 2.67$. We have superimposed the analytical results (dashed lines) for selected lateral modes $E^{\nu}(X)$ onto the numerical solutions (solid lines) in Figures 5.4 and 5.5. Excellent agreement is observed for the $\nu = 8, 9, 10$ and 11 modes, for which $|\Gamma| \ll 1$. However, even as $|\Gamma| \to 1$, the agreement is still reasonable, as illustrated by the $\nu = 1$ mode.

As expected, there is a resonance between the $\nu = 9$ and $\nu = 10$ modes because their lateral wavevectors bracket the Bragg wavevector, π/Λ. The peaks of the nearfield lie almost exactly *under* the stripes for the $\nu = 10$ mode, while for the $\nu = 9$ mode they lie *between* the stripes. Thus, the greatest gain discrimination is achieved between these two modes; this splitting (in the domain of complex-valued refractive index) is exactly analogous to electron wave propagation in crystals near the Brillouin zone edge, where a potential energy splitting of twice the potential amplitude is achieved. Both modes have a "half-cosine"or first-order envelope, however, being nearly symmetrically displaced from the Bragg wavevector[8]. Likewise, we expect the $\nu = 8$ and 11 modes to share second-order envelopes, since together

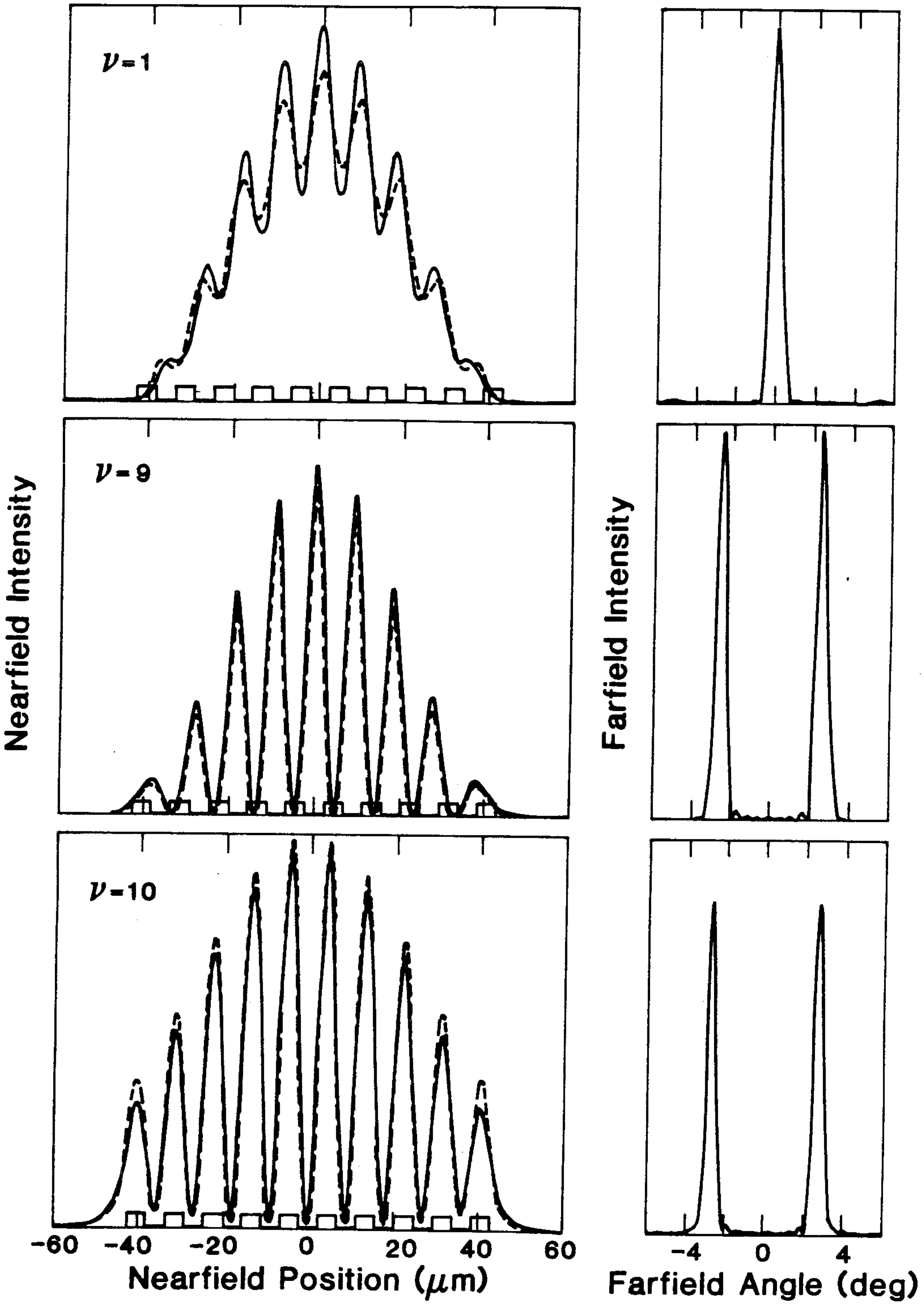

Figure 5.4 *Nearfield and farfield intensities for the* $\nu = 1, 9$ *and 10 lateral modes found by numerical solution (solid lines) compared to the analytical solution (dashed lines). The injection electrodes are positioned as indicated in the nearfield plots.*

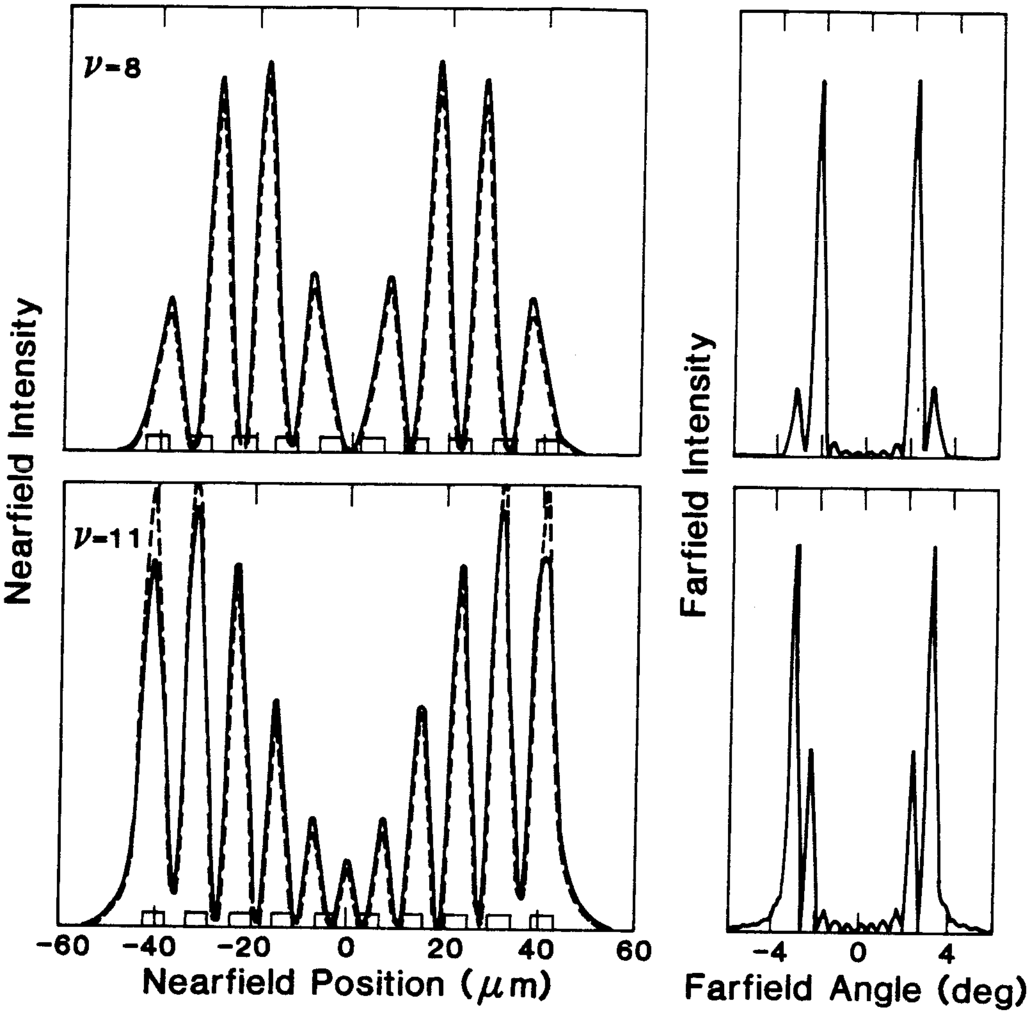

Figure 5.5 *Nearfield and farfield intensities for the ν = 8 and 11 lateral modes found by numerical solution (solid lines) compared to the analytical solution (dashed lines). The injection electrodes are positioned as indicated in the nearfield plots.*

they undergo a gain splitting similar to the $\nu = 9$ and 10 modes. Figure 5.5 illustrates that this is indeed the case. Further, the $\nu = 1$ mode has 9 secondary peaks in the nearfield (*not* 10, as would be expected from coupled-mode theory) because it is displaced 9 modes from the Bragg wavevector.

At this point, we should remark that the general solution of the wave equation (5.5) in a periodic medium (*i.e.*, taking $n_{eff}^2(x)$ as a general Fourier series) is a Bloch function, of the form

$$E_K(X) = u_K(X)e^{iKX} \ , \tag{5.16}$$

where K is the lateral wavevector, and $u_K(X)$ is a function having the same periodicity as the medium. Expanding $u_K(X)$ into a Fourier series, and writing separately solutions even and odd in X, give

$$\begin{aligned} E_{even}(X) &= \sum_{-\infty}^{\infty} a_n \cos(K+2n)X \ , \\ E_{odd}(X) &= \sum_{-\infty}^{\infty} b_n \sin(K+2n)X \ . \end{aligned} \tag{5.17}$$

These solutions, with particular values of the a_n and b_n, are known as Mathieu functions[10]. The approximation of our solution (5.15) to the exact solution (5.17) becomes apparent if we rewrite the former, letting $1 - \Gamma = K$, as

$$\begin{aligned} E_{even}(X) &= \cos KX + r_+ \cos(K-2)X \ , \\ E_{odd}(X) &= \sin KX + r_+ \sin(K-2)X \ . \end{aligned} \tag{5.18}$$

That is, to arrive at (5.15), we have taken advantage of the fact that near the Bragg resonance, $K \simeq 1$, and hence only two terms of the series (5.17) are of significant amplitude and synchronicity. This is *strictly* valid only for the $\nu = 9$ and $\nu = 10$ lateral modes, above. For the $\nu = 1$ mode, $K \simeq 0$. The discrepancy between the dashed and solid lines of Figure 5.4 ($\nu = 1$ mode) could be largely removed by including the $(K+2)$ term of the summation (5.17) into our solution (5.18). Including both $(K \pm 2)$ terms is akin to considering both the ±1 "diffraction orders" of grating reflection. It can be appreciated from (5.5), however, that the term $(n_{eff}^2 - n_0^2) \cdot E$ generates all "diffraction orders," and hence the general solution for $E(X)$ is of the form (5.17). The accuracy of the approximate solution (5.18) thus depends upon the number of terms of the summation (5.17) included in it.

To summarize, our analytical coupled-wave model accounts for the lateral modes both observed in, and calculated numerically for, N-stripe semiconductor injection lasers. By making an analytical expansion around the Bragg wavevector, we are able to describe lateral modes of order $\nu = 1$ to $\nu = 2N - 1$. Modes of higher order could be accounted for (if they exist), by including more terms in the summation (5.17), or by expansion around integer multiples of the Bragg wavevector. In any case, our analysis reveals the lateral modes of multiple-stripe semiconductor lasers to be determined largely by distributed feedback resonances of the carrier-induced lateral gain and index perturbation, rather than by superposition of the modes of individual stripe lasers.

5.2 Broad Area Tandem Semiconductor Lasers

Recently, broad area lasers fabricated from low threshold density, quantum well material were identified as candidates for stable, single-lobed farfield operation at high power[11,12]. This success has been attributed partly to the excellent uniformity afforded by state-of-theart crystal growth technology, and partly because the self-focusing nonlinearity that is due to gain saturation decreases in proportion to the threshold gain. Both allow nonlinear modes of phase-locked filaments to maintain spatial coherence over wide apertures at elevated power levels (see Chapter Two). However, the tolerances required of the material growth, and of the processing consistency, to achieve a satisfactorily high level of uniformity are extremely small. As a result, only a small fraction of devices exhibit this desirable behavior. In order to enhance the stability of the nonlinear modes against destabilizing material defects, fabrication inhomogeneities, or temperature gradients, additional steps must

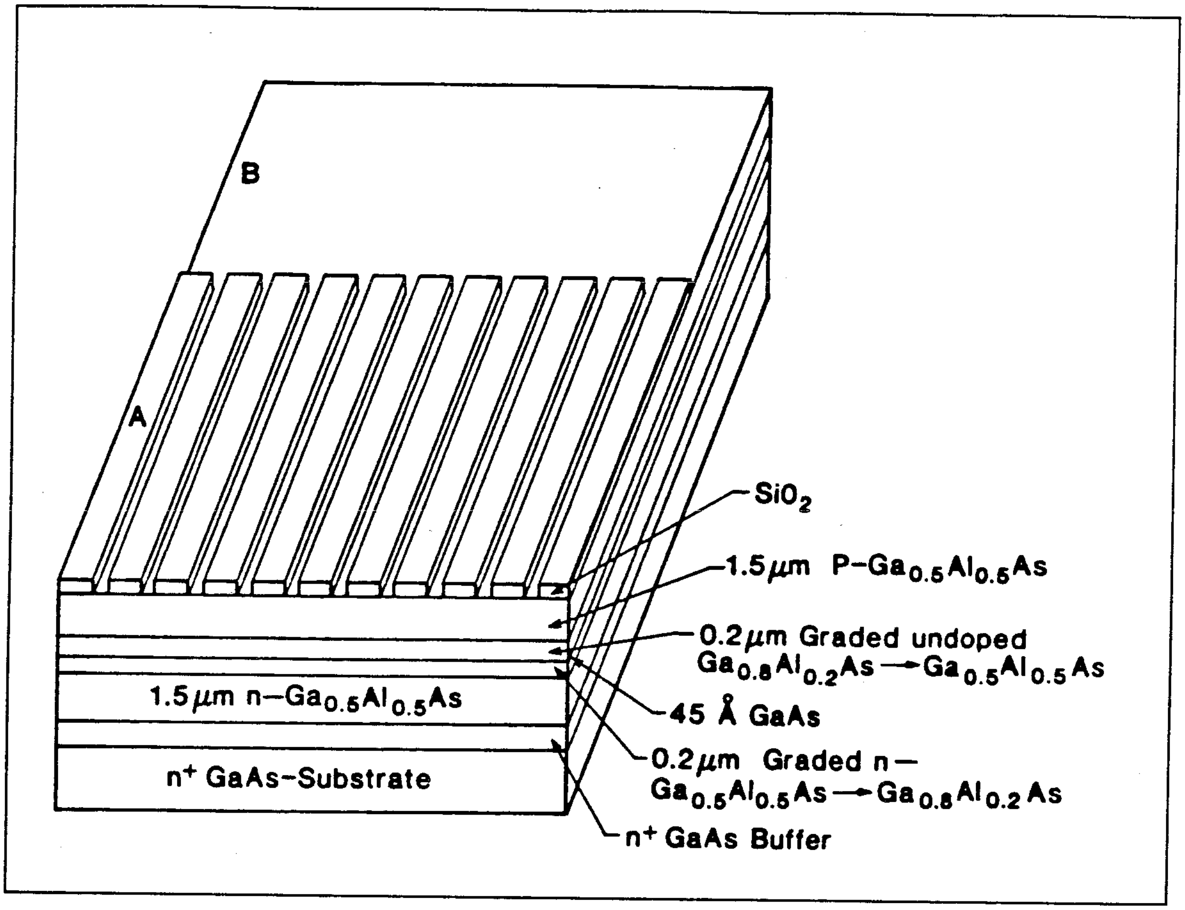

Figure 5.6 *Broad area tandem laser structure. The rear section (B) is a broad area contact 60 μm wide, while in the forward section (A), current is injected through 10 stripes 2 μm wide on 6 μm centers.*

be taken. In this section, we report experimental findings on a broad area laser structured to provide such enhanced stability.

Our approach to the problem of controlling the mode of oscillation of a wide-area semiconductor laser is to "seed" the mode at threshold which we expect to be favored under high-power operation, when gain saturation plays a dominant role. As shown in Figure 5.6, the proposed laser consists of two longitudinal sections in tandem. The rear section (B) is a simple gain-guide, broad area structure 60 μm wide. Ideally, this structure is expected to support lateral modes above threshold consisting of an integer number of phase-locked "filaments"[13,14]. However, the gain discrimination between such modes is small and easily disrupted by material imperfections; hence complicated, non-reproducible mode patterns usually result. In the forward section (A), current is injected through 10 closely spaced, parallel stripes opened in an oxide isolation layer. Allowing for current spreading, this results in a slight *lateral gain modulation* (LGM) within the active layer. The modes of such a multiple stripe structure were calculated in Section 5.1. The present work was motivated by the resemblance of the fundamental ($\nu = 1$) LGM mode, shown in Figure 5.4, to the gain-saturated, broad area modes of Chapter Two. For example, the *peaks* in the nearfield intensity of the fundamental LGM mode correspond to *valleys* in the spatial gain profile, being situated as they are between the current injection stripes. In addition, the wavefront of the LGM mode is modulated in the same fashion as that of the nonlinear broad area mode, which gives rise to a narrow, single-lobed farfield. If, therefore, the period of the LGM is chosen to *match* the saturated filament spacing[13], Δx_{sat}, of the nonlinear broad area mode, we expect the seeded fundamental LGM mode to *remain* favored at high pump levels.

To identify important design parameters other than the LGM period, we consider a simple linear model to determine the spatial mode with the highest modal gain near threshold. Figure 5.7 shows the intensity profiles of the *unsaturated* $\nu = 1$ and $\nu = 10$ modes of both the LGM and broad area sections (see inserts) and their mode intensity gains per pass. Since the LGM is slight, it acts as a perturbation to the gain; thus the LGM section supports approximately as many modes as the uniform gain section ($\simeq 50$). In the LGM section, the $\nu = 10$ mode has the highest modal gain because its lateral wavevector closely matches the wavevector of the complex-valued refractive index grating induced by the LGM[15,16]. Unfortunately, as with a gain-guided laser array, this mode is not the fundamental mode, and its associated farfield is twin-lobed. The modal gain coefficient of the fundamental

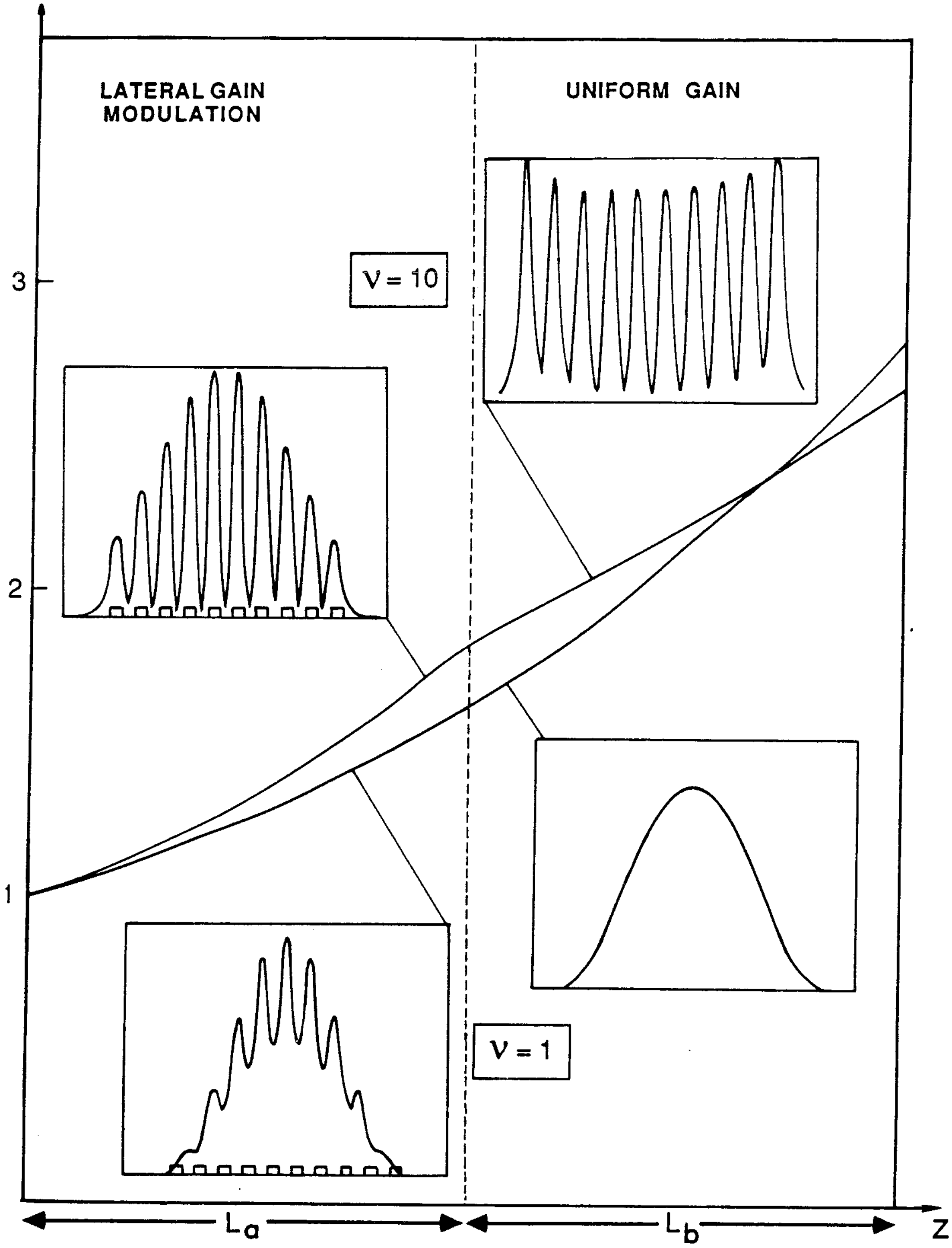

Figure 5.7 *Intensity gain per pass of the unsaturated $\nu = 1$ and $\nu = 10$ lateral modes of the LGM and broad area sections. The lateral mode intensity profiles are shown in the insets. Coupling to other modes is small, and for simplicity we neglect it.*

mode ($\nu = 1$) is reduced by an amount $\Delta\gamma_b$ from that of the $\nu = 10$ mode. In the broad area section, the situation is reversed. The unsaturated $\nu = 1$ mode is best confined to the gain region and consequently its losses into the unpumped cladding regions are lowest. Here, the $\nu = 10$ mode has a lower gain coefficient by $\Delta\gamma_a$. Numerical simulation shows that the $\nu = 1$ modes couple primarily to each other, as do the $\nu = 10$ modes. Since these two *composite* modes have the highest modal gains, all others are neglected. As Figure 5.7 indicates, the gain per pass of the $\nu = 1$ composite mode is higher than that of the $\nu = 10$ composite mode *when* the length, L_b, of the broad area section satisfies

$$L_b > \frac{\Delta\gamma_a}{\Delta\gamma_b} L_a \ , \tag{5.19}$$

where L_a is the length of the LGM section. Thus, it is the *ratio* of lengths of broad area to LGM sections which is the important design parameter. Gain discrimination is achieved simply by varying the distributed modal losses within the two longitudinal sections. Of course, the analysis leading up to (5.19) is valid only near threshold; a complete model must take into account spatially nonuniform gain saturation. Note again, however, that in the LGM section the local intensity peaks of the fundamental mode lie *between* the local gain maxima of the LGM. This is in contrast to the fundamental array supermode[1], but is exactly the requirement for a self-consistent, gain-saturated broad area mode[13,14]. Hence, by proper choice of the LGM period, we expect the seeded mode to be stable at high power.

Broad area tandem lasers were fabricated from standard, low threshold current density GaAs/GaAlAs GRINSCH-SQW crystals grown by MBE (see Figure 5.6). After depositing SiO_2 over the wafer, the broad area and stripe contacts were opened by standard photolithography. For the LGM section, 2 μm openings on 6 μm centers were chosen. A shallow Zn diffusion was performed to provide ohmic contact to the p-type upper cladding layer. Cr/Au and AuGe/Ni/Au were evaporated for p-

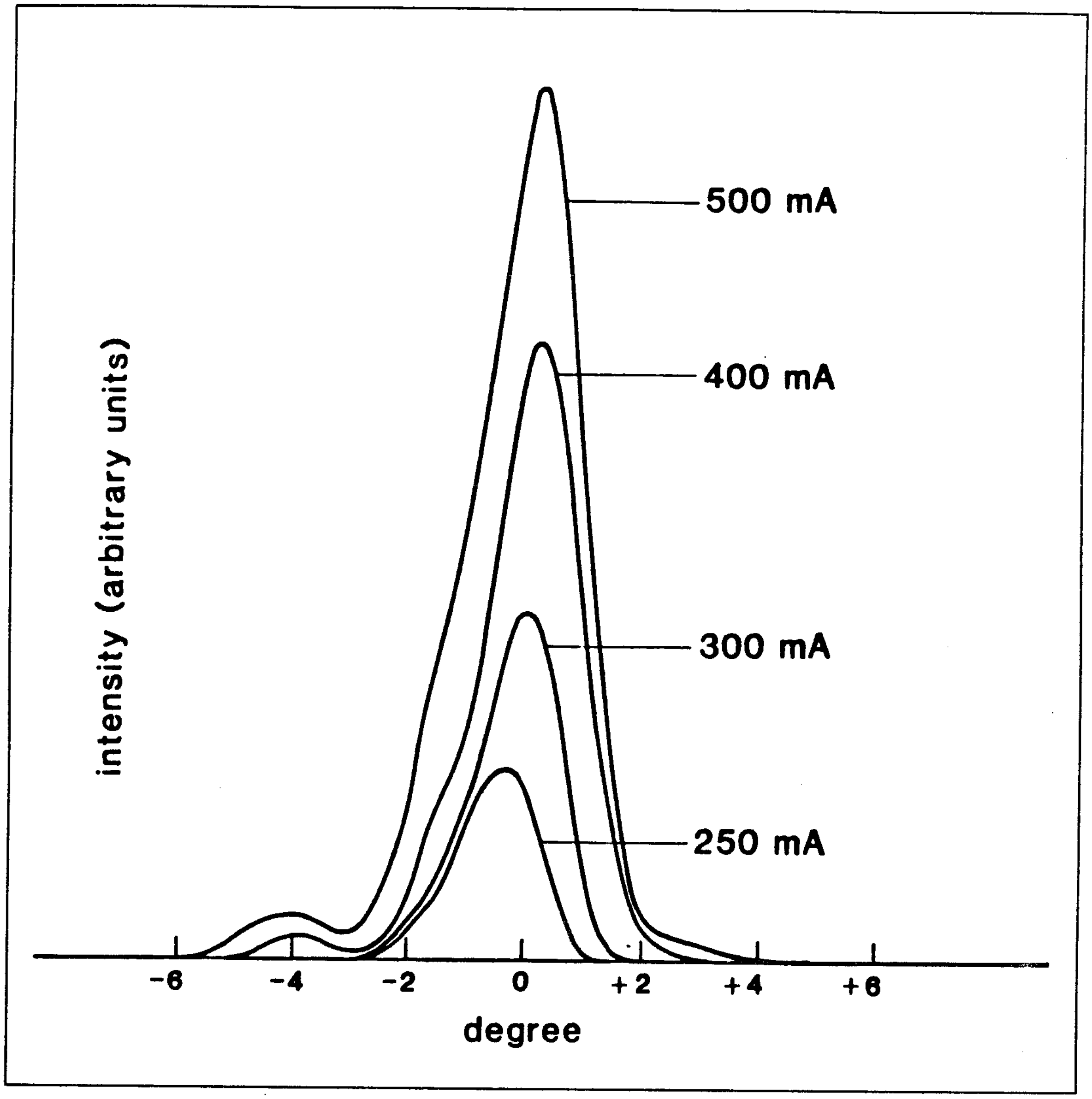

Figure 5.8 *Farfield pattern of the tandem laser at various current levels above threshold (I_{th} =180 mA).*

and n-type contacts, respectively. The wafer was then cleaved into bars, each one consisting of an LGM section and a uniform gain section. The lasers were tested under pulsed, low duty-cycle conditions to minimize thermal effects.

As expected, lasers having only an LGM section most often yielded a twin-lobed farfield. Similarly, devices with only uniform gain sections did not reliably produce a single-lobed output beam. On the other hand, tandem devices emitted into stable, single-lobed radiation patterns, *provided* the broad area section was long enough. For example, lasers with 200 μm-long LGM sections and 140 μm-long broad area sections operated stably in a single-lobed mode. A typical farfield pattern is shown in Figure 5.8. The narrowest beam measured, at 1.1° near threshold, was only 1.4× the diffraction limit for a 60μm aperture. The single-lobed radiation pattern was maintained up to $I = 1.5\ A$, which is $\simeq 8\ I_{th}$ ($I_{th} = 180$ mA). At an external differential quantum efficiency approaching 42% (0.6 mW/mA) *per facet*, this current level translates into output powers exceeding 750 mW.

To summarize, we have introduced a lateral gain modulation section in tandem longitudinally with a uniform gain section in order to seed the in-phase, lateral broad area mode which we expect to be favored at high pump levels. We have also identified the important design parameters as being the ratio of lengths of the LGM and broad area sections, and the LGM period. This new structure has been tested on GRINSCH-SQW lasers and has provided stable, single-lobed farfields 1.4× the diffraction limit when the broad area section was sufficiently long.

5.3 Conclusions

In this chapter, we have introduced a new technique for the analysis of multiple stripe semiconductor lasers, and applied it to the design of a high-power, structured broad area laser. This technique, coupled-wave analysis, is predicated on the strong interelement coupling between adjacent gain-induced waveguides. Unlike index guides, only a small amount of guiding is provided by the discontinuity in refractive index between the core and cladding regions of gain guides. Rather, photons ore *generated* in the core regions and *escape* to the cladding regions. Thus, in multiple stripe, gain-guided lasers, a significant amount of light is coupled between adjacent waveguides. Since reflections from the refractive index discontinuities are small, we have employed a model that embodies the *distributed* nature of the reflections from *many waveguides*, thereby providing lateral coupling between the counter-propagating plane waves.

The coupling between gain-induced waveguides is in contrast to that employed by adjacent index-guided waveguides. There, light within each element is guided by total internal reflection at the refractive index discontinuities between core and cladding regions. Coupling between adjacent elements is accomplished via a slow power leakage through the evanescent fields, in analogy to electron tunneling between adjacent quantum wells. The theory that describes coupled index-guided elements, coupled-*mode* theory, is the *dual* of that which we have employed to describe coupled gain-guided elements, coupled-*wave* theory.

In practice, gain-guided elements are far easier to fabricate than index-guided elements, because the current injection path defines the waveguide geometry. However, because then the waveguide profile is entirely dependent upon the steady-state carrier distribution, it changes in proportion to the intensity of stimulated emission. Consequently, the lateral modes of such lasers are, in general, intensity-dependent. Thus, our approach in the design of the broad area tandem laser was to seed the mode at threshold that we expect to be self-consistent with a heavily saturated gain profile. Unfortunately, the broad farfields measured (a few times the diffraction limit) indicate that the discrimination between different lateral modes is not yet great enough to ensure single-mode operation.

In the next chapter, we design and fabricate a device of similar geometry, the diffraction-coupled array. In contrast to the tandem laser, this device is based on index-guiding. Since the waveguide profiles of index guides are designed to be minimally dependent upon the carrier population, we expect stable performance at high powers, *provided* adequate mode discrimination can be provided.

References

[1] E. Kapon, J. Katz, and A. Yariv, "Supermode analysis of phase-locked arrays of semiconductor lasers," *Opt. Lett.*, vol. 10, no. 4, pp125-127 (1984).

[2] J.K. Butler, D.E. Ackley, and D. Botez, "Coupled-mode analysis of phase-locked injection laser arrays," *Appl. Phys. Lett.*, **44**, 293-295 (1984).

[3] E. Kapon, C. Lindsey, J. Katz, S. Margalit, and A. Yariv, "Coupling mechanism of gain-guided integrated semiconductor laser arrays," *Appl. Phys. Lett.*, **44**, 389-391 (1984).

[4] J.P. Hohimer, G.R. Hadley, and A. Owyoung, "Interelement coupling in gain-guided diode laser arrays," *Appl. Phys. Lett.* **48**, 1504-1506 (1986).

[5] G.R. Hadley, J.P. Hohimer, and A. Owyoung, "High-order ($\nu > 10$) eigenmodes in ten-stripe gain-guided diode laser arrays," *Appl. Phys. Lett.* **49**, 684-686 (1986).

[6] W.K. Marshall and J. Katz, "Direct analysis of gain-guided phase-locked semiconductor laser arrays," *IEEE Journal of Quantum Electronics* **22**, 827-832 (1986).

[7] J.E. Epler, N. Holonyak, R.D. Burnham, T.L. Paoli, R.L. Thornton, and M.M. Blourke, "Transverse modes of gain-guided coupled-stripe lasers: external cavity control of the emitter spacing," *Appl. Phys. Lett.* **47**, 7-9 (1985).

[8] H. Kogelnik and C.V. Shank, "Coupled-wave theory of distributed feedback lasers," *J. Appl. Phys.* vol. 43, no. 5, 2327-2335 (1972).

[9] J.R. Andrews, T.L. Paoli and R.D. Burnham, "Diffraction effects in a diode array traveling wave amplifier," *Appl. Phys. Lett.* **51**, 1676-1678 (1987).

[10] M. Abramowitz and I. Stegun, eds., *Handbook of Mathematical Functions*, Dover Publications (New York, 1972).

[11] W.T. Tsang, "Extremely low threshold (AlGa)As graded-index waveguide separate confinement heterostructure lasers grown by molecular beam epitaxy," *Appl. Phys. Lett.* **40**, 217-219 (1982).

[12] A. Larsson, M. Mittelstein, Y. Arakawa, and A. Yariv, "High efficiency broad area single quantum well lasers with narrow single-lobed farfield patterns prepared by molecular beam epitaxy," *Electron. Lett.* **22**, 79-81 (1986).

[13] D. Mehuys, R. Lang, M. Mittelstein, J. Salzman, and A. Yariv, "Self-stabilized nonlinear lateral modes of broad area lasers," *IEEE J. Quant. Electron.* **QE-23**, 1909-1920 (1987).

[14] J. Salzman, A. Larsson, and A. Yariv, " Phase-locked controlled filament laser," *Appl. Phys. Lett.* **49**, 611-613 (1986).

CHAPTER

Six

Supermode Control in Diffraction-Coupled Laser Arrays

6.0 Introduction

High-power operation of wide-area (GaAl)As lasers into a stable, diffraction-limited output beam remains elusive despite an intensive research effort over the past 15 years. The uncontrolled filamentation inherent in the double heterostructure, broad area lasers of the 1970's led to the development of the laser array structure[1-3] in the early 1980's. Conventional semiconductor laser arrays are formed by placing many single-mode waveguides in close proximity, so that the dominant coupling mechanism is evanescent overlap. Successful coupling has been achieved up to modest power levels ($\simeq 100\ mW$), but the farfield beamwidth has invariably broadened at higher output powers. This is symptomatic of incomplete spatial coherence and/or multi-lateral mode operation. Furthermore, in practice the eigenmode with the highest modal gain in these "distributed-coupling" arrays is not the fundamental supermode, but that which has adjacent array elements coupled π radians out-of-phase. The result is an undesirable double-lobed farfield.

Diffraction-coupled arrays represent one approach towards achieving fundamental supermode operation, and consequently have received growing attention[4-7]. In this geometry, illustrated in Figure 6.1(a), the channels of the array are *optically isolated* for some length L, and then are allowed to couple by "diffraction" of the channel waveguide modes in a common end region of length D. Thus, the coupling is *discrete*, rather than *distributed* along the length of the array. Nevertheless, the

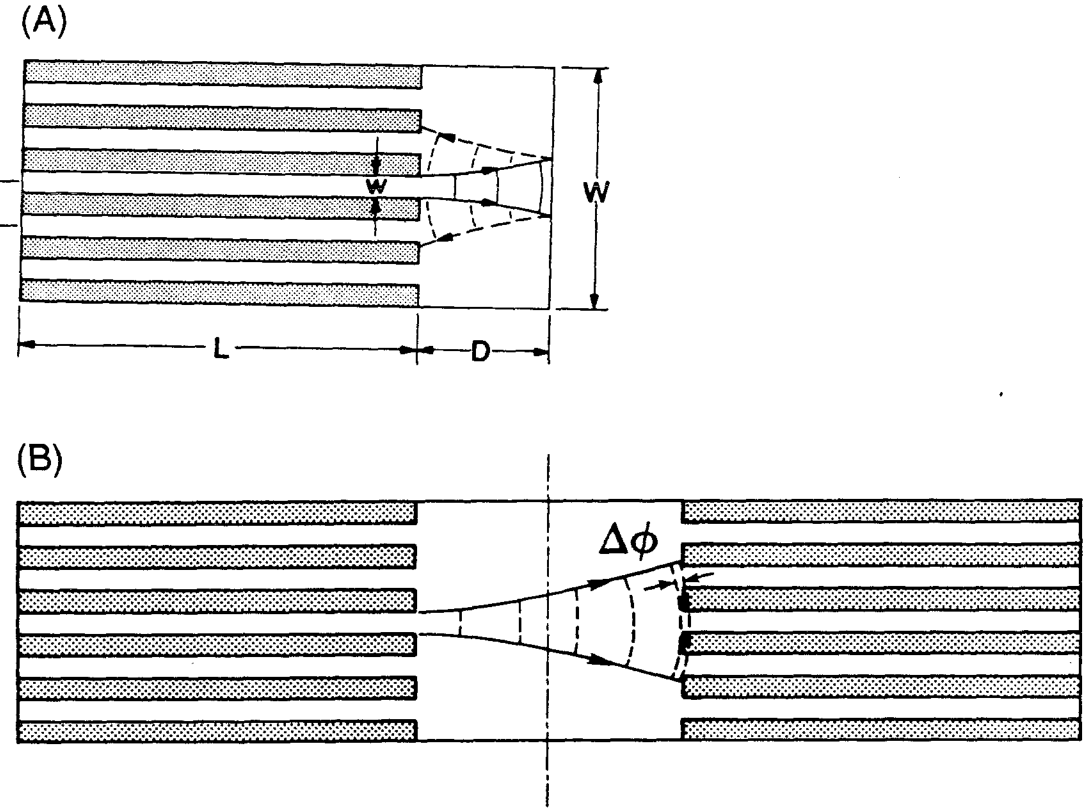

Figure 6.1 *Diffraction-coupled array geometry: (a) Definition of parameters. The shaded areas represent optical isolation. The array channels have width w and length L, while the diffraction region is of width W and length D. The array period is ℓ. (b) Device unfolded about the right-hand facet to illustrate the definition of the phase difference $\Delta\varphi$.*

lateral modes of diffraction-coupled arrays can each be represented as a *coherent* superposition of the modes of the individual array element waveguides; that is, as *supermodes*[1]. As we shall show, gain discrimination between supermodes arises because of the difference in their Fresnel diffraction patterns. For a given device geometry, specifically the diffraction cavity length, D, and the center-to-center spacing, ℓ, of the array waveguides, one such supermode couples most efficiently *back* into the array elements, after diffraction in the end region and reflection from the facet. Thus, the array/diffraction region interface acts as a mode-selective aperture, or spatial filter. In this chapter, we shall show that by proper device design, very large supermode discrimination can be achieved. Furthermore, the geometry can be optimized to *select* the lasing supermode.

A significant advantage of diffraction-coupled arrays over other array structures is that the interelement coupling is determined *not* by its growth or fabrication procedure, but by the *device geometry.* Figure 6.1(b) shows the single-sided device of Figure 6.1(a) "unfolded" so that a round trip within the composite resonator now corresponds to one traverse from the leftmost plane to the rightmost plane. A critical design parameter is the phase difference $\Delta\varphi$, which arises because of the *difference* in optical path length traversed by the field diffracting from channel i and coupling to itself versus coupling into channels $i \pm 1$. This phase difference is illustrated in Figure 6.1(b). To first order, $\Delta\varphi$ is given by

$$\Delta\varphi \simeq \frac{\pi n_{eff}}{2} \frac{\ell^2}{\lambda D} , \tag{6.1}$$

where λ is the free-space wavelength, and n_{eff} is the effective index within the diffraction region. In deriving (6.1), we have assumed the channel separation ℓ to be much smaller than the length D of the diffraction region (*i.e.*, small-angle approximation). If D is chosen so that the phase difference between the self-reflection and that from nearest neighbors is 2π, for example, adjacent elements are expected to lock *in-phase* and the array should operate in the fundamental supermode. On the other hand, if D is such that $\Delta\varphi \simeq \pi$, we expect adjacent elements to lock out-of-phase and the array would operate in the highest-order supermode. Equation (6.1) indicates that to achieve a given $\Delta\varphi$, the diffraction region length D should be chosen to satisfy

$$D = \frac{\ell^2}{(\lambda/n_{eff})(\Delta\varphi/\frac{1}{2}\pi)} . \tag{6.2}$$

In this chapter, we investigate control of the lasing supermode by optimization of the length of the diffraction region. The remaining sections present a more precise numerical model for solution of the lateral modes of diffraction-coupled arrays as a function of D, and describe experiments conducted to test the theory.

6.1 Supermode Theory

For the purpose of analysis, consider an array with N channels, each of suitable width w and effective index step Δn_{eff} to support a single waveguide mode, $e_n(x)$, where x is the lateral dimension. Let $\mathbf{e}$ be an $N \times 1$ column vector whose elements are the complex amplitude of the field in each channel at the left-hand edge of the array region. This vector is then propagated down the length of the array and reflected at its interfaces by suitable matrices $\mathbf{P}$, $\mathbf{R}_\ell$, and $\mathbf{R}_r$, as shown in Figure 6.2(a). Requiring $\mathbf{e}$ to reproduce itself after one round trip gives the oscillation condition:

$$\mathbf{e} = \mathbf{R}_\ell \mathbf{P} \mathbf{R}_r \mathbf{P}\ \mathbf{e}\ . \tag{6.3}$$

Here $\mathbf{P}$ is the propagation matrix in the channeled section and $\mathbf{R}_\ell$, $\mathbf{R}_r$ are *effective* reflectivity matrices at the left-hand and right-hand edges of the *array* region (*i.e.,* $\mathbf{R}_r$ includes the effect of the diffraction region). Assuming identical channels of length L, the propagation matrix is simply $\mathbf{P} = \exp(i\sigma L)\mathcal{I}$, where $\mathcal{I}$ is the identity matrix, and σ, the unknown propagation constant, is given by $\sigma = (n_0/c)\omega - i(\gamma/2)$. Here ω is the radian frequency, γ is the required threshold gain, n_0 is the effective index of the channel and c is the speed of light in free space. The left-hand reflection matrix is simply $\mathbf{R}_\ell = r_0\mathcal{I}$, where r_0 is the amplitude reflectivity of each TE channel mode at the GaAs-air interface ($r_0 \simeq \sqrt{R}$, $R \simeq 0.3$). The round-trip condition (6.3) can then be written as

$$\left(r_0 e^{i2\sigma L}\mathbf{R}_r - \mathcal{I}\right)\mathbf{e} = \mathbf{0}\ . \tag{6.4}$$

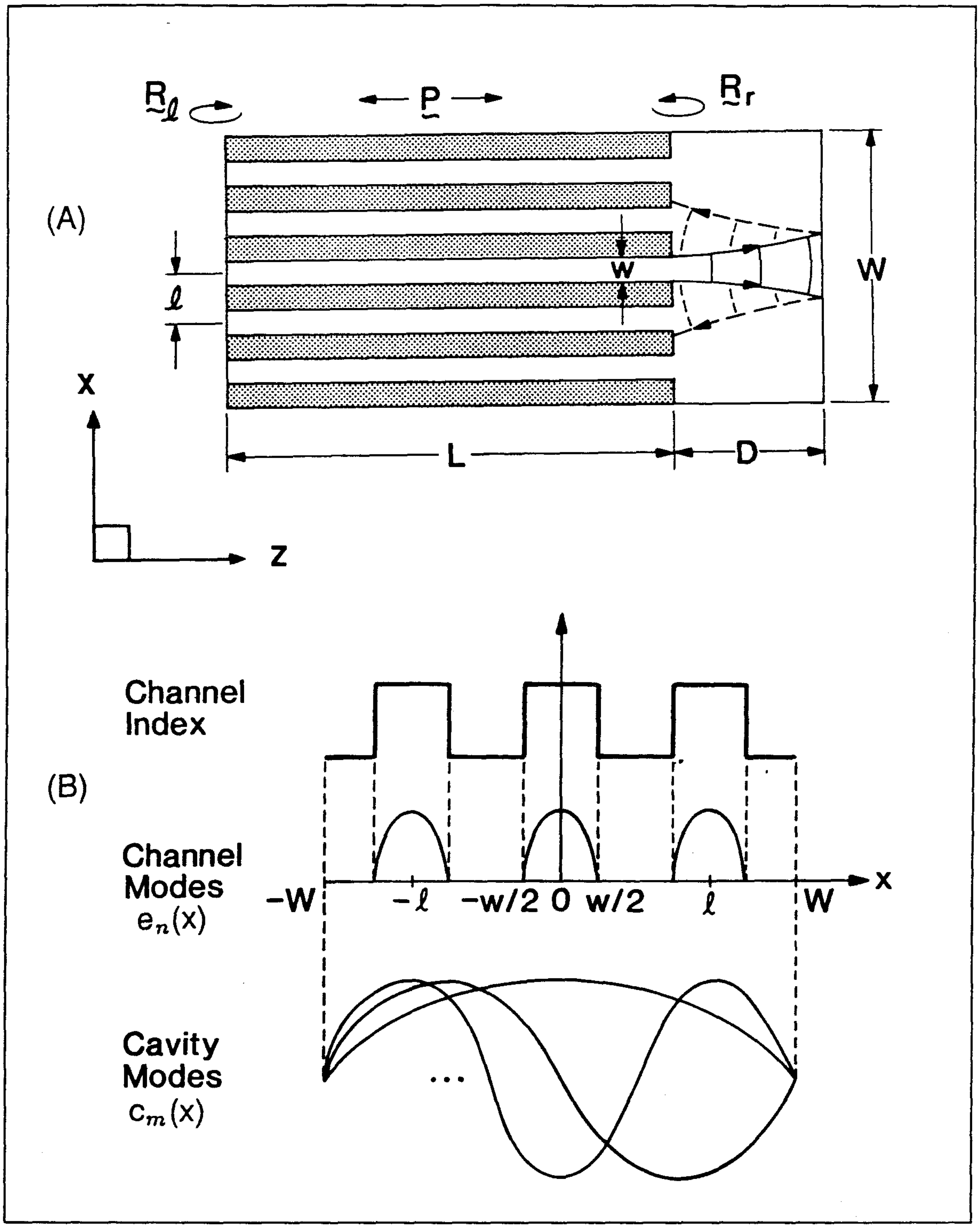

Figure 6.2 *(a) Propagation and effective reflection matrices for the supermode theory. (b) Channel modes* $e_n(x)$ *are those of the structure in cross section within the length* L *in (a). Cavity modes* $c_m(x)$ *are those of the structure in cross section within the length* D *in (a).*

Hence, $r_0^{-1}\exp(-i2\sigma L)$ is an eigenvalue of the matrix $\mathbf{R_r}$ and the array supermodes are its eigenvectors. It remains only to compute the effective reflection matrix $\mathbf{R_r}$ of the diffraction region, which embodies the interelement coupling.

We model the diffraction region as a cavity of width W, which supports a large number, M, of "slab waveguide" modes $c_m(x)$. Their amplitudes can be described by an $M \times 1$ column vector $\mathbf{c}$. To compute the reflection matrix $\mathbf{R_r}$, we first couple the channel modes $\mathbf{e}$ into the cavity basis $\mathbf{c}$ via an $N \times M$ coupling matrix $\mathbf{V}$: $\mathbf{e} = \mathbf{V}\mathbf{c}$. The cavity modes can then be propagated and reflected from a planar mirror (using their known propagation constants β_m) via the $M \times M$ matrix $\mathbf{P}'$ whose elements are $P'_{mn} = r_0 \exp(i2\beta_m D)\delta_{mn}$, where δ_{mn} is the Kronecker delta. After projecting back onto the channel basis with the transpose $\mathbf{V^T}$ of the coupling matrix, $\mathbf{e}_{after} = \mathbf{V}\mathbf{P}'\mathbf{V^T}\,\mathbf{e}_{before}$, so that the reflection matrix for the diffraction region is:

$$\mathbf{R_r} = \mathbf{V}\mathbf{P}'\mathbf{V^T}\ . \tag{6.5}$$

Note that $\mathbf{V}\mathbf{V^T} \simeq \mathcal{I}$ (small radiation loss), but $\mathbf{V^T}\mathbf{V} \neq \mathcal{I}$ (reflecting significant coupling loss). Different array supermodes excite different superpositions of the cavity modes; the difference in supermode diffraction patterns thus depends strongly on D through the different round-trip phases $2\beta_m D$ of the cavity modes.

For our calculations, we have assumed strong effective-index guiding for both the array and diffraction regions, so that the channel and coupling cavity modes are described by

$$\begin{aligned} e_n(x) &= \sqrt{\frac{2}{w}}\cos\left[\pi\frac{(x-nl)}{w}\right], \quad x \in \left[nl \pm \frac{w}{2}\right] \\ c_m(x) &= \sqrt{\frac{2}{W}}\sin\left[m\pi\frac{(x+W/2)}{W}\right], \quad x \in \left[\pm\frac{W}{2}\right] \end{aligned} \tag{6.6}$$

as is shown in Figure 6.2(b). The propagation constants β_m in the diffraction region are approximately $\beta_m^2 = k_0^2 n_0^2 - m^2\pi^2/W^2$, where $k_0 = 2\pi/\lambda$ is the free-space

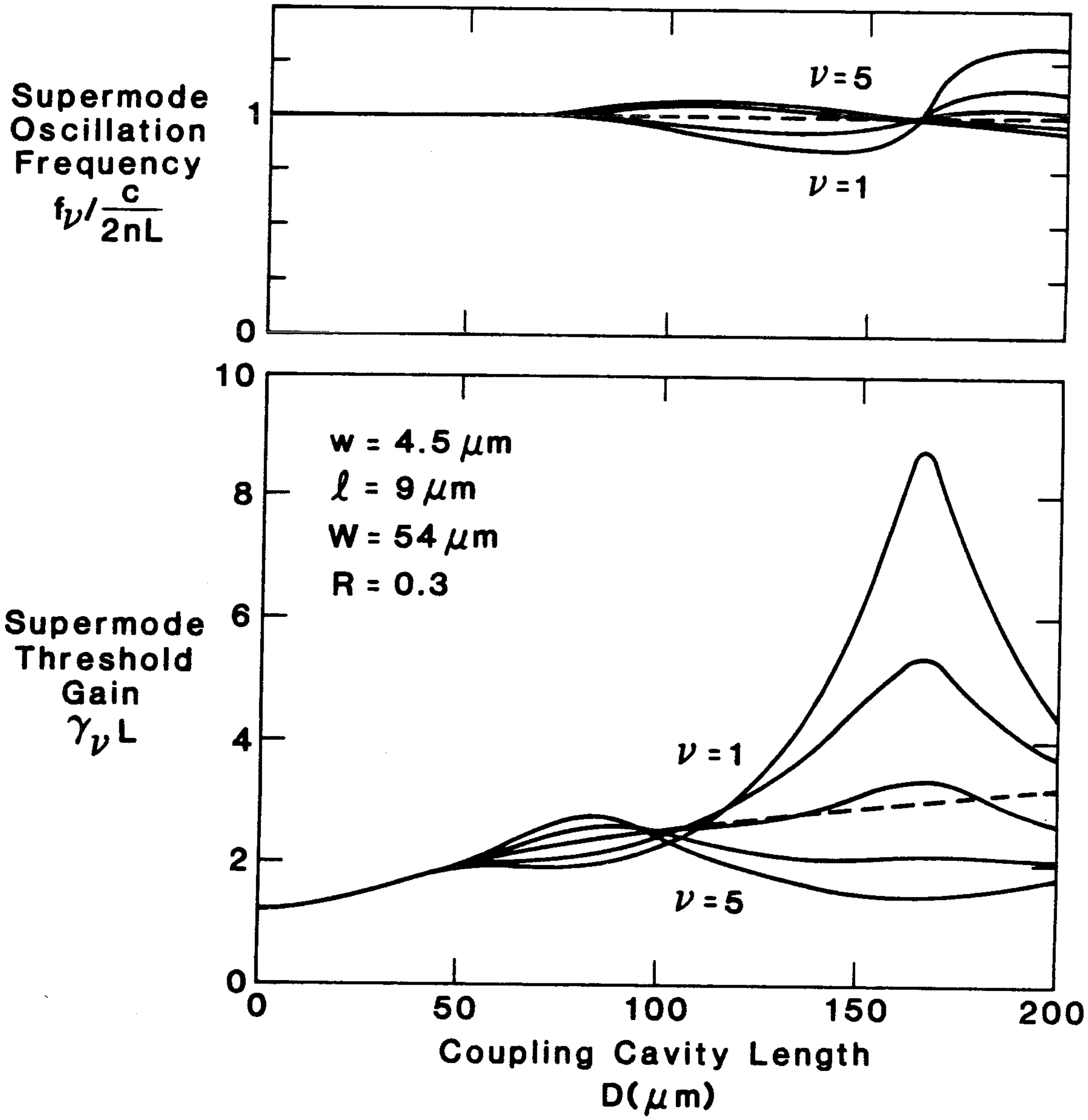

Figure 6.3 *Theoretical threshold gain and oscillation frequency for the supermodes of a 5-element diffraction-coupled array, as a function of coupling length,* D. *The* $\nu = 1$ *mode is the fundamental supermode. The dashed line gives the result for uncoupled lasers.*

Figure 6.3 can be understood more easily by considering a simplified theory. Numerical calculation reveals $\mathbf{R_r}$ to be approximately of the tridiagonal form

$$\mathbf{R_r} \simeq \begin{pmatrix} r & \kappa & \dots & 0 \\ \kappa & r & \dots & 0 \\ \vdots & \vdots & \ddots & \vdots \\ 0 & \dots & \kappa & r \end{pmatrix} , \tag{6.8}$$

where $r = v_{n,n}$ is the self-reflection term, and $\kappa = v_{n,n\pm 1}$ is that coupled into nearest neighboring channels $n \pm 1$. Coupling into *next*-nearest neighbors is negligible compared with κ, and is thus neglected. In this simplified case, the eigensolutions can be determined analytically, and the eigenvectors $\{e^j_\nu\}$ and their propagation constants $\{\sigma_\nu\}$ satisfy:

$$e^j_\nu = \sin\left(j\frac{\nu\pi}{N+1}\right) , \qquad j = 1, 2, \dots N \tag{6.9a}$$

$$r_0^{-1} e^{-i2\sigma L} = r + 2\kappa \cos\left(\frac{\nu\pi}{N+1}\right) , \qquad \nu = 1, 2, \dots N , \tag{6.9b}$$

where ν is the supermode index ($\nu = 1$ is the fundamental supermode, $\nu = N$ the highest-order supermode) and j is the channel index. Note that the supermodes $\{e^j_\nu\}$ are identical to those of distributed coupling arrays[1]. Unlike distributed coupling arrays, however, the coupling constant κ of a diffraction-coupled array is a strong function of the length D of the diffraction region. Consequently, the threshold gain γ_ν and oscillation frequency ω_ν corresponding to each supermode $\{e^j_\nu\}$ also vary strongly with D. Since the eigenvectors $\{e^j_\nu\}$ in (6.9a) are independent of κ, the actual lateral mode profile is independent of D. Let us examine γ_ν and ω_ν for the cases of in-phase ($\nu = 1$) and out-of-phase ($\nu = N$) supermodes. In the limit of large N, $\cos(\frac{\pi}{N+1}) \to 1$ and $\cos(\frac{N\pi}{N+1}) \to -1$. Denoting the $\nu = 1$ supermode by '+' and the $\nu = N$ by '−', Equation (6.9b) reduces to $r_0^{-1} \exp\{-i2\sigma_\pm L\} = r \pm 2\kappa$. Then $\gamma_\pm$ and $\omega_\pm$ are given by:

$$\gamma_\pm L \simeq \ln\frac{1}{|r_0 r|} \mp 4\left|\frac{\kappa}{r}\right| \cos\angle\frac{\kappa}{r} , \tag{6.10a}$$

$$\frac{\omega_\pm}{c/2n_0 L} \simeq 2\pi\cdot m + \angle r_0 r \pm 2\left|\frac{\kappa}{r}\right| \sin\angle\frac{\kappa}{r} . \tag{6.10b}$$

Equation (6.10a) indicates that $\gamma_+ < \gamma_-$ for $\cos \angle\kappa/r > 0$; that is, for $-\pi/2 < \angle\kappa/r < \pi/2$, the fundamental supermode has the lowest threshold gain, and will therefore be the first mode to lase. On the other hand, $\gamma_- < \gamma_+$ in the complementary region $\pi/2 < \angle\kappa/r < 3\pi/2$. It can also be inferred from (6.10) that the frequency splitting $\omega_+ - \omega_-$ is in quadrature to the threshold gain splitting $\gamma_+ - \gamma_-$. These features are all qualitatively evident in Figure 6.3.

6.2 Experiment: Supermode Control

In this section, the predictions of the preceding theory are experimentally tested. We have fabricated 7-element diffraction-coupled arrays from GaAs/GaAlAs GRINSCH multiple quantum well material grown by MBE. Figure 6.4 illustrates a perspective cross-section view through the device. Briefly, the array elements are 4.5 μm-wide ridge waveguides formed by wet chemical etching through the contact and upper cladding layers to within 0.1 to 0.2 μm of the active region. A Cr/Au contact evaporated over the device formed ohmic contacts to the top of the ridge waveguides, and to the diffraction region (*i.e.*, to the p^+-GaAs contact layer), while a Schottky barrier was formed between the ridges where the p-AlGaAs cladding layer was exposed[1]. A final photolithography defined the width of the contact to the array and diffraction regions.

It is of paramount importance that the diffraction-coupled array be fabricated in a manner that minimizes the distributed coupling between adjacent array elements. As such, we have chosen to fabricate air-ridge waveguides by wet chemical etching through the contact and upper cladding layers to very close proximity to the active region. To determine how close is desirable, a numerical computation of the effective index of refraction beneath each ridge was performed. Figure 6.5 illustrates schematically a ridge waveguide etched in the V-groove direction down to the interface between the p-cladding and p-GRIN layers of the laser structure. The

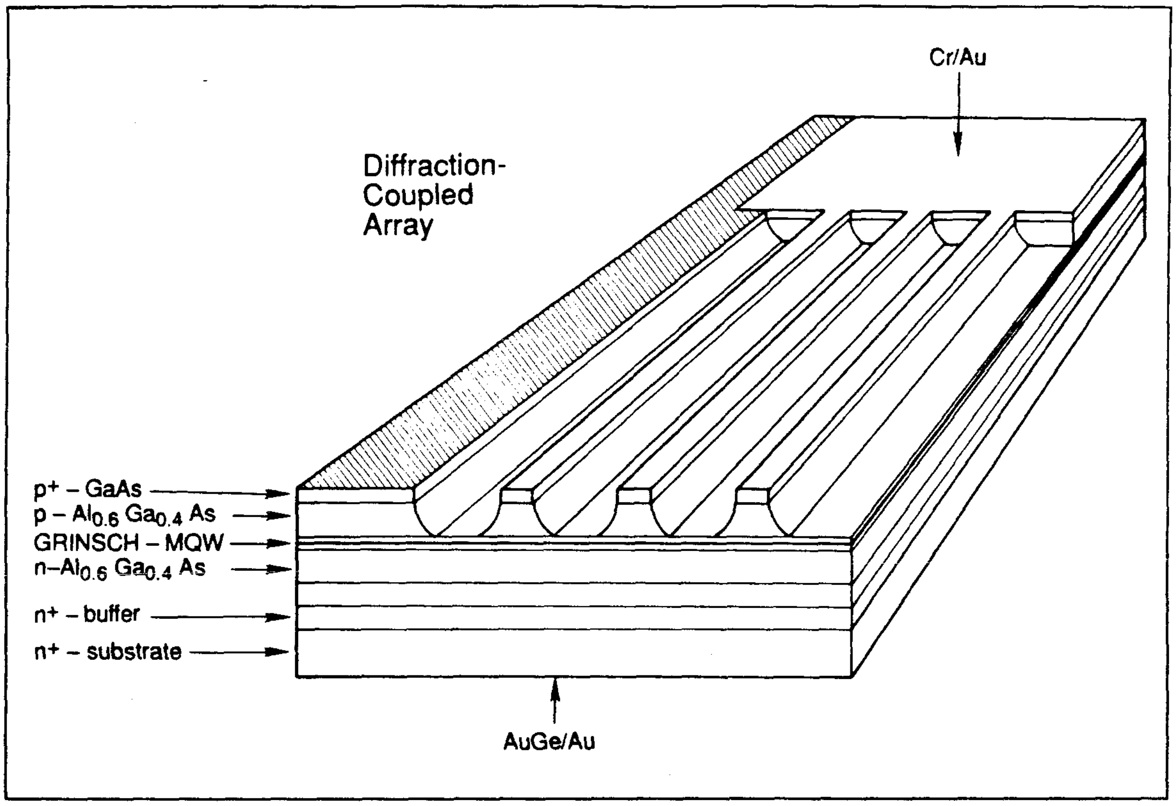

Figure 6.4 *Perspective view of fabricated diffraction-coupled array. The array elements (foreground) were formed by etching ridge waveguides down close to the MQW (multiple quantum well) active region, providing strong effective index guiding. The diffraction region is gain-guided.*

change Δn_{eff} in effective index as a function of lateral position x spanning the edge of the ridge is shown underneath. The lateral waveguide modes of the entire 4.5 μm-wide guide were found numerically, and their effective indices are also shown. If the etch is stopped just at the edge of the p-GRIN layer, the waveguide supports 4 lateral modes. In order to confine just the fundamental lateral mode, the ridge etch should be stopped approximately 0.1-0.2 μm above the p-GRIN layer. However, such a mode would not be well-confined; thus, in order to ensure effective isolation between the channels, a relatively large separation of 9 μm was chosen.

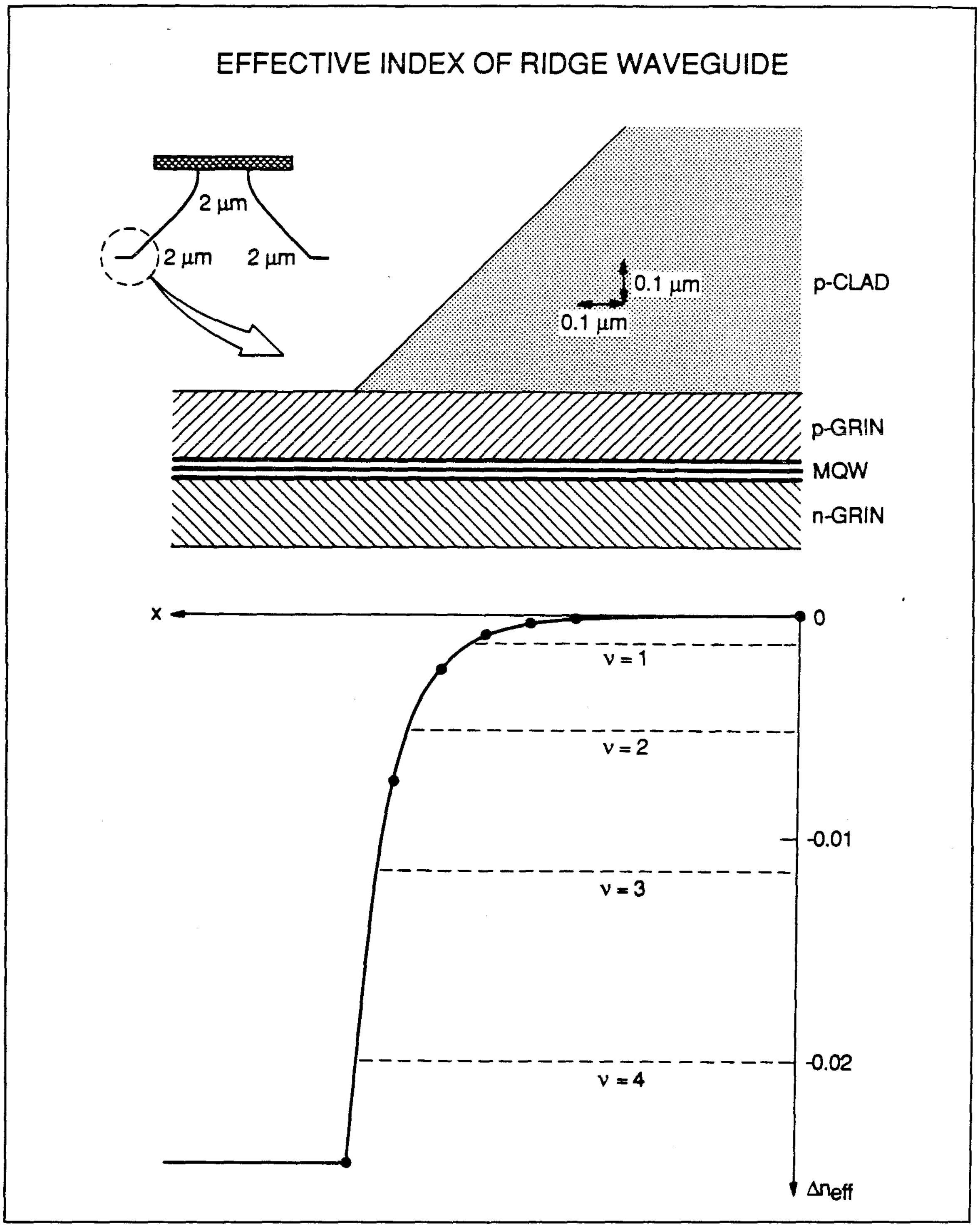

Figure 6.5 *Cross-section diagram of an air-ridge waveguide etched in the V-groove direction (top), and the lateral effective index profile underneath (bottom). The 4.5 μm-wide waveguide, etched down to the top of the p-GRIN layer, supports 4 lateral modes, with eigenvalues as shown.*

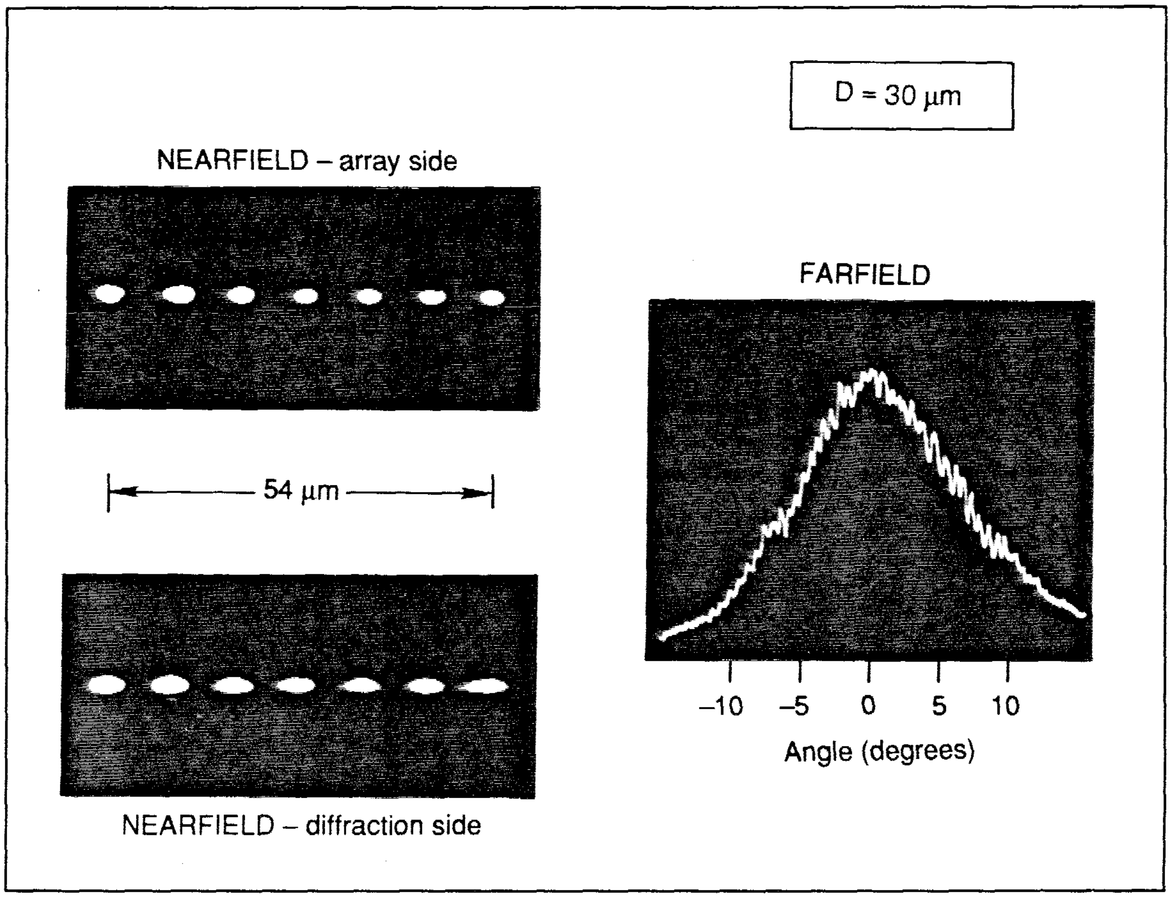

Figure 6.6 *Experimental result for a diffraction cavity of length $D = 30$ μm. Nearfield imaged on the array facet (top left), on the diffraction side (bottom left), and farfield on the diffraction side (right). The broad farfield indicates that emission from the array elements is incoherent.*

Diffraction-coupled array lasers were processed from this wafer and tested under low duty-cycle, pulsed conditions. The effect of the diffraction region length was observed experimentally by cleaving devices with D varying up to 150 μm in length. The array region length was kept constant at approximately 250 μm for all devices. Figures 6.6, 6.7 and 6.8 show the nearfield intensity as imaged on both array and diffraction sides of the laser, and the farfield on the diffraction side for devices cleaved to 3 different diffraction region lengths.

Arrays with short diffraction regions ($D < 50\mu$m) showed little or no evidence of coherence between elements, as inferred from farfields and spectrally-resolved nearfields. For example, integrated nearfield and farfield images for a device with $D = 30$ μm are illustrated in Figure 6.6. The nearfield on the array side shows 7 oval spots, each about 4 μm in width, indicating lasing within each of the waveguide elements. On the diffraction side, the spots are a little wider, since the modes are allowed to diffract freely in the lateral dimension within the coupling region. The farfield is broad ($\simeq 12^o$ FWHM), and featureless. This is consistent with incoherent emission from a set of 4 μm wide emitters. As expected, such a short diffraction region does not allow enough coupling to dynamically phase-lock the elements of the array.

On the other hand, devices with longer diffraction regions did exhibit considerable coherence across the array. Figure 6.7(a) shows the two nearfields and farfield for a device with $D = 80$ μm which, according to Figure 6.3, should oscillate in the fundamental ($\nu = 1$) supermode. The nearfield on the array side again shows 4 μm wide spots on 9 μm wide centers. Evidence of spatial coherence is observed in the diffraction-side nearfield and in the farfield, however, if we compare the experimental result to the theoretical expectation shown in Figure 6.7(b). The theoretical calculation shows the nearfield expected on both the array (dashed line) and diffraction (solid line) sides, and also the farfield (which is identical on both sides) for a 5-element array of the same geometry as that fabricated. We find that the diffraction patterns observed in the nearfield and farfield on the diffraction side of the array agree very well with the analytical prediction. The experimental result shown in Figure 6.7(a) was recorded at an elevated output power level of 100 mW to indicate that considerable gain discrimination is available before the deleterious effects of gain saturation are seen.

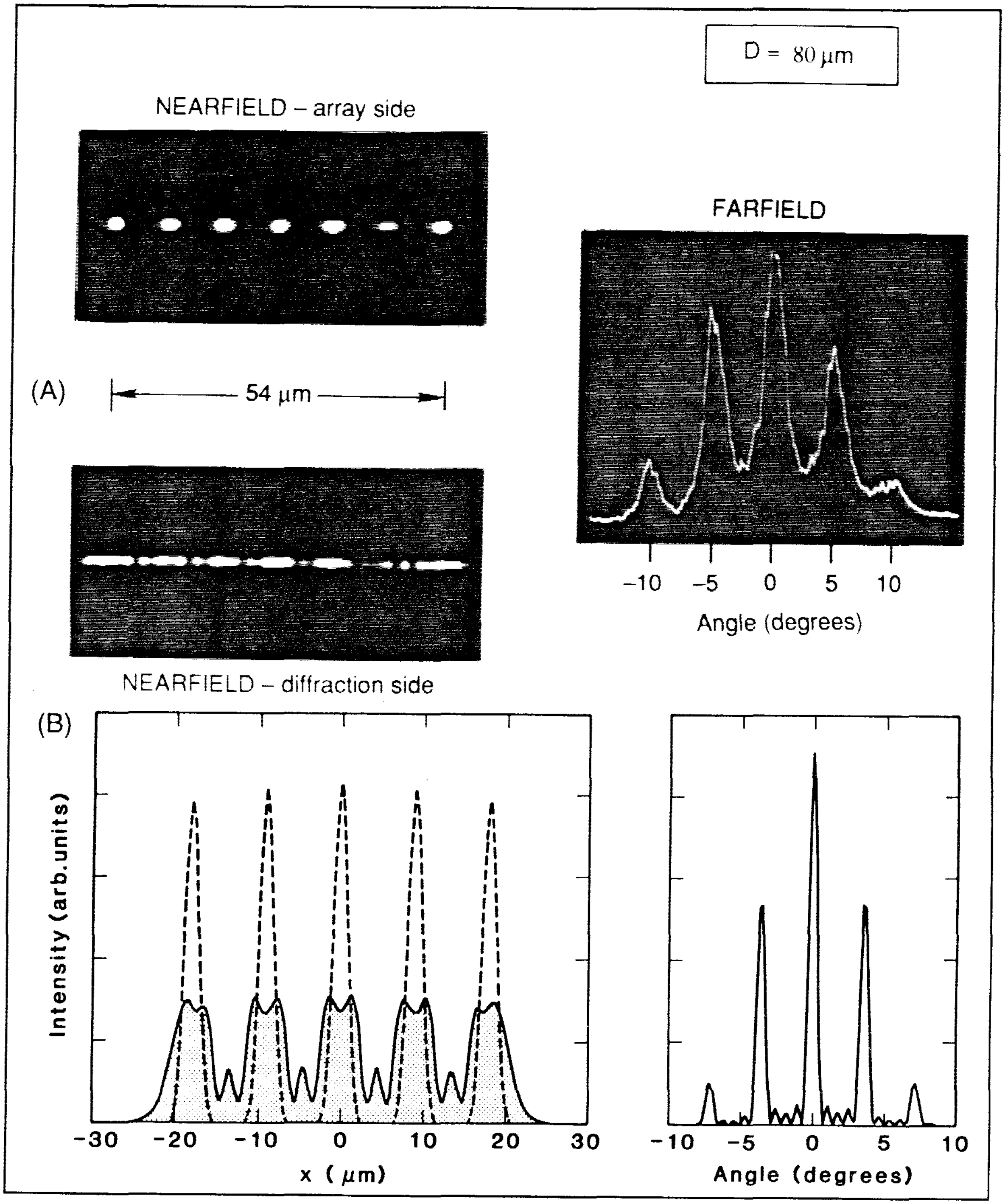

Figure 6.7 *(a) Experimental result for a diffraction cavity of length* $D = 80\ \mu m$*. Nearfield imaged on the array facet (top left), on the diffraction side (bottom left), and farfield on the diffraction side (right), at an output power level of 100* mW*. The array elements are phase-locked in the fundamental supermode. (b) Theoretical expectation for the same device: nearfield intensity at the array interface (dashed line) and at the diffraction cavity facet (solid line, shaded), and the farfield.*

The theoretical analysis of Section 5.1 predicts that the lasing supermode can be controlled by varying the length of the diffraction region. To verify this prediction, we have cleaved devices with longer diffraction regions, $D = 150$ μm in length, to compare with the $D = 80$ μm long devices. The experimental results are shown in Figure 6.8(a), again at the 100 mW power level. Contrary to the 80 μm length, the farfield does not exhibit a lobe in the forward (0°) direction, but rather two prominent lobes at $\pm 2.75^\circ$, which is consistent with adjacent elements on 9 μm centers phase-locked π radians out-of-phase, as in the higher-order supermodes. Operation in the $\nu = 7$ supermode is confirmed by examination of the diffraction pattern in the nearfield. The experiment shows twice the number of spots (14) as the number of waveguides, and is consistent with the theoretically calculated diffraction pattern shown in Figure 6.8(b) (for a 5-element device).

6.3 Discussion: The Cost of Mode Discrimination

Supermode discrimination is not achieved without cost. The mode-selective filter formed by the array/diffraction region interface causes substantial loss for even the lowest-loss mode. The resulting high threshold gains necessitate the use of a multiple quantum well active region; even so, elevated threshold currents and reduced differential quantum efficiencies are observed from diffraction-coupled arrays. As shown in Figure 6.9, the threshold and differential quantum efficiency of $D = 80$ μm devices were 400 mA and 42%, respectively. This is to be compared with 200 mA and 66% for broad area lasers of comparable size, fabricated from the same wafer. The simultaneous appearance of increased threshold, lower differential quantum efficiency, and clean nearfields and farfields is closely correlated with achieving a good etch to within 0.1 to 0.2 μm of the active region. At this

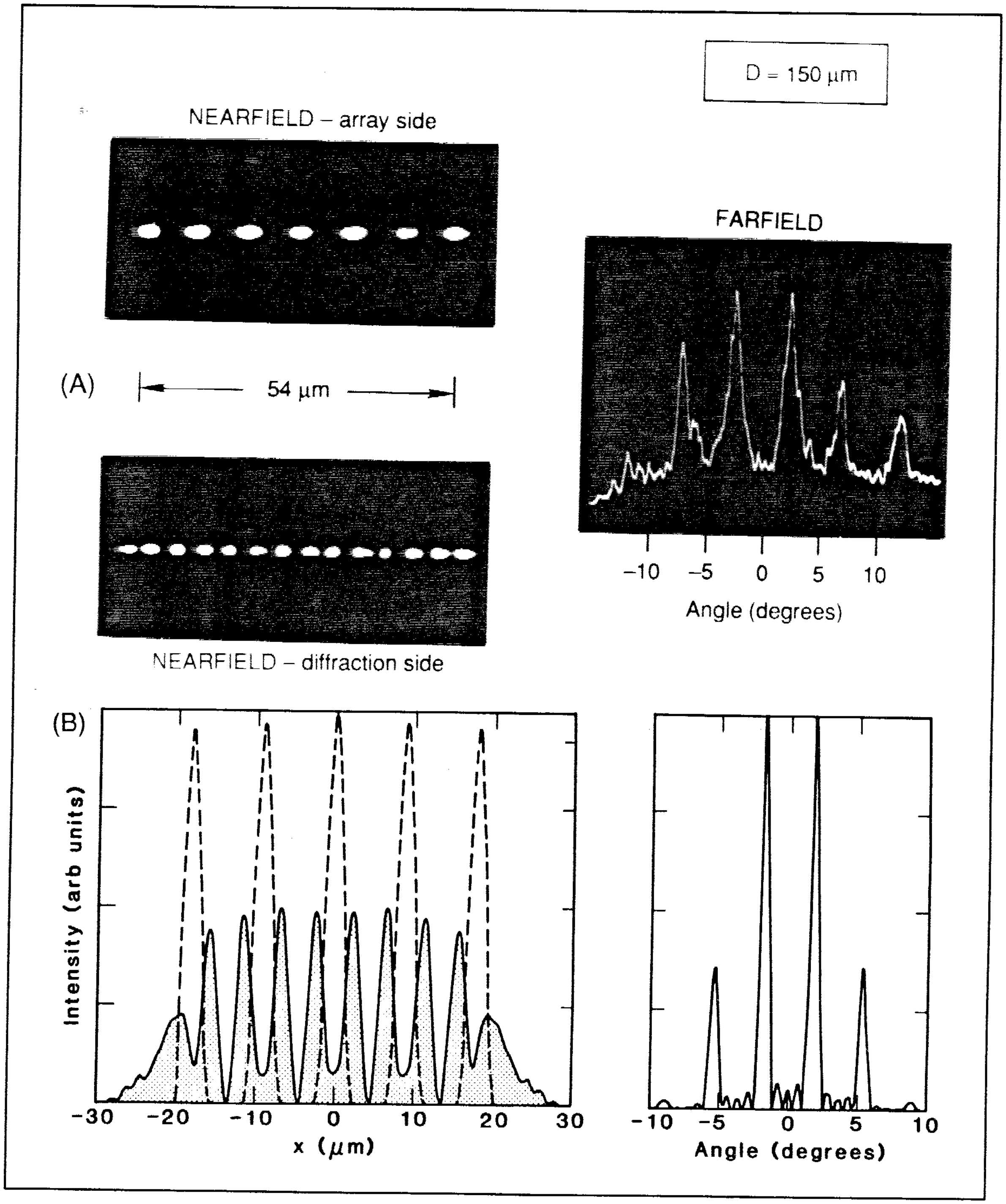

Figure 6.8 *(a) Experimental result for a diffraction cavity of length $D = 150\ \mu m$. Nearfield imaged on the array facet (top left), on the diffraction side (bottom left), and farfield on the diffraction side (right), at an output power level of 100 mW. The array elements are phase-locked in the highest-order supermode. (b) Theoretical expectation for the same device: nearfield intensity at the array interface (dashed line) and at the diffraction-cavity facet (solid line, shaded), and the farfield.*

point, light is strongly confined to the channels of the array region, thereby minimizing evanescent overlap between the channels. However, the coupling loss at the array/diffraction region interface then becomes significant.

As indicated in Figures 6.7(b) and 6.8(b), the supermode diffraction pattern expands to fill the coupling cavity, and unit coupling back into the array channels is *not* achieved. We re-emphasize that the differing coupling losses experienced at this interface by the different supermodes gives rise to the gain discrimination between them. The sketch at the top of Figure 6.9 indicates how the forward and backward traveling-wave intensity varies as a function of position within the single-sided diffraction-coupled array. We assume that all of the light couples into the diffraction region from the channels in the forward direction, but that only a fraction f (< 1) of the light reflected from the right-hand facet is coupled back into the channels. Furthermore, the remaining fraction $1 - f$ is assumed to be scattered or absorbed. In that case, the *effective* reflection from the right-hand side is *reduced* with respect to the left-hand side. Consequently, the power output P_d from the diffraction side *exceeds* that of the array side P_a by the factor:

$$\frac{P_d}{P_a} = \frac{1}{\sqrt{f}} \qquad (\geq 1) \,. \tag{6.11}$$

A measurement of P_d/P_a therefore determines the coupling factor f. Since $P_d/P_a \simeq 1.4$ for the $D = 80$ μm device of Figure 6.9, we infer that $f \simeq 0.5$ for the fundamental supermode. Of course, the coupling efficiencies of all other supermodes are reduced below this value; this reduction is manifest in the elevated threshold gains of the $\nu = 2$-5 modes in Figure 6.3.

Finally, the gain discrimination *at any particular* D can be increased or decreased by variation of the channel width, w. Figure 6.10 plots the supermode threshold gain and oscillation frequency of each supermode as a function of w,

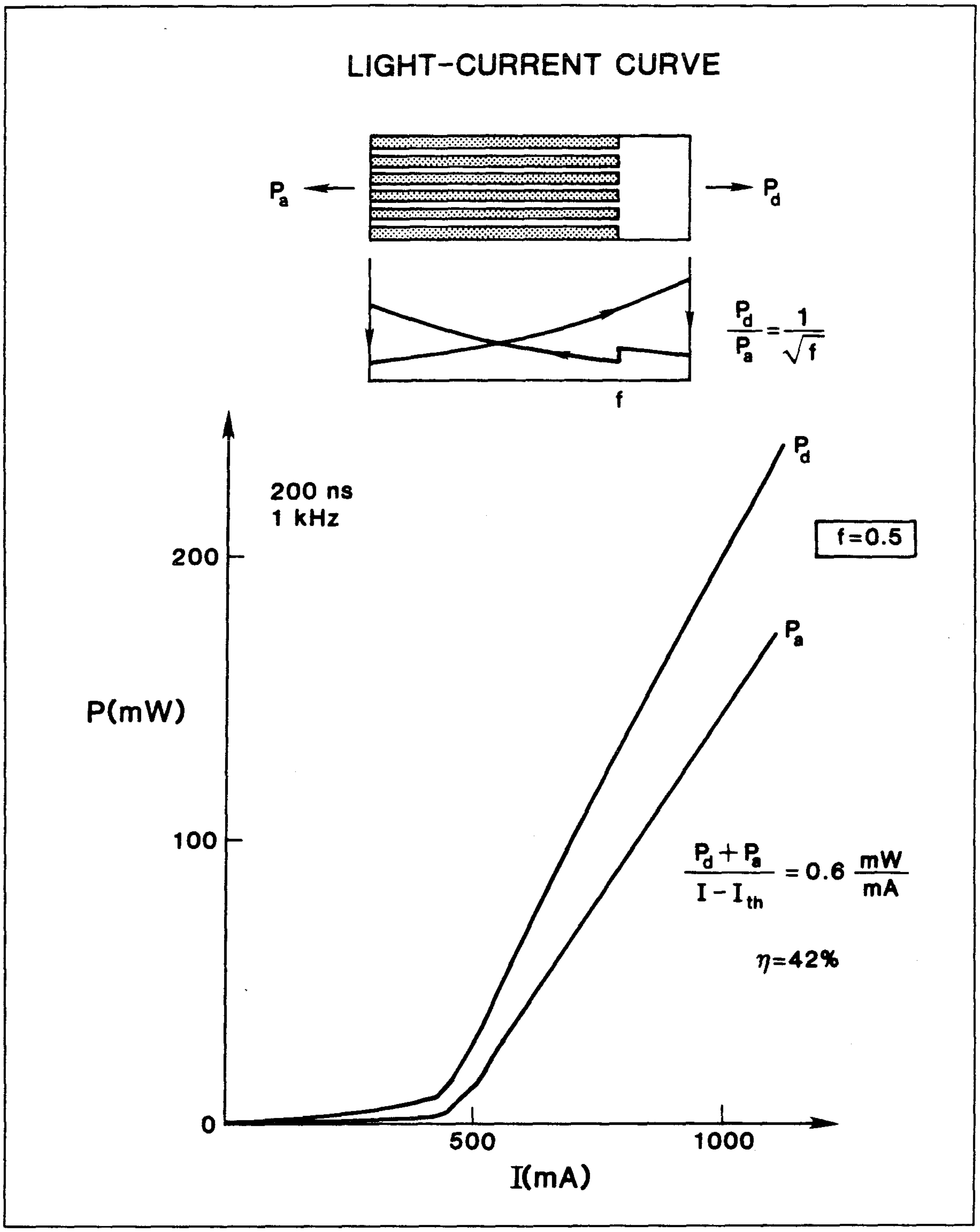

Figure 6.9 *Experimental light-current curve for the* $D = 80\ \mu m$ *device. Power output from the diffraction end exceeds that of the array end by 40%, giving a coupling loss* f *at the array/diffraction cavity interface (see top inset) of 50%.*

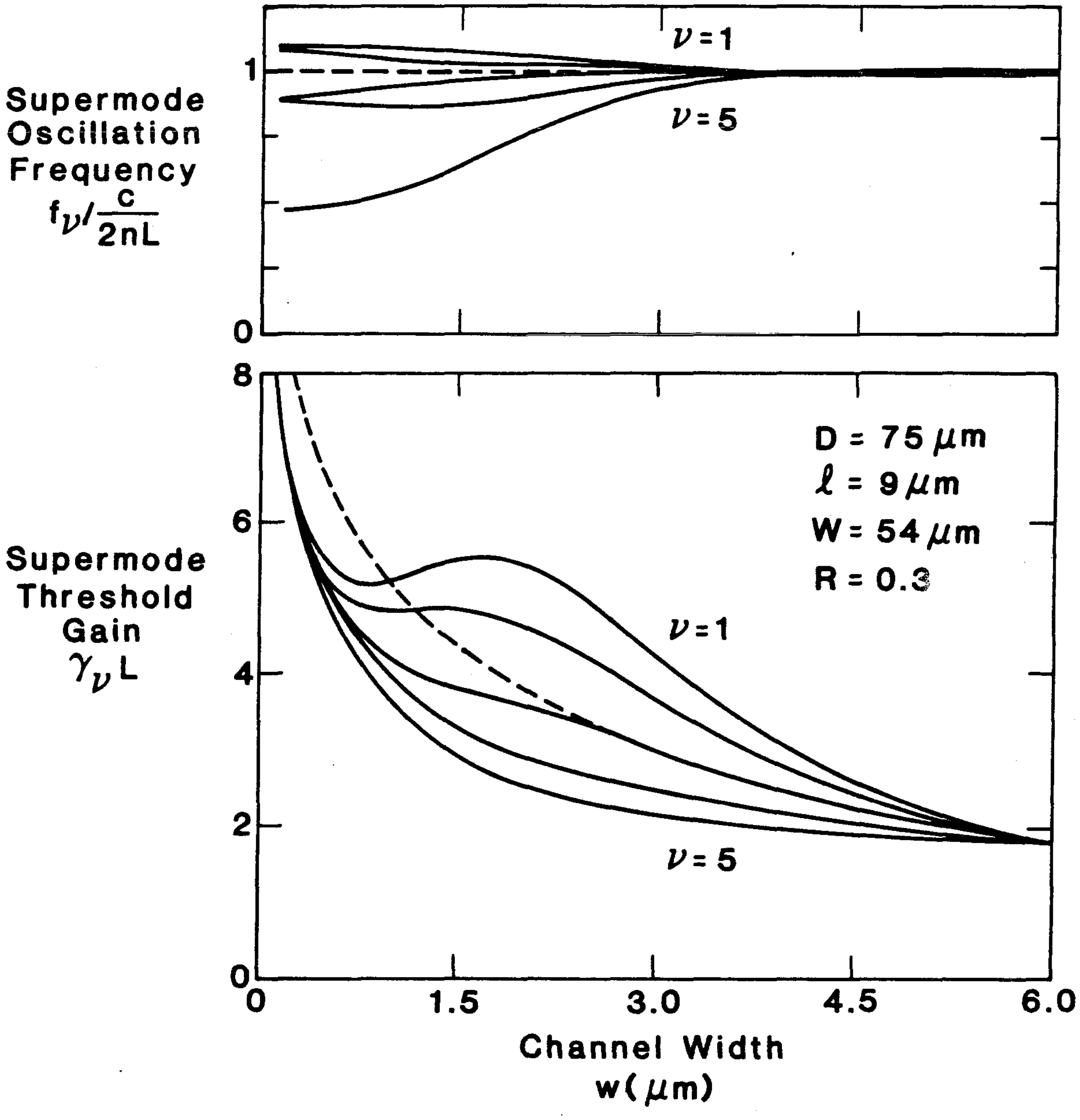

Figure 6.10 *Supermode threshold gain and oscillation frequency as a function of channel width, w, for the fixed diffraction region length $D = 75$ μm.*

varying between 0 and 6 μm, at the fixed cavity length $D = 75$ μm. As w is increased, the divergence of each channel mode ($\simeq \lambda/w$ for $D > w^2/\lambda$) is reduced. There are two effects: (a) the self-coupling r is increased because of greater overlap of the slowly diverging modes with the wider array channels, which increases the effective reflectivity and lowers the threshold gains, and (b) the cross-coupling κ is reduced because of the decreased mode divergence, which reduces the supermode gain discrimination. As w is decreased, the supermode gain discrimination does not increase indefinitely, but peaks at $w \simeq 2$ μm. Since both the self-coupling r and the cross-coupling κ must ultimately go to zero, all threshold gains approach infinity and the curves become degenerate as $w \rightarrow 0$. While the best gain discrimination is achieved at a narrow channel width of $w \simeq 2$ μm, the corresponding farfield is far from ideal. The fill factor w/ℓ is so small (about 20%) that numerous sidelobes are visible, and the fraction of total power contained in the central lobe is relatively small. This fraction can be increased, therefore, only by increasing w/ℓ; according to Figure 6.10, this is achieved at a cost of decreased mode discrimination.

6.4 Conclusions

To summarize, we have demonstrated, both theoretically and experimentally, control of the lasing supermode in diffraction-coupled semiconductor laser arrays. Operation in the fundamental and highest-order supermodes at an output power level of 100 mW was achieved by optimizing the length of the diffraction region. However, the large modal gain discrimination and supermode control are achieved *at the expense* of significant coupling losses at the array/diffraction region interface, which results in higher threshold currents and lower differential quantum efficiency than would be found in broad area lasers or distributed coupling arrays of comparable dimensions.

Hence, the $\nu = 1$ supermode is favored at $2D = Z_t/4$ ($\Delta\varphi = 2\pi$), while the $\nu = N$ supermode is favored at $2D = Z_t/2$ ($\Delta\varphi = \pi$). Stable fundamental supermode operation of a two-dimensional array of vertical-cavity, surface-emitting lasers could therefore be achieved by diffractive coupling through a transparent substrate whose thickness satisfies the quarter-Talbot plane condition.

References

[1] E. Kapon, J. Katz, and A. Yariv, "Supermode analysis of phase-locked arrays of semiconductor lasers," *Opt. Lett.*, vol. 10, no. 4, 125-127 (1984).

[2] J.K. Butler, D.E. Ackley, and D. Botez, "Coupled-mode analysis of phase-locked injection laser arrays," *Appl. Phys. Lett.*, **44**, 293-295 (1984).

[3] E. Kapon, C. Lindsey, J. Katz, S. Margalit, and A. Yariv, "Coupling mechanism of gain-guided integrated semiconductor laser arrays," *Appl. Phys. Lett.*, **44**, 389-391 (1984).

[4] J. Katz, S. Margalit, and A. Yariv, "Diffraction-coupled phase-locked semiconductor laser array," *Appl. Phys. Lett.* **42**, 554-556 (1983).

[5] S. Wang, J.Z. Wilcox, M. Jansen, and J.J. Yang, "In-phase locking in diffraction-coupled phased array diode lasers," *Appl. Phys. Lett.* **48**, 1770-1772 (1986).

[6] J.Z. Wilcox, M. Jansen, J.J. Yang, S.S. Ou, M. Sergant, and W. Simmons, "Supermode selection in diffraction-coupled semiconductor laser arrays," *Appl. Phys. Lett.* **50**, 1319-1321 (1987).

[7] J.Z. Wilcox, M. Jansen, J. Yang, G. Peterson, A. Silver, W. Simmons, S.S. Ou, and M. Sergant, "Supermode discrimination in diffraction-coupled laser arrays with separate contacts," *Appl. Phys. Lett.* **51**, 631-633 (1987).

[8] N. Basov, F. Belenov, and V. Letokhov, "Diffraction synchronization of lasers," *Soviet Physics - Technical Physics* **10**, 845-850 (1965).

[9] E. Kapon, C. Lindsey, J. Katz, S. Margalit, and A. Yariv, "Chirped arrays of diode lasers for supermode control," *Appl. Phys. Lett.* **45**, 200-202 (1984).

[10] J.R. Leger, "Coherent operation of AlGaAs laser arrays using coupled microcavities and binary optical elements," paper FL1, *CLEO'89*: Conference on Lasers and Electro-Optics, April 24-28 (1989), Baltimore MD.

Equation (6.9a) stated that the electric field amplitudes that comprise the supermodes of index-guided laser arrays are *not equal* across the array. As a consequence, supermodes of the unsaturated array are no longer consistent with the unequally saturated gain and refractive index profiles above threshold. Figure 7.1 illustrates qualitatively the changes in waveguide parameters that result from gain saturation, and the self-consistent supermode profiles one might expect *a priori*. In this chapter, we calculate the supermodes that *are* self-consistent with gain-saturated, index-guided laser arrays. Because of the nonlinear nature of the problem, the supermodes so calculated depend on the pumping level above threshold.

7.1 Nonlinear Supermodes of Diffraction-Coupled Arrays

In order to illustrate these concepts, we extend the below-threshold analysis of diffraction-coupled arrays introduced in Chapter Six to the above-threshold regime. The propagation constant, σ, previously assumed to be identical for all channels in the array, is modified to reflect the local intensity-dependence of the complex refractive index. Because of intensity-induced detuning of the phase velocities of adjacent channel waveguide modes, the interelement coupling is modified. The present analysis determines the consequences of this modification for the array supermodes.

We begin by recalling the self-consistency equation, (6.3), for diffraction-coupled arrays:

$$(\mathbf{R}_\ell \mathbf{P} \mathbf{R}_\mathbf{r} \mathbf{P} - \mathcal{I})\mathbf{e} = 0, \qquad \mathbf{e} = \begin{pmatrix} e_1 \\ \vdots \\ e_N \end{pmatrix}, \tag{7.1}$$

where $\mathbf{e}$ is the column vector comprised of the electric field modal amplitudes within the N channels of the array, $\mathbf{R}_{\ell,\mathbf{r}}$ are the effective reflection matrices of the left and right diffraction regions, respectively, $\mathcal{I}$ is the identity matrix, and $\mathbf{P}$ is the propagation matrix in the uncoupled array region. To allow for intensity-induced

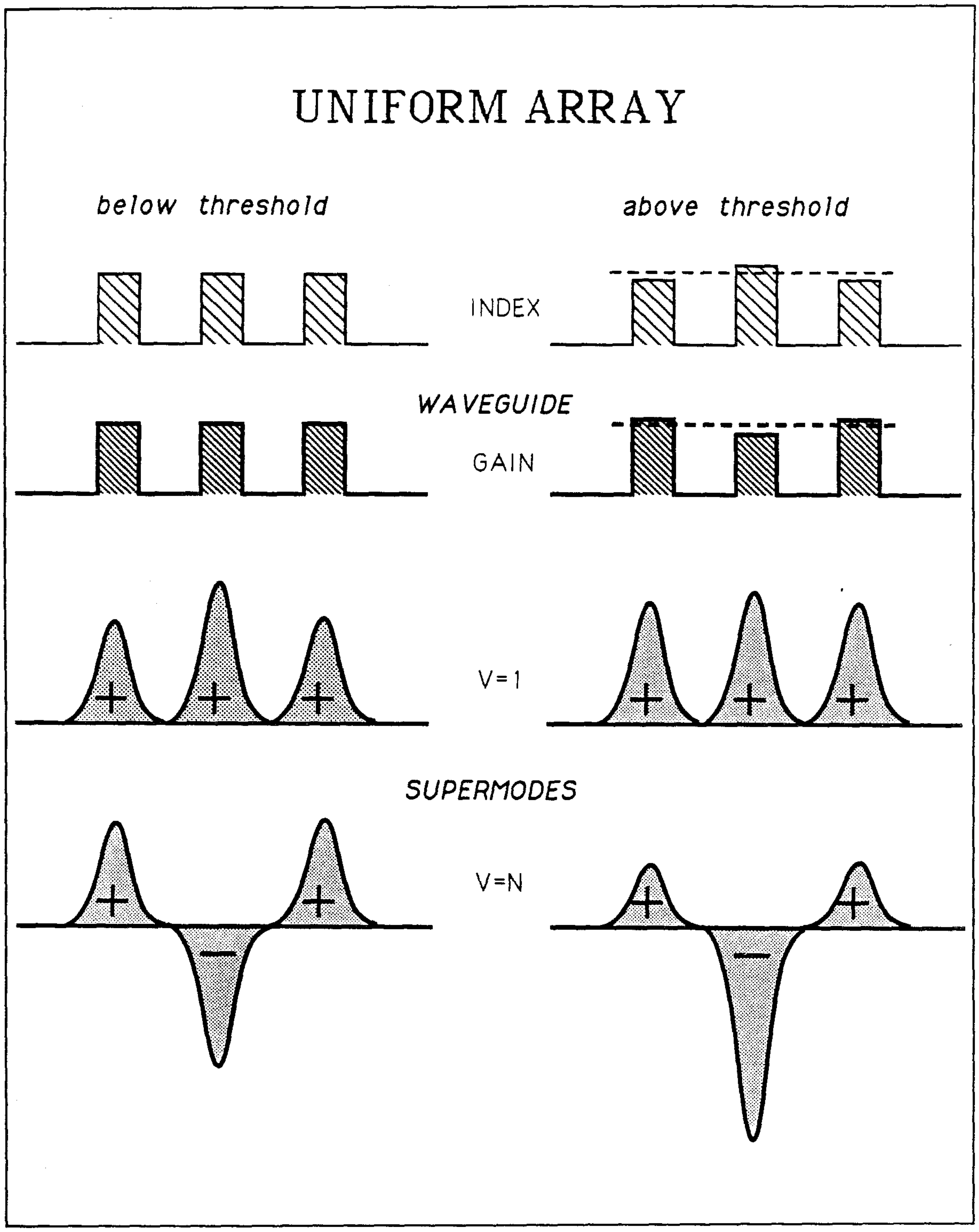

Figure 7.1 *The supermode profiles of uniform, unsaturated laser arrays (left) are not self-consistent above threshold. Modulation of the carrier population by non-uniform stimulated emission introduces gain and index perturbations that modify the supermode intensity profiles (right).*

detuning of the propagation constant, the propagation matrix $\mathbf{P}$, formerly $\mathbf{P} = e^{i\sigma L}\mathcal{I}$, is modified to

$$\mathbf{P} = \begin{pmatrix} e^{i\sigma_1 L} & 0 & \dots & 0 \\ 0 & e^{i\sigma_2 L} & \dots & 0 \\ \vdots & \vdots & \ddots & \vdots \\ 0 & 0 & \dots & e^{i\sigma_N L} \end{pmatrix} , \tag{7.2}$$

where $\sigma_n = \sigma_n(|e_n|^2)$. Implicit in the matrix formalism is the assumption that each channel can be modeled as a point: that is, within each channel the gain and index are approximately independent of position. If the channel waveguides are designed so as to support only a single lateral mode, then the approximation of constancy in the lateral dimension is valid because higher-order *supermodes* reach threshold at lower injected currents than do higher-order *channel modes* induced by the nonlinearity. Of more significance is the assumption of index constancy in the *longitudinal* dimension. An exact solution requires modeling saturation of the gain by modes traveling in *both* the $+z$ and $-z$ directions: $\sigma_n = \sigma_n(|e_n^+ + e_n^-|^2) \simeq \sigma_n(|e_n^+|^2 + |e_n^-|^2)$. In general, $|e_n^+|^2 + |e_n^-|^2$ is not a constant along the length of the laser[1], particularly in the case of asymmetric devices (in Chapter Six, we considered devices with single-sided diffraction regions). However, if the coupling loss at the array/diffraction region interface is not too high, the approximation is validated.

In general, we should also model diffraction in the coupling cavity as a nonlinear process. Gain saturation, with its accompanying self-focusing, alters the optical path length in the coupling cavity (and therefore the phase of coupling constant, and the modal gain discrimination), as well as reducing the cross-talk between channels (therefore reducing the magnitude of the coupling constant). To suppress these deleterious effects, a *transparent* diffraction region should be employed; we consider that case here. In practice, transparency can be accomplished by current pumping with a separate contact[2], or by regrowth of a higher bandgap material[3]. Thus, as in Chapter Six, we model diffraction of the channel modes as a linear

Thus, $\lambda \equiv r_0^{-1} e^{-i(\sigma_1+\sigma_2)L}$ is an eigenvalue (*i.e.*, propagation constant), and $\mathbf{e}$ is an eigenvector (*i.e.*, supermode), of $\mathbf{T}(\mathbf{e})$, the matrix to be diagonalized. Since $\mathbf{T}$ depends on $\mathbf{e}$ through the saturated gain and refractive index, the eigenvalue equation is *nonlinear.*

Our next task is to determine the dependence of the nonlinear channel detuning $\Delta(\mathbf{e})$ on the electric field vector $\mathbf{e}$. The intensity-dependence of the effective index of refraction $n_{eff}(|E|^2)$ was derived in Chapter Two (Equation (2.13)). The intensity-dependent propagation constant $\sigma(|E|^2) = k_0 n_{eff}(|E|^2)$ is therefore

$$\sigma(|E|^2) = \frac{n_0}{c}\omega - i\frac{\gamma}{2} + \frac{\gamma}{2}(b+i)\frac{|E|^2/E_{sat}^2 - (J - J_{th})/J_{sat}}{1 + |E|^2/E_{sat}^2} \ . \tag{7.7}$$

By introducing normalized field point quantities e_i and pump level j via

$$\begin{aligned} E_i &= E_{sat} \cdot e_i \ , \\ j &= \frac{J - J_{th}}{J_{sat}} \ , \end{aligned} \tag{7.8}$$

then the gain-saturated propagation constant of the i^{th} channel is written

$$\sigma_i(|e_i|^2) = \frac{n_0}{c}\omega - i\frac{\gamma}{2} + \frac{\gamma}{2}(b+i)\frac{|e_i|^2 - j}{1 + |e_i|^2} \ . \tag{7.9}$$

Therefore, the *mismatch* Δ in propagation constants that is due to nonlinear detuning is:

$$\Delta \equiv (\sigma_1 - \sigma_2)L = \frac{\gamma L}{2}(b+i)\frac{(1+j)(|e_1|^2 - |e_2|^2)}{(1+|e_1|^2)(1+|e_2|^2)} \ . \tag{7.10}$$

Equation (7.10) is a key result. It states that the nonlinear detuning between adjacent channels is proportional to the difference in optical intensities within these channels. The constant of proportionality is the product of the normalized threshold gain, γL, and the antiguiding factor, b. Gain saturation, embodied by the denominator of (7.10), prohibits Δ from increasing indefinitely.

Having determined $\Delta(\mathbf{e})$, we turn to the business at hand of solving the eigenvalue problem (7.6). The characteristic equation of the round-trip matrix $\mathbf{T}(\mathbf{e})$ is, from (7.5) and (7.6),

$$(re^{i\Delta} - \lambda)\Big[(re^{i\Delta} - \lambda)(re^{-i\Delta} - \lambda) - 2\kappa^2\Big] = 0. \tag{7.11}$$

For the unsaturated case $\Delta = 0$, the 3 solutions $\lambda_1 = r + \sqrt{2}\kappa$, $\lambda_2 = r$, and $\lambda_3 = r - \sqrt{2}\kappa$ give the propagation constants for the lateral modes $(e_1, e_2, e_3) = (1, 1, 1)$, $(1, 0, -1)$, and $(1, -1, 1)$, respectively. These modes will henceforth be denoted as the $(+\,+\,+)$, $(+0-)$, and $(+\,-\,+)$ supermodes. For $\Delta \neq 0$, $\lambda_2 = re^{i\Delta}$ and its corresponding eigenvector is $(e_1, e_2, e_3) = (1, 0, -1)$; the $(+0-)$ supermode thus remains unchanged under the influence of gain saturation. This is not the case for the fundamental $(+{+}+)$ and highest-order $(+-+)$ supermodes, however, which are derived from the quadratic equation within the square brackets of Equation (7.11). Let us denote $\lambda_+ = \lambda_1$ and $\lambda_- = \lambda_3$. The solution to Equation (7.11) for $\Delta \neq 0$ is:

$$\lambda_\pm = r\cos\Delta \pm \sqrt{2\kappa - r^2 \sin^2\Delta}\ . \tag{7.12}$$

The corresponding eigenvectors are determined, via (7.5) and (7.6), by the equation:

$$\kappa\, e_1 + (re^{-i\Delta} - \lambda)\, e_2 + \kappa\, e_3 = 0\ . \tag{7.13}$$

For the $(+\,+\,+)$ and $(+\,-\,+)$ supermodes, $e_3 = e_1$. By substituting $\lambda = \lambda_\pm(\Delta)$ from (7.12), Equation (7.13) becomes

$$\frac{2}{(e_2/e_1)} = i\frac{r}{\kappa}\sin\Delta \pm \sqrt{2 + (i\frac{r}{\kappa}\sin\Delta)^2}\ . \tag{7.14}$$

Equation (7.14), subject to (7.10), is the nonlinear, self-consistent equation for the eigenvector (e_1, e_2, e_1). At this point there are 3 real-valued unknowns: $|e_1|$, $|e_2|$, and $\angle e_2$. The phase $\angle e_1$ can be set to zero without loss of generality. Equation (7.14) represents 2 real equations; an additional equation is required for the solution.

The final equation is determined by demanding that the e_i be chosen so as to conserve energy. Above threshold, energy is conserved by requiring the modal gain γ to become clamped at its threshold value. In order for the modal gain γ to remain clamped above threshold, the eigenvalue $\lambda = r_0^{-1} e^{-i(\sigma_1+\sigma_2)L}$ must assume the same value for all values of e_i and j as it does for $e_i = 0$ and $j = 0$ (*i.e.*, the below-threshold case). The field-dependent part of λ is

$$\sigma_1 + \sigma_2 = 2\Big(\frac{n_0}{c}\omega - i\frac{\gamma}{2}\Big) + \gamma(b+i)\left[\frac{|e_1|^2 - j}{1+|e_1|^2} + \frac{|e_2|^2 - j}{1+|e_2|^2}\right] . \tag{7.15}$$

To satisfy energy conservation, Equation (7.15) therefore requires

$$\frac{|e_1|^2 - j}{1+|e_1|^2} + \frac{|e_2|^2 - j}{1+|e_2|^2} = 0. \tag{7.16}$$

Equation (7.16) relates the field amplitudes $|e_1|$ and $|e_2|$ to the pump level j, as required from any statement of energy conservation. This equation is only an approximation: since the diffraction losses vary slightly as a function of nonlinear detuning, the complex modal propagation constant is a weakly dependent function of the pump current.

Together, Equations (7.14) and (7.16) represent 3 real equations in 3 real unknowns. As a result, the nonlinear supermodes (e_1, e_2, e_1) can be determined as a function of pump level j. Figure 7.2 (left) illustrates the solution of these equations for the $(+++)$ supermode at 3 values of excess current density j above threshold. We find that as the pump current increases above threshold, the intensity envelope of the $(+++)$ supermode becomes flattened ($|e_2|/e_1 \to 1$, e_1 real), while the phase of the central, high-intensity channel is advanced relative to the outer channels. Taking into account our traveling-wave convention, this corresponds to a wavefront that is retarded in the center for propagation along the $+z$ axis. Figure 7.2 (right) illustrates the *ratios* $|e_2|/e_1$ and $\angle e_2/e_1$ as a function of j, for different values of the normalized coupling constant $|\kappa/r|$. All curves have $\angle\kappa/r = 0$. Figure 7.3 (left)

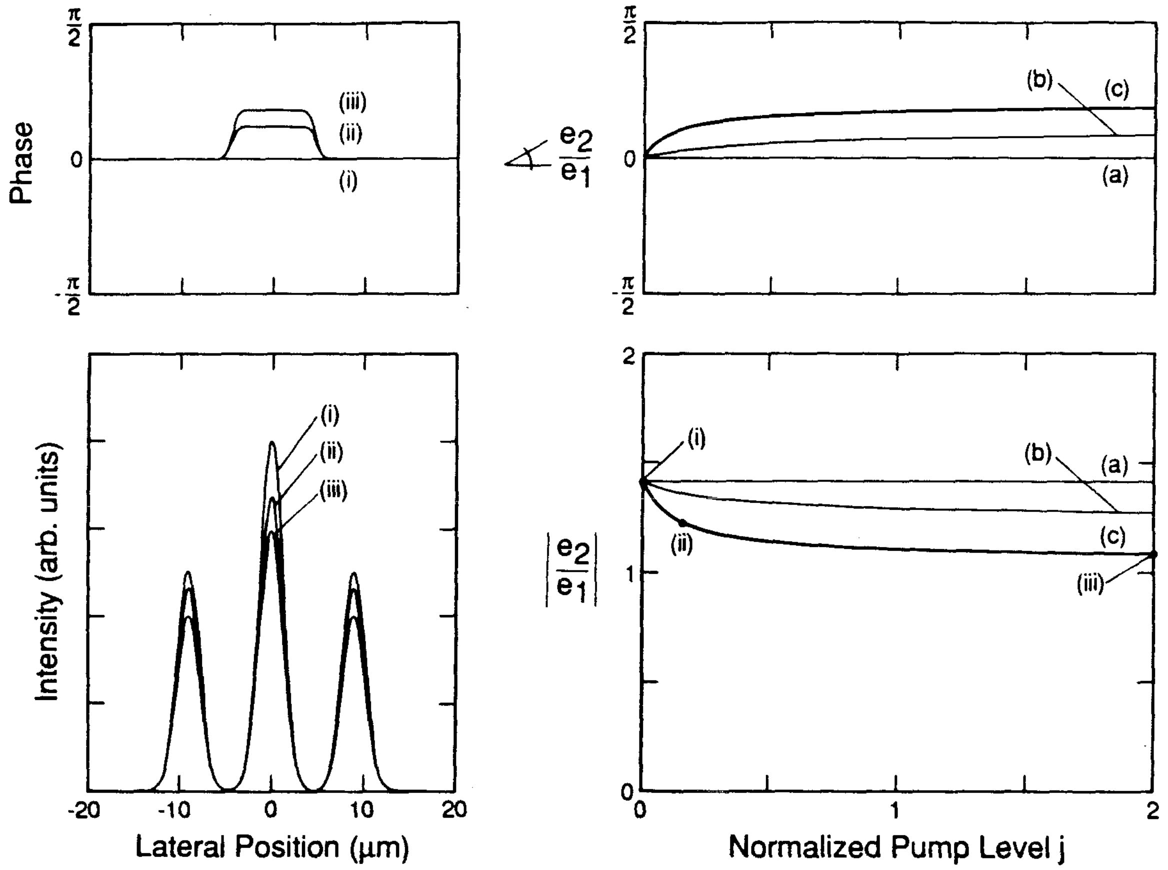

Figure 7.2 *Nearfield intensity and phase (left; bottom and top) of the* $(+++)$ *supermode at normalized pump levels (i)* $j = 0$, *(ii)* $j = 0.2$, *and (iii)* $j = 2$. *The amplitude and phase of* e_2/e_1 *are shown as a function of* j *(right; bottom and top) for 3 values of relative coupling (a)* $\kappa/r = \infty$, *(b)* $\kappa/r = 0.6$, *and (c)* $\kappa/r = 0.1$. *The coupling constant is real-valued.*

illustrates the corresponding solution for the $(+-+)$ supermode. For the same coupling strengths, the $(+-+)$ supermode has its power concentrated more and more into the central channel as the pump strength is increased, as illustrated in Figure 7.3 (right). This power accumulation is accompanied by a phase shift in the central element *opposite* to that of the $(+++)$ supermode. Note in all cases that gain saturation causes the supermode envelope to stabilize quite rapidly as the pump level is increased beyond threshold.

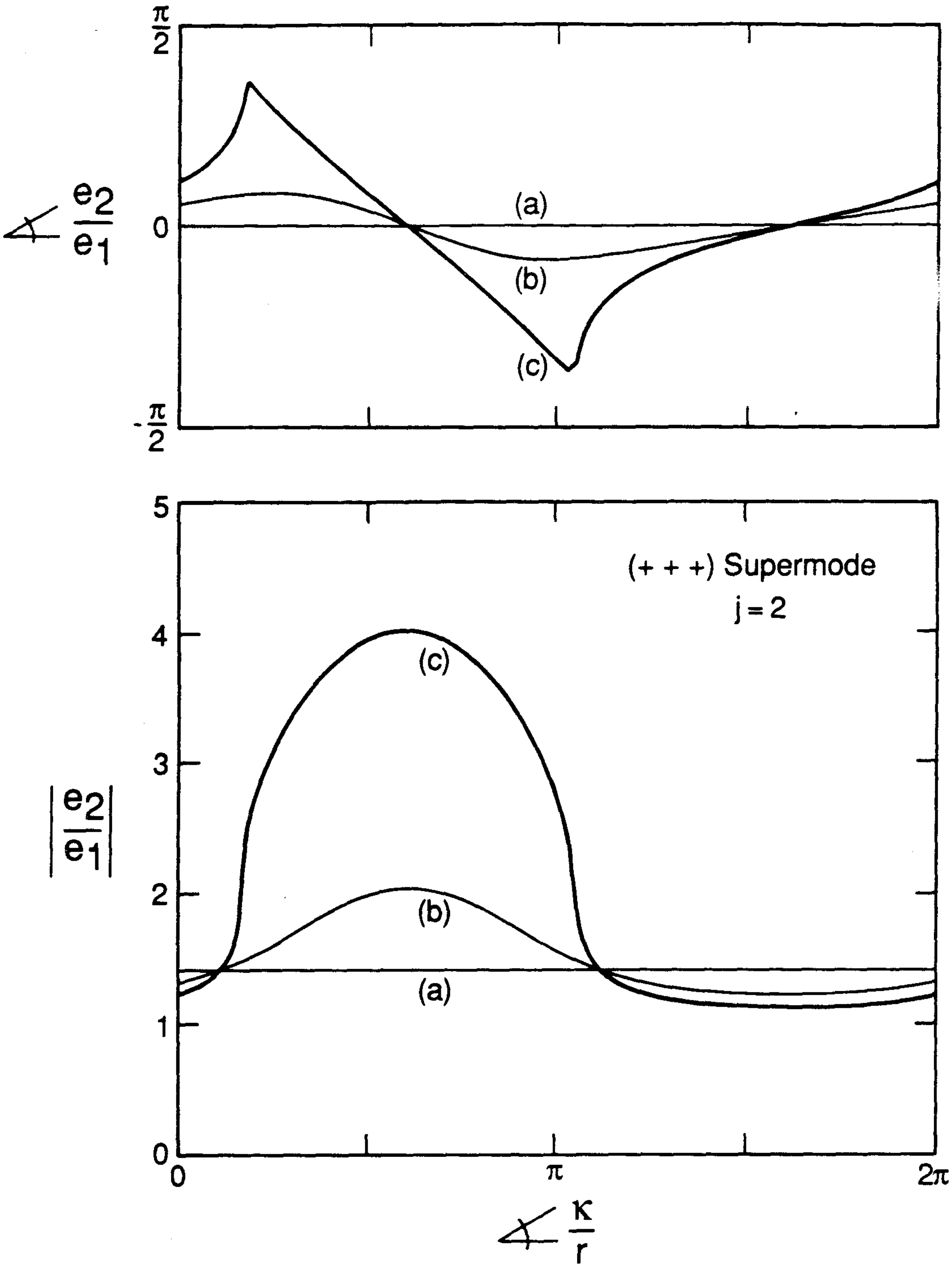

Figure 7.4 *Amplitude (bottom) and phase (top) of the ratio e_2/e_1 for the $(+\ +\ +)$ supermode as a function of coupling constant phase, $\angle\kappa/r$, for 3 values of $|\kappa/r|$: (a) ∞, (b) 1.0, and (c) 0.4. The antiguiding factor used was $b = 2.5$.*

for the $(+\,+\,+)$ supermode at the fixed pumping value $j = 2$. The phase detuning $\angle e_2/e_1$ is zero at the values of $\angle\kappa/r$ for which the amplitude detuning $|e_2|/e_1 - \sqrt{2}$ is maximized (*i.e.*, $|e_2|/e_1$ approaching 1 or ∞). Conversely, the phase detuning $\angle|e_2|/e_1 - m\pi$ is greatest (*i.e.* $\angle e_2/e_1$ approaching $\pm\pi/2$) where the amplitude detuning is zero. The latter case occurs when $\angle\kappa/r$ compensates for the phase of the complex index of refraction in the nonlinear gain term:

$$\angle\kappa/r = -\tan^{-1} b + m\pi, \qquad m \text{ an integer.} \tag{7.17}$$

It is most desirable in terms of modal stability to operate the $(+\,+\,+)$ supermode where $\angle\kappa/r = 2\pi - \tan^{-1} b$, and the $(+\,-\,+)$ supermode where $\angle\kappa/r = \pi - \tan^{-1} b$. The plot of the $(+\,-\,+)$ supermode corresponding to Figure 7.4 has been omitted since, from Equation (7.14), e_2^- can be expressed in terms of e_2^+ via the relation:

$$e_2^+(\angle\kappa/r) = e_2^-(\angle\kappa/r \pm \pi)\ . \tag{7.18}$$

When (7.17) is satisfied, the phase detuning is zero and the amplitude detuning is such that the supermode envelope is flattened to near uniform intensity. This corresponds to minimum divergence and maximum Strehl ratio in the farfield, as we shall see in Section 7.2.

As we have now characterized the general features of the solution, we solve specifically for the supermodes of diffraction-coupled arrays. Figure 7.5 shows how the amplitude and phase of the normalized coupling constant κ/r vary as a function of diffraction-region length for the array considered in Chapter Six. As the length D decreases towards zero, $|\kappa/r|$ falls off very quickly and the phase oscillates through multiples of 2π. Figure 7.6 shows the saturated $(+\,+\,+)$ and $(+\,-\,+)$ supermodes as a function of diffraction region length. Specifically, we plot $|e_2|/e_1$ and $\angle e_2/e_1$ at the pumping level $j = 2$, which is sufficient to ensure near-complete saturation of the gain. As expected, where $\angle\kappa/r \simeq 2\pi - \tan^{-1} b$, the $(+\,+\,+)$ supermode intensity is flattened and the phase detuning is minimal. This condition is satisfied at $D \simeq 90\ \mu$m. Conversely, the $(+\ -\ +)$ supermode envelope is flattened near $D \simeq 200\ \mu$m, where $\angle\kappa/r \simeq \pi - \tan^{-1} b$. Thus, near the diffraction region length where the linear analysis of Chapter Six predicts one supermode to have the lowest threshold gain, that *same* supermode performs optimally in the nonlinear regime. However, the exact location of optimum nonlinear performance is *shifted* to longer D's with respect to the location of optimum gain discrimination, by the phase of the complex-valued nonlinear index detuning, $-\tan^{-1} b$.

7.2 Comments on Supermode Stability

The supermode solutions in Figure 7.6 are not shown for $D < 60\ \mu$m. This is because, experimentally, the lateral coherence was observed to be very poor for devices with such short diffraction regions (see Figure 6.6). As Figure 7.6 indicates, the normalized coupling constant $|\kappa/r|$ decreases rapidly to less than a few percent in this region, while its phase $\angle\kappa/r$ changes from $\simeq 2\pi$ at $D = 60\ \mu$m to $\simeq 5\pi$ at $D = 0$. The resulting supermode discrimination, which varies as $|\kappa/r| \cos \angle\kappa/r$ according to Equation (6.10a), is very small and undergoes rapid oscillations in D (see Figure 6.3). Consequently, competition between supermodes for the available gain is vigorous within this regime. In addition, through amplitude-phase coupling ($b \neq 0$), this competition between supermodes can lead to dynamic instability and sustained pulsations in the laser array output. A stability analysis of diffraction-coupled arrays derived from solution of the time-dependent, coupled-mode equations^5 shows that a supermode with threshold gain γ and oscillation frequency ω is stable when:

$$\gamma - \gamma_0 < 0 \quad , \tag{7.19a}$$

$$\left|\frac{\omega - \omega_0}{\omega_0}\right| < \frac{\lambda}{2n_{eff}}|\gamma - \gamma_0| \; . \tag{7.19b}$$

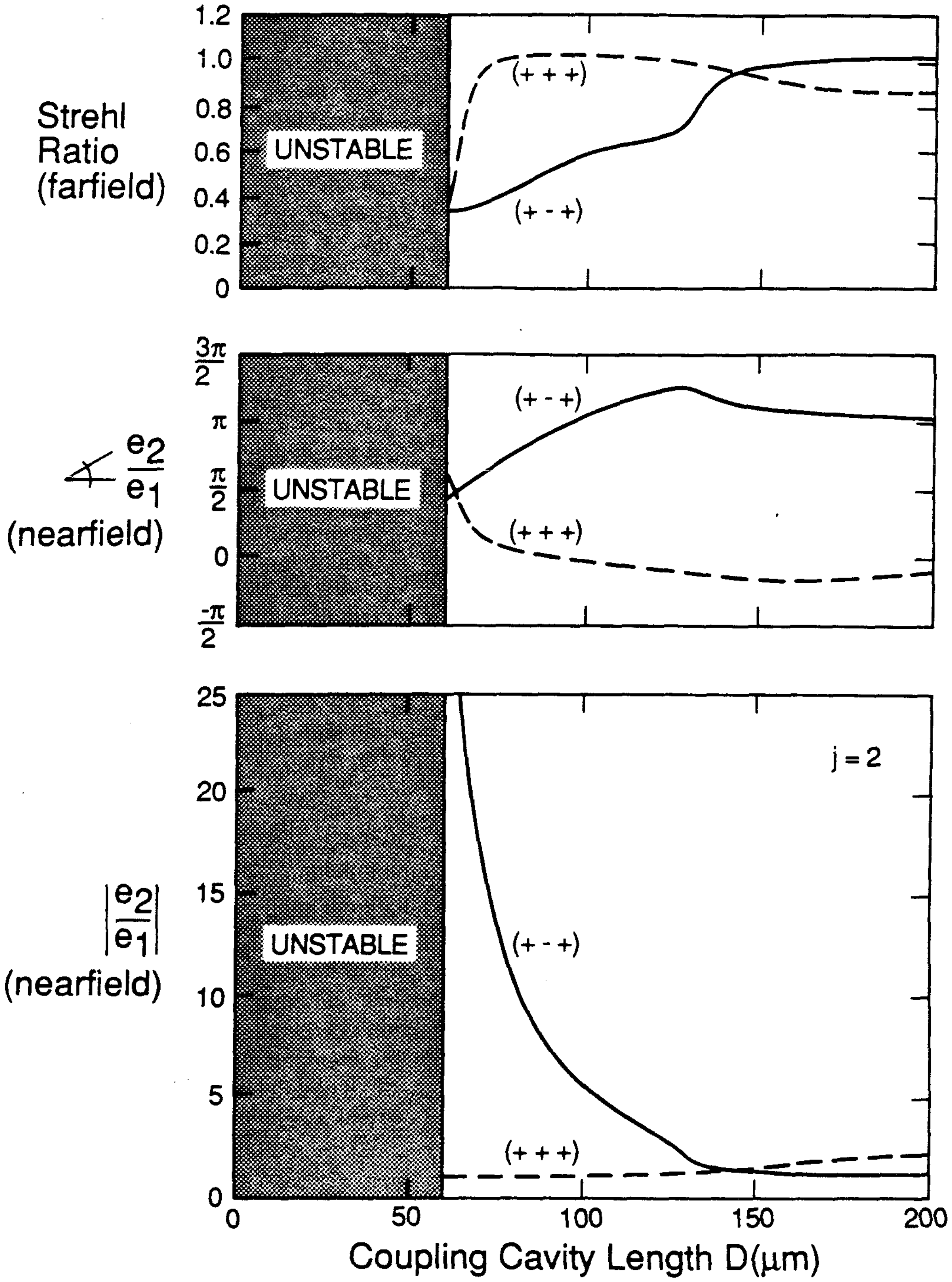

Figure 7.6 *Saturated* $(+++)$ *and* $(+-+)$ *supermodes as a function of diffraction-cavity length,* D*, at the normalized pump current level* $j = 2$*. Amplitude (bottom) and phase (middle) of the ratio* e_2/e_1 *in the nearfield, and the corresponding Strehl ratio (top) in the farfield.*

lateral modes of diffraction-coupled arrays. Furthermore, the gain margin $|\gamma - \gamma_0|$ vanishes wherever the supermode gains cross ($D = 50$, 100 μm in Figure 6.3). Stable regions of D are therefore restricted to windows, about the optimized values, where (7.19b) is satisfied. We expect then, for our device, the $(+\,+\,+)$ supermode to be stable for devices with coupling regions of approximate length $D = 75 \pm 15$ μm, and the $(+\,-\,+)$ supermode to be stable for $D = 160 \pm 50$ μm.

Finally, recent calculations and experiments on distributed-coupling arrays reveal regions of instability even within the injection-locking bandwidth[8-11]. In particular, the high-frequency side of the injection-locking bandwidth can be characterized by a locked state in which the optical intensity pulsates chaotically, when initiated by a step input current, because of competition between supermodes and amplitude-phase coupling ($b \neq 0$) because of fluctuations in carrier density.

7.3 Farfield and Strehl Ratio

In this section, we determine the consequences of gain saturation on the array farfield pattern. In particular, we characterize the farfield by its *Strehl ratio*, defined as the ratio of peak intensity under gain saturation to that just below threshold[12]. Given the complex modal amplitudes (e_1, e_2, e_3) of the nonlinear supermodes in the nearfield, the farfield can be calculated analytically. For convenience, we assume that each channel mode is Gaussian in shape, with complex amplitude e_i, so that the supermode nearfield $S(x)$ is:

$$S(x) = \sum_{i=-1}^{+1} e_i \, e^{-(\frac{x-l_i}{w})^2} \, , \tag{7.21}$$

where $l_{\pm 1} = \pm l$, the channel separation, and w is the half-width of each channel. For the $(+\,+\,+)$ and $(+\,-\,+)$ supermodes, $e_3 = e_1$; in that case the farfield Θ becomes

$$\Theta(k) \cong |\mathcal{F}(S)|^2 = \pi w^2 e^{-\frac{w^2 k^2}{2}} |e_2 + 2e_1 \cos kl|^2 \, , \tag{7.22}$$

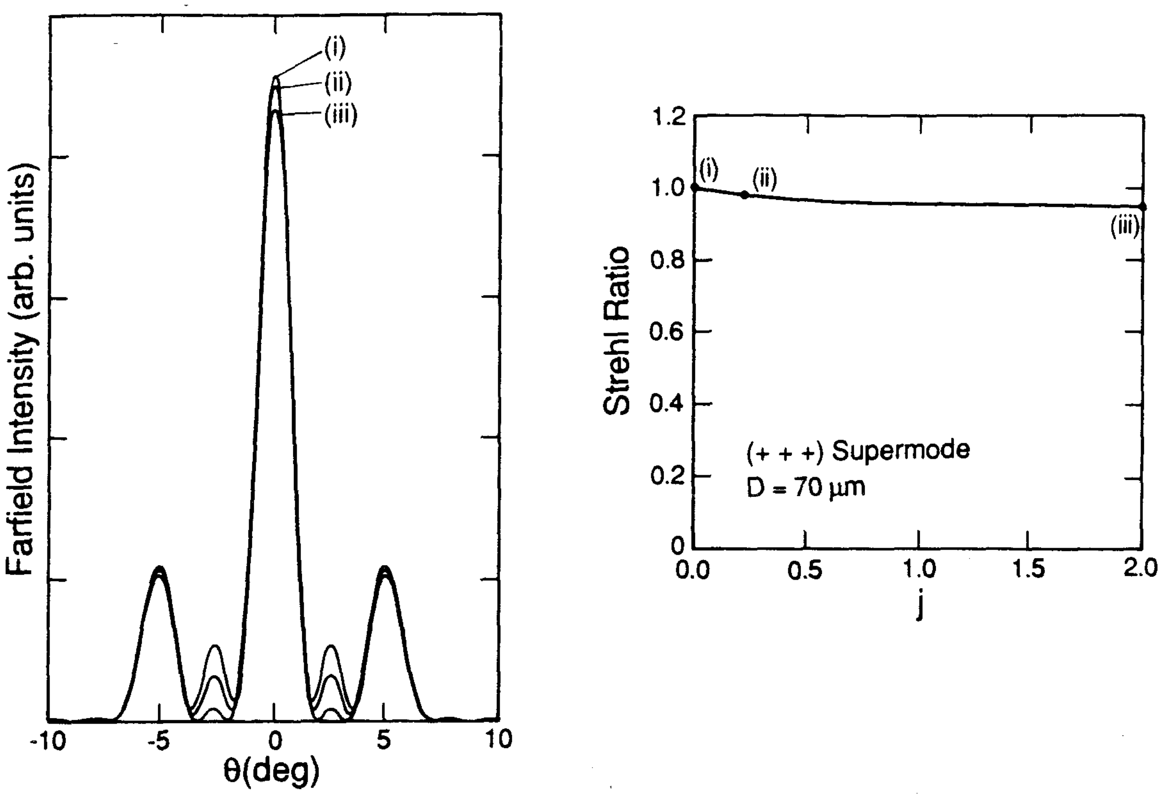

Figure 7.7 *Farfield intensity (left) and Strehl ratio (right) of the* $(+++)$ *supermode at* $D = 70$ *μm as a function of pump current* j. *The farfields are illustrated at the 3 values (i)* $j = 0$, *(ii)* $j = 0.2$, *and (iii)* $j = 2$.

where $\mathcal{F}$ denotes Fourier transformation, and $k \equiv (2\pi/\lambda)\tan\theta$ is the transform variable with θ being the radiation angle in the farfield. The term inside the absolute value signs in Equation (7.22) represents the grating array factor, which is spatially modulated by the Gaussian channel factor preceding it.

Figure 7.7 illustrates the farfield intensity and Strehl ratio, as a function of excess current pumping j above threshold, of the $(+++)$ supermode at $D = 70$ μm. For this value of D, the coupling constant phase $\angle\kappa/r$ is 2π; thus, maximum gain discrimination from the $(+-+)$ supermode is achieved. As a result of the nonlinear detuning in the nearfield phase front, the Strehl ratio in the farfield degrades slightly from 1.0 to approximately 0.95 at $J \simeq 2J_{th}$.

This degradation is worse if we detune $\angle\kappa/r$ from the value 2π to $\simeq 2.1\pi$ by decreasing the diffraction region length from 70 μm to 63 μm. Because of enhanced nearfield phase detuning (approaching $-\pi/2$ at $J = 2J_{th}$), the Strehl ratio degrades very quickly to less than 0.7 times the threshold value. This degradation is illustrated in Figure 7.8. Noteworthy is the fact that the full-width-half-maximum of the central farfield lobe does *not* change significantly with pump current; rather, additional energy appears at angles $\pm\theta$ corresponding to interelement phase differences of $kl = \pm\pi$.

Detuning in the other direction, however, has the opposite effect. Figure 7.8 illustrates again the farfield and Strehl ratio, at $D = 90$ μm, for the $(+\,+\,+)$ supermode ($\angle\kappa/r = 1.67\pi$). Although the nearfield intensity envelope is flattened as before, the phase detuning from "flat-phase" is *negligible*. Resulting from the increased "effective width" in the nearfield, the Strehl ratio actually *increases* by a few percent at $J = 2J_{th}$ over the below-threshold value. The length $D = 90$ μm corresponds closely to the condition $\angle\kappa/r = 2\pi - \tan^{-1} b$ ($b = 2.5$), identified in (7.17) as the point at which the detuning caused by gain saturation is exactly compensated by the coupling constant. Here, the electric fields of adjacent channels add *constructively* upon coupling through the diffraction region. As such, the optimum value of D under the nonlinearity (*i.e.,* that giving the highest Strehl ratio) is detuned to longer D than the unsaturated case, but at the expense of reduced gain discrimination. The same effects are apparent for the $(+\,-\,+)$ supermode near $D = 160$ μm, where $\angle\kappa/r = \pi$. The Strehl ratio degrades with current pumping j to shorter D's, while at longer D (190 μm), it improves to values a few percent greater than unity.

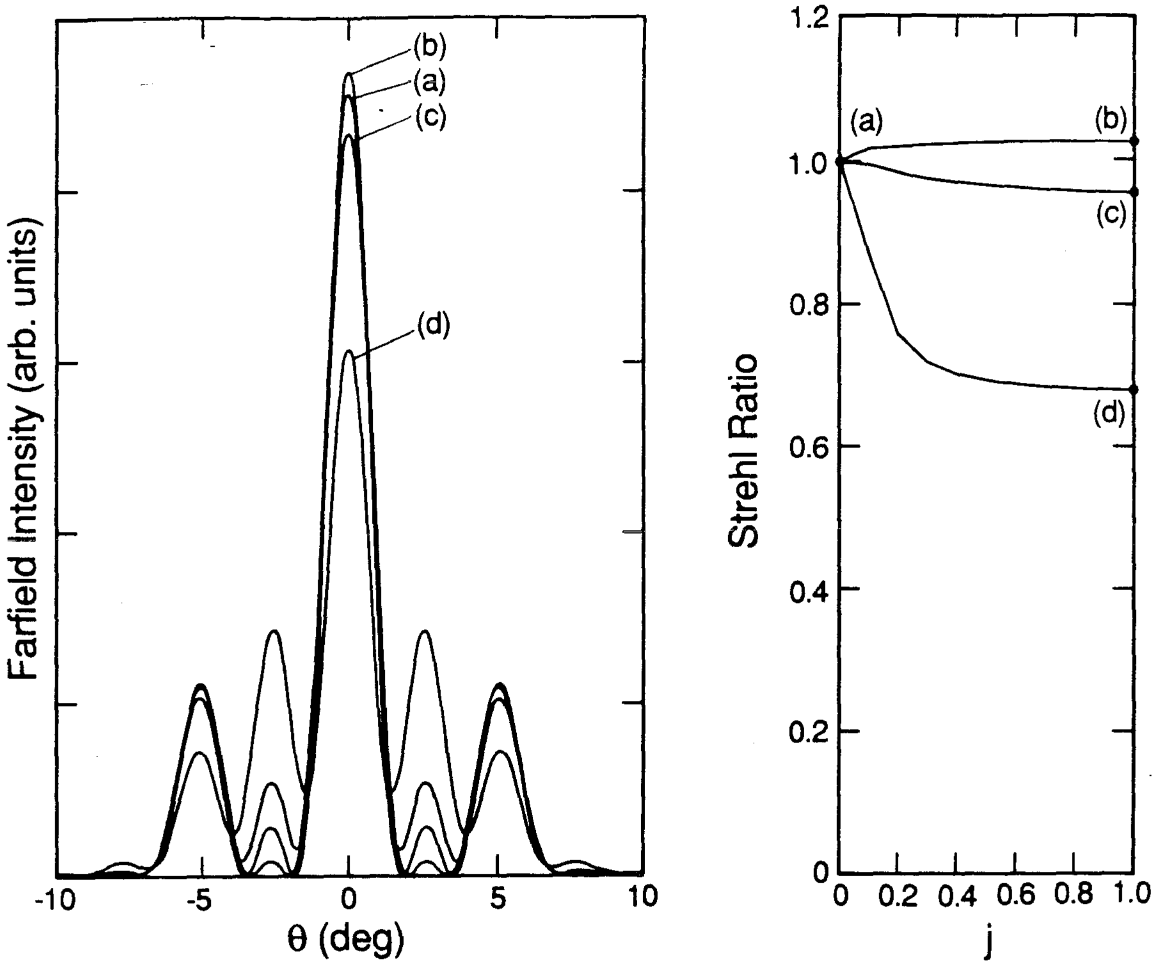

Figure 7.8 *Strehl ratio (right) of the* $(+ + +)$ *supermode at* $D = 70\ \mu m$, $D = 63\ \mu m$, *and* $D = 90\ \mu m$ *as a function of* j. *Farfields (left) are shown at* $j = 0$ *and at* $j = 1$.

7.4 Extension to Distributed-Coupling Arrays

In this section, we show how the formalism (and subsequent conclusions) developed previously for discretely-coupled diffraction-coupled arrays can be applied, via a limiting process, to distributed-coupling arrays. As such, the analysis is essentially a nonlinear coupled-mode theory.

Figure 7.9 illustrates how we will consider a *unit cell* of the distributed-coupling array to be an "unfolded" diffraction-coupled array. Let L be the total length of

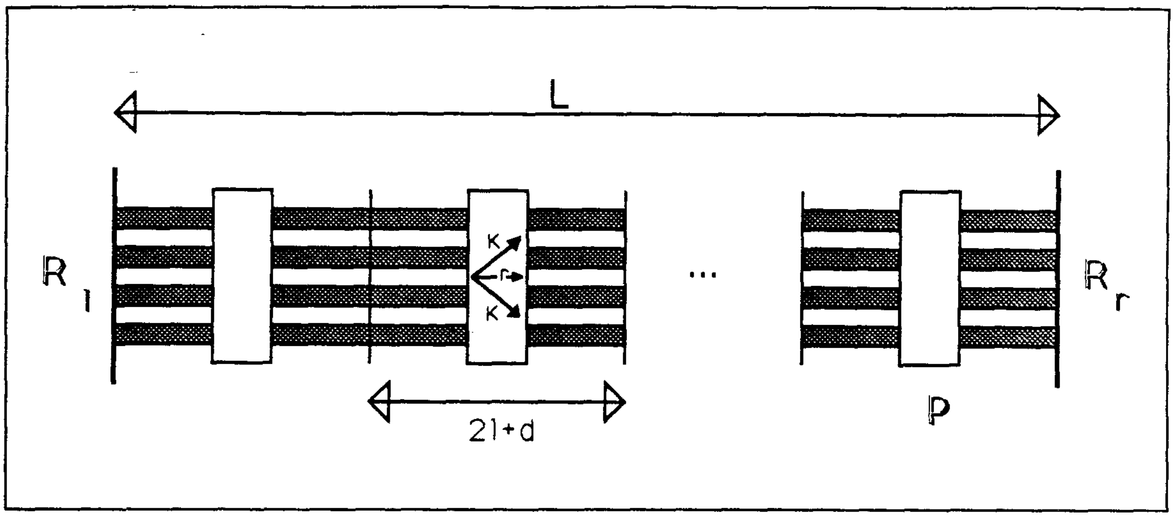

Figure 7.9 *Model of distributed-coupling arrays constructed via end-to-end coupling of diffraction-coupled arrays.*

the distributed-coupling array; it is divided into an integer number of unit cells, each of length $2(l+d)$ where l and d are lengths corresponding to the array and diffraction regions. If we let the number of unit cells go to infinity, while keeping the total length fixed, so that $L/2(l+d) \rightarrow \infty$, then the diffractive coupling within each unit cell effectively models distributed coupling along the total length L.

The self-consistency equation is again Equation (7.1), with $\mathbf{R}_\ell = \mathbf{R}_\mathbf{r} = r_0\mathcal{I}$ and $\mathbf{e}$ as before. However, the propagation matrix $\mathbf{P}$ will be the *product* of propagation matrices within each unit cell. Since the latter are all identical, we have (following (7.5))

$$\mathbf{P} = e^{i(\sigma_1+\sigma_2)L} \begin{pmatrix} r_l e^{i\Delta_l} & \kappa_l & 0 \\ \kappa_l & r_l e^{i\Delta_l} & \kappa_l \\ 0 & \kappa_l & r_l e^{i\Delta_l} \end{pmatrix}^{L/2l} , \tag{7.23}$$

where $\Delta_l = (\sigma_1 - \sigma_2)l$ is the nonlinear detuning accumulated by propagation along length l, and κ_l is the complex-valued cross-coupling within each unit cell. Since $\Delta \propto l$, as $l \rightarrow 0$, we can approximate $e^{i\Delta} \simeq 1 + i\Delta$ and then

$$\mathbf{P} = e^{i(\sigma_1+\sigma_2)L} \lim_{l\rightarrow 0} \left\{ \mathcal{I} + \frac{l}{L}\mathbf{p}^{L/l} \right\} , \tag{7.24}$$

where

$$\mathbf{p} = \begin{pmatrix} i\mathit{\Delta} & \kappa & 0 \\ \kappa & -i\mathit{\Delta} & \kappa \\ 0 & \kappa & i\mathit{\Delta} \end{pmatrix} ,$$

$$\mathit{\Delta} = \mathit{\Delta}_l \cdot \frac{L}{l} = (\sigma_1 - \sigma_2)L , \qquad (7.25)$$

$$\text{and } \kappa = \frac{\kappa_l}{r_l} \cdot \frac{L}{l} .$$

Here $\mathbf{p}$ is the propagation matrix within each unit cell, and $\mathit{\Delta}$, κ are the nonlinear detuning and diffractive-coupling constant prorated over the finite length L of the array. The self-coupling term r_l has been factored out of the matrix and absorbed into the $\exp i(\sigma_1 + \sigma_2)L$ term because it represents a distributed loss and phase shift common to *all* channels. Using the identity

$$\lim_{m \to \infty} \left(1 + \frac{z}{m}\right)^m = e^z , \qquad (7.26)$$

Equation (7.24) reduces to

$$\mathbf{P} = e^{i(\sigma_1+\sigma_2)L} \, e^{\mathbf{p}} . \qquad (7.27)$$

The eigenvalue equation akin to Equation (7.6) is therefore

$$\left(e^{\mathbf{p}} - r_0^{-2} e^{-i(\sigma_1+\sigma_2)L} \mathcal{I}\right) \mathbf{e} = \mathbf{0} . \qquad (7.28)$$

Hence, $\lambda = r_0^{-2} e^{-i(\sigma_1+\sigma_2)L}$ are the eigenvalues of $e^{\mathbf{p}}$. Computation of the matrix $e^{\mathbf{p}}$ is straightforward if we first diagonalize $\mathbf{p}$ according to

$$\mathbf{p} = \mathbf{U} \mathbf{\Lambda} \mathbf{U}^{\mathrm{H}} , \qquad (7.29)$$

where Λ is a complex-valued diagonal matrix whose eigenvalues are the same as those of $\mathbf{p}$, and $\mathbf{U}$ is a complex-valued unitary matrix whose column vectors are the eigenvectors of $\mathbf{p}$. It is easy to show that

$$e^{\mathbf{p}} = \mathbf{U} e^{\mathbf{\Lambda}} \mathbf{U}^{\mathrm{H}} . \qquad (7.30)$$

Since $\mathbf{\Lambda}$ is diagonal, then $e^{\mathbf{\Lambda}}$ is also diagonal. If the eigenvalues of $\mathbf{p}$ are λ_p, then the eigenvalues of $e^{\mathbf{p}}$ and $e^{\mathbf{\Lambda}}$ are e^{λ_p} (that is, $\lambda = e^{\lambda_p}$). The eigen*vectors* of $e^{\mathbf{p}}$ are the same as those of $\mathbf{p}$. The eigenvalues and eigenvectors of the distributed coupling array are found from (7.28) and are summarized as follows:

$$
\begin{aligned}
(+0-)\ \text{supermode}: \qquad & \sigma_1 + \sigma_2 = -\frac{i}{L} \ln\left(\frac{1}{r_0^2} + \frac{\Delta}{L}\right) , \\
& e_3 = -e_1 , \\
& e_2 = 0 , \\
(+\pm+)\ \text{supermodes}: \qquad & \sigma_1 + \sigma_2 = -\frac{i}{L} \ln\left(\frac{1}{r_0^2} \pm \frac{\sqrt{2\kappa^2 - \Delta^2}}{L}\right) , \\
& e_3 = e_1 , \\
& \frac{2}{e_2/e_1} = i\frac{\Delta}{\kappa} \pm \sqrt{2 + (i\frac{\Delta}{\kappa})^2} .
\end{aligned}
\qquad (7.31)
$$

Equations (7.31) are identical to Equation (7.16) with the substitution $\sin \Delta \rightarrow \Delta$ appropriate for a coupled-mode formulation. Noting that the ratio Δ/κ is independent of the array length L, and that Δ is always small compared to unity, we conclude that differences between the gain-saturated supermodes of *distributed coupling* versus *discrete coupling* arrays are negligible.

7.5 Conclusions

To summarize, we have calculated the supermodes of index-guided laser arrays that are self-consistent with nonuniformly saturated gain and refractive index profiles. Our results indicate that, in general, the nonlinearity introduces wavefront aberrations into the supermodes that degrade the Strehl ratio of the farfield pattern. That is, although the beamwidth of the central lobe in the farfield is not a sensitive function of pump current, the proportion of energy contained within that central lobe decreases as a function of increasing pump energy. However, freedom exists in diffraction-coupled arrays to tailor the phase of the coupling constant so as to *compensate* for the intensity-induced wavefront detuning. The analysis predicts that for optimum Strehl ratio, the length of diffraction region should be shifted to longer D than that predicted by the below-threshold analysis of Chapter Six. This improvement in Strehl ratio is achieved at the expense of mode discrimination between supermodes.

A clearer understanding of the farfield degradation can be gleaned by considering the intensity-induced changes in gain and refractive index as a spatial perturbation tht mixes the unsaturated supermodes. The mixing is consistent with the predictions of simple perturbation theory for a nondegenerate eigenmode. The nonlinear eigenfunction $|n(j)>$ (denoting the n^{th}-order supermode) is altered from the linear one $|n(0)>$ via[13]

$$|n(j)>=|n(0)>+\sum_{m\neq n}\frac{<m(0)|W(j)|n(0)>}{\beta_n^2-\beta_m^2}|m(0)>+\ldots \tag{7.32}$$

where $W(j)$ is the current-dependent perturbation, β_n is the unsaturated supermode propagation constant, and $<m(0)|W(j)|n(0)>$ is the usual overlap integral. Even though the nonlinear eigenvalue problem is not self-adjoint, the orthogonality of the below-threshold eigenfunctions enables the application of perturbation theory here. It is straightforward to show from (7.32) that

$$\begin{aligned}|1(j)> &= |1(0)>+\alpha(j)|3(0)>\ ,\\ |2(j)> &= |2(0)>\ ,\\ |3(j)> &= |3(0)>-\alpha(j)|1(0)>\ ,\end{aligned} \tag{7.33}$$

where $\alpha(j)=<1(0)|W(j)|3(0)>/(\beta_1^2-\beta_3^2)$. When $|1(j)>$ or $|3(j)>$ is the lasing supermode, the resulting spatial perturbation $W(j)$ is proportional to $|3(0)>$. Hence, $<1(0)|W(j)|3(0)>\neq 0$, implying that the $(+++)$ and $(+-+)$ supermodes are strongly mixed. All other overlap integrals are negligible. Equation (7.33) states that for a given fixed D, the $(+++)$ and $(+-+)$ supermode envelopes change in a complementary fashion. This prediction is borne out by Figure 7.6. The mixing of $(+-+)$ into $(+++)$ is manifest with the appearance, in Figure 7.8, of sidelobe energy at farfield angles $\pm\theta$ corresponding to lateral k-vectors that satisfy $kl = \pm\pi$. This farfield degradation is due *not* to a breakdown in spatial coherence, but to wavefront aberrations introduced by the gain saturation nonlinearity. Extension of this perturbation analysis to N-element arrays would predict mixing of several higher-order supermodes with the fundamental. Thus, the appearance of a broad intensity background in the farfield at elevated power levels is to be expected from even *ideally* fabricated semiconductor laser arrays.

Coupled semiconductor lasers are mutually injection-locked oscillators. This analogy is especially evident from the geometry of diffraction-coupled arrays. However, the natural frequencies of individual array elements must be nearly identical for the mutual power injection to result in stable phase locking. In practice, this requirement places stringent tolerances on material growth and device fabrication. Furthermore, intensity-induced detuning between waveguides of different average optical intensity can lead to coherence collapse. While acting to the detriment of coupled laser oscillators, this property may be taken advantage of in the fabrication of photonic switching devices. For example, the nonlinear directional coupler[14] realizes all-optical switching as follows: At low input powers, optical energy is exchanged periodically between two coupled, phase-matched waveguides, as in the linear case[15]. Above a critical input power, however, the waveguides become detuned to such an extent that no switching occurs. Thus, switching can be accomplished by variation of the input power level. The techniques developed in this thesis may be applied to the design of, for example, multi-element switching amplifiers.

Within this thesis, the results of our investigation into broad area structures have elucidated the duality between gain-guided and index-guided lasers, and can be summarized as follows:

(i) Gain-guided structures possess inherently strong interelement coupling, but suffer from poor mode discrimination. The distinction between broad area laser and laser array is blurred for these devices; in either case, gain saturation results in multimode operation at current levels just above threshold.

(ii) Conversely, index-guided structures may be designed to possess large mode discrimination, but generally suffer from weak interelement coupling. As a result, the tolerances on material growth and device fabrication are formidable. Commercial devices are highly priced because of low yield.

The achievement of high power into a single mode requires structures that possess strong interelement coupling and large mode discrimination. For example, as resonant coupling provides large longitudinal mode discrimination in a distributed feedback laser, so might a structure based on resonant coupling of waveguides in the lateral direction provide large lateral mode discrimination. However, such structures must also be designed so as to *desensitize* mode shapes and propagation constants to perturbations caused by temperature or intensity gradients, and by material and fabrication inhomogeneities. Only then will single-mode, single-frequency semiconductor laser emission persist into the high-power regime.

References

[1] K. Lau and A. Yariv, "High-frequency current modulation of semiconductor lasers," in *Semiconductors and Semimetals, vol. 22,* (Academic Press, Orlando 1985).

[2] J. Wilcox, M. Jansen, J. Yang, G. Peterson, A. Silver, W. Simmons, S. Ou, and M. Sergant, "Supermode discrimination in diffraction-coupled laser arrays with separate contacts," *Appl. Phys. Lett.* **51**, 631-633 (1987).

[3] C. Chang-Hasnain and E. Kapon, private communication (May, 1989).

[4] J. Katz, E. Kapon, S. Margalit, and A. Yariv, "Rate equation analysis of phase-locked semiconductor laser arrays under steady-state conditions," *IEEE J. Quant. Electr.* **QE-20**, 875-879 (1984).

[5] N. Basov, E. Belenov, and V. Letokhov, "Diffraction synchronization of lasers," *Soviet Physics - Technical Physics* **10**, 845-850 (1965).

[6] H. Haus, *Waves and Fields in Optoelectronics*, 229, (Prentice-Hall, New York 1984).

[7] E. Garmire, "Tolerances for phase-locking of semiconductor laser arrays," paper [893-15], *OE-Lase:* Optoelectronics and Laser Applications in Science and Engineering, Jan. 10-17 1988, Los Angeles CA.

[8] H. Winful and S. Wang, "Stability of phase-locking in coupled semiconductor laser arrays," *Appl. Phys. Lett.* **53**, 1894-1896 (1988).

[9] S. Wang and H. Winful, "Dynamics of phase-locked semiconductor laser arrays," *Appl. Phys. Lett.* **52**, 1774-1776 (1988).

[10] R. Elliott, R.K. DeFreez, T.L. Paoli, R. Burnham, and W. Streifer, "Dynamic characteristics of phase-locked multiple quantum well injection lasers," *IEEE J. Quant. Electr.* **QE-21**, 598-602 (1985).

[11] R. Lang, "Injection locking properties of semiconductor lasers," *IEEE J. Quant. Electr.* **QE-18**, 976-983 (1982).

[12] W. Streifer, D. Welch, J. Berger, and D. Scifres, "Above-threshold analysis of ideal Y-junction semiconductor laser arrays," *Appl. Phys. Lett.* **54**, 409-411 (1989).

[13] A. Yariv, *Theory and Applications of Quantum Mechanics*, 117 (Wiley, New York 1982).

[14] S.M. Jansen, "The nonlinear coherent coupler," *IEEE J. Quant. Electr.* **QE-18**, 1580-1583 (1982).

[15] A. Yariv, "Coupled-mode theory for guided-wave optics," *IEEE J. Quant. Elect.* **QE-9**, 919-933 (1973).